# Flow in the Vascular System Post Stent Implantation: Examining the Near-Stent Flow Physics to Guide Next-Generation Stent Design

by

Chekema Prince

A thesis
presented to the University of Waterloo
in fulfillment of the
thesis requirement for the degree of
Doctor of Philosophy
in
Mechanical Engineering

Waterloo, Ontario, Canada, 2014

## AUTHOR'S DECLARATION

I hereby declare that I am the sole author of this thesis. This is a true copy of the thesis, including any required final revisions, as accepted by my examiners. I understand that my thesis may be made electronically available to the public.

# Abstract

The prevalence of cardiovascular disease (CVD) has increased dramatically due in part to the increased rates of obesity in North America. Atherosclerosis, the most prevalent type of CVD, is a progressive disease characterized by the build-up of plaque within the arteries. The plaque development leads to the narrowing of arteries, referred to as stenosis, and restricts crucial blood flow to the organs of the body. This condition is often treated by the implantation of a stent, a wire mesh scaffold device placed in the region of an atherosclerotic plaque after balloon angioplasty. The stent was developed to improve the clinical outcome of angioplasty procedures by mitigating the effects of elastic recoil by the vessel wall and maintaining vessel patency after angioplasty. Since the introduction of stents as a treatment option over a decade ago, in-stent restenosis (ISR) has been an iatrogenic outcome and remains an unsolved limitation of the interventional treatment device, resulting in stent failure and additional surgical procedures to restore blood flow. Many improvements have been made in stent design in order to reduce the likelihood of ISR, but none have eliminated the problem. Endothelial cells lining vessel walls transduce local hemodynamic loading in the stent vicinity, such as wall shear stress magnitude (WSS), into biochemical signals that lead to the progression of ISR. Hence, resolving the hemodynamics in the vicinity of the stent is crucial to reducing the rates of stent failure.

The objective of the study is to address the problem of ISR by clearly elucidating the flow physics induced by stent implantation, accounting in particular for vessel curvature, by first considering idealized stent models, then progressing to an actual stent model. Stent designs are typically based upon data originating solely from studies of flow in straight vessels, which, once optimized for this configuration, may lead to suboptimal performance when placed in tortuous vessels. Previous stent studies have almost categorically neglected the effects of curvature on the flow physics, despite the fact that even extremely mild curvature changes the axial WSSM distribution within the vessel and induces the development of secondary flows, which alters the advection of chemicals released into the lumen. Using computational fluid dynamics (CFD) techniques, this study seeks to (i) determine the impact of stent strut amplitude and frequency on primary and secondary flow structures; (ii) determine the significance of the stent strut shape in the size of the stagnation zone; (iii) evaluate flow behavior in the transition region from smooth walled to stented vessel; and (iv) examine the collection of these effects in a full stent model geometry in a curved tube. This study takes a systematic approach, dissecting the impact of the

stent first into simplified foundational components, then investigating each component and finally synthesizing the components into a full stent model with the long-term goal of optimizing stent design to reduce the rate of restenosis. As well, the study findings can aid in understanding the signal transduction mechanisms of the endothelial cells, which play a role in the development of ISR, and reduce the cardiovascular disease mortality rate by improving the clinical outcome of treatment procedures. Further, the study findings contribute to the fundamental understanding of flow in curved pipes with wall protrusions, the impact of the choice of the constitutive model of the fluid, and the hemodynamic environment in the vicinity of the stent.

# Acknowledgements

Committee Members

# Table of Contents

# List of Figures

# List of Tables

# List of Abbreviations

*RCA* – Right Coronary Artery

TAWSS – Time averged wall shear stress

TAWSSM – Time averged wall shear stress magnitude

TAWSSG – Time averged wall shear stress gradient

WSS – Wall shear stress

WSSM – Wall shear stress magnitude

WSSG – Wall shear stress gradient

# List of Symbols

| | |
|---|---|
| $a$ | pipe radius |
| $a_{\omega 0}$ | boundary layer thickness based upon zero vorticity contour |
| A | cross-sectional area of the pipe |
| AS | angled strut |
| $C_{f\varphi}$ | circumferential skin friction |
| $C_{fa}$ | axial skin friction |
| $c$ | converging strut region |
| $D$ | diameter of tube |
| $d$ | diverging strut region |
| $d_n$ | coefficients for Van Dyke's series solution |
| $E$ | node east of the P node in numerical grid |
| $f_{e.}$ | the face between the $P$ node and $E$ node |
| $f_w$ | the face between $W$ node and $P$ node |
| $G$ | axial pressure gradient |
| I | inner wall |
| IS | strut intersection |
| $i$ | power law index |
| $j$ | Yasuda exponent |
| $K$ | Dean number |
| L | axial distance along pipe centerline |
| $l$ | wavelength |
| $l_a$ | stent cell axial length |
| $l_c$ | circumferential distance between struts intersections |
| $\dot{m}$ | mass flow rate |
| $m$ | total number of circumferential protrusions |
| $N$ | grid number |
| $n$ | number of protrusions |
| O | outer wall |
| $p$ | pressure |

| | |
|---|---|
| $P$ | reference node in numerical grid |
| $Q$ | volumetric flow rate |
| $Q_c$ | volumetric flow rate in the curved pipe |
| $Q_s$ | volumetric flow rate in the straight pipe |
| $r_{tube}$ | radius of the tube |
| $R$ | radius of curvature |
| $R\theta$ | arclength |
| $R_c$ | resistance coefficient |
| $Rc_c$ | coefficient of resistance in a curved pipe |
| $Rc_s$ | coefficient of resistance in a straight pipe |
| Re | Reynolds number |
| $r\alpha$ | local polar coordinate system |
| $S_{M_i}$ | momentum source |
| $\bar{V}$ | spatially averaged velocity |
| $V_i$ | velocity vector |
| $\|V\|$ | velocity magnitude |
| $W$ | node west of the P node in numerical grid |
| $X,Y,Z$ | global fixed coordinate system |
| $x,y,z$ | local Cartesian system |
| $r\ \varphi$ | local polar coordinate system |

Greek Symbols

| | |
|---|---|
| α | polar coordinate angle within pipe cross-section |
| Γ | vortex circulation |
| δ | radius to radius of curvature ratio (= $a/R$) |
| $\varepsilon$ | protrusion height |
| θ | angle from entrance to exit of the curved pipe |
| $\theta_e$ | interior angle for an equiangular face/cell |
| $\theta_{min}$ | minimum angle in the face or cell |
| $\theta_{max}$ | maximum angle in the face or cell |
| κ | Dean number (alternative definition) |
| $\lambda$ | second viscosity coefficient |

| | |
|---|---|
| $\mu$ | dynamic viscosity of the working fluid |
| $\mu_0$ | low shear viscosity |
| $\mu_\infty$ | infinite shear viscosity |
| $\nu$ | kinematic viscosity of the working fluid |
| $\varphi$ | local polar coordinate |
| $\rho$ | density of the working fluid |
| $\tau_x, \tau_y, \tau_z$ | wall shear stress component |
| $\overline{\tau_a}$ | average axial wall shear stress |
| $\lvert\tau\rvert$ | wall shear stress magnitude |
| $\lvert\nabla\tau\rvert$ | wall shear stress gradient magnitude |
| $\vec{\omega}$ | vorticity |
| $\xi$ | protrusion width |
| $\psi$ | primary flow intrastrut angle |

# Chapter 1
# Introduction

Curvature in the vascular system produces complex flow structures in the blood vessels, characterized by skewed axial velocity profiles and secondary flows. Recent literature has focused on the role these complex flow structures play in cardiovascular health and disease[1,2]. In particular, secondary flow has been linked to the inception and progression of atherosclerosis, the most prevalent cardiovascular disease. Atherosclerosis is a condition in which plaque builds up within the lumen of the vessel and results in stenosis, a narrowing of the vessel lumen [3]. This condition causes the reduction of normal blood flow to vital organs of the body. Atherosclerosis can lead to stroke, heart attack, and loss of life. An inadequate diet has been proven to introduce disease catalysts, such as cholesterol, into the vascular system [4]. These catalysts can be transported by primary and secondary flows to specific locations on the vascular wall and trigger the formation of plaques [5,6].

Advances in medical technology have led to the development of many atherosclerosis treatments. Most significantly, balloon angioplasty is used to restore blood flow by breaking up plaques via the expansion of the vessel lumen. A wire mesh scaffold, called a stent, is implanted after the angioplasty procedure and prevents the elastic properties of the vessel walls from causing the vessel to collapse. The introduction of the stent into the vasculature provides the overall benefit of ensuring the blood vessel will remain open after angioplasty. Unfortunately, the normal blood flow pattern typically found in healthy blood vessels will not be restored due to the presence of the mechanical device. In particular, the normal axial and secondary flow patterns may be altered and result in in-stent restenosis or stenosis proximal or distal to the stent. The work exhibited in this proposal aims to understand the impact of stent implantation on flow behavior in curved vessels, with the ultimate goal of providing guidelines for improving stent design.

## 1.1 Background

### 1.1.1 *Vessel Wall Anatomy*

The vascular wall is composed of three layers which, listed from the outer wall to the luminal side, are the adventia, the media and the intima, as shown in Figure 1.1. The adventia, the outermost layer, is entirely composed of fibroelastic connective tissue, nutrient vessels and

autonomic nerves[7]. The nutrient vessels, such as vaso vasorm, provide blood supply and nourishment for the adventia and the outer parts of the media of large vessels. The media layer, the middle and thickest layer, provides structural support and is predominately comprised of smooth muscle cells (SMC) and elastin lamina [7]. The SMC are in a quiescent state under normal healthy conditions, and proliferate in response to vessel injury or disease state[8,9]. The smooth muscle cells allow the blood vessel to undergo vasoconstriction (reduction of the lumen diameter due to SMC contraction) and vasodilation (increase in lumen diameter due to SMC relaxation) [10]. The vasoreactivity of SMCs is controlled by autonomic nerves and local chemical signals in order to dictate blood flow. The elastin lamina provides structural support and allows the vessel to stretch and contract during vascular remodeling [7].

The intima, the innermost and thinnest layer, contains the endothelium, comprised of a single layer of endothelial cells (EC). ECs line the inner surface of all blood vessels and act as biosensors to monitor the luminal environment [11]. Bio-sensing elements, such as protein receptors and adhesion molecules on the cell surface, can detect changes in blood composition and hemodynamics [12-14] . ECs transduce the signals received from the lumen into biochemical signals that influence vessel function and structure [13]. They control important vascular homeostatic functions, such as thrombolysis and coagulation processes, inflammatory and immunological reactions, and vasoconstriction and vasodilation [7]. The ECs participate in these homeostatic processes by regulating vascular wall permeability and controlling the production, secretion, and metabolism of biochemical substances.

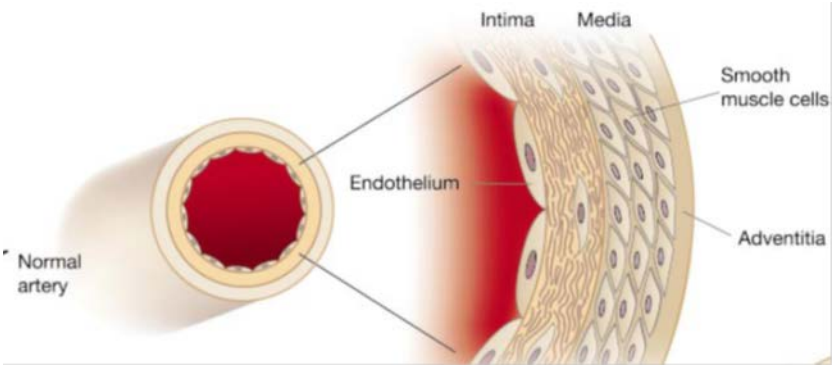


**Figure 1.1 An illustration of the three layers of the vascular wall, listed from the outer wall to the luminal side: the adventitia, media and the intima (Adapted from [6]).**

ECs act as a thromboresistant layer to prevent circulating platelets from adhering to and aggregating on the vessel wall [15,16]. Platelets are small, disk shaped cell fragments about 2-4μm in

diameter that circulate in the blood stream [10]. They play a key role in the stoppage of bleeding by aggregating to form a plug and initiating a sequence of events that lead to blood clot formation[10]. To prevent platelet aggregation in healthy vessels, platelet derived serotonin, adenosine diphosphate (ADP) and thrombin bind to receptors on the endothelial surface, which initiates a biochemical cascade releasing vasodilators such as nitric oxide (NO) and prostaglandins[15]. Specifically, NO mediates the relaxation of SMC in the media layer resulting in increased blood flow and inhibition of the coagulation processes [15]. In addition, NO has been shown to promote endothelial regeneration and leukocyte transmigration into the vessel wall. Endothelial dysfunction or damage to the endothelium can cause an imbalance between vasoconstriction and vasodilatation, and procoagulant and anticoagulant factors, leading to a vascular environment conducive to vascular disease.

Recent literature has focused on the mechanosensing properties of ECs. In particular, the impact of WSS on EC structure and function has been investigated extensively[17,18]. WSS is proportional to the frictional force generated by a moving viscous fluid, in this case blood, at the vessel walls [17]. For a Newtonian fluid, it is equal to the product of the fluid viscosity and wall-normal velocity gradient, $\tau_w = \mu \frac{\partial u}{\partial r}$ , where μ is the dynamic viscosity and $\frac{\partial u}{\partial r}$ is wall-normal velocity gradient [19]. However, blood is composed of 55% blood plasma that is predominately water and 45% formed elements such as platelets, white blood cells and red blood cells [10]. Blood is known to be non-Newtonian and shear thinning mainly due to the suspension of red blood cells. The red blood cells aggregate in the center of the blood vessel defining a region largely dominated by non-Newtonian effects[20,21].This leads to the formation of a cell free or cell deprived blood plasma layer adjacent to the endothelium where WSS is dictated by Newtonian flow behavior [21].Thus, non-Newtonian effects are small for relatively large vessels and would play a more significant role in smaller vessels[21].

Shear stress causes EC deformation resulting in the elongation of the cell in the direction of flow[22,23]. The structural changes of ECs as a result of mechanical forces have been shown to modify intracellular signaling, gene expression, protein expression, and cell function [12]. These changes in EC physiology affect biochemical pathways that control vessel health and structure. For example, the endothelium's role in vascular remodeling is mediated by WSS through the release of vasoconstrictors and vasodilators. Increased blood flow can lead to increases in WSS that result in endothelium release of the vasodilators PGI2 and NO and decreased amounts of the vasoconstrictor endothelin-1 (ET1), culminating in hemodynamic-induced vasodilation [24].

### 1.1.2 *Atherosclerosis*

According to World Health Organization (WHO) estimates, 17.5 million people died of cardiovascular disease (CVD) in 2005, accounting for 30% of all deaths globally. In the US, 1 in 2.9 deaths were caused by CVD, and direct and indirect costs were estimated to be $286 billion for 2007 [25]. Understanding the etiology and progression of CVD can save the lives of millions of people worldwide. Atherosclerosis is a chronic progressive CVD that creates life threatening blockages and is characterized by the build-up of plaque within arteries [8]. The plaque, comprised of lipids and fibrous elements, results in the narrowing and stiffening of arteries, see Figure 1.2 [3]. The narrowing of the arteries results in the restriction of crucial blood flow to the organs of the body.

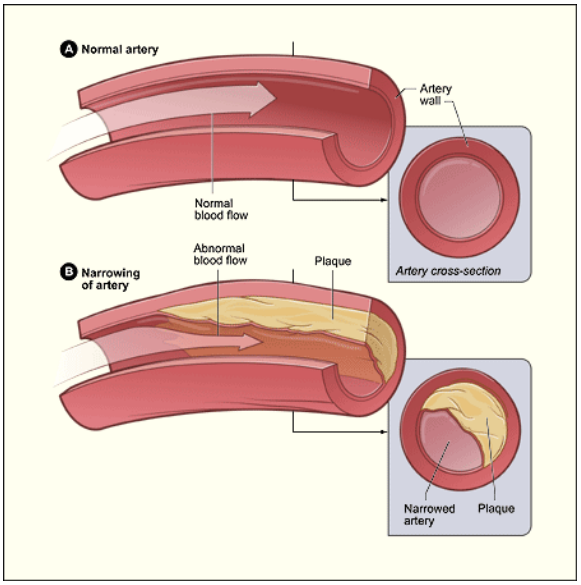


**Figure 1.2 An illustration of blood vessel narrowing as a result of plaque buildup (Adapted from [86]).**

Many studies have linked the development and progression of atherosclerosis to vascular hemodynamics [8,12,14,26]. Branches and curves within the vascular system produce hemodynamic conditions that make these areas more susceptible to plaque deposition, see Figure 1.3. Areas of low WSS have been correlated with atherosclerotic plaque formation [27,28]. The regions of the vessel wall with low WSS magnitude but high WSS gradient shows increased EC turnover rate. The turnover rate has been correlated with increased permeability of EC to macromolecules such as low-density lipoproteins (LDL). Studies have shown increased permeability to LDLs in

atherosclerotic prone sites contributing to disease progression in these regions [12]. Atherosclerotic plaque contains macrophages, which are derived from monocytes [6]. Monocytes are a type of white blood cell that is attracted to the vessel wall by signaling factors released by ECs [29,30]. Local hemodynamics may play a role in the transport of monocytes to the vessel wall. Low WSS may enhance monocytes adhesion by providing slower moving monocytes more opportunity to adhere by activating the expression of adhesion molecules on endothelial cells [5].

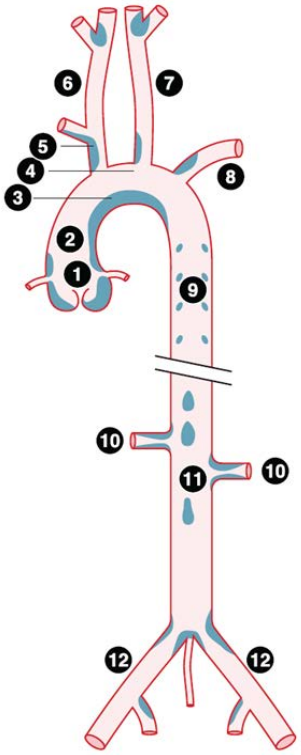


**Figure 1.3 A schematic of a longitudinal representation of the major arterial vasculature and locations of arterial branches and curves where atherosclerosis preferentially develops. Adapted from [85].**

### 1.1.3 *Disease Intervention: Stent Implantation*

The build-up of atherosclerotic plaque in a blood vessel causes stenosis, which is the narrowing of the vessel lumen[10]. This condition is often treated using balloon angioplasty, which is a procedure that uses a catheter-tip balloon to return the lumen to its native diameter in the

region of the atherosclerotic plaque [31]. A stent, a wire mesh scaffold, is placed in the reopened region to mitigate the effects of elastic recoil by the vessel wall and to maintain vessel patency after angioplasty [32,33]. The stent is preloaded in a collapsed form upon a catheter and enters the vascular system via the femoral arteries or radial arteries [34]. From the entry location, the device is advanced distally through the tortuous vascular system and delivered to the region of the atherosclerotic lesion and expanded within the vessel. There are a large number of stents with different geometrical and mechanical features available on the market. Since initial trials in 1986, stent designs have evolved to balance the need of long term stability with the acute requirement of easy delivery to the target site and deployment [33,35]. The long term stability of the stent depends on the device not only supporting the vessel wall but promoting the reinstitution of a healthy endothelium.

The basic structural design of a stent includes an array of repeating wire elements referred to as struts. A stent ring is a series of struts that traverse the circumference of the circular structure. Adjacent strut rings are joined by bridges, which connect the rings to form a repeating pattern. The targeted vessel for deployment and the size of the atherosclerotic lesion dictate the diameter and length of the stent to be implanted. The typical stent can vary in length from 8mm – 38mm and diameter from 2.25mm – 4mm. The thickness of the wire struts can range from 0.05mm to 0.14mm.

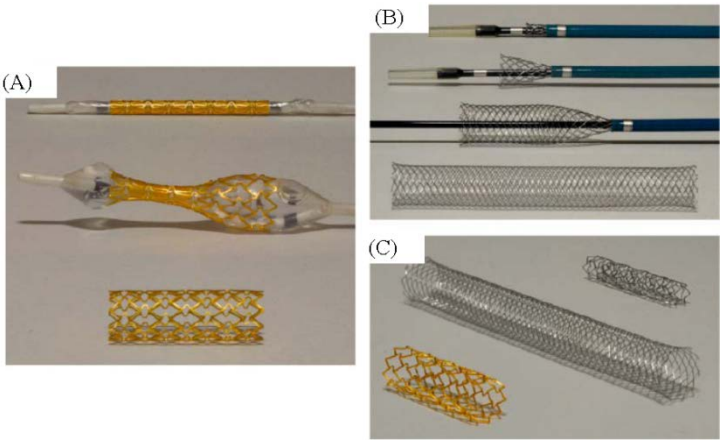


**Figure 1.4 Various stent designs: (A) Balloon-Expandable Stent, (B) Self-expanding stent, (C) Range of stent geometries (Adapted from [29]).**

Commercially available stents are typically categorized by the method of deployment, strut pattern, and the material and functionality of the wire struts. Based on the method of deployment, the stents are classified as balloon expandable stents or self-expanding stents [36]. A balloon-expandable stent, see Figure 1.4(A), is manufactured in a compressed state and put over a balloon catheter to be guided into the area of narrowing. When the balloon is inflated, the stent deforms and is expanded to secure it to the vessel walls. Self-expanding stents, see Figure 1.4 (B), are compressed into catheters that are guided to the treatment site and expand radially toward the vessel wall upon release from the catheter [31]. The common stent-to-artery diameter ratio is 1.1 to 1.2 times the diameter of the native vessel in order to ensure that the stent is securely fastened to the vessel walls[37]. In the expanded form, the ideal stent would have radial rigidity and recoil control to minimize migration and foreshortening [32,35].

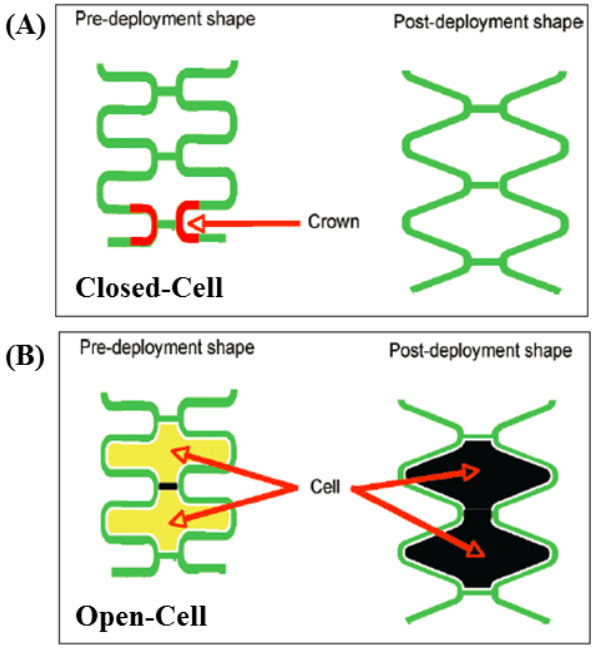


**Figure 1.5 A schematic demonstrating the closed-cell (A) and open-cell (B) configuration configuration of typical stent design (Adapted from [33]).**

The strut patterns are classified into two main categories, open-cell design stents and closed-cell design stents. A schematic of the pre-deployment and post-deployment configuration of the two design types are shown in Figure 1.5. The number and arrangement of connectors between stent cells differentiate closed-cell designs from open-cell designs. Closed-cell designs

are characterized by small intrastrut areas and adjacent ring sections in which all internal inflection points are connected by bridge elements, as shown in Figure 1.5 (A) [38]. Closed-cell designs provide uniform scaffolding to support the vessel walls but limited flexion between adjacent sections. Open-cell designs have larger intrastrut areas and significantly less bridge connectors allowing more flexion due to fewer connection points between adjacent sections, as shown in Figure 1.5 (B). Open cell designs offer better conformability to vessel curvature, which is important for maintaining native hemodynamics; however, vessel prolapse is increased by the larger intrastrut areas [34,39].

Biocompatible materials, such as stainless steel, nitinol, titanium, and cobalt-chromium, are materials typically used in the wire mesh of stents [40]. These materials are chosen for their strength, corrosion resistance, radiopacity and for their ability to promote endothelization. Metal alloys, such as cobalt-chromium, are presently being used in stent designs with thinner struts without compromising strength and corrosion resistance [34]. Recently, bioabsorbable stents made of materials such as polyethylene terephthalate and poly-L-lactate have been developed to provide support to the vessel walls during the healing process while ultimately degrading over time [41,42]. Bioabsorbable stents offer several advantages over conventional permanent designs, including restoration of vascular motion and native flow patterns [42].

A completely biocompatible material has yet to be developed, though recent advances in biomaterials have decreased the incidence of rejection by the body. The adsorption of proteins to the artificial surfaces can affect the integration of artificial implants, such as stents, into the body's environment or the function of an artificial device. When artificial surfaces are exposed to blood, plasma proteins adhere to the surface in a sequential order, each replacing the previous after a period of time [43].This behavior is called the Vroman effect and starts with the arrival of albumin, then immunoglobulinG (IgG) and fibrinogen, and ends with high-molecular weight kininogen (HMWK). Fibrinogen is a glycoprotein that can be converted to fibrin, a protein involved in the clotting of blood. Fibrogen adhered to an artificial surface, not replaced in the adhesion chain by HMWK, can cause platelet adhesion and thrombogensis [43,44]. Pfeiffer *et al*. reported fibrinogen adsorbed to the surface was replaced faster by HMWK in regions of secondary flow [43]. This rapid turnover reduces the platelet formation and thrombogenesis on artificial surfaces.

#### *1.1.3.1 Restenosis: Stent Failure*

In-stent restenosis (ISR) is an unsolved limitation of stent implantation, despite the fact that stents have been shown to be an effective tool for the treatment of atherosclerosis. ISR is an exaggerated healing response to vessel injury induced during angioplasty and stent deployment. Vessel injury consists of endothelial cell denudation and exposure of subendothelial thrombogenic components to circulating blood. Further vessel injury is brought about by vessel expansion during balloon inflation and stent deployment that stretches the media and adventia layers resulting in smooth muscle cell necrosis [45]. ISR development consists of several phases including thrombosis, inflammation, cellular proliferation, and extracellular matrix production [32,46]. The cellular proliferation phase, referred to as neointimal hyperplasia (NIH), is the most deleterious and is characterized by the synthesis of SMCs leading to occlusion of the stent due to cell growth [32].

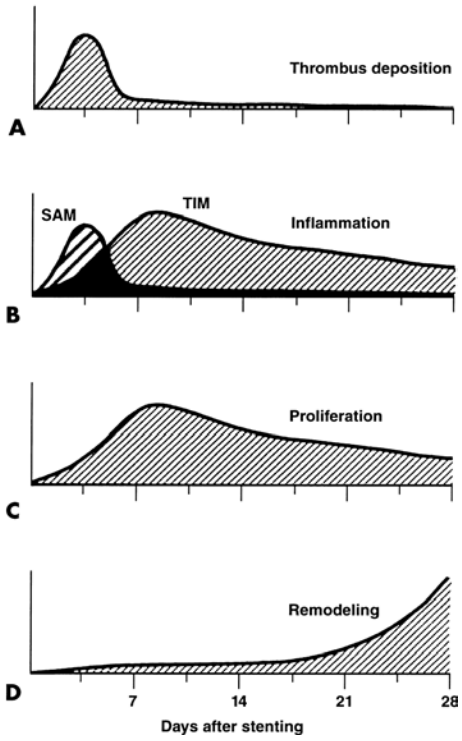


**Figure 1.6 An illustration of the 4 phases of vascular repair after stent induced vessel injury. (SAM – Surface adherent monocytes; TIM- Tissue infiltrating monocytes) Adapted from [47]**

The development of ISR is characterized by four phases of vascular repair, as shown in Figure 1.6(A, B). The timeline for restenosis development begins at the moment of the vessel injury with a thrombogenic and inflammatory response (Figure 1.6 (A, B)). The maximum thrombogenic and inflammatory response occurs within the first seven days post-stent implantation. Thrombus formation entails the recruitment of platelets to the site of endothelial denudation, where the thrombotic resistant layer has been removed, exposing the subendothelial matrix, as shown in Figure 1.7. The recruitment of platelets involves the interaction between circulatory and subendothelial adherent components. Circulating plasma von Willebrand factor (vWf), which normally has limited bonding potential with platelet receptors, is immobilized in subendothelial collagen. High shear stress conditions cause the immobilized vWF to undergo a conformational change, exposing multiple binding sites that can adhere to platelet surface receptors [47-49]. Platelets are captured in the injured vessel wall by a bond between platelet surface receptor glycoprotein GPIb-V-IX complex and collagen-bound vWf in the subendothelial matrix [47]. The initial bond is weak, but capable of holding the platelet near the surface where it can traverse the vessel wall until a stronger bond is established. Stable platelet adhesion occurs when surface receptor glycoprotein VI (GPVI) binds with fibrillar collagen (Figure 1.7). Once firmly adhered, the platelet becomes activated through its interaction with adhesion proteins, including vWF, fibrinogen and fibronectin.

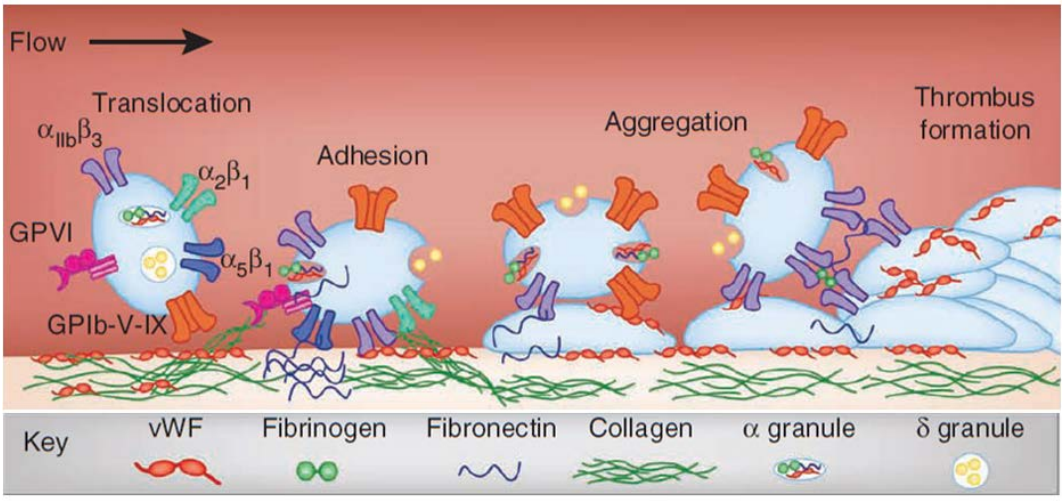


**Figure 1.7 An illustration of major ligands and receptors mediating platelet adhesion and activation at site of vascular injury. (Adapted from [47])**

Activated platelets spread out on the surface and release biochemical messengers that promote platelet aggregation and thrombus growth[10]. Recent studies have shown that local changes in blood flow can also encourage platelet aggregation without platelet activation or the release of biochemical messengers [50]. At shear rates of 10,000$s^{-1}$, large aggregates can develop independent of platelet activation. Platelet aggregation induced by shear gradients is a prothrombotic mechanism that can undermine the effectiveness of commonly used antithrombotic drugs [47]. Thrombus deposition does not significantly reduce the lumen diameter at this stage and does not play a major role in the final neointimal tissue volume [51,52].

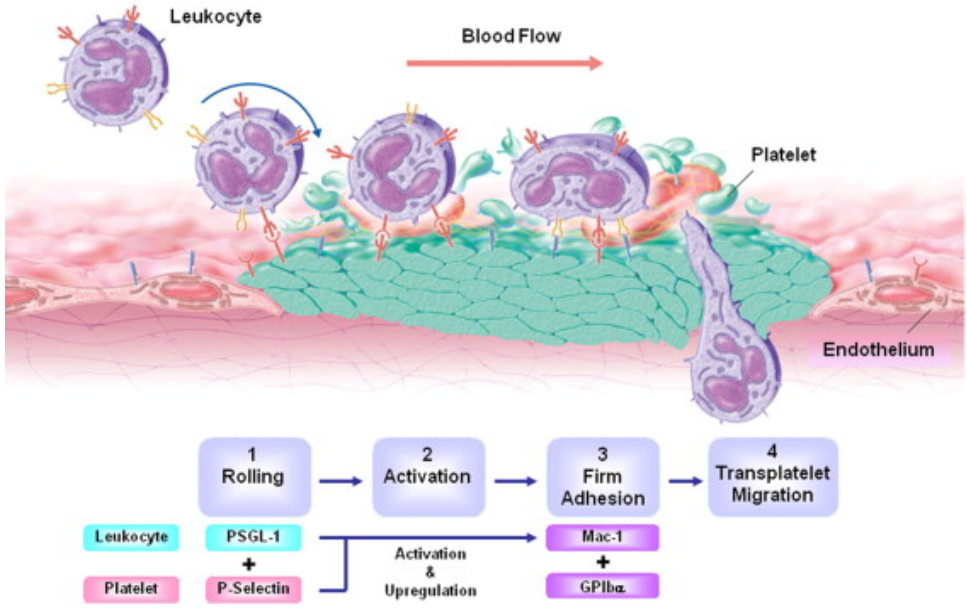


**Figure 1.8 An illustration of leukocyte adhesion and transplatelet migration (Adapted from [50]).**

The inflammatory response occurs in conjunction with thrombus formation, as shown in Figure 1.6 (B). The inflammatory response entails the recruitment of leukocytes to the injury site by activated platelets, as shown in Figure 1.8. Leukocytes, or white blood cells, account for less than 1% of the total blood volume, but are crucial to the body's defense against disease[10]. Proinflammatory molecules, such as P-selectin, are released by activated platelets and aid in the recruitment of leukocytes to the vessel wall[53,54]. The initial tethering of the leukocyte is facilitated by a weak bond between leukocyte receptor P-selectin glycoprotein ligand-1 to platelet P-selectin that causes the leukocyte to slow down [55]. The leukocyte begins to roll along the platelet

layer on the intimal surface. Once firm adhesion or second capturing of the leukocyte occurs, there is trans-platelet migration of the leukocyte into the vessel wall. The number of surface adherent leukocytes decreases 3-7 days after stent implantation as tissue infiltration progresses. Previous studies have indicated that inhibition of leukocyte adhesion reduces neointimal growth after balloon and stent induced vascular injury [56]. Low WSS provides two hemodynamic vehicles for increased leukocyte adhesion [5]. Firstly, low WSS increases the availability of slow moving leukocytes near the vessel wall and allows the adhesion molecules on the leukocyte the opportunity to interact with activated platelets and not be overcome by the axial load due to the fluid dynamics. Secondly, flow behavior in regions characterized by low WSS have been shown to alter chemo attractant convection away from the vessel wall, resulting in higher local concentrations that promote leukocyte adhesion.

Smooth muscle cell proliferation occurs 3-7 days after stent implantation, as shown in Figure 1.6 (C). SMCs are typically quiescent and in a normal hemostatic condition and have low levels of proliferation. In a healthy vessel, ECs serve as a barrier between SMCs and circulating growth factors. In addition, ECs produce growth inhibitory factors, such as NO, that regulate SMC proliferation[57]. The absence of the EC layer due to vessel injury exposes SMCs to circulatory growth factors, as well as growth factors released from surface adherent platelets and leukocytes. As a result of the new mitogenic environment, the SMCs transition to a proliferative state in which rapid cellular division occurs. The initial proliferation is localized in the medial layer and cells in the G1 phase of the cell cycle, as shown in, as shown in Figure 1.9, migrate to the intimal layer. The neointimal layer, comprised of SMCs and extracellular matrix, resides in regions of the intima where endothelial cell re-growth has not occurred within 7 days after vessel injury [57]. The uncontrolled SMC proliferation in the intimal layer leads to NIH and occlusion of the stented vessel. The inflammatory response and subsequent NIH is proportional to the degree of penetration of the vessel wall by stent struts, suggesting that the inflammatory response has a critical role in the development of ISR [46]. Delayed EC replication from proximal and distal regions allows uncontrolled SMC proliferation to occlude the stent lumen [15,57]. Concurrently, flow conditions can cause the regenerated endothelium to have impaired functionality and weakened barrier integrity [15].

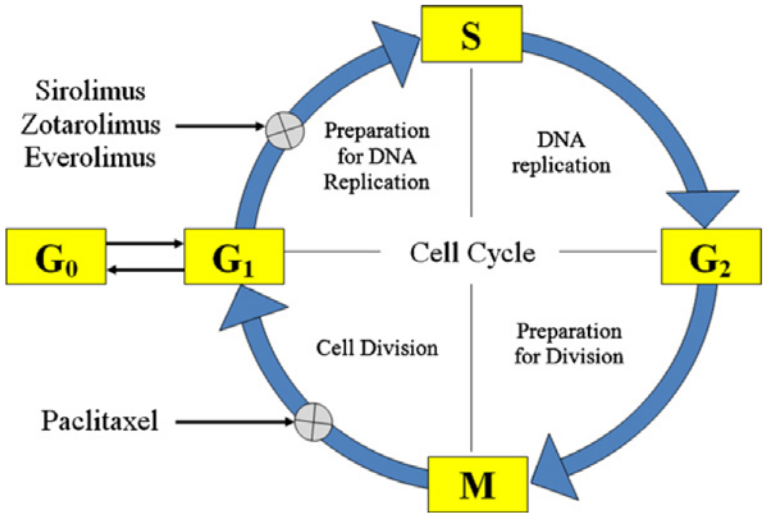


**Figure 1.9 An illustration of SMC cell cycle and phases of antiproliferative drug intervention (Adapted from [1]).**

Drug eluting stents (DES) are currently being developed to reduce the body's adverse reactions to stent implantation, but their benefit is still being debated [58]. DES are comprised of three components, the stent platform, an antiproliferative drug or therapeutic agent and a drug carrier vehicle (such as a biodegradable polymer) to control drug elution [32,34]. The antiproliferative drugs are coated onto the struts or loaded into reservoirs within the struts and eluted into the vessel walls and lumen. These drugs suppress cell division of the SMCs of the media layer by disrupting the cell cycle. Two commonly used drugs are Sirolimus and Paclitaxel, which differ in the phase of the cell cycle that is disrupted, as shown in Figure 1.9 [32,34]. Sirolimus (also known as rapamycin) and its drug derivatives inhibit transition from the G1 phase to the S phase of the cell cycle. Paclitaxel arrest the cell cycle in the G0-G1 and G2-M phase. DES implantation has been implicated in delayed re-endothelization and late (> 30days) and very late (> 1 year) stent thrombosis, reducing the acute benefit of reducing restenosis[32].

Stent design optimization is a problem of a system of interrelated variables in which conflicting factors make stent design challenging. The clinical performance of a stent relies on a balance between structural integrity and the hemodynamic environment induced by the stent. The structural integrity entails flexibility and radial stiffness that is dictated by the strut material and geometric parameters. Concurrently, stent geometry has been identified as a key element in establishing a hemodynamic environment that not only inhibits the occurrence of neointimal hyperplasia, but promotes the restitution of a healthy, functional endothelium. Stent strut

configuration dictates the hemodynamic environment within the stent, as well as proximal and distal to the stented region[33]. Designs optimized for their structural integrity may induce hemodynamic conditions that lead to stent failure by a maladaptive physiological response to altered flow behavior. On the other hand, designs optimized based on hemodynamic parameters may lack structural integrity. In order to find the balance between structural and hemodynamics requirements of stent design, it is important to understand how current stent designs impact the hemodynamic environment to determine what structural aspects lead to adverse physiological reactions.

### 1.1.4 *Advances in Fluid Mechanics Related to Hemodynamics*

The geometry of the vascular system leads to complex blood flow, entailing pulsatile and steady flow, laminar and turbulent flow, flow separation and secondary flow regimes. Many of the complex fluid motions exhibited in the vascular system can be studied using a simplified *in vitro* mechanical pipe system. Given the prevalence of curvature in the vascular system, the study of flow in curved pipes is directly applicable to the study of flow in the vasculature. The aortic arch is an example of curvature in the circulatory system and prompted the development of *in vitro* and numerical models of curved pipes to mimic the flow through the arch [59-62]. As well, the flow induced by interventional devices such as stents corresponds to well-known flow situations such as forward/backward facing step flow. The flow behavior in the stented region during the acute stage of implantation has been described as the interaction of flow over a series of adjacent backward and forward facing steps[33]. The stagnation zones and WSS distribution induced by the backward and forward facing step interaction can be used to predict potential regions of NIH formation.

*1.1.4.1* *Flow in Curved Pipes with Smooth Walls*

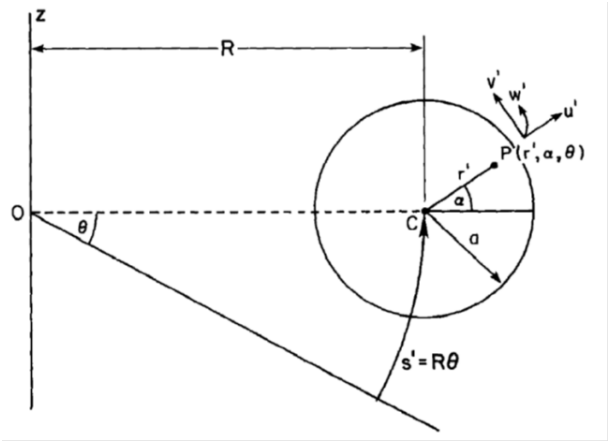


**Figure 1.10 Toroidal Coordinate System (Adapted from [50]).**

Work by Dean provided the analytical foundation for fully developed steady flow through curved pipes with circular cross-sections, infinitesimal pipe radius to- radius-of-curvature ratio, $\delta$, and no torsion [63]. Dean simplified the Navier-Stokes equations in a toroidal coordinate system shown in Figure 1.10 in his solution. In the toroidal coordinate system, $a$ is the radius of the circular pipe, $R$ is the radius of curvature, $\alpha$ is the angle within the pipe cross-section increasing counter-clockwise from the plane of curvature and $\theta$ represents the angle from the entrance to the exit of the curved pipe. From his work the non-dimensional parameter, now bearing his name, was introduced to relate centrifugal forces to viscous forces. The Dean number is defined as

$$\kappa = \mathrm{Re}\sqrt{\frac{a}{R}} \qquad \textbf{Equation 1.1}$$

where Re is the Reynolds number. The Reynolds number used to calculate the Dean number is defined as,

$$Re = \frac{2a\bar{V}}{\nu} \qquad \textbf{Equation 1.2}$$

where $\nu$ is the kinematic viscosity, and $\bar{V}$ is the spatially averaged velocity $\bar{V} = \frac{Q}{\pi a^2}$ (Q is the volumetric flow rate). The Dean number is often also defined as,

$$K = \frac{Ga^3}{\mu\nu}\left(\frac{2a}{R}\right)^{\frac{1}{2}} \qquad \textbf{Equation 1.3}$$

where G is the axial pressure gradient and μ is the dynamic viscosity. For pipes with infinitesimal curvature, the average velocity $\bar{V}$ is related to G in the same manner as for a straight pipe, that is, $G = 8\mu\bar{V}/a^2$. These forms are related by

$$K = 2^{5/2}\kappa \qquad \textbf{Equation 1.4}$$

for $K < 28$, whereas for higher Dean numbers, the forms are related by the friction ratio C [64], as

$$C = \frac{\bar{\tau_c}}{\bar{\tau_s}} = \left(\frac{K}{\kappa}\right)2^{-5/2} \qquad \textbf{Equation 1.5}$$

where for a fixed pressure gradient, $\bar{\tau_c}$ is the average axial WSS in a curved pipe and $\bar{\tau_s} = 4\mu\bar{V}/a$ is the average axial WSS in a straight pipe. The friction ratio *C* is unity for small Dean numbers and increases with the Dean number. Experimental and numerical studies have been conducted to determine the friction ratio for higher Dean numbers [64-66]. See Berger et al. for a discussion on additional alternative definitions of the Dean number [67].

Dean solved the simplified Navier-Stokes equations by expanding the solution in a series of powers of the Dean number. Based on Dean's assumption of a small radius to radius-of-curvature, the solution is only valid for values of $\kappa$ up to 16.58 ($K$ = 96). Dean's work and subsequent studies have established that tube curvature causes the point of maximum axial velocity to shift away from the center of the tube radius of curvature and induces secondary flows within the tube cross-section in the form of two counter-rotating vortices mirrored about the plane of the bend [68-70].

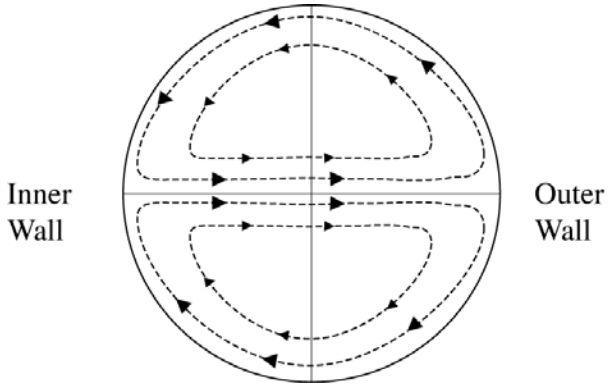


**Figure 1.11 Dean Vortices within the cross-section of a bend.**

Figure 1.11 shows a schematic of the pair of counter-rotating vortices that develop within the cross-section of the pipe at low Dean number. These secondary flow vortices carry fluid toward the outer wall of the bend along the horizontal centerline and the fluid is returned along the "top" and "bottom" wall of the bend. For a given pressure gradient, Dean observed that volumetric flow rate in a curved pipe is reduced in comparison to a straight pipe. Dean concluded that the decreased volumetric flow rate in the curved pipe is a consequence of secondary flow induced by the pipe curvature. He determined that the ratio of the volumetric flow rate in the curved pipe, $Q_c$ , to the volumetric flow rate in the straight pipe, $Q_s$, was a function of the Dean number. Dean's seminal work focused on low Dean numbers while subsequent studies have extended his work to include, for example, finite curvature [62], developing flow [71], torsion [72], and wavy walls [73].

White *et al*. confirmed experimentally the curvature-volumetric flow rate relationship observed by Dean and explored the relationship for higher Dean numbers [65]. White's experiments were conducted with pipes of various curvature ratios and used Reynolds number values up to 13,000. For a fixed *Q*, White measured the pressure gradient in the fully developed region of the bend. The average WSS in the stream-wise direction in the pipe is determined from the expression for average axial WSS in a straight pipe, $\overline{\tau_w} = \frac{2a\Delta P}{4L}$, where $\Delta P$ is the change in pressure between two axial locations a distance *L* apart in the pipe. White defined a coefficient of resistance as $R_c = \frac{\overline{\tau_w}}{\rho \bar{V}^2}$ where $\rho$ is the density of the fluid. White concluded that curvature increased the coefficient of resistance in a curved pipe, $Rc_c$ in comparison to the coefficient in a straight pipe, $c_s$ , for a certain range of Reynolds numbers. The range of Reynolds numbers for which this finding applied depended on the curvature of the pipe. This finding corroborates Dean's conclusions since

an increase in the average WSS in the curved pipe would result in a decreased volumetric flow rate. Further, White's work confirmed the ratio of the coefficients is also a function of the Dean number.

Van Dyke expanded Dean's perturbation solution to 24 terms and the solution is theoretically valid as $K$ goes to infinity [64]. Van Dyke's calculated friction ratios matched those measured in White's experiments for mildly curved pipes. The predicted behavior of the friction factor ratio for larger Dean numbers (more curvature) falls below the results published from experimental and numerical studies. Van Dyke explains that the reason for the discrepancy may be due to how the Dean number is allowed to tend to infinity. In addition, there may be an intermediate regime of unsteady laminar motion between the laminar and turbulent flow conditions that may be characterized by higher friction factors that are not resolved in his solution.

Flow visualization studies and numerical solutions have found more complicated vortical patterns than the two-vortex structure predicted by Dean at higher Dean numbers, including multiple sets of vortex pairs within the tube cross-section [74-76]. The additional vortices are generally observed to form in a region toward the "outer" wall of the bend. The multiple vortex patterns are shown to exist also in pipes with semicircular cross-sections, in which the inner wall is flat and the outer wall is curved, or vice versa. Daskopoulos and Lenhoff numerically explore bifurcations in the solution of the Navier-Stokes equations for steady, fully-developed flows in curved pipes with infinitesimal curvature and no torsion over a large range of Dean numbers [76]. They employ a symmetric boundary condition along the plane of the bend in order to reduce the computational cost and find the two-vortex solution is stable up to a critical Dean number, beyond which both two and four-vortex solutions are possible. Daskopoulos and Lenhoff finds the two-vortex solution is stable up to $K = 956$. Beyond this critical Dean number, a stable and an unstable four-vortex solution is established. As observed experimentally by Cheng and Mok [75], the additional vortices form near the outer wall of the bend, and their behavior depends on the stability of the four-vortex solution. In the stable solution, the area of the vortex near the outer wall is approximately constant, as shown in Figure 1.11, and the vortex strength increases with the Dean number. In the unstable solution, the vortex near the outer wall shrinks and weakens as the Dean number increases and the axial velocity profiles are similar to those observed in the two-vortex solution.

Siggers and Waters present solutions for steady flow in curved pipes with finite curvature ratios by retaining the Coriolis as well as the traditional centrifugal terms in the governing

equations [62]. They observe the critical Dean number increases as the pipe curvature increases, which is in agreement with flow visualization studies [75]. Based on Daskopoulos' results, Pedley concludes that gradually increasing the Dean number from a low value will result in two-vortex flow but sudden perturbation could result in four-vortex flow [77]. Pedley also suggests that the existence of more than one steady solution implies that the solution is very sensitive to initial or boundary conditions and minor changes in the geometry or pressure-gradient. These small changes could result in dramatically different flow patterns.

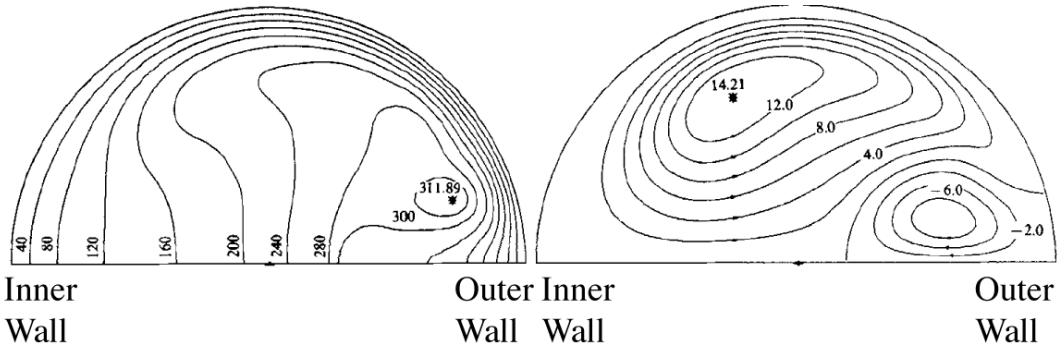


**Figure 1.12 Axial velocity contour (left column) and the streamlines of the secondary flow (right column) for the stable four-vortex solution for $K$ = 3000 for upper half of pipe geometry. (Adapted from [59])**

*1.1.4.2 Flow in Pipes with Non-smooth Walls*

The study of flow behavior in curved pipes with non-circular cross-sections, such as an elliptical tube and one with a wavy cross-section, has demonstrated the impact of wall shape on flow behavior. Topokoglu and Ebadian investigate the reduction in flow rate in elliptical pipes for various Reynolds numbers and curvature ratios [78]. The study explores a range of elliptical cross-section aspect ratios and finds that for a fixed Reynolds number and curvature ratio, the reduction in flow rate due to pipe curvature decreases with "flatter" cross-sections due to a corresponding moderation in the secondary flow. Wang presents a study of Stokes flow through a circular tube with small-amplitude three-dimensional bumpy walls and a follow-up study with a helically corrugated tube [79,80]. The bumpy-walled tube aims to model flow over endothelial cells that line blood vessels. Wang reports an inverse relation between the flow rate and the number of protrusions. In addition, the number of protrusions and the wavelength aspect ratio can be optimized to maximize the flow rate, suggesting that blood vessels optimize their geometry to

minimize flow resistance [81,82]. For the helically corrugated tube, an optimal helical pitch can be determined to maximize bulk fluid rotation to produce optimal mixing. Pozrikidis confirms Wang's results using an alternative coordinate system and extends his work to helically corrugated large-pitched tubes with arbitrary cross-sections [83].

In the field of hemodynamics, the study of flow through coiled pipes with noncircular cross-sections is also applicable to protrusions introduced into the vascular system by the implantation of a stent. Stent struts alter the flow structures induced by the curvature in the vascular system. For instance, the struts protrude into the near wall boundary layer that dictates vortex patterns. Protrusion height of the stent struts has been shown to influence biochemical pathways that determine the efficacy of the device [37,84]. *In vitro* studies of the flow modification by the implantation of a stent have modeled stent struts as circumferential protrusions with varying frequency and amplitude [40,85,86]. Peterson presents a perturbation solution to the problem of fully developed steady flow within a curved tube of infinitesimal curvature ratio and a wavy-walled cross-section[73]. The solution is based on a simplified model of flow in a curved tube with an implanted stent, where the stent struts are modeled as a series of infinitely long ribs stretching axially along the length of the curved tube. The solution predicted the flow behavior based on the number of protrusions, $n$, and the protrusion height, $\varepsilon$, as shown in Figure 1.13. The wall waviness decreases the strength of the secondary flow when compared to a pipe with a smooth circular cross-section. Further, the introduction of the wavy wall increases the average circumferential WSS, regardless of the number of protrusions. The solution is limited in its approximation of stent flow, since it neglects any stream-wise protrusions, leading and trailing edge effects, and the inception of curvature. Furthermore, the perturbation solution is limited to small Dean numbers, long wavelength bumps in comparison with their height, and no torsion.

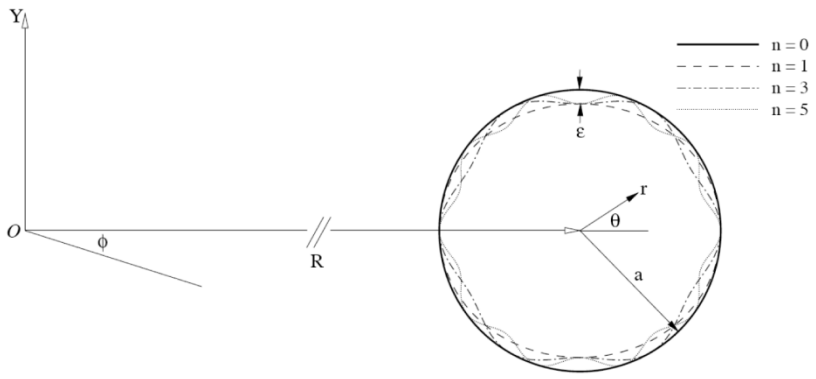


**Figure 1.13 Schematic showing geometry based in Peterson perturbation solution, where *n* represents the number of protrusions and *ε*, the protrusion height.**

*1.1.4.3* *Flow in Pipes with Stent Like Protrusions*

Computational fluid dynamics (CFD) has become a ubiquitous tool for characterizing the hemodynamics effects of stent implantation that are difficult to quantify *in vivo*. CFD aids in the understanding of the macro- and micro- aspects of blood flow through stented vessels and their influence on neointimal growth. In particular, CFD modeling has facilitated the optimization of stent designs by elucidating the impact of stent design on near wall flow patterns. Stent design optimization based on CFD results focuses on the single objective of determining the stent geometric properties that produce a hemodynamically optimal environment but neglects the key structural consideration of stent design. Finite element analysis (FEA) is a frequently used computational modeling technique that is employed to determine the mechanical implications of stent implantation leading to the optimal stent design based on structural integrity[87-89].Despite the limitations of CFD stent optimization, the information garnered from these studies can be combined with FEA results to determine deleterious variations in stent geometry that will lead to ISR and poor structural integrity.

A majority of the CFD studies focusing on stent optimization include model geometries of stented straight vessels. Slotted tube stents with a diamond strut pattern are frequently investigated in order to identify the general trends in stent induced flow behavior [86,90,91]. LaDisa Jr. *et al*. found the stagnation zones surrounded the stent struts regardless of changes in strut properties. In addition, a decrease in strut thickness resulted in a decrease in the percentage of the vessel area

exposed to low WSS. An increase in the number of struts subsequently increased the area of the vessel exposed to low WSS in the range found optimal for intimal thickening. The number of struts has been shown to cause circumferential arterial deformation due to straightening of the vessel between adjacent struts after stent implantation [85]. The polygonal cross-section resulted in a larger intrastrut area exposed to elevated spatial and temporal wall shear stress gradient (WSSG) and adverse distributions of WSS suggesting that configurations with a high number of strut intersection that maintain a circular cross-section would be beneficial to the hemodynamic environment. The strut orientation angle with respect to the primary flow direction is a geometric parameter directly related to the number of struts and the strut width. It has been shown that struts more aligned with the primary flow direction decrease the amount of low WSS at the vessel wall[85,86]. Specifically, intrastrut angle of approximately 40° was found to be hemodynamically optimal, regardless of the vessel size and intrastrut area, for minimizing the area of low time average WSS [90].

Berry *et al.* used dye injection flow visualization and CFD to evaluate flow patterns in braided wire stents in a coronary artery model [92]. The tested stents differed in the number of helical wires braided together to form the stent and the wire diameter to vessel diameter ratio. Study results showed the dependence of stagnation zone development and shape on the wire spacing of the stent. The development of stagnation zones is important since fluid particle residence times would be higher in these regions resulting in platelet activation or thrombogenesis. CFD provided quantitative flow results near the stent struts and showed in cases where the wire spacing was less than six wire diameters that the stagnation zones always extended from one wire to the next. In stent designs where wire spacing was greater than six diameters, the flow reattached between the wires and the stagnation zones were separated for a portion of, or for the entire cardiac cycle. In addition to stagnation zones, low shear stress regions were found between the wires.

Recent stent designs, such as open-cell configurations, are able to better conform to vessel curvature. These designs have prompted the investigation of flow behavior within a curved stented vessel. LaDisa, Jr. *et al*. investigated the differences in the distribution of indices of WSS between an implanted stent that conforms to or straightens the native vessel curvature[93]. The study finds distribution of WSS differs substantially depending on vessel conformity. The differences in WSS distribution was most pronounced in the proximal and distal areas of the stented region. This is largely due to the fact that stents that do not conform to vessel curvature “kink” the vessel at a

sharp angle at the entrance and exit of the stented region. The study confirms that stents that conform to vessel curvature produces the least disruption to the native flow environment.

## 1.2 Study Objectives

Many improvements have been made in stent design in order to reduce the likelihood of ISR but none have eliminated the problem. Endothelial cells lining vessel walls transduce local hemodynamic behavior in the stent vicinity, such as WSS, into biochemical signals that lead to the progression of ISR. Hence, resolving the hemodynamics in the vicinity of the stent is crucial to elucidating the cause of and reducing rates of stent failure. The objective of the study is to address the problem of ISR by clearly defining the flow physics induced by stent implantation, accounting in particular for vessel curvature, by first considering idealized stent models, then progressing to an actual stent model. Stent designs are typically based on data originating solely from flow in straight vessels, which, once optimized for this configuration, may lead to suboptimal performance when placed in tortuous vessels. Previous stent studies have almost categorically neglected the effects of curvature on the flow physics, despite the fact that even extremely mild curvature changes the axial WSS distribution within the vessel and induces the development of secondary flows, which alters the advection of chemical signals released into the lumen.

Using CFD techniques, this study seeks to (i) determine the impact of stent strut amplitude and frequency on primary and secondary flow structures; (ii) determine the significance of the stent strut shape; (iii) evaluate flow behavior in the transition region from smooth walled to stented vessel; and (iv) examine the collection of these effects in a full stent model geometry in a curved tube. This study takes a systematic approach, dissecting the impact of the stent first into simplified foundational components, then investigating each component and finally synthesizing the components into a full stent model with the long-term goal of optimizing stent design to reduce the rate of restenosis. As well, the study findings can aid in understanding the signal transduction mechanisms of the endothelial cells, which play a role in the development of ISR, and reduce the cardiovascular disease mortality rate by improving the clinical outcome of treatment procedures.

Through an iterative design process, a series of computational models has been developed, each with increasing complexity, to determine the stent geometric characteristics that will induce a flow environment less prone to the development of ISR. The flow parameters considered include WSS magnitude, gradients, and distribution, which have been linked to the development of ISR in

previously published works. For each model, the strut height, frequency, and profile (smooth or square) are varied parametrically to achieve desired flow conditions; the Dean number is varied as well to resolve the flow physics in various regions of the vascular system. The strut height and frequency parameters are within the range found in commercial stents on the market. The stent edge angle is altered since it is reported to effect endothelial cell migration by altering flow separation regions and subsequent WSS distribution [94]. The chosen pipe curvatures closely represent the curvature of stented vessels. The initial CFD models will focus on steady flow behavior within the stented artery regions; the first model includes only circumferential protrusions similar to the geometry used in the analytical work by Peterson. In this model, particular attention is paid to the impact of strut protrusion on secondary flow structures since they can carry chemical mediators to the vascular wall, which act as key stimuli for ISR [95]. The next model includes a realistic stent model that combines longitudinal and circumferential struts to closely mimic commercial stents. This model will elucidate if longitudinal struts have a greater impact on WSS distributions as compared to the circumferential struts. As well, flow behavior at the entrance and exit of the stented region will be examined. The flow behavior at the entrance and exit of the stent is dictated by the transition from the native vessel region to the stented region and vice versa. Lastly, the final CFD model will focus on unsteady flow behavior characteristic of stented vessels.

*In vivo* blood flow is predominantly pulsatile and blood behaves in a non-Newtonian manner. Despite these attributes, several CFD studies have utilized Newtonian fluid models and the rationale for using these models is based on the flow characteristics of blood components. Generally, red blood cells are observed to predominately travel in the center of vessels with layers of nearly cell-free Newtonian fluid plasma between them and the vessel walls [20]. The Newtonian fluid plasma in the near wall region will dictate the wall shear stress imposed on the endothelial cells, which is one of the primary foci of ISR development. However, a recent study has found that the WSS distribution induced by stent struts differs between a Newtonian and non-Newtonian fluid model [96]. Thus, the present study includes both fluid models to compare the effects in a curved stented vessel.

The computational model does not take into account the compliance and elasticity of healthy arterial walls. Previous researchers found that compliance is important when considering local pressure gradients and pulse propagation, but does not significantly affect the overall velocity distribution [97]. The present study is focused on bulk flow features and does not consider

local pressure gradients. In addition, previous studies have reported very low compliance in the stented segment of the artery [92,98]. Thus, these observations justify the use of the proposed CFD model to understand *in vivo* flow physics in the stent vicinity.

The novelty of this study lies in the following: (i) the examination of steady and unsteady flow within a stent that conforms to vessel curvature; (ii) exploration of stent geometric properties in a curved stented vessel; and (iii) exploration of utilizing a Newtonian and Non-Newtonian model with a curved stented vessel. Previous studies focused on steady or unsteady flow through a straight stent. Given the introduction of stents that conform to vessel curvature and the difference in the WSS distribution at the inner and outer walls of the stent, the results of this study will highlight the benefit of a stent design with a non-uniform circumferential geometry for a curved stented vessel. The uniform geometry may have benefits structurally for the stent design. Previous research has explored the impact of fixed stent geometric properties for a curved vessel. However, the presented work will explore the impact of alterations in the geometric properties in the curved stented vessel. Lastly, the comparison of flow behavior induced by a Newtonian and non-Newtonian fluid model in a curved stented vessel has not been previously investigated to my knowledge.

The study is divided into three main components that will be referred to as Study A, B, and C in this thesis. Study A includes wavy wall geometry as simplified stent model and extends the work of Peterson to examine higher Dean numbers, larger amplitude protrusions, and finite curvature for fully-developed steady flow of an incompressible, Newtonian fluid using CFD. Two different curvature ratios are considered; the first geometry has a very small curvature ratio, approximating the infinitesimal curvature ratio of analytical studies, while the second geometry has a small but non-negligible curvature ratio. Flow behavior in the wavy-walled pipe is investigated parametrically in this study by comparing it to the flow behavior in the circular pipe. Study B includes a realistic stent geometry that is based on commercially available stents. This component provides a close examination of the impact of vessel curvature and stent protrusion for a range of physiological Dean numbers, clinically relevant stent protrusions, and fixed curvature based on the coronary artery. As well, this component examines the stented flow behavior for fully-developed steady flow of an incompressible, Newtonian and Non-Newtonian fluid. Lastly, Study C is a modification to Study B in which an unsteady waveform is utilized to closer mimic in vivo conditions for the coronary artery and carotid artery. The average Reynolds number for the coronary and carotid arteries are approximately 100 and 364, respectively. Particular attention is

paid to WSS for all study components, as it is a parameter to which cells lining an arterial vessel are particularly responsive.

The studies included in this thesis are designed to address unanswered questions that constitute the contribution of this work to the fields of fluid dynamics and stent development. The contribution of this work can be classified into three broad categories: (i) providing a fundamental understanding of flow in curved pipes with wall protrusions, (ii) highlighting the impact of the constitutive fluid model on the characterization of physiological flow, and (iii) broadening the understanding of the hemodynamic environment in the vicinity of current stent designs. Previous studies have focused on characterizing flow in straight and curved pipes with wall protrusions [73,80,83]. The research exploring flow in curved pipes with non-smooth walls is limited to pipes of infinitesimal curvature and low Dean number flow. The present work expands beyond these limits and includes non-smooth protrusions in the axial and circumferential directions.

Several studies have focused on the ongoing debate as to whether a Newtonian or non-Newtonian model should be utilized to characterize the physiological flow behavior[99,100]. For example, flow in large arteries is often simulated using Newtonian models; however, non-Newtonian behavior has been identified as important in the immediate vicinity of a stent segment [19,96]. The contribution of the present work to existing knowledge of the impact of the constitutive model choice is to outline the effects of the model choice on the evaluation of stent performance. Further, the present work demonstrates that the Newtonian model provides a conservative estimate of potential NIH development due to the stent presence.

Numerical models used to evaluate the hemodynamic environment in the vicinity of current stent designs has focused on a limited parameter space. In addition, the main focus has been on the derived parameters from the flow behavior, such as the WSS, rather than a detailed examination of the flow field. Cumulatively, previous work examining the stent induced flow field focused on the outcome of the flow behavior and not what leads to the manifestation of the flow behavior. The present work correlates a detailed examination of the flow environment induced by the stent presence with the critical flow conditions for NIH development. The role of secondary flow in the convective transport of NIH stimuli to the vessel wall is also highlighted in the present work. Lastly, previous researchers utilized steady flow simulations as an equivalent to the time-averaged flow behavior garnered from unsteady simulations. The present work compared the impact of evaluating stent performance based on steady or unsteady simulations.

The thesis is organized as follows: the problem statement and numerical model are described in Chapter 2; the results and discussion for Study A are presented in Chapter 3; the results and discussion for Study B are presented in Chapter 4; the results and discussion for Study C are presented in Chapter 5; and conclusions are drawn in Chapter 6. Finally, the future work is discussed in Chapter 7.

# Chapter 2*

# Study A: Flow in Curved Pipe with Wavy Walls

(*Text included in Chapter 3 is adapted from a paper published by Prince *et al.* in the Journal of Fluids Engineering[101])

## 2.1 Problem Statement

The physical problem under consideration is the behavior of an incompressible, Newtonian fluid flowing through a curved pipe with axially-aligned, small-amplitude protrusions under steady, fully-developed flow conditions. The frequency and amplitude of the protrusions are varied parametrically, as are the curvature ratio of the pipe and the flow speed. The geometry is a first-order approximation of a stent design and representative of a later stage of vascular healing after stent implantation. Three coordinate systems are defined in Figure 2.1; a global, fixed Cartesian coordinate system *XYZ*, a local Cartesian system within the tube cross-section *xyz*, and a local polar coordinate system $r\varphi$, also within the tube cross-section. The *XYZ* coordinate system is used to define the geometry and is the coordinate system used in the numerical solution. The curved pipe winds around the Z-axis with a fixed radius of curvature, *R*. The global velocity components in the *X*, *Y*, and *Z* directions are given by *U*, *V*, and *W*, respectively. The local coordinate systems are used in the data analysis. The local Cartesian coordinate system is oriented such that the *yz* plane corresponds to a given pipe cross-section and the axial flow is oriented along the positive *x* direction. The *y*-axis points toward the outer wall of the pipe (away from the center of the radius of curvature), and the *z*-axis is formed using the standard right hand convention. The velocity components in the *x*, *y*, and *z* directions are *u*, *v*, and *w*, respectively. The local polar coordinate system, $r\varphi$, is used to describe the position within the cross-section of the tube, with $\varphi$ being defined as positive in the counter-clockwise direction from the positive *y*-axis. The origin of both local coordinate systems is fixed at the center of the tube cross-section a distance *R* from the global origin *O*. The axial distance along the pipe is determined by the arc length, $R\theta$, where $\theta$ is the angle from the tube entrance to a specified axial location.

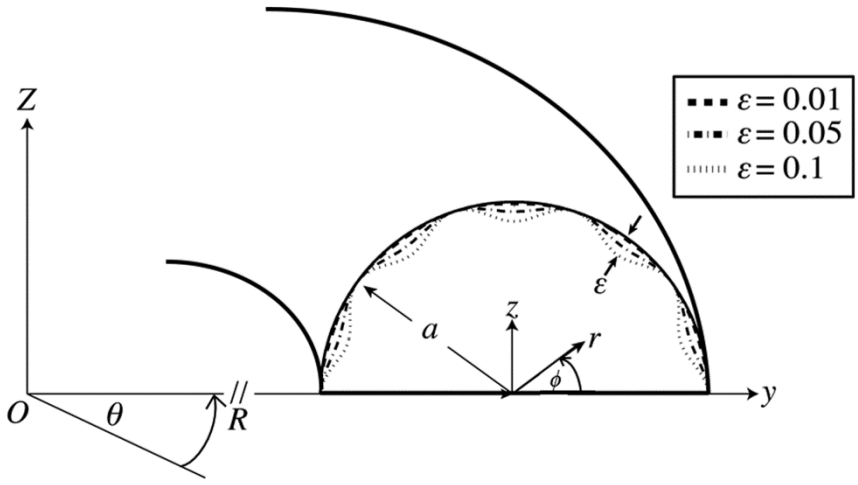


**Figure 2.1 Model geometry and coordinate system definitions**

The curved pipe is modeled as rigid-walled with nominal tube radius $a$ and curvature ratio $\delta = a/R$. Two curvature ratios are examined; the first curvature ratio, $\delta$ = 1.45×10-4, termed "mild curvature" herein, is very small and serves as an approximation of the infinitesimal curvature ratio examined analytically by Peterson [73]. For this curvature ratio, the effect of the Coriolis terms in the governing equations, while not neglected entirely, are nevertheless very small [62]. The second curvature ratio is $\delta = 1.25\times10^{-2}$, herein referred to as "finite curvature". The total arc length of the modeled pipe section is 60$D$, where $D = 2a$, corresponding to $\theta = 1°$ for the mildly curved pipe and $\theta = 85.97°$ for the finite curved pipe.

The wavy wall geometry, first introduced by Peterson [73], is defined as

$$r_{\text{tube}}(\phi) = a[1 - \varepsilon \sin^2(n\phi)] \qquad \textbf{Equation 2.1}$$

where $r_{\text{tube}}$ is the radius of the tube as a function of the polar coordinate $\varphi$, $\varepsilon$ is the amplitude of the protrusions non-dimensionalized by the nominal tube radius $a$ (see Figure 2.1), and 2$n$ is the total number of protrusions around the circumference of the model pipe. The cross-sectional area is constant along the length of the pipe; that is, the protrusions stretch axially along the length of the curved tube. Note that $\varepsilon = 0$ corresponds to a circular cross-section. The number of protrusions $n$, and their amplitude $\varepsilon$, are varied parametrically. Simulations are conducted with $n$ = 5 and $\varepsilon$ = 0.01, 0.05, and 0.1 and with $n$ = 8 and $\varepsilon$ = 0.05. The case of $\varepsilon$ = 0.05 represents a typical stent protrusion height into a coronary artery [102], while the other values of $\varepsilon$ represent the range of

thinner or thicker stent struts. We note that the protrusions have the effect of decreasing the cross-sectional area of the pipe as

$$A = \pi a^2 \left(1 - \varepsilon + \frac{3}{8}\varepsilon^2\right) \qquad \textbf{Equation 2.2}$$

Furthermore, we note that the reduction in cross-sectional area is independent of the number of protuberances, *n*. For each value of $\varepsilon$ and *n*, the Dean number is varied to determine its impact on the flow physics.

The Dean numbers investigated for the mildly and finite curved pipes are listed in Table 2.1. Since laminar flow is of interest, the Dean numbers are restricted to $K \leq 100$ for the mildly curved pipe and $K \leq 2500$ for the finite curved pipe. The desired Dean number *K* was converted to $\kappa$ using Equation A. 5 in order to determine the required inlet average velocity. To compute *C* required in Equation A. 5, we adopt Van Dyke's modified Dean series, which agrees well with experimental data and numerical predictions of the friction ratio for $K < 850$ before slowly deviating [64]. Using regression analysis, Hasson developed an equation for *C* based upon experimental data, which produces $K = 1030$ and $K = 2770$ instead of $K = 1000$ and $K = 2500$ for the average velocity suggested by Van Dyke. However, variations in the flow behavior between $K = 1000$ and $K = 1030$ or between $K = 2500$ and $K = 2770$ are expected to be negligible, so the method by which the friction ratio and in turn the inlet velocity are calculated should not influence the interpretation of flow behavior. We note that the prescribed Dean number is based upon the nominal pipe radius and does not account for the change in the cross-sectional area with the inclusion of the wavy wall. This results in a reduction in the volumetric flow rate and marginally lowers the effective Dean numbers, roughly offsetting the error in Van Dyke's estimate in comparison with Hasson's at higher Dean numbers.

**Table 2.1 Dean numbers investigated for each curvature ratio.**

| Mildly Curved Pipe $\delta = 1.45\times10^{-4}$ | Finite Curved Pipe $\delta = 1.25\times10^{-2}$ | |
|---|---|---|
| 1 | 10 | 500 |
| 10 | 25 | 1000 |
| 25 | 50 | 2500 |
| 50 | 100 | |
| 100 | 250 | |

## 2.2 Numerical model

Ansys CFX Version 12.1 is used to solve the unsteady three-dimensional Navier-Stokes equations in the fixed *XYZ* Cartesian coordinate frame [103]. Ansys CFX employs a finite volume solution method for solving a discretized control volume formulation of the Navier-Stokes equations. In the present simulation, the working Newtonian fluid has a density of 997 kg/m$^3$ and a dynamic viscosity of $8.899 \times 10^{-4}$ Pa·s. The stipulated boundary conditions are no slip and no penetration along the tube wall. In the absence of torsion or other asymmetric influence, the flow in curved pipes is symmetric about the plane of the bend [62]. Consequently, a symmetry plane is defined at $Z = 0$, which sets the $W$-component of velocity at the plane and the velocity gradients normal to the plane equal to zero, that is, $W(X,Y,0) = \partial U/\partial Z|_{Z=0} = \partial V/\partial Z|_{Z=0} = \partial W/\partial Z|_{Z=0} = 0$. A uniform velocity profile is prescribed at the pipe inlet, whose magnitude is determined from Equation A. 5 as discussed previously. A constant average static pressure of 0 Pa is set at the pipe outlet, allowing spatial pressure variations within the control surface.

### 2.2.1 *Grid and flow development*

The spatial domain of the modeled wavy wall geometry is discretized using hexahedral elements. Figure 2.2 (A) shows the grid arrangement at all cross-sections of the pipe for both the mild and finite curvature. It is characterized by a boundary layer region inflated with structured elements of high aspect ratios to resolve the steep velocity gradients near the wall. The maximum total thickness of the inflation layer is 0.08*a*, and each successive layer from the wall is 1.2 times

thicker than the preceding layer. By sweeping the cross-stream grid design in the stream-wise direction through the angle $\theta$ between the inlet and the outlet, a structured grid pattern is generated on the symmetry plane, as shown in Figure 2.2 (B) for the mildly curved pipe geometry. The geometry is divided into 600 axial units, equivalent to a distance of 0.1$D$ between nodes in the stream-wise direction.

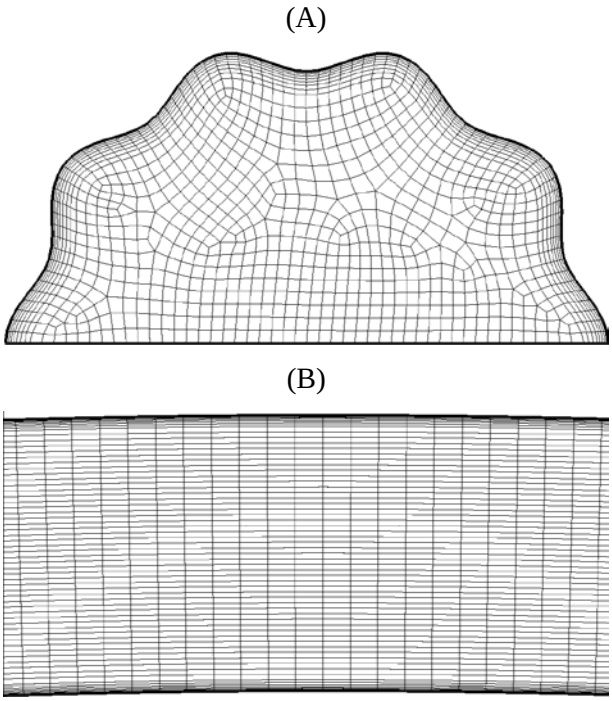


**Figure 2.2 Hexahedral mesh in the (A) pipe cross-section and (B) on a portion of the symmetry plane which has 600 divisions in the stream-wise direction for $\varepsilon$ = 0.1, $n$ = 5, and $\delta = 1.25 \times 10^{-2}$**

To obtain fully-developed flow, the simulation is initiated by imposing a uniform inlet velocity in accordance with the desired Dean number $K$ at the pipe entrance as shown in Figure 2.3. The converged solution is designated as Run #1. A coordinate transformation is subsequently performed on the velocity profile obtained at the pipe exit and the resultant velocity profile serves as the inlet velocity data for a second simulation through the same geometry; the simulation thus completed is designated as Run #2. This procedure is performed until the flow field becomes fully-developed, which generally occurs between Runs #2 and #3.

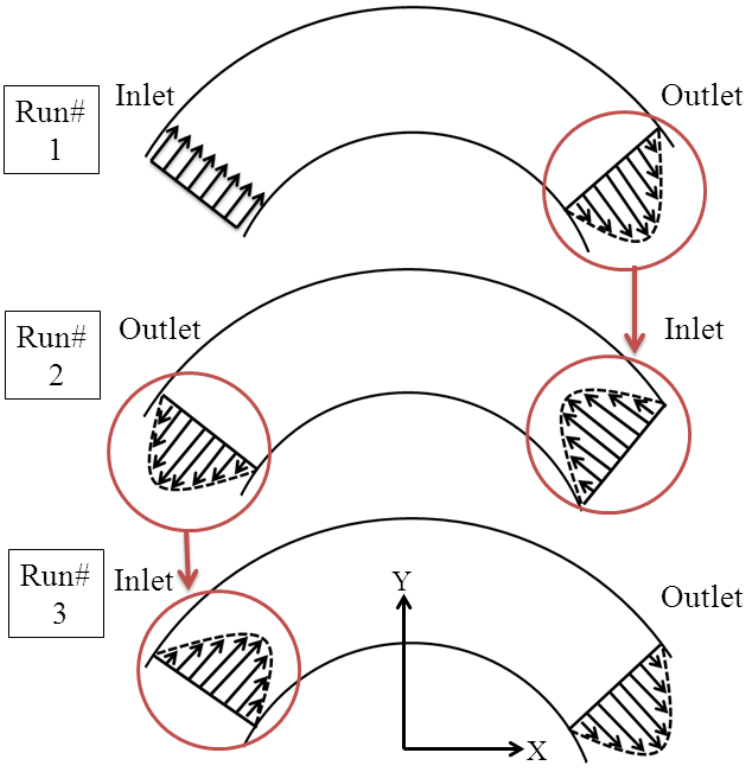


**Figure 2.3 Procedure used to achieve fully developed flow**

A drop in mass flow rate, $\dot{m}$, was observed between the outlet of Run #1 and the outlet of Run #2. The drop is due to the calculation of two different velocities by Ansys CFX at each IP. An advecting velocity, $\hat{u}$, is predicted by Ansys and used to calculate mass flow rate at the IP. An advected velocity,$\tilde{u}$, is also predicted and used to determine the diffusion of momentum across the face. The $\dot{m}$ for Run #1 is equal to $\dot{m}_{R1} = \rho \hat{u} A|_{outlet}$. The velocity value extracted from the nodes at the outlet of Run # 1 is $\hat{u}$ and is not equal to $\tilde{u}$. Thus, the $\dot{m}$ for Run # 2 is determined based on $\tilde{u}$ from Run #1 and is equal to $\dot{m}_{R2} = \rho \tilde{u} A|_{outlet}$. Thus, there is a small discrepancy between $\dot{m}_{R1}$ and $\dot{m}_{R2}$ based on the different velocity values used for the computations.

### 2.2.2 *Grid independence*

For the mildly curved pipe, a grid independence study is conducted at the upper limit of the Dean numbers that retain laminar flow, $K$ = 100, which has the steepest near wall velocity gradients. For the finite curved pipe, the study is conducted at $K$ = 2500. The wavy-walled pipe with $\varepsilon$ = 0.1 is chosen to demonstrate grid independence as this represents the most extreme

protrusion height in this study. Several grids are tested with increasing numbers of elements to determine the optimal grid size for the CFD study. The grid independence study is based on the converged solution for Run #1 (See §2.2.1), wherein the flow is not fully-developed, but the effect of grid size can still be assessed. Four grids are used in the grid independence study and the dimensions of the grid elements are decreased by a factor of 1.5 between each successive grid. The number of inflation layers range from 2 to 8 while their total thickness remains constant. Table 2.2 summarizes the number of nodes corresponding to each mesh.

**Table 2.2 Number of nodes for the mesh geometries used in the grid independence study.**

| | Mildly Curved Pipe $\delta = 1.45\times10^{-4}$ | Finite Curved Pipe $\delta = 1.25\times10^{-2}$ |
|---|---|---|
| Grid 1 | 59,249 | 57,638 |
| Grid 2 | 128,372 | 126,496 |
| Grid 3 | 277,091 | 263,858 |
| Grid 4 | 853,420 | 839,597 |

The final grid is chosen based on solution independence of the average axial WSS, $\overline{\tau_a}$ and the ratio of the total pressure averaged over the cross-section at the inlet to that at the outlet, $\overline{P_I}/\overline{P_O}$. The average axial WSS is assessed within the plane 30*D* from the pipe entrance. Table 2.3 and Table 2.4 summarize the values of $\overline{\tau_s}$ and the pressure ratio obtained for each grid for the mildly and finite curved pipe geometries, respectively. The percent difference between the parameters for successive grids is calculated as (Grid[N] – Grid[N-1])/Grid[N] × 100, where N represents the grid number and is included in Table 2.3 and Table 2.4. While $\overline{\tau_a}$ evaluates local grid independence, the pressure ratio characterizes the global flow domain. The parameter $\overline{\tau_a}$ exhibits greater fluctuation from one grid to another since the characterization of the velocity gradient near the wall is sensitive to the grid size. The solution is deemed independent when the percent difference for $\overline{\tau_a}$ and the pressure ratio is less than 1% for successive grids. The final grid used for all subsequent evaluations of flow behavior is Grid 4. In addition to satisfying the grid independence criteria, Grid 4 has a fine grid density with attainable computational requirements enabling a better approximation of WSS behavior than coarser grids.

**Table 2.3 Parameter data obtained from grids at the plane 30*D* from pipe entrance for the mildly curved geometry.**

| Mildly Curved Pipe ($\delta = 1.45\times10^{-4}$) $K = 100$ | | | | |
|---|---|---|---|---|
| | $\overline{\tau_a}$ [N/m$^2$] ($10^{-3}$) | Percent Difference [%] | $\overline{P_I}/\overline{P_O}$ | Percent Difference [%] |
| Grid 1 | 3.9453 | | 4.1794 | |
| Grid 2 | 3.8923 | -1.3609 | 4.1623 | -0.4105 |
| Grid 3 | 3.8705 | -0.5645 | 4.1675 | 0.1242 |
| Grid 4 | 3.8694 | -0.0287 | 4.1760 | 0.2044 |

**Table 2.4 Parameter data obtained from grids at the plane 30*D* from pipe entrance for the finite curved geometry.**

| Finite Curved Pipe ($\delta = 1.25\times10^{-2}$) $K = 2500$ | | | | |
|---|---|---|---|---|
| | $\overline{\tau_a}$ [N/m$^2$] ($10^{-2}$) | Percent Difference [%] | $\overline{P_I}/\overline{P_O}$ | Percent Difference [%] |
| Grid 1 | 1.0609 | | 4.5246 | |
| Grid 2 | 1.0423 | 1.7844 | 4.4868 | -0.8428 |
| Grid 3 | 1.0375 | 0.4626 | 4.4683 | -0.4141 |
| Grid 4 | 1.0339 | 0.3540 | 4.4579 | -0.2340 |

## 2.3 Numerical Results and Discussion

In the following subsections, we present the general features of flow through a curved pipe with wavy walls. In addition, we detail the influence of Dean number, protrusion amplitude, the number of protrusions, and the pipe curvature on the flow physics. The simulation results illustrating the impact of the wavy wall geometry are comprised of bulk velocity data as well as derived parameters including WSS, vorticity, and circulation. The wavy wall characteristics are compared to the numerically-predicted solution and published results for flow through a curved pipe with a circular cross-section. Given the non-Newtonian fluid properties of blood, the WSS values predicted by the Newtonian model used in this study will deviate from *in vivo* data due to blood interaction with vessel walls and stent struts. Specifically, Walter presents experimental results indicating WSS in the vicinity of the stent struts are higher in the presence of a Non-Newtonian blood analog compare to a Newtonian fluid [96]. This observation should be considered when utilizing the present results to predict *in vivo* flow behavior induced by the presence of a stent.

### 2.3.1 *Overview of Flow Behavior in Curved Pipe with Wavy Walls*

In this section, the common flow features induced by the presence of the wavy wall are discussed for all Dean numbers, $K$, and protrusion heights, $\varepsilon$, explored in this study. The general flow features are similar in the mildly curved and finite curved pipe. As such, the numerical results for the finite curved pipe will be used to illustrate the effect of the wavy wall and pipe curvature given the wider range of Dean numbers investigated. For all geometric configurations, pipe curvature results in the location of the maximum velocity shifting toward the outer wall of the pipe. Figure 2.4(A) highlights this via an axial velocity contour plot for $K = 100$ for the circular pipe and $\varepsilon = 0.1$. The outward skew is due to the domination of the centrifugal force, caused by the acceleration of the fluid around the curvature of the bend, over the force arising from the radial pressure gradient, which drives fluid toward the inner wall [104]. The result is the faster moving fluid at the center of the cross-section being forced toward the outer wall of the bend. Furthermore, the outward shift of the maximum axial velocity results in a steeper axial velocity gradient normal to the wall in the region near the outer wall. With the inclusion of wavy walls, in the region near the peaks the axial velocity gradient normal to the wall is steeper than at troughs of the protrusion profile, as seen by the contour spacing in Figure 2.4(A).

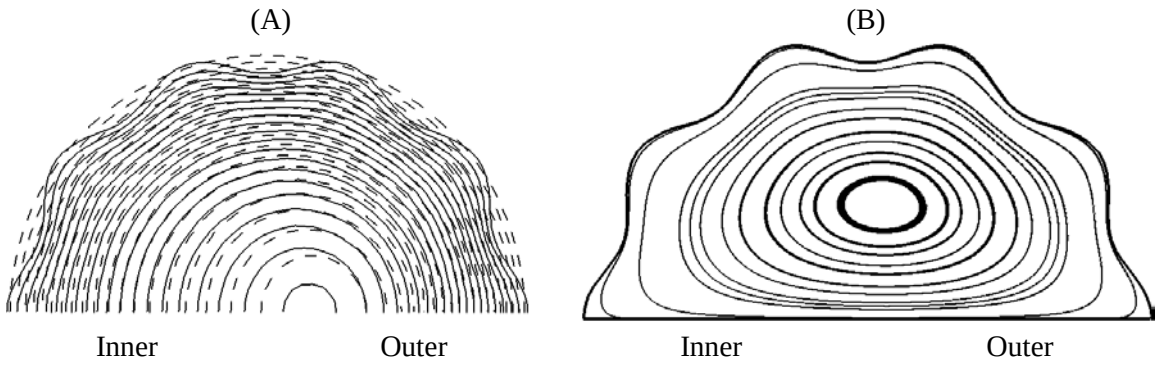


**Figure 2.4 Axial velocity contours (A) and secondary flow structure (B) for $K$ = 100 for $\varepsilon$ = 0.1, $n$ = 5, and $\delta = 1.25\times10^{-2}$. In (A), the solid lines and dashed lines represent contour lines for the wavy-walled pipe and circular pipe, respectively. For the secondary flow structures (B), the flow is carried from the inner wall toward the outer wall along the horizontal centerline.**

The pipe curvature induces secondary flow in the cross-section of the wavy-walled pipe similar to the flow behavior observed in circular cross-sections. The secondary flow structures for the circular pipe are not presented but can be found in the two-vortex solution of Daskopoulos and Lenhoff[76]. The secondary flow structure for $K$ = 100 and $\varepsilon$ = 0.1, presented in Figure 2.4(B), is characterized by the counter-rotating Dean vortices. The introduction of the wavy wall reduces the secondary flow strength and slightly decreases the free stream velocity due to the increased pipe surface area.

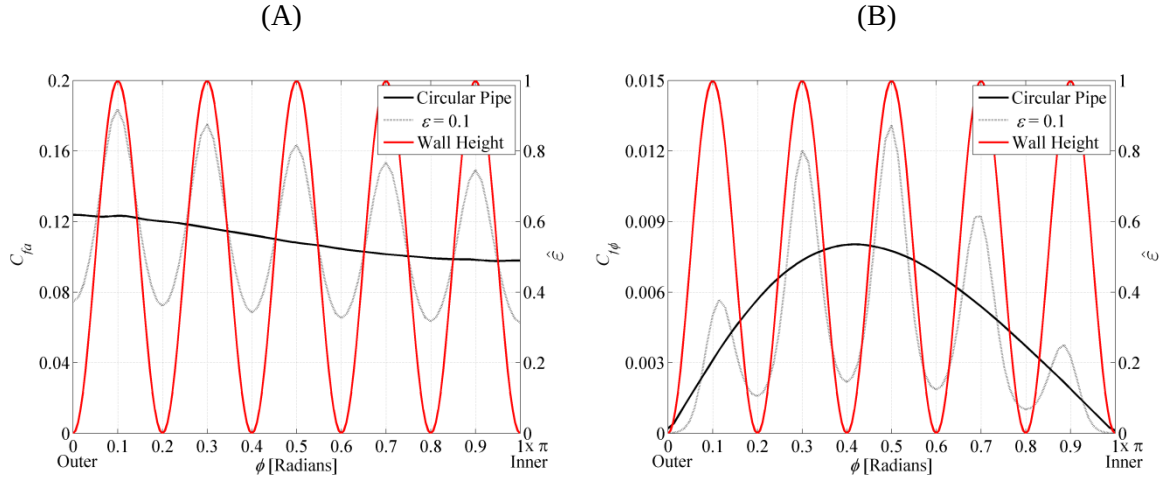


**Figure 2.5 Effect of the inclusion of the wavy wall on the axial ($C_{f\alpha}$) and circumferential ($C_{f\phi}$) skin friction for $K$ = 100 for circular pipe and $\varepsilon$ = 0.1, $n$ = 5, and $\delta = 1.25 \times 10^{-2}$.**

As expected from the velocity contours (see Figure 2.4), the introduction of the wavy walls impacts the WSS distribution considerably. In Figure 2.5, the WSS distributions with $\varepsilon = 0.1$ are compared for $K = 100$ and $\delta = 1.25 \times 10^{-2}$. The ordinate on the left displays the skin friction $C_f = \tau/\rho\bar{V}^2$, where ρ is the fluid density and τ represents the WSS component, be it axial and circumferential. Specifically, $C_{fa}$ corresponds to the skin friction based on the axial WSS component and $C_{f\varphi}$ corresponds to the skin friction based on the circumferential WSS component. The ordinate on the right displays the non-dimensional protrusion height $\hat{\varepsilon} = sin^2(n\phi)$, where a value of 1 indicates the maximum protrusion height. The grid marks on the abscissa indicate the values of $\varphi$ coinciding with the peaks and troughs of the protrusions along the pipe circumference. Note that $\varphi = 0$ corresponds to the outer wall and $\varphi = \pi$ is at the inner wall.

For the circular pipe, the WSS components vary smoothly from the outer wall to the inner wall of the pipe. The axial WSS (see Figure 2.5(A)) monotonically decreases from the outer to inner wall with the global maximum located at the outer wall ($\varphi = 0$) and the global minimum located at the inner wall ($\varphi = \pi$), while the circumferential WSS distribution is zero at the inner and outer walls and is maximum between $\varphi = 0$ and $\pi/2$. By contrast, the WSS components for the wavy-walled pipe have a spatially harmonic distribution due to the protrusions. The global maximum axial WSS for the wavy-walled pipe under the specified conditions is located at $\varphi \approx \pi/10$, which is shifted toward the inner wall ($\varphi = \pi$) when compared to the corresponding circular pipe location due to the presence of a trough at $\varphi = 0$ when n is an odd number. The oscillations in the axial WSS distribution gradually decay from the outer wall ($\varphi = 0$) to the inner wall ($\varphi = \pi$). For the circumferential WSS distribution, the oscillation is greatest around $\varphi = \pi/2$ and decreases toward the inner and outer wall (see Figure 2.5(B)). As expected, in general the local maximum WSS components for the wavy-walled pipe are located around the protrusion peaks and the local minimum WSS components are located in the troughs between the peaks.

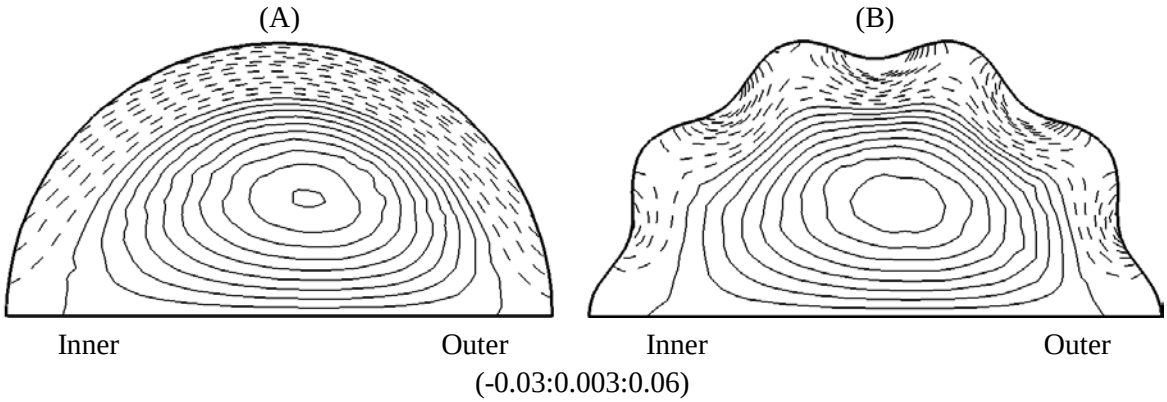


**Figure 2.6 Contour plot of the axial vorticity for the circular pipe (A) and the wavy-walled pipe (B) with $\varepsilon$ = 0.1 and $n$ = 5 for $K$ = 100 and $\delta = 1.25\times10^{-2}$. The spacing between contour levels is given in brackets underneath each figure (Min: Interval: Max).**

At high Dean numbers, the predominant tool for numerically studying the flow in curved tubes is a boundary layer approximation, wherein it is assumed that the viscous effects are confined to a region along the wall [62,76]. Given the more complicated wall geometry in this study, the boundary layer method is eschewed in favor of a direct computation. However, in an effort to compare the present study with previous boundary layer-based work, we plot contours of the axial component of vorticity to aid in qualitatively identifying the "inviscid core" and "boundary layer" regions. Figure 2.6 presents the axial vorticity contour plot for $K$ = 100 for the circular pipe Figure 2.6(A)) and the wavy-walled pipe (Figure 2.6(B)) with $\varepsilon$ = 0.1. The axial vorticity is negative near the wall (indicated by the dashed lines in Figure 2.6), which we use as a marker to delineate the "boundary layer" region. The vorticity becomes positive towards the interior of the cross-section (indicated by the solid lines in Figure 2.6). Additional flow features extracted from the vorticity distribution depend on the Dean number and will be addressed in the subsequent section. These features include the thickness of the "boundary layer", the characteristics of the positive vorticity region in the interior of the cross-section, and the vortex strength.

### 2.3.2 *Effect of Dean number, K*

The influence of the Dean number on steady flow through a curved tube with a circular cross-section is well documented [62,69,74,76,105]. Consequently, the simulation results for the circular cross-section are used as the baseline for comparison in assessing the impact of varying the Dean number on the flow behavior for the wavy wall geometry. The $\varepsilon$ = 0.05 case is used as this

geometry is constructed such that it has the same cross-sectional area as the circular cross-section geometry. In general, the flow behavior exhibits the same general characteristics in the wavy-walled pipe as in the circular pipe as Dean number increases. The left column of Figure 2.7 shows contour plots of the axial velocity for a select subset of Dean numbers $K$ = 500, 1000, and 2500. The solid lines indicate the axial velocity behavior for the wavy-walled pipe and the dashed lines indicate the axial velocity behavior for the circular pipe. The degree of shift of the maximum velocity towards the outer wall due to pipe curvature increases with $K$. In addition, the contour lines become parallel and nearly perpendicular to the symmetry plane in the central section of the pipe for both geometries at $K$ = 2500 (see Figure 2.7 (C) left column). Collins and Dennis attribute this velocity distribution to the development of an inviscid core region in which the axial velocity tends to become largely a function of the $y$-axis [66]. The influence of the wavy walls is largely confined to a region near the walls in all cases. The right column of Figure 2.7 depicts the change in the secondary flow structure as the Dean number increases for $\varepsilon$ = 0.05 for the same subset of Dean numbers. Compared to the symmetric flow structure at $K$ = 100 (see Figure 2.7(B)), the Dean vortices become distorted as $K$ increases. The centers of the Dean vortices shift away from the plane of symmetry into the upper region and toward the inner wall. Daskopoulos and Lenhoff report a similar finding for a circular pipe, in which the center of the secondary flow vortex initially moves toward the outer wall and subsequently moves toward the inner wall with further increases in the Dean number [76].

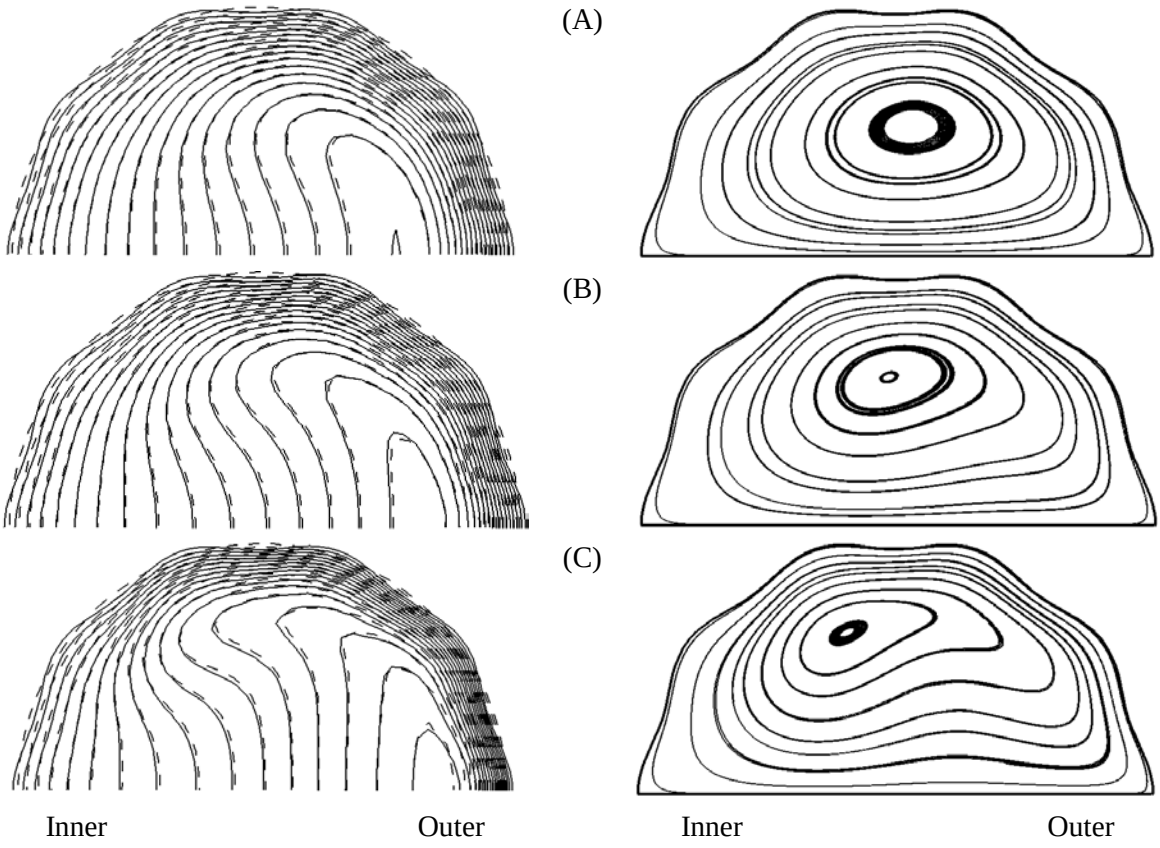


**Figure 2.7 Axial velocity contours (left column) and secondary flow structures (right column) for (A) $K$ = 500, (B) 1000, and (C) 2500 for $\varepsilon$ = 0.05, $n$ = 5, and $\delta = 1.25\times10^{-2}$. For the axial velocity contours (left column), the solid lines indicate the wavy-walled pipe with $\varepsilon$ = 0.05 and the dashed lines indicate the circular pipe. For the secondary flow structures (right column), the flow is carried from the inner wall toward the outer wall along the horizontal centerline.**

Further analysis of the velocity behavior is conducted by examining the $v$-component velocity profile along the horizontal centerline ($z$ = 0) presented in Figure 2.8. For plotting convenience each velocity profile is normalized by its maximum value. A positive value on the plot indicates fluid motion toward the outer wall of the pipe. At low Dean number, the fluid motion toward the outer wall ($y/a$ = 1) is fastest near the center of the pipe, corresponding to the peak in the $v$-component of velocity. At high Dean number, the cross-stream velocity slows down in the central region, eventually resulting in a double-peak velocity profile with high velocity in regions near the inner and outer walls. The higher Dean number is above the critical Dean number identified by Daskopoulos and Lenhoff [76] as a bifurcation point, whereby at least two stable solutions exist to the governing equations, one having a single vortex pair and the other having two vortex pairs in the cross-section. They indicate that the second vortex pair forms at the outer

wall, which is consistent with the velocity trend observed here. Thus, it is feasible that, while no second vortex pair was observed in the current study, that the flow is trending towards a second vortex pair formation.

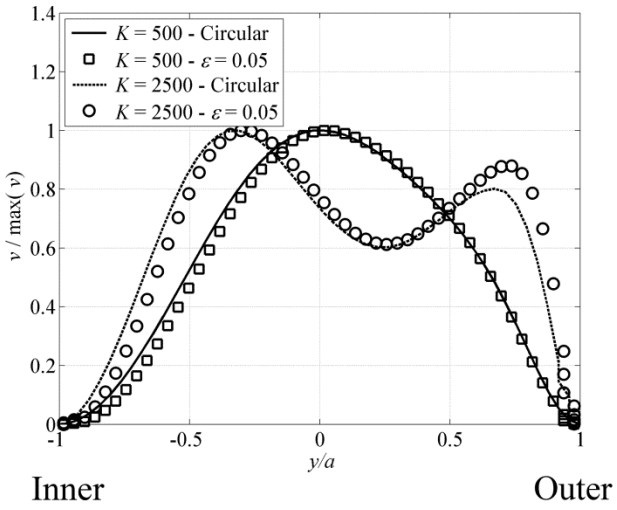


**Figure 2.8 Profile of the *v*-component of velocity along the y-axis for $\varepsilon = 0.05$, $n = 5$, and $\delta = 1.25\times10^{-2}$ at various Dean numbers. Each profile is normalized by its maximum velocity value ($K = 500$ – Circular Pipe: $5.67 \times 10^{-4}$ m/s, $\varepsilon = 0.05$: $5.70 \times 10^{-4}$ m/s; $K = 2500$ – Circular Pipe: $9.20 \times 10^{-4}$ m/s, $\varepsilon = 0.05$: $9.24 \times 10^{-4}$ m/s) and the position along the y-axis is normalized by the pipe radius *a*.**

The variation of the axial ($\tau_a$) and circumferential ($\tau_\varphi$) WSS with *K* is presented in Figure 2.9 for the finite curved pipe ($\delta = 1.25 \times 10^{-2}$). In each subfigure, the left ordinate displays the WSS component normalized by its maximum value. These maximum WSS values are listed in Table 2.5 for reference. Unsurprisingly, the maximum wall shear stress increases with K, with the circumferential WSS being less than the axial WSS for the Dean numbers presented. For the circular pipe, the circumferential WSS is of the same order of magnitude as the axial WSS at low Dean numbers and drops to approximately one order of magnitude less than the axial WSS at higher Dean numbers. For the wavy-walled pipe, the circumferential WSS is approximately two orders of magnitude less than the axial WSS at low Dean number. In general, the average WSS is greater for the wavy wall geometry. From Figure 2.9, as *K* increases, the location of the maximum axial and circumferential WSS shifts slightly outward. This observation is due to the shift in the location of the maximum axial velocity and vortex center toward the outer wall. In addition, the

decay in the axial WSS oscillations from outer to inner wall is more severe as the Dean number increases. The peaks in the circumferential WSS shift away from the protrusion peaks depending upon the secondary flow patterns, shown for specific cases in Figure 2.7.

**Table 2.5 Maximum value of axial and circumferential WSS components for a subset of Dean numbers for the circular pipe and $\varepsilon = 0.05$, $n = 5$, and $\delta = 1.25 \times 10^{-2}$.**

| | Circular Pipe | | Wavy-Walled Pipe ($\varepsilon = 0.05$) | |
|---|---|---|---|---|
| | Max ($\tau_a$) [N/m$^2$] ($10^{-2}$) | Max ($\tau_\varphi$) [N/m$^2$] ($10^{-3}$) | Max ($\tau_a$) [N/m$^2$] ($10^{-2}$) | Max ($\tau_\varphi$) [N/m$^2$] ($10^{-3}$) |
| $K$ = 100 | 0.0047 | 0.0302 | 0.0567 | 0.0041 |
| $K$ = 500 | 0.2756 | 0.3381 | 0.3370 | 0.4234 |
| $K$ = 1000 | 0.5753 | 0.7782 | 0.6860 | 1.0250 |
| $K$ = 2500 | 1.7231 | 2.2203 | 2.0037 | 2.9962 |

In order to determine the effect of Dean number on the boundary layer region and inviscid core, contours of the axial component of vorticity are plotted in Figure 2.10 for $K$ = 100 and $K$ = 2500. As discussed in Section 3.1, the axial vorticity is negative near the wall and becomes positive towards the interior of the cross-section. At high Dean number (above the critical value introduced by Daskopoulos and Lenhoff [76]), a second region of negative vorticity emerges toward the outer wall (Figure 2.10(B)) in a position that nearly coincides with the location of the formation of the additional vortices for the four-vortex solution. The presence of this region suggests the early stages of development of these additional vortices that rotate opposite to the direction of Dean vortices [76]. To elucidate the thickness of the boundary layer region as the Dean number increases, Figure 2.11(A) presents a plot of the zero axial vorticity contours for various values of $K$. In addition, Figure 2.11(A) shows for $K \geq 1000$ that the size of the region of negative vorticity located toward the outer wall increases with $K$. With further increase of the Dean number the boundary layer region near the outer wall thins.

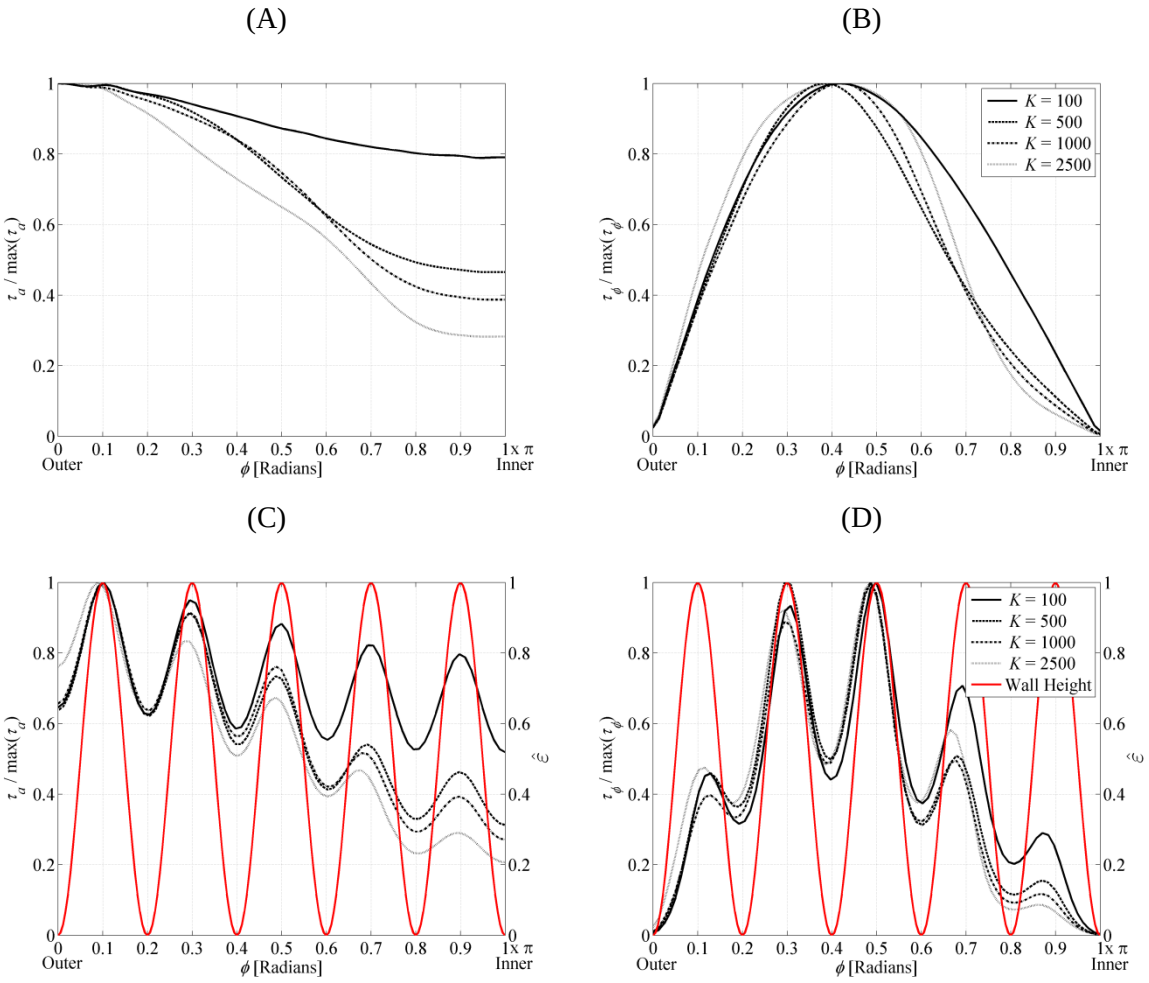


**Figure 2.9 (A) Axial and (B) circumferential WSS for the circular pipe and (C) axial and (D) circumferential WSS for $\varepsilon = 0.05$, $n = 5$, and $\delta = 1.25\times10^{-2}$. All WSS profiles are normalized by their maximum values. The normalized protrusion heights are also plotted for positional reference in the wavy wall cases. Note that $\varphi = 0$ corresponds to the outer wall.**

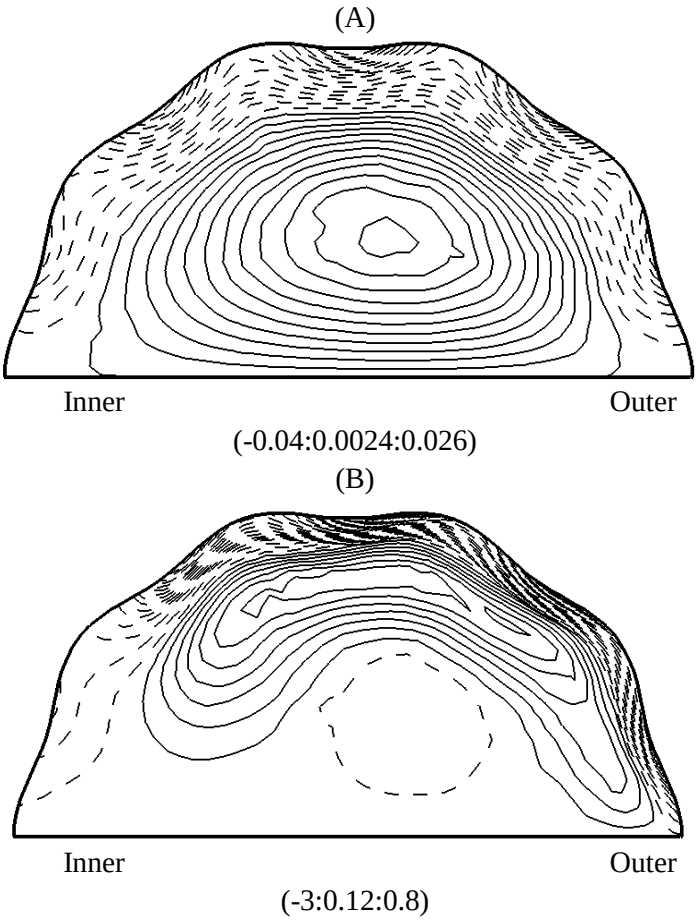


**Figure 2.10 Contour plot of the axial vorticity for (A) $K$ = 100 and (B) $K$ = 2500 for $\varepsilon$ = 0.05, $n$ = 5, and $\delta$ = 1.25×10$^{-2}$. The spacing between contour levels is given in brackets underneath each figure (Min: Interval: Max).**

Approximating the boundary layer thickness, $a_{\omega 0}$, as the radial distance between the wavy wall and the near-wall contour line of zero vorticity, we present $a_{\omega 0}$ normalized by $r_{\mathrm{tube}}$ of a bend with $\varepsilon$ = 0.05, for $K$ = 100, 500, 1000, and 2500 in Figure 2.11(B). For all values of $K$, $a_{\omega 0}$ generally increases from the outer to inner wall of the bend, with some local fluctuations superposed. At the outer wall ($\varphi$ = 0), $a_{\omega 0}/r_{\mathrm{tube}}$ decreases from approximately 20% of the tube radius for $K$ = 100 to 5% for $K$ = 2500, while remaining relatively constant near the inner wall. That is, as $K$ increases, the boundary layer thickness in the outer wall region becomes thinner. This trend matches the accounts of the secondary boundary layer for a circular pipe by Berger *et al.* [67]. Figure 2.12 presents the circulation computed in the cross-sectional plane based on the axial vorticity versus $K$. The circulation is used as a measure of the strength of the Dean vortex for a

given *K*. The circulation increases with *K* regardless of the shape of the bend wall. The effect of the wavy wall on the circulation is very small when compared to the circular pipe for $K < 2500$. For $K = 2500$, the introduction of the wavy wall causes the circulation to increase by approximately 4% compared to the circular pipe. The increased circulation for the wavy-walled pipe compared to the circular pipe is associated with the increase in the *v*-component of velocity along the horizontal centerline in the central and outer wall region of the pipe (see Figure 2.8).

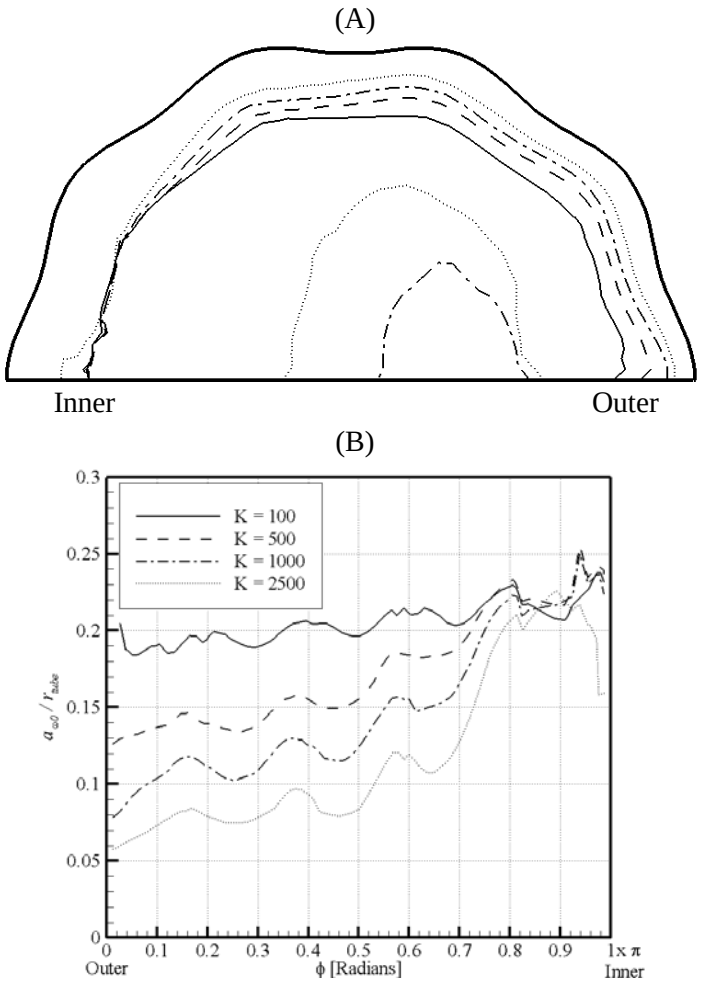


**Figure 2.11 (A) Contour plot of zero vorticity region, and (B) thickness of the boundary layer region $a_{\omega 0}$ normalized by the tube radius $r_{tube}$ for $\varepsilon = 0.05$, $n = 5$, and $\delta = 1.25\times10^{-2}$.**

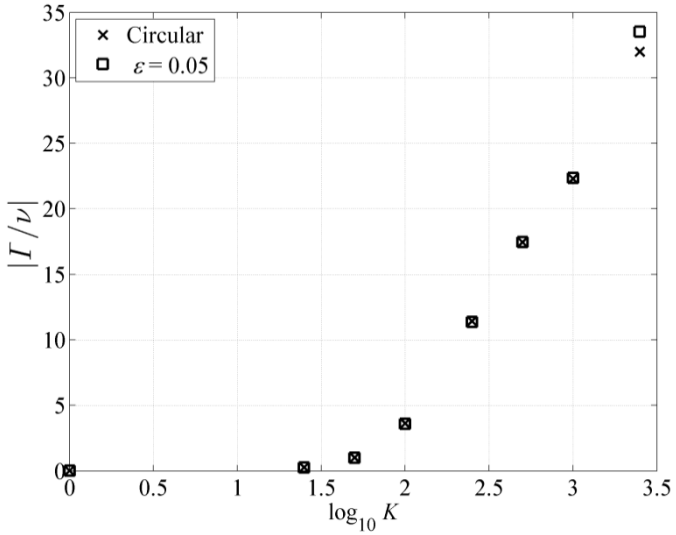


**Figure 2.12 Non-dimensional circulation of the secondary flow as a function of the Dean number for various protrusion heights at $n$ = 5 and $\delta = 1.25\times10^{-2}$.**

### 2.3.3 *Effect of Protrusion Height, ε*

In this section, the effect of the protrusion height is investigated for low and high values of $K$. We note that since the cross-sectional area of the pipe reduces as $\varepsilon$ increases (see Equation A**. 7**) and the average velocity is held constant for a given Dean number, an increase in the protrusion height slightly reduces the effective Dean number. This reduction in the effective Dean number explains some aspects of the observed flow behavior as $\varepsilon$ increases. Particularly, the maximum axial velocity increases with $\varepsilon$ and its location shifts toward the inner wall of the pipe. The inward shift of the maximum axial velocity with increasing $\varepsilon$ is correlated with a decrease in the Dean number for pipes with circular cross-sections. The increase in the maximum axial velocity is characteristic of straight pipes as the cross-sectional area is reduced for a fixed volumetric flow rate. The effect of the protrusion height on the $v$-velocity component along the horizontal centerline ($z$ = 0) is presented in Figure 2.13 for $K$ = 500 and $K$ = 2500 with $n$ = 5 and $\delta = 1.25\times10^{-2}$. With larger $\varepsilon$, the location of the maximum $v$-component of velocity shifts toward the outer wall. For $K$ = 500, as $\varepsilon$ increases, the $v$-component of velocity along the horizontal centerline decreases near the inner and outer wall (see Figure 2.13 (A)). A physical interpretation is that the circumferential protrusions retard the motion of the fluid returning to the inner wall within the secondary flow boundary layer and the effect is rendered more remarkable with increased

protrusion into the cross-section. Further, the *v*-component of velocity moderately increases with $\varepsilon$ near the pipe center ($0 < y/a < 0.5$) (see Figure 2.13 (A)). For $K = 2500$ the *v*-component of velocity decreases within one-half radius from the inner wall but otherwise increases as $\varepsilon$ increases (see Figure 2.13(B)). It therefore indicates that the wavy wall may have an impact on the secondary flow behavior above the critical Dean number in the region toward the outer wall, which is where the secondary flow boundary layer is thinnest.

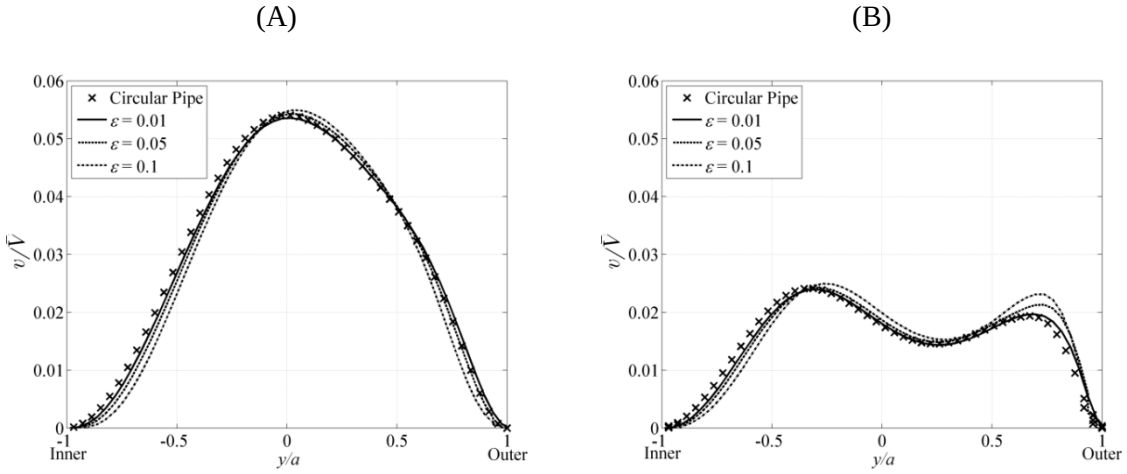


**Figure 2.13 Cross-stream velocity profiles for (A) $K = 500$ and (B) $K = 2500$ for various protrusion heights with $n = 5$ and $\delta = 1.25\times10^{-2}$.**

The effect of $\varepsilon$ based on the numerical solution is compared to Peterson's perturbation solution using the mildly curved pipe geometry ($\delta = 1.45\times10^{-4}$) [73]. Axial and cross-stream velocity profiles are compared to Peterson's perturbation solution in Figure 2.14 for $K = 1$ and 100. For $K = 1$, the numerically determined axial velocity profile along the horizontal centerline ($z = 0$) overlaps that of the perturbation solution for $\varepsilon = 0.01$ (see Figure 2.14(A)). For higher values of $\varepsilon$, however, disparity between the perturbation and numerical solutions manifests. The perturbation solution assumes that $\varepsilon n << 1$, so it is reasonable that the solutions diverge as $\varepsilon$ increases for a fixed value of *n*. With increasing $\varepsilon$, maximum axial velocity based on the numerical solution increases slightly, by approximately 2%. By contrast, the perturbation solution shows a consistent drop in the axial velocity along the horizontal centerline as $\varepsilon$ increases resulting in a decrease in the maximum axial velocity. Peterson assumes in his formulation of the perturbation solution for a mildly curved pipe that the axial pressure gradient is fixed and it is related to the average and maximum axial velocity in the same way as in a straight pipe. Therefore, as the cross-sectional area shrinks, the maximum axial velocity decreases. For the numerically-predicted solution, the

average velocity is held constant, allowing the pressure gradient to vary. As in a straight pipe, the pressure gradient will adjust to maintain the fixed average velocity, leading to no change in the maximum axial velocity. The deviation of the axial velocity profile for the perturbation solution compared to the numerically-predicted solution is due in part to the limitation in the validity of the perturbation solution for higher $\varepsilon$ and the difference in the fixed flow parameters for each solution. On the other hand, both the perturbation and numerically-predicted solutions depict a decrease in the *v*-component of horizontal centerline velocity as $\varepsilon$ increases. The similar trend notwithstanding, the perturbation solution predicts a larger drop in the *v*- component of velocity with higher $\varepsilon$.

Consider now the upper limit of the range of Dean numbers for the mildly curved pipe for the perturbation solution, $K = 100$. For $\varepsilon = 0.01$ the numerically-predicted profile of the axial velocity along the horizontal centerline closely matches Peterson's perturbation solution in the vicinity of the inner and outer walls but deviates in the central region (see Figure 2.14(B)). From the numerical simulations, the maximum axial velocity is observed to increase with $\varepsilon$, but the perturbation solution predicts the contrary, as well as a shift of the maximum axial velocity more toward the outer wall of the bend. For $\varepsilon = 0.01$, the *v*-component for the numerical solution is less than the perturbation solution between the pipe center and the outer wall (see Figure 2.14(D)). Again, the perturbation solution shows a greater decrease in the v-component of the velocity along the horizontal centerline with larger $\varepsilon$ than the numerically-predicted solution. The deviation between the perturbation solution and the numerically-predicted solution for K = 100 can be attributed to the limitation of the validity of the perturbation solution to $K \leq 96$.

The protrusion amplitude is observed to impact the WSS, "boundary layer" thickness and vortex strength. For all values of $\varepsilon$, Figure 2.15 presents the skin friction based on the axial and circumferential WSS components for $K = 500$, $n = 5$, and $\delta = 1.25\times10^{-2}$. As $\varepsilon$ increases, the skin friction increases in the vicinity of the peaks and decreases in the troughs between the peaks. In turn, WSS gradients increase around the circumference of the pipe with the largest increase occurring near the outer wall. There is no shift in the location of the maximum and minimum skin friction with $\varepsilon$. As $\varepsilon$ increases, the slope of $C_{f\varphi}$ decreases for low Dean numbers in the region toward the outer wall (Figure 2.15(B)), but is observed to increase for higher *K* (Figure 2.9 (D)). This further indicates the difference in the impact of the wavy wall on either side of the critical Dean number. Figure 2.16 presents a contour plot of zero vorticity for various protrusion heights at $K = 2500$ and $\delta = 1.25\times10^{-2}$. Note again that a second region of negative vorticity is formed off

the tube center toward the outer wall of the pipe at $K$ = 2500. Figure 2.16 shows that the area of the region decreases as $\varepsilon$ increases. This is likely due to the reduction in the effective Dean number with increasing $\varepsilon$, as discussed previously. Overall, the boundary layer thickens as the protrusion height increases. For $K$ < 2500, the circulation strength decreases as $\varepsilon$ increases (data not shown). This corroborates the decrease in the v-component of velocity along the horizontal centerline as shown in Figure 2.13(A). The drop in circulation as $\varepsilon$ increases is the greatest for $K$ = 100 at approximately 15% and lowest for $K$ = 1000 at nearly 4%. For $K$ = 2500, the circulation increases as $\varepsilon$ increases by approximately 3% and also corresponds with the increase in the v-component of velocity shown in Figure 2.13(B).

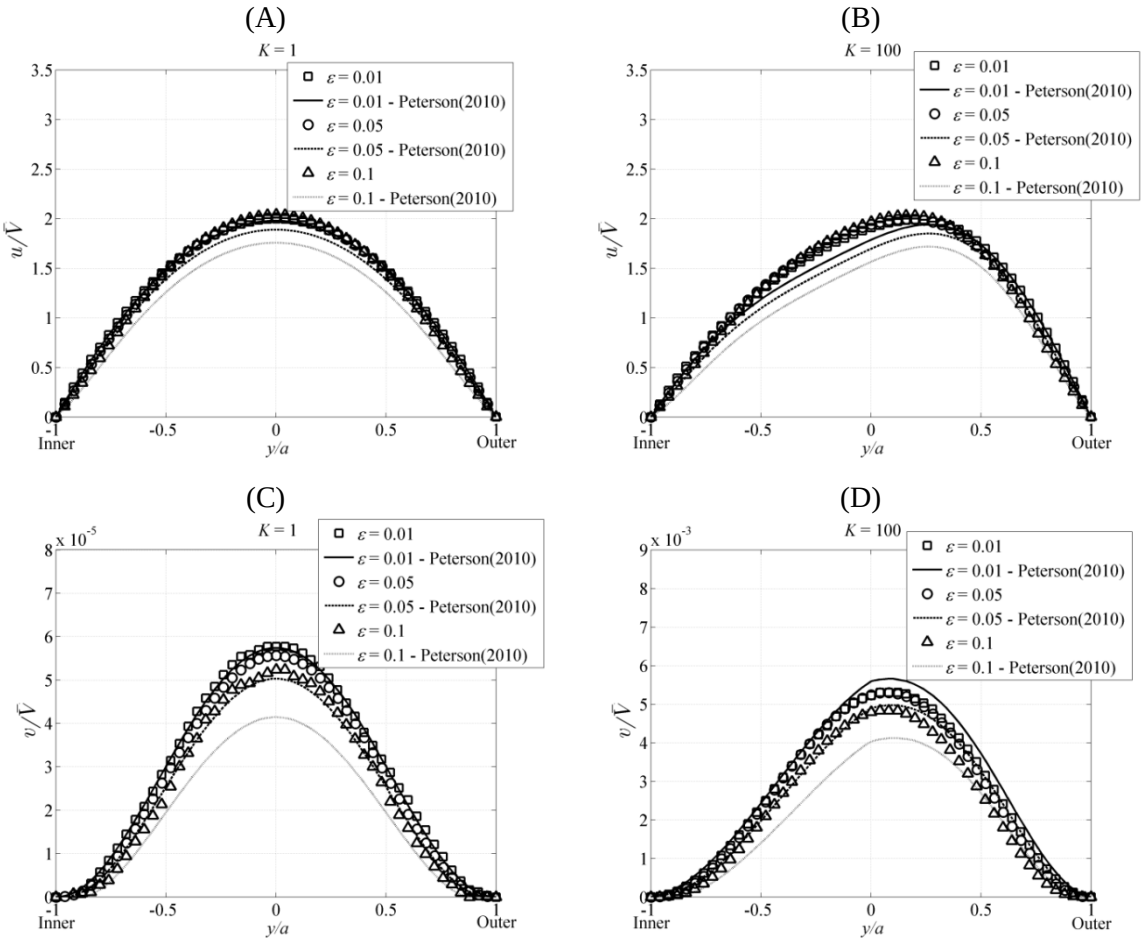


**Figure 2.14 Comparison of the numerically predicted axial (1st row) and cross-stream velocity profiles (2nd row) with the perturbation solution of Peterson (2010) for $K$ = 1 (1st column) and $K$ = 100 (2nd column) with $n$ = 5 and $\delta = 1.45\times10^{-4}$.**

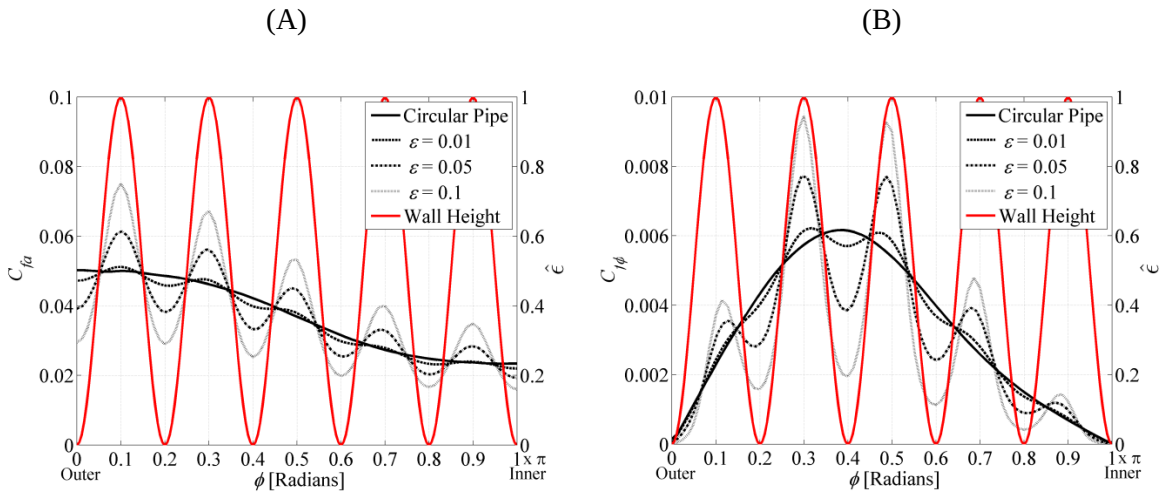


**Figure 2.15 Effect of $\varepsilon$ on the (A) axial and (B) circumferential skin friction for $K$ = 500, $n$ = 5, and $\delta = 1.25\times10^{-2}$.**

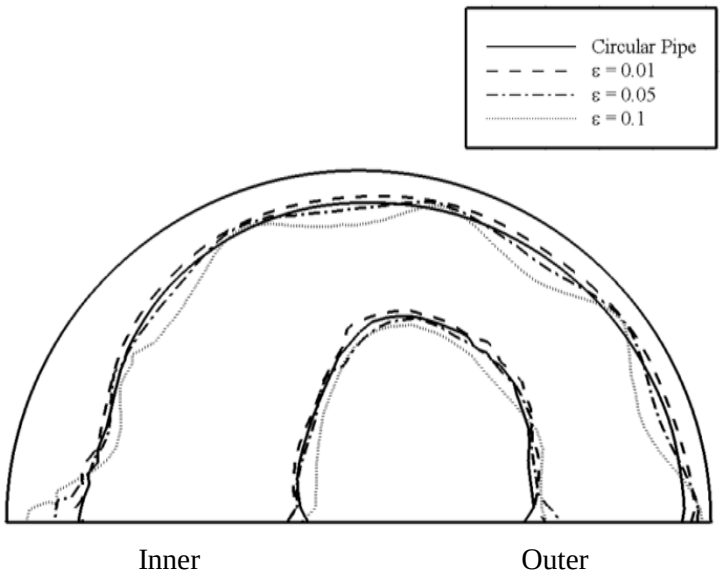


**Figure 2.16 Zero vorticity contour for various protrusion heights at $K$ = 2500 and $\delta = 1.25\times10^{-2}$.**

### 2.3.4 *Effect of Curvature for K = 100*

In order to assess the effect of curvature, the numerical results for $K$ = 100 are compared for the mildly curved ($\delta = 1.45\times10^{-4}$) and finite curved ($\delta = 1.25\times10^{-2}$). For brevity, the data for this comparison will not be presented in this paper but important observations will be discussed. For a fixed Dean number, the balance of the centrifugal inertial force to the viscous forces should be the same for each pipe. Siggers and Waters note distinct changes in flow behavior as the curvature ratio is increased from $\delta$ = 0.1 to 0.3 for a fixed Dean number [62]. The curvature ratios for the pipes in the present study are quite small compared to the finite pipe curvature ratios investigated by Siggers and Waters. Thus, only minor changes in flow behavior are expected when comparing the pipe geometries. It should be highlighted that in order to achieve the same Dean number in the mildly curved pipe and finite curved pipe, the average velocity is greater for the mildly curved pipe (see Equation A. 4). In turn, the volumetric flow rate for the finite curved pipe is lower compared to the mildly curved pipe. The difference in volumetric flow rate plays a role in the comparison of flow behavior for the different curvature ratios.

The axial velocity decreases as $\delta$ increases due to the difference in volumetric flow rate for the curvature ratios. The magnitude and distribution of the secondary flow velocity are found to be independent of curvature due to the fixed Dean number, though this would likely change for larger curvature ratios when the Coriolis forces become significant. The location of maximum axial WSS at $\varphi = \pi/10$ near the outer wall does not change for the different curvature ratios. This observation corroborates the finding by Siggers and Waters, where the location of maximum axial WSS was found near the outer wall for $\delta < 0.2$ [62]. As $\delta$ increases, the axial WSS decreases at every point, likely due to the lower average inlet velocity. The vorticity magnitude and distribution are independent of the curvature ratio over the range studied. Interestingly, the circulation decreases as $\delta$ increases. This again may be attributed to the lower volumetric flow rate through the finite curved pipe. The greatest decrease is observed for $\varepsilon$ = 0 and $\varepsilon$ = 0.05 (~4%) and minimum for $\varepsilon$ = 0.01 (~1%).

### 2.3.5 *Effect of the Number of Perturbations, n*

The effect of increasing $n$ from 5 to 8 on flow characteristics is observed to be the same for $\varepsilon$ = 0.05 and $\varepsilon$ = 0.1 for $\delta = 1.25\times10^{-2}$; as such, changes in the flow behavior with protrusion number are demonstrated here using a protrusion height of $\varepsilon$ = 0.05. Moreover, the trends

discussed are consistent for all values of *K*. As *n* increases, there is a decrease in the axial velocity near the outer wall and an increase near the inner wall. The *v*-component of velocity increases with *n* near the inner wall and decreases with *n* near the outer wall. The increase in the components of velocity near the inner wall appears to be approaching the value for the circular pipe. This trend is expected since as *n* goes to infinity the wall profile would approach the shape of a circular pipe. A similar trend is predicted by Peterson's perturbation solution [73].

The pipe cross-section with $n = 5$ versus $n = 8$ is illustrated in Figure 2.17(A) along with the skin friction distribution as a function of *n* (Figure 2.17(B, C)). The difference between the global maximum and minimum axial skin friction increases with n (Figure 2.17(B)). The location of the global maximum $C_{fa}$ shifts toward the outer wall ($\varphi = 0$) and its magnitude increases with n (Figure 2.17(C)). The location of global maximum $C_{f\varphi}$ varies between $n = 5$ and $n = 8$, depending on the geometry at $\varphi = \pi/2$. When n is odd, there is a protrusion peak at $\varphi = \pi/2$, and the maximum circumferential WSS is located in its vicinity. When n is even, there is a trough at $\varphi = \pi/2$, so the location of the global maximum circumferential WSS shifts to the next peak in the direction of the outer wall.

Due to the redistribution of protrusions as *n* increases, the secondary flow boundary layer thickness changes slightly. Near the inner wall $a_{\omega 0}$ remains unchanged as *n* increases. On the other hand, $a_{\omega 0}$ at the outer wall is greater for $n = 8$ as compared to $n = 5$. This is due to the location of a protrusion peak closer to the outer wall for the $n = 8$ geometry. The circulation strength decreases as *n* increases and the reduction in strength increases with *K*, which is in agreement with Peterson's perturbation solution [73]. It is believed that this is a result of the increase in the surface area, and thus friction, as *n* increases. In the present case, the greatest decline in circulation strength is observed for $K = 2500$ which decreases by 5% for $\varepsilon = 0.05$ and 12% for $\varepsilon = 0.1$.

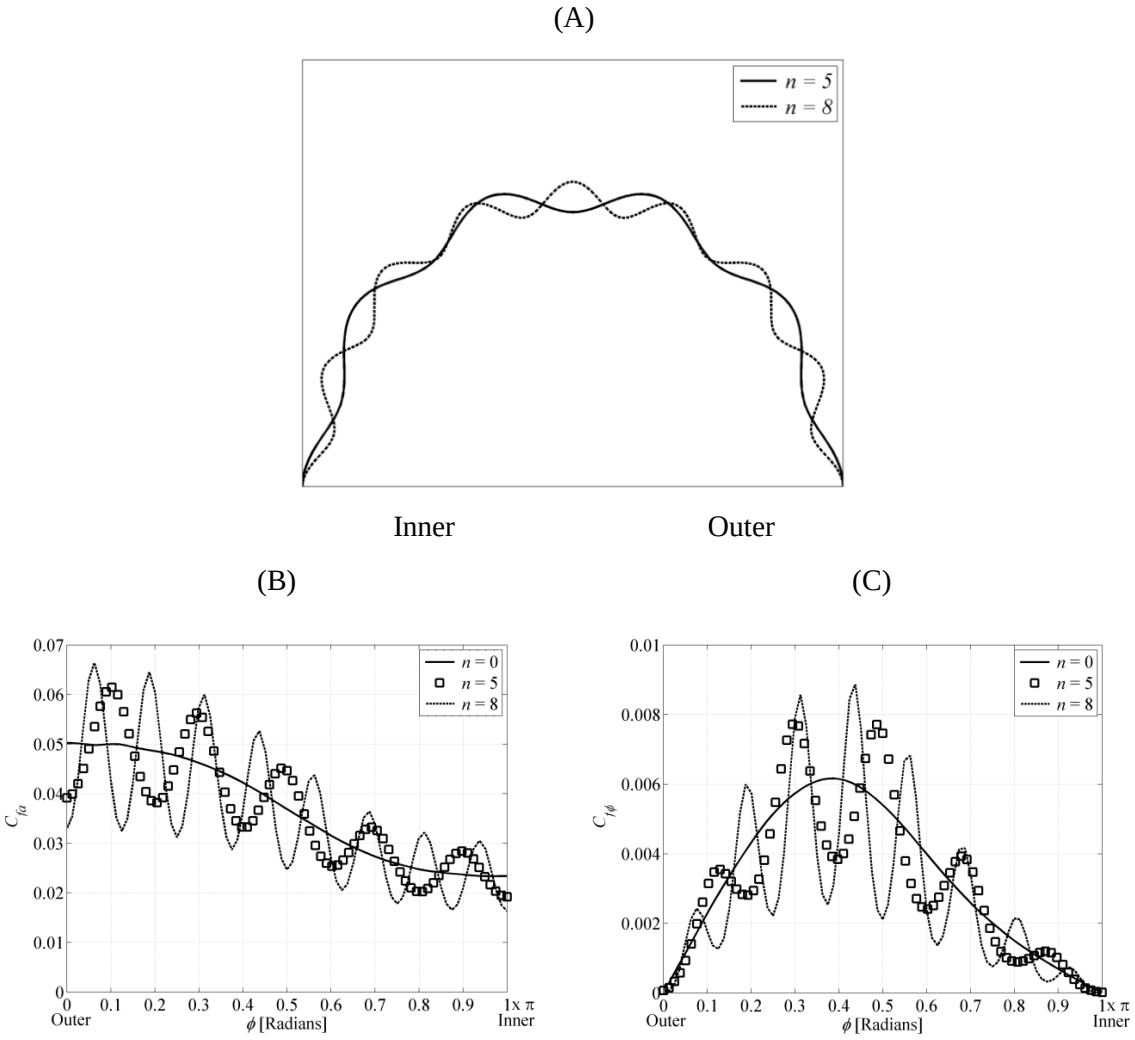


**Figure 2.17 The wall shape (A) for pipe cross-section with $n$ = 5 versus $n$ = 8. Effect of $n$ on the (B) axial, and (C) circumferential skin friction for $K$ = 500, $\varepsilon$ = 0.05, and $\delta$ = 1.25×10$^{-2}$ ($n$ = 0 represents a circular pipe).**

## 2.4 Summary of Wavy Wall Study

Herein, we presented a CFD study of steady fully-developed flow through curved pipes of small curvature ratios with axially aligned wavy walls in the cross-section. The modeled geometries included protrusions of various height and frequency. Since previous analytical work assumed infinitesimally small curvature, which cannot be modeled using the available software suite, the flow conditions were approximated by using pipes with small but finite curvature to minimize the influence of Coriolis forces. The impact of curvature as well as the wavy wall

geometry were addressed by assessing changes in the bulk velocity and derived parameters such as wall shear stress, vorticity and secondary flow circulation. For the range of Dean numbers investigated, the flow velocity exhibits the same general characteristics in the wavy-walled pipe as in the circular pipe with the same cross-sectional area. The inclusion of protrusions predominantly influences the near wall region. In particular, the axial velocity gradient normal to the wall is steeper at peaks than at troughs of the periodic protrusions. The WSS components are observed to vary along the circumference harmonically due to the fluid motion over the protrusions with local maxima and minima located around the protrusion peaks and troughs, respectively. The influence of the pipe curvature on the WSS distribution is demonstrated by the decrease in the axial WSS from the outer wall to the inner wall of the pipe, due to the shift in the maximum axial velocity toward the inner wall. The impact of wall waviness on derived flow parameters, such as vorticity, is also relegated to the near-wall region. The vorticity pattern matches published results for the circular pipe over the bulk of the cross-section, with secondary flow boundary layers generally thinning as the Dean number increased near the outer wall. In addition, the strength of the secondary flow increases with the Dean number, as in pipes with circular cross-sections. The changes in flow behavior with further increase in pipe curvature were not explored in the present study. However, similarities between the flow behavior in the wavy-walled pipe and pipes with circular cross-sections established in this report suggest that increased curvature in the wavy walled pipe would result in flow behavior previously observed for circular pipe studies [62].

With larger $\varepsilon$ the $v$-component of velocity near the inner wall is reduced indicating a reduction in the motion of fluid returning along the upper wall of the pipe. When compared to the perturbation solution by Peterson [73], the numerically-predicted velocity profile deviated from the perturbation solution with protrusions of greater amplitudes due to the limitation of the perturbation solution to $\varepsilon n \ll 1$. As for the impact of $\varepsilon$ along the walls, the WSS components increase near the protrusion peaks and decrease in the troughs between the protrusions as $\varepsilon$ increases. Subsequently, the average axial WSS is observed to decrease as $\varepsilon$ increases and matches the first order effect of the wavy wall in Peterson's perturbation solution. Concurrently, the strength of the secondary flow decreases as $\varepsilon$ increases for $K < 2500$ but increases for $K = 2500$. The increase in the vortex strength for $K = 2500$ is corroborated by the overall increase in the $v$-component of velocity along the horizontal centerline as $\varepsilon$ increases. The effect of curvature on the flow behavior in the wavy-walled pipe was minimal since the differences in curvature for the numerical pipes were relatively small. A decrease in the axial velocity magnitude and circulation

was noted. This behavior is attributed to the difference in the average inlet velocity for the curvature ratios in order to achieve the same Dean number value. The fixed Dean number also results in the secondary flow magnitude being independent of curvature.

The effects of increasing $n$ from 5 to 8 on flow characteristics are the same for various protrusion heights. Moreover, the trends discussed are consistent for investigated values of $K$. The change in the number of protrusions was expected to change the WSS distribution and as $n \rightarrow \infty$ the distribution should approach that of the circular pipe. This is made apparent by the outward shift in the location of maximum axial WSS as $n$ increases. The location of the maximum circumferential WSS shifts toward the outer wall and its magnitude increases with $n$. Overall, the area of the geometry experiencing low WSS increases due to an increase in the number of troughs with $n$. Lastly, the strength of the secondary flow decreases as $n$ increases and is likely due to the additional circumferential surface area slowing fluid motion.

# Chapter 3

# Study B: Steady Flow in Curved Pipe with a Realistic Stent Model

## 3.1 Problem Statement

The physical problem under investigation is the fluid dynamics induced by flow through a curved pipe with a realistic stent model under steady, fully developed flow conditions. Newtonian and non-Newtonian fluid models are utilized to discuss their impact on flow behavior and associated near wall conditions pertinent to stent performance. The geometric model components, presented in Figure 3.1, represent a section of curved vessel with an implanted stent model. We extend the work of Prince *et al*. to examine geometrically realistic stent designs[101]. Numerical simulations enable the evaluation of flow behavior in the vicinity of protrusion configurations that closely mimic commercially available stent designs. Further, the model facilitates the examination of flow behavior at the entrance and exit of the stented region. The flow behavior at the entrance and exit of the stent is dictated by the transition from the native vessel region to the stented region and back again. The frequency and aspect ratio of the protrusions are varied parametrically, as is the Dean number, within a physiologically relevant range. Three coordinate systems are defined in Figure 3.2; a global fixed Cartesian coordinate system *XYZ*, a local Cartesian system within the tube cross-section *xyz*, and a local polar coordinate system r$\varphi$, also within the tube cross-section. The same coordinate system is defined for the geometric model presented in Prince *et al.*, which includes a full description of its orientation.

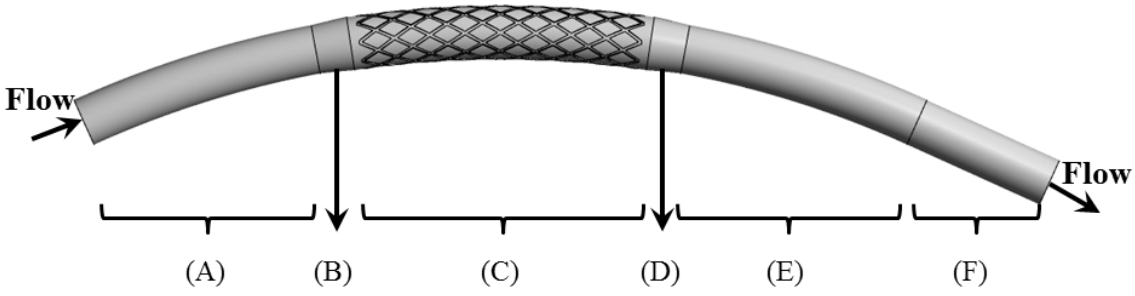


**Figure 3.1 Overview of the stented model vessel, consisting of an entrance section (A) to ensure a fully developed flow into the stented region (C), an exit section (E) to allow the examination of exit effects, and lastly, a straight pipe region (F). An expansion region (B) and taper region (D) are located proximal and distal to the stented region, respectively.**

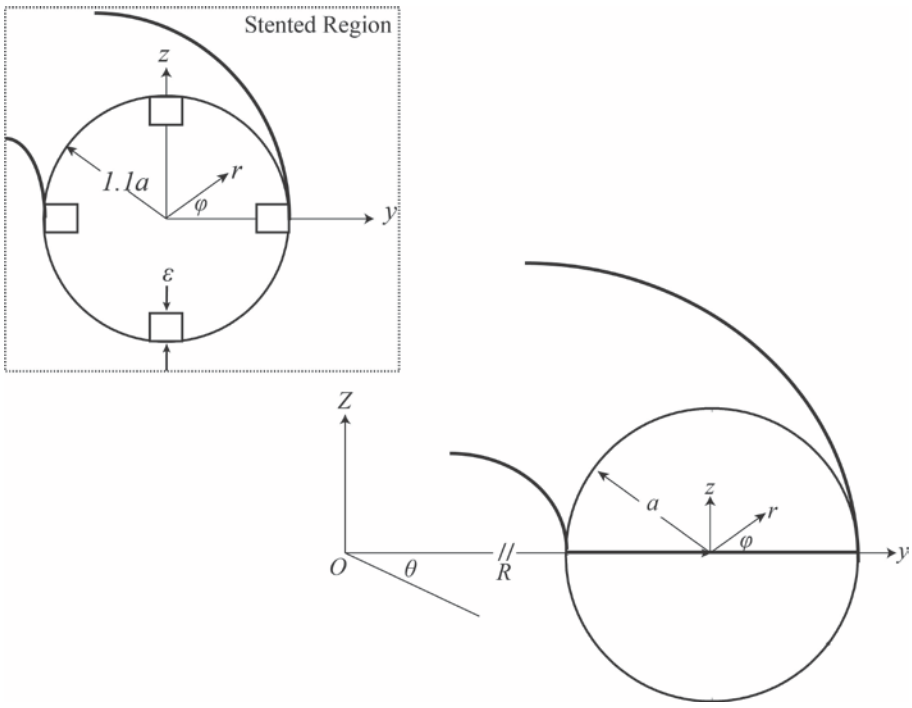


**Figure 3.2 Stented vessel geometry displayed with the defined coordinate systems in the smooth walled section and the stented region (see inset).**

In the absence of torsion or other asymmetric influences, the flow in curved pipes is symmetric about the plane of the bend[62]. The symmetric condition has been established for smooth walled pipes but remains unexplored for curved pipes with wall protrusions, particularly protrusions with a step-like shape [93]. While it is anticipated that the flow will be symmetric for the particular geometries explored herein, to facilitate future studies with asymmetric protrusion distributions, the stented vessel is modelled with a full circular cross-section, as shown in Figure 3.2. The stented vessel model is rigid walled with a nominal tube radius $a$ and a fixed curvature ratio of $\delta = a/R = 2.4\times10^{-2}$, where $R$ is the radius of curvature of the pipe as it winds around the $Z$-axis. The curvature ratio emulates the geometry of the right coronary artery (RCA), a vessel prone to atherogenesis in the proximal vessel region, and thus a common site for stent implantation[106,107]. Notably, the curvature ratio is greater than that of the "finite" curved pipe investigated by Prince *et al*., suggesting a more significant influence of Coriolis forces[62]. The stented vessel model has a total arc length of 20.70$D$, corresponding to $\theta = 48.68°$. The entrance and exit regions, shown in Figure 3.1 (A) and Figure 3.1(E) respectively, are each 5$D$ in arc length. The stented region, shown in Figure 3.1 (C), is 6.2$D$ in arc length. The computational vessel is modeled with a stent-

to-artery diameter of 1.1:1, representative of the standard manufacturer recommended expansion ratio to ensure the stent is securely fastened to the vessel wall *in vivo*[86]. Expansion (Figure 3.1(B)) and taper regions (Figure 3.1(D)), each approximately 0.78*D* in length, are located proximal and distal to the stented region, respectively, to model the vessel dilation due to stent implantation. The length of the tapered regions is based upon previous studies in straight vessels with model stents[91]. The transition from the entrance and exit regions to the taper regions are not smoothed, to (*i*) facilitate comparisons with previous studies in straight vessels, and (*ii*) since this will be a conservative "worst case" scenario, where stent implantation creates a sharp kink at the proximal and distal ends. A straight pipe section, 3*D* in length, is included distal to the exit vessel in order to ensure the solution in the curved region is not impacted by the prescribed outlet boundary condition, as discussed in Section 4.2.

The wall protrusions are rectangular in cross-section and arranged circumferentially and axially along the vessel wall. The cross-sectional geometry of the protrusions is characterized by variations in the aspect ratio, *AR*, of the protrusion width, $\xi$, to protrusion height, $\varepsilon$ (Figure 3.1). The protrusion width and height are non-dimensionalized by the radius of the native vessel, *a*. The total number of circumferential protrusions is *m* at the proximal end of the stent. Table 3.1 summarizes the permutations in the protrusion configurations investigated and introduces a shorthand notation for referring to the geometric models. It should be noted that the protrusion width reported in Table 3.1 represents the protrusion width within a cross-section extracted from an intersection of the helical strut pattern. The wire widths of the stented design AR2 and AR3 are 0.084mm and 0.053mm, respectively. The circumferential protrusion pattern is constructed by defining the desired protrusion pattern in the *yz* plane located at the start of the stent, as shown in the inset of Figure 3.2, located distal to the expansion region at 5.78*D* from the pipe entrance. Initially, the centerline of a single rectangular protrusion is defined at $\varphi$ = 0 and replicated circumferentially with an equal spacing of $\Delta\varphi = \frac{2\pi}{m}$ within the plane. The protrusion pattern in the axial direction is defined by sweeping the planar protrusion pattern axially along left and right helical paths, which initiate in the *yz* plane and terminate at the end of the stented region. The helical pattern is defined by $x = c\varphi$ where $c$ = 0.929*D* is the helical pitch. The helical pitch is selected in order to create the same number of strut intersection axially as the number of circumferential struts at the stent entrance. The helical protrusions intersect to form diamond shaped stent cells, as shown in Figure 3.1, that mimic stent designs on the market, such as the Medtronic Driver Stent (Medtronic)[90]. Note that the stent begins and ends at intersection nodes,

indicated by the square regions at the corners of the stent cell diamond in Figure 3.3, and thus has no "bare wires" at either extremity. Furthermore, in this study the stent nodes are always symmetric about the plane of the bend.

**Table 3.1 Geometries investigated and shorthand notation.**

| $m$ | $\xi$ | $\varepsilon$ | Aspect Ratio ($AR = \xi/\varepsilon$) | Abbreviation |
|---|---|---|---|---|
| 8 | 0.14 | 0.07 | 2.05 | N8_AR2 |
| 4 | 0.14 | 0.07 | 2.05 | N4_AR2 |
| 4 | 0.24 | 0.07 | 3.43 | N4_AR3 |
| 4 | 0.24 | 0.04 | 5.87 | N4_AR6 |

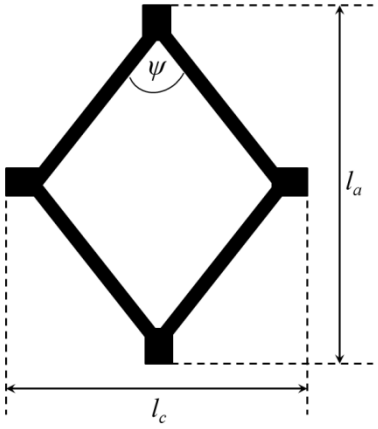


**Figure 3.3 Sketch of a representative stent cell, indicating cell axial length, $l_a$, and circumferential distance between struts, $l_c$, primary flow intrastrut angle, $\psi$.**

The stented region consists of four or eight axial and circumferential repeating diamond stent cells for prescribed values of $m = 4$ and $m = 8$, respectively. Stent cell patterns vary between manufacturers; however, the diamond cell configuration is characteristic of many designs on the market, which often have diverging and converging stent strut configurations[86,90]. The dimensions of the stent cells included in the model geometries are presented in Table 3.2. The stent cell axial

length ($l_a$) and the circumferential distance between adjacent struts ($l_c$) are non-dimensionalized by the native vessel diameter 2*a*. The intra-strut angle with respect to the primary direction of flow, $\psi$, differs slightly based on the prescribed protrusion frequency and dimensions. This minor variation in $\psi$ is not expected to contribution in an appreciable manner to differences in flow behavior within each stent design. The intra-strut area, an important geometric parameter for the WSS distribution, is listed for the various stent cell geometries in Table 3.2. The area is normalized by the total surface area of the stented region, which spans from the inception of the expansion region to the terminus of the taper region of the vessel investigated. The stent cells of commercially available designs have an intrastrut area of 1– 3mm$^2$ and no optimal area has been determined[90]. Note that the intrastrut area for the 4-strut stent geometries is nearly 5 times greater than the 8-strut model. This design feature will greatly impact the reattachment zones surrounding stent struts.

**Table 3.2 Geometric characteristics of modeled geometries.**

| | Geometries | | | | | | | |
|---|---|---|---|---|---|---|---|---|
| | N8_AR2 | | N4_AR2 | | N4_AR3 | | N4_AR6 | |
| | Outer | Inner | Outer | Inner | Outer | Inner | Outer | Inner |
| $l_c$ | 0.36 | 0.36 | 0.79 | 0.79 | 0.74 | 0.74 | 0.74 | 0.74 |
| $l_a$ | 0.63 | 0.59 | 1.38 | 1.30 | 1.29 | 1.22 | 1.29 | 1.22 |
| $\Psi$[°] | 60.39 | 62.59 | 59.90 | 62.58 | 59.90 | 62.59 | 60.29 | 62.59 |
| Intra-strut Area [$10^{-3}$] | 4.03 | 3.82 | 19.49 | 18.53 | 17.19 | 16.33 | 17.19 | 16.33 |

For each geometry, the Dean number is varied to determine its impact on the flow physics. The form of the Dean number used in the present study is

$$K = \frac{Ga^3}{\mu\nu}\left(\frac{2a}{R}\right)^{1/2} \qquad \textbf{Equation 3.1}$$

where *G* is the axial pressure gradient, $\mu$ is the dynamic viscosity, and $\nu$ is the kinematic viscosity. The Dean numbers investigated in this study are $K$ = 70, 450, and 1450, which are all in the laminar flow regime. The range of Dean numbers encompass the change in geometry and the

change in flow rate in the RCA during the cardiac cycle[107]. We note that the prescribed Dean number is based upon the nominal pipe radius and does not account for the increase in the cross-sectional area in the stented region or reduction in the cross-sectional area due to the inclusion of the wall protrusions. The combined changes in wall shape and vessel radius in the stented region results in an increase in the cross-sectional area of approximately 15% compared to the native vessel cross-section and subsequent marginal increase of approximately 4% in the effective Dean number. Overall, the prescribed Dean numbers and protrusion dimensions are chosen to compare the numerical simulation results for the curved pipe geometry to published results for a straight stented vessel.

## 3.2 Numerical model

Ansys CFX Version 14.0 is used to solve the unsteady three-dimensional Navier-Stokes equations in the fixed *XYZ* Cartesian coordinate frame[103]. Ansys CFX employs a finite volume solution method for solving a discretized control volume formulation of the Navier-Stokes equations, as discussed in Chapter 2. The advection terms in the discretized conservation equations are solved using a second order accurate scheme. The iterative algorithm terminates and the solution is considered converged when the root mean square (RMS) normalized values of the discrete flow equation residuals are below $10^{-5}$. The stipulated boundary conditions are no slip and no penetration along the tube wall and a fully developed velocity profile, discussed in more detail in Section 3.2.1, is prescribed at the pipe inlet. A constant average static pressure of 0 Pa is set at the pipe outlet, allowing spatial pressure variations within the control surface. As previously discussed, the straight section of the exit vessel (Figure 3.1(E)) is included in the model to mitigate any effects this boundary condition may have on the flow physics in the regions of interest.

To determine the influence of blood rheology on the behavior of blood flow in vessels such as the RCA, both Newtonian and non-Newtonian working fluids are used in the present numerical simulations to identify regions and flow conditions in the stented vessel where non-Newtonian effects are important. The working Newtonian fluid has a density of 1060 kg/m$^3$ and a dynamic viscosity of $3.7 \times 10^{-3}$ Pa·s, parameters that are commonly used in Newtonian blood models[86,96]. The working non-Newtonian fluid viscosity is based on the Carreau-Yasuda model, which captures the non-Newtonian behavior of blood at shear rates less than 100s$^{-1}$ and tends toward Newtonian behavior at shear rates above this threshold[99]. The shear rate is defined as

$$\dot{\gamma} = \left\{ 2\left[ \left(\frac{\partial u}{\partial x}\right)^2 + \left(\frac{\partial v}{\partial y}\right)^2 + \left(\frac{\partial w}{\partial z}\right)^2 \right] + \left(\frac{\partial u}{\partial y} + \frac{\partial v}{\partial x}\right)^2 + \left(\frac{\partial u}{\partial z} + \frac{\partial w}{\partial x}\right)^2 + \left(\frac{\partial v}{\partial z} + \frac{\partial w}{\partial y}\right)^2 \right\}^{\frac{1}{2}} \quad \textbf{Equation 3.2}$$

where *u*, *v*, and *w* are the velocity components in the *x*, *y*, and *z* directions, respectively.

The apparent viscosity dictated by this model is given as

$$\mu = \mu_\infty + \frac{(\mu_0 - \mu_\infty)}{(1 + (\lambda\dot{\gamma})^j)^i} \quad \textbf{Equation 3.3}$$

where the input parameters are the low shear viscosity $\mu_0 = 1.6 \times 10^{-1}$ Pa·s, the infinite shear viscosity $\mu_\infty = 3.5 \times 10^{-3}$ Pa·s, the time constant $\lambda = 8.2$ s, the power law index $i = 1.23$, and the Yasuda exponent $j = 0.64$ [21,108,109]. The model is empirically derived from experimental data on blood viscosity measured at particular shear rates, $\dot{\gamma}$. Figure 3.4 shows a plot of the apparent blood viscosity as a function of the shear rate for the Newtonian and non-Newtonian models considered. In Figure 3.4, the apparent viscosity for the Carreau-Yasuda model tends to the constant Newtonian value at high shear values above approximately $100s^{-1}$. There is a gradual increase in the apparent viscosity predicted by the Carreau-Yasuda model for shear rates below approximately $100s^{-1}$, thus capturing the thixotropic behavior of blood.

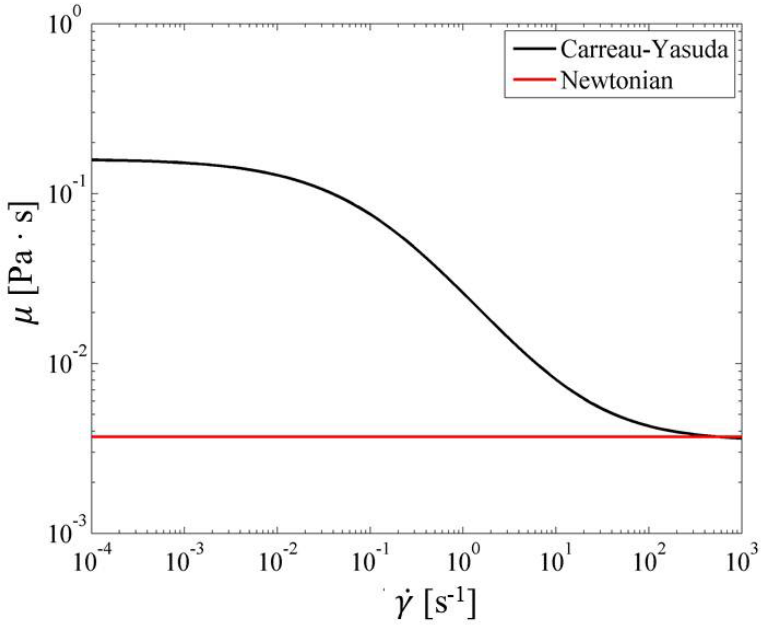


**Figure 3.4 Apparent viscosity as a function of the shear rate for the Newtonian and non-Newtonian fluid models considered.**

The primary process that initiates ISR is excessive NIH development, which subsequently leads to total stent occlusion by uncontrolled tissue growth. As discussed in Chapter 1, this growth is triggered by chemical stimuli as a consequence of endothelial cell denuding, platelet adhesion, and SMC signaling. Stent-induced abnormal hemodynamics can promote excessive NIH development by altering WSS distributions and encouraging the advection of NIH stimuli to the vessel wall. Several hemodynamic variables are widely used to identify sites within the stented region where NIH development is more likely due to variable values above or below critical physiological thresholds. The mathematical descriptions of important hemodynamic variables are provided below.

Ansys CFX uses second order accurate approximations to determine parameters in the solution domain. Hence, the calculation of the velocity gradient used to determine the WSS and additional dependent variables are assumed to be second order accurate. The WSS magnitude (WSSM) distribution within the stented region is the main focus of many studies seeking to characterize the stent induced flow disturbance. The WSSM is defined as

$$|\tau| = \sqrt{{\tau_x}^2 + {\tau_y}^2 + {\tau_z}^2} \qquad \textbf{Equation 3.4}$$

where $\tau_x$, $\tau_y$, and $\tau_z$ are the WSS components based on the global coordinate system presented in Figure 3.2. Regions of the vessel wall subjected to low WSSM (< 0.5 N/m$^2$) tend to exhibit endothelial cell dysfunction, increased permeability, and uptake of NIH stimuli. Higher WSSM values, within a physiological range in the arterial system between 1 and 7 N/m$^2$, have been reported to decrease endothelial cell proliferation and reduce the likelihood of NIH development[110]. On the other hand, elevated WSSM values above 7 N/m$^2$ can have detrimental effects on the vascular environment, causing endothelial injury and denudation when levels reach approximately 40 N/m$^2$.

The WSS gradient magnitude (WSSG), which captures the nonuniform distribution of WSS, has also been linked to higher endothelial cell permeability and affects the process of endothelization post implantation[110]. The WSSG is calculated as,

$$|\nabla\tau| = \sqrt{\left(\frac{\partial\tau_x}{\partial x}\right)^2 + \left(\frac{\partial\tau_y}{\partial y}\right)^2 + \left(\frac{\partial\tau_z}{\partial z}\right)^2} \qquad \textbf{Equation 3.5}$$

Regions that are susceptible to NIH have been correlated with regions where the vessel wall is exposed to WSSG greater than 200N/m$^3$ [86]. The WSSG and the WSSM parameters are used to explore how differences in the stent design might lead to WSS distributions that promote NIH development.

### 3.2.1 *Mesh and Flow Development*

The spatial domain of the modeled stented vessel geometry is discretized using hexahedral elements. Figure 3.5 shows the grid arrangement at the cross-sections of the unstented (Figure 3.5(A)) portion of the vessel and an example cross-section for the stented region of the geometry N8_AR2. The mesh configuration for the remaining stented geometries are comparable with minor modifications to accommodate for the different protrusion frequencies and aspect ratios. A common feature within each cross-section is the “butterfly” structured mesh in the core region of the vessel. The near wall region is characterized by a boundary layer region inflated with structured elements of high aspect ratios to resolve the steep velocity gradients near the wall. The first inflation layer thickness is 0.004*a* and each successive layer from the wall is 1.2 times thicker than the preceding layer with a maximum of 11 layers. In the unstented region, a structured mesh

is employed throughout the cross-section of the vessel. In contrast, an unstructured mesh is implemented in the near strut region between the butterfly mesh and inflation layer of the stented section of the vessel in order to allow the mesh to conform to the complex strut configuration. The geometry is divided into approximately 300 axial units, equivalent to a distance of 0.06*D* between nodes in the stream-wise direction. Figure 3.5(C) shows a slice through the mesh in the plane of the bend in the stented region.

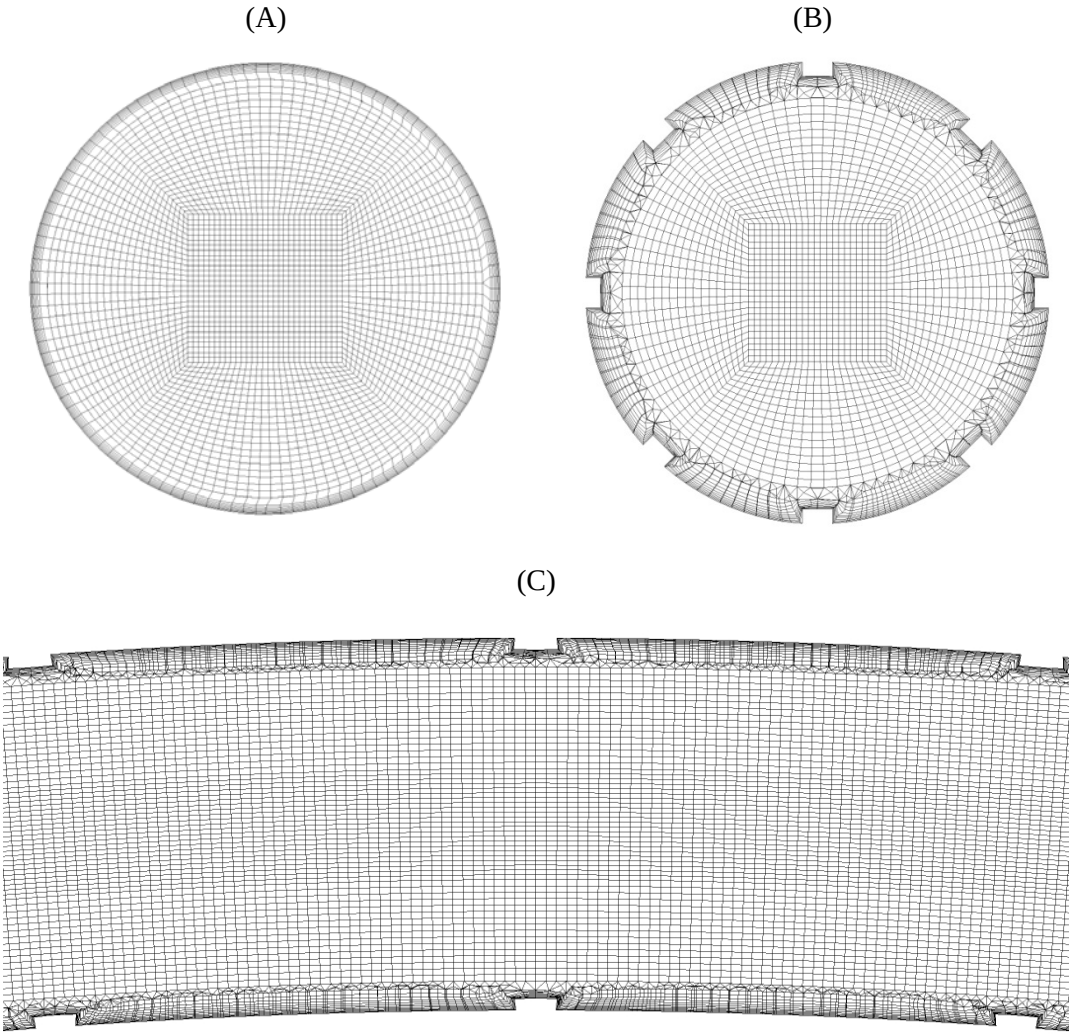


**Figure 3.5 Hexahedral mesh in the pipe cross-section in the (A) unstented region, (B) stented region of the vessel model, and (C) axial slice at the *z* = 0 plane.**

To obtain a fully-developed inlet profile for the stented vessel, a numerical solution was generated using an unstented vessel approximately 60*D* in length. A uniform inlet velocity, in

accordance with the desired Dean number *K*, is imposed at the pipe entrance. The fully developed velocity profile from the converged solution is extracted at a location 50*D* from the entrance of the pipe. A coordinate transformation is subsequently performed and the resultant velocity profile is used as the inlet velocity data for the stented vessel. We acknowledge that the fully developed flow condition used in the presented numerical simulations in this body of work is not a realistic representation of *in vivo* flow conditions. The main focus of this work is to examine the impact of geometric variation on stent design and a consistent inlet flow condition was needed to isolate geometrically induced flow disturbance. Hence, the creation of a biomimetic model of arterial blood flow was not deemed necessary for the evaluation of stent induced flow disturbance.

The simplifying assumptions made in Study B are as follows:

- Fully developed flow into the stented region
- Rigid wall pipe
- Circular cross-section throughout the stented region
- Fixed vessel curvature with no torsion
- Steady and incompressible flow

### 3.2.2 *Grid Independence*

For the stented vessel, a grid independence study is conducted at the upper limit of the Dean numbers, $K = 1450$, which induces the steepest near wall velocity gradients of all cases considered. All of the stent design variations are used to demonstrate grid independence given the possible impact of strut design on near wall flow behavior and the need to determine the impact of grid design in this region. Several grids are tested with increasing numbers of elements to determine the optimal grid size for the CFD study. Four grids are used in the grid independence study and the dimensions of the grid elements are decreased by 25% between each successive grid. The number of inflation layers range from 8 to 13 while the total thickness of the inflation region remains constant. Table 3.3 summarizes the number of nodes corresponding to each mesh.

**Table 3.3 Number of nodes for the mesh geometries used in the grid independence study.**

| | N8_AR2 | N4_AR2 | N4_AR3 | N4_AR6 |
|---|---|---|---|---|
| Grid 1 | 300,377 | 289,713 | 293,454 | 298,973 |
| Grid 2 | 617,012 | 606,311 | 601,843 | 609,909 |
| Grid 3 | 1,135,401 | 1,124,658 | 1,122,749 | 1,131,219 |
| Grid 4 | 2,326,538 | 2,265,310 | 2,211,481 | 2,183,895 |

The final grid is chosen based upon solution independence of the WSSM averaged over the vessel walls and the ratio of the total pressure averaged over the cross-section at the inlet to that at the outlet of the stented region, $\overline{P_I}/\overline{P_O}$. In addition, the size of the stented region exposed to a WSSG above the critical threshold of 200 N/m$^3$ is compared for the mesh configurations in the grid independence study. Table 3.4, Table 3.5, and Table 3.6 summarize the values of WSSM, $\overline{P_I}/\overline{P_O}$ , and WSSG, respectively, obtained for each grid for all of the geometries. The percent difference between the parameters for successive grids is calculated as (Grid[N] – Grid[N-1])/Grid[N] × 100, where *N* represents the grid number and is included in the tables. The WSSM and pressure ratio are used to evaluate global grid independence given the difficulty of determining local grid independence due to spatial changes in the domain. Table 4.4 and Table 4.5 present the change in the spatially averaged WSSM and total pressure ratio for each grid and stent design. The area of the region exposed to high WSSG is used to evaluate the grid independence based on a spatially changing parameter. The geometry N8_AR2 is utilized to determine the solution independent grid based on the WSSG parameter since it is expected to induce the largest gradients given the maximum protrusion height and frequency. The solution is deemed independent when the percent difference for the grid independence parameters are less than 1% for successive grids. The final grid used for all subsequent evaluations of flow behavior is Grid 3 for all geometric cases. The computational time required to run the simulations was approximately 30 minutes using 4 cores with Intel i7 processors at 3.07Ghz.

**Table 3.4 Spatially averaged WSSM along the vessel wall for various grids.**

| | N8_AR2 | | N4_AR2 | | N4_AR3 | | N4_AR6 | |
|---|---|---|---|---|---|---|---|---|
| | $\|\tau\|$ [Pa] | Percent Difference [%] | $\|\tau\|$ [Pa] | Percent Difference [%] | $\|\tau\|$ [Pa] | Percent Difference [%] | $\|\tau\|$ [Pa] | Percent Difference [%] |
| Grid 1 | 16.54 | | 17.43 | | 17.88 | | 18.38 | |
| Grid 2 | 16.61 | 0.39 | 17.54 | 0.58 | 17.89 | 0.08 | 18.36 | -0.15 |
| Grid 3 | 16.65 | 0.30 | 17.58 | 0.27 | 17.92 | 0.17 | 18.41 | 0.28 |
| Grid 4 | 16.67 | 0.09 | 17.57 | -0.07 | 17.91 | -0.09 | 18.37 | -0.21 |

**Table 3.5 Total pressure ratio at the stent inlet to the stent outlet for various grids.**

| | N8_AR2 | | N4_AR2 | | N4_AR3 | | N4_AR6 | |
|---|---|---|---|---|---|---|---|---|
| | $\overline{P_I}/\overline{P_O}$ | Percent Difference [%] | $\overline{P_I}/\overline{P_O}$ | Percent Difference [%] | $\overline{P_I}/\overline{P_O}$ | Percent Difference [%] | $\overline{P_I}/\overline{P_O}$ | Percent Difference [%] |
| Grid 1 | 1.27 | | 1.25 | | 1.25 | | 1.21 | |
| Grid 2 | 1.25 | -2.12 | 1.21 | -3.47 | 1.22 | -2.55 | 1.18 | -2.65 |
| Grid 3 | 1.25 | -0.20 | 1.21 | -0.12 | 1.21 | -0.71 | 1.17 | -0.63 |
| Grid 4 | 1.23 | -1.39 | 1.19 | -1.44 | 1.20 | -0.57 | 1.17 | -0.64 |

**Table 3.6 Area of Region exposed to high WSSG ( >200 N/m$^3$) for N8_AR2 for $K$ = 1450.**

| | Area [m$^2$] ($10^{-4}$) | Percent Difference [%] |
|---|---|---|
| Grid 1 | 2.00 | |
| Grid 2 | 2.01 | 0.49 |
| Grid 3 | 2.02 | 0.40 |
| Grid 4 | 2.04 | 1.08 |

## 3.3 Numerical Results and Discussion

In this section, we discuss the general flow patterns induced by the placement of a realistic stent model in a curved vessel and comment on the subsequent influence of regional flow patterns on the potential development of NIH in the coronary artery. The CFD results provide insight into how the stent design affects the flow proximal and distal to, as well as within, the stented region. Furthermore, we highlight the influence of the Dean number, number of protrusions, and the protrusion aspect ratio on the fluid dynamics in the vicinity of the stent model. The evaluation of the numerical results focuses on the impact of the stent design on bulk velocity behavior as well as localized flow parameters such as WSSM and WSSG. Given its importance in the development of NIH, the spatial variation of the WSSM distribution in a particular stent model, as well as a comparison between the four different stent models, is discussed. Localized flow parameters are also important for quantitative comparisons of flow behavior between Newtonian and non-Newtonian blood viscosity models. The WSS distribution is used to ascertain whether the use of the Newtonian blood model is appropriate over a wide range of shear rates present in the stented region and how this model affects the prediction of NIH development. These data are used to quantify the regions where non-Newtonian constitutive behavior is significant and potentially important. Lastly, the numerical results are compared to straight pipe protrusion studies of LaDisa *et al*., as well as smooth walled curved pipe geometries, to highlight the effect of vessel curvature and comment on pre/post stent implantation flow behavior.

### 3.3.1 *Overview of Flow Behavior in a Curved Pipe with a Realistic Stent Model*

An overview of the flow development induced by the presence of the realistic stent model in a curved vessel is presented for all Dean numbers, *K*, protrusion aspect ratios, AR, and fluid viscosity models investigated in this study. In this section, the numerical results generated using the Newtonian model will be used to demonstrate the general characteristics of flow behavior in the stented vessel model that pertain to virtually all studied cases. The WSSM distribution induced by the presence of stent struts will be discussed in reference to the critical threshold values of WSS (less than 0.5 $N/m^2$), and WSSG (greater than 200 $N/m^3$), that is shown to lead to ISR development. Since these threshold values are based upon cellular response, they do not scale in any obvious way with the vessel geometry. As such, the values of WSS will be reported in dimensional form to allow for direct comparison to published physiological data on vessel response to hemodynamic conditions.

The discussion of primary and secondary flow characteristics will focus on behavior at selected planes within the fluid domain. In particular, selected planes that exemplify the strut orientations that are repeated axially will be used to foster discussion of flow behavior in the stented region. These selected planes are shown in Figure 3.6 with the labels used to refer to their strut configuration in this document. The intersection planes are distinguished by the position of the strut in the first quadrant, defined as $0 \leq \varphi < \frac{\pi}{2}$. For the plane classified as "Intersection 1" (Figure 3.6(A)), the first strut is centered at $\varphi = \pi/m$ and the remaining circumferential struts in the plane are spaced at intervals of $\varphi = 2\pi/m$ around the circumference. For the planes classified as "Intersection 2" (Figure 3.6(C)), the first strut is located at $\varphi = 0$ and the remaining circumferential struts in the plane are located at intervals of $\varphi = 2\pi/m$ around the circumference. For the plane classified as "Angled Strut" (Figure 3.6(B) and (D)), the plane is extracted from the midpoint between the strut intersections, where the struts axially converge or diverge. The regions between the struts are labeled as "*c*" for an orientation in which the struts are converging in the axial direction and labeled as "*d*" for an orientation in which the struts are diverging in the axial direction. The number of protrusions in the cross-section for the "Angled Strut 1" and "Angled Strut 2" are the same; however the locations of the converging and diverging regions are opposite between these two cross-sections.

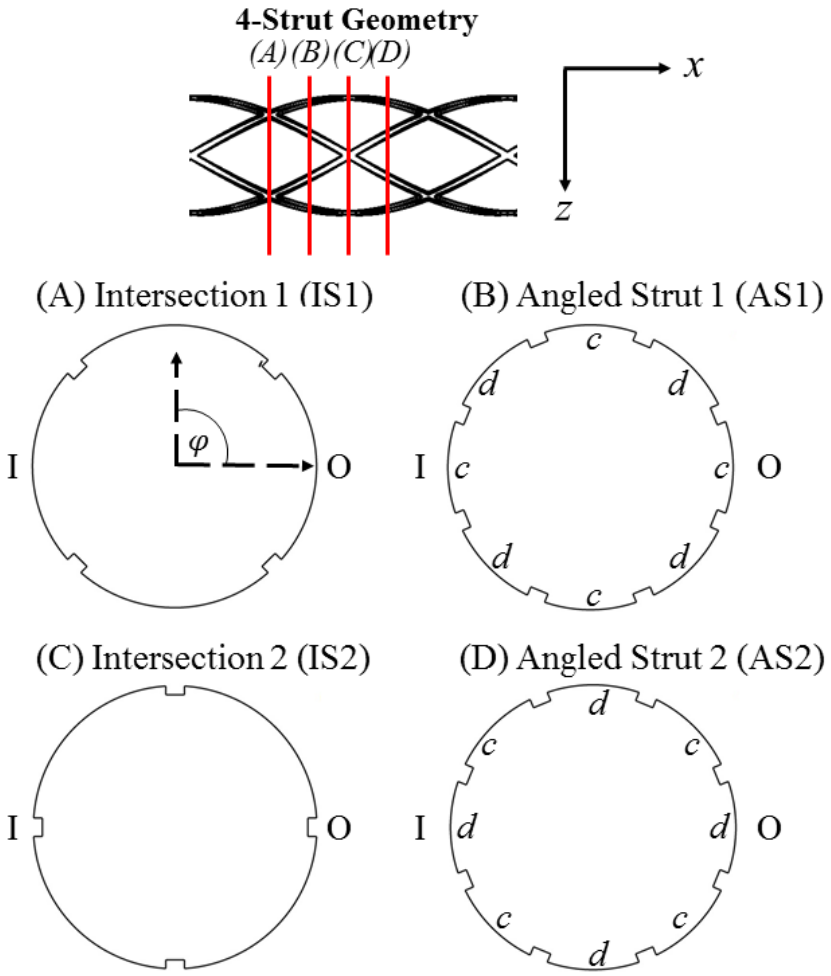


**Figure 3.6 Configuration and naming convention of struts at selected planes in the stented region. I and O indicate the inner and outer wall, respectively.**

An important feature of the flow behavior in a smooth walled curved pipe is the secondary hemodynamics consisting of the Dean vortex structures in the cross-section of the vessel, as described in Chapter 3. The presence of the struts in the curved vessel generates complex vortex interactions in the vicinity of the strut protrusions. Vortex identification techniques such as *Q*-criterion, $\lambda_2$-criterion, and total vorticity data can be used to elucidate the impact of strut protrusions on vortex formation[111,112]. In this study, numerical flow visualization of vortex behavior in the vicinity of the stent is achieved by utilizing isosurfaces of the *Q*-criterion. The *Q*-criterion defines a vortex as a spatial region with a positive second invariant of the velocity

gradient tensor, $\nabla\vec{V}$[111,112]. The second invariant, $Q$, for an incompressible fluid is defined as $Q = \frac{1}{2}[|\Omega|^2 - |\Upsilon|^2] > 0$ , where $\Omega$ is the vorticity tensor and $\Upsilon$ is the rate of strain tensor. Thus, the $Q$-criterion is positive when the vorticity magnitude is greater than the strain rate magnitude.

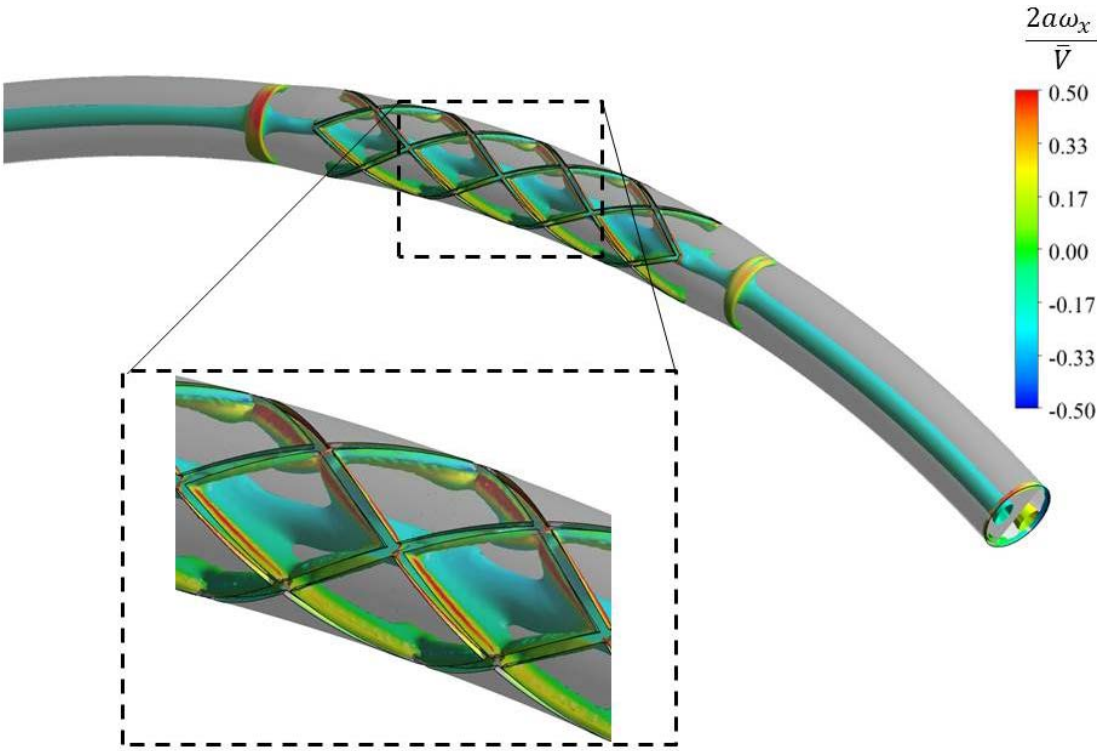


**Figure 3.7 Isosurface of $Q$ = 6500 for NS4_AR2 for $K$ = 450, colored by the non-dimensional axial vorticity. Flow is from right to left, with the pipe entrance visible on the right-hand side.**

The vortex topology in the stented vessel is visualized in Figure 3.7 for the NS4_AR2 case at $K$ = 450 using an isosurface of $Q$ = 6500. The isosurface is colored by the normalized axial component of vorticity, $2a\omega_x/\bar{V}$ ,where $\omega_x$ is the axial component of the vorticity and $\bar{V}$ is the average axial velocity. Note that an opaque plane at $z$ = 0 has been inserted to improve the visualization in the stented region; thus, except at the pipe entrance on the right side of the figure, only one half of the tube is visualized in this figure. The most persistent features in Figure 3.7 are the two vortex tubes corresponding to the Dean vortices, which extend from the inlet to the outlet of the vessel. These coherent tube structures illustrate the Dean vortex presence in the smooth walled entrance of the vessel. Though mostly obscured by the opaque plane at $z$ = 0, the sign of the axial vorticity is opposite in the obscured half of the tube to that in the visible half. This can be

observed at the very entrance to the vessel, where both Dean vortices are seen and have opposite signs of axial vorticity, and thus opposite senses of rotation, as discussed in Chapter 3.

A magnified view of the vortex topology in the expansion and taper region is shown in Figure 3.8. The vortex tubes shift away from the “top” and “bottom” walls of the vessel and toward the center region of the vessel as the fluid travels through the expansion region (Figure 3.8 (A)). Within the taper region the opposite behavior is observed, the vortex tubes shift away from the center region of the vessel and toward the “top” and “bottom” walls of the vessel (Figure 3.8 (B)). The shift in the position of the vortex tube indicates a change in the position of the Dean vortices in the cross-section of the vessel. The change in position of the Dean vortices is likely due to the change in local pressure distribution due to changes in the vessel curvature near the walls of the expansion and taper region. More specifically, in the expansion region, for example, the radius of curvature of the outer wall is reduced by the area change, while the radius of curvature is increased at the inner wall. The axial streamline curvature increases at the inner wall and decreases near the outer wall; this leads to a localized reduction in the radial pressure gradient in the plane of the bend near the outer wall and an increase near the inner wall. The geometrically-induced alteration in the pressure gradient distribution results in a migration of the Dean vortices towards the “top” and “bottom” wall and closer to the inner wall (see Figure 3.8 (A)). A similar argument can be made at the contraction section, wherein the changes of the radii of curvature are the opposite, and thus the vortex migrates away from the “top” and “bottom” wall and closer to the outer wall (see Figure 3.8 (B)).

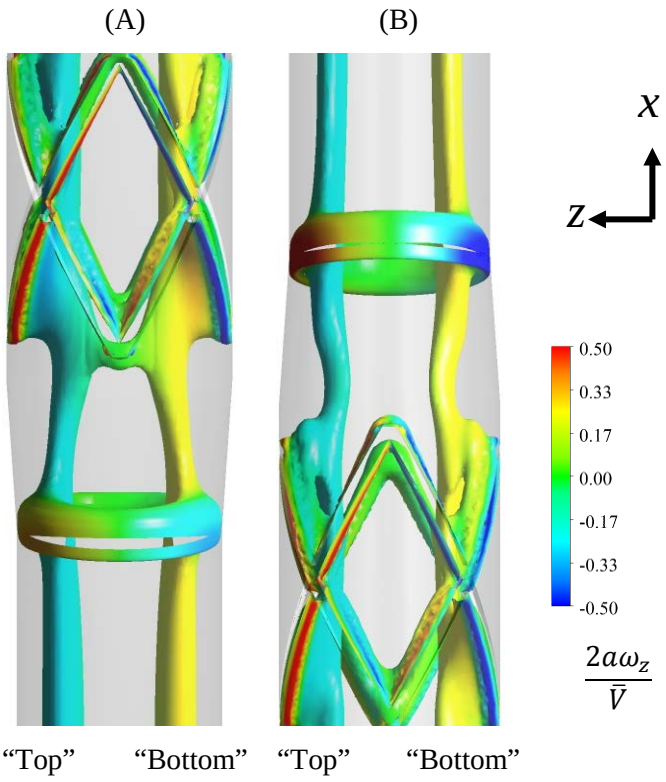


**Figure 3.8 Vortex topology in the expansion (A) and taper region visualized using an isosurface of *Q* = 6500 for NS4_AR2 for *K* = 450, colored by the non-dimensional axial vorticity. The flow moves from bottom to top in each subfigure.**

The formation of a coherent ring structure is observed at the entrance of the expansion region and exit of the taper region in Figure 3.7 and Figure 3.8. The ring structure exists only locally in the stated regions and does not appear to persist once the fluid has traveled distal to these regions. The expansion region geometry is effectively a diverging nozzle in which the rate of area expansion is gradual enough that the flow does not separate and vortex rings are not formed and shed (it is evident from the vector fields that a vortex ring does not roll up, despite the vorticity created at the expansion). In addition, the taper region acts as a converging nozzle, which accelerates the mean flow influencing the boundary layer thickness and the navigation of the fluid at the exit of the taper region. The coherent ring structure identifies rotation induced by the navigation of the fluid near the walls of the entrance of the expansion region and the exit of the taper region. It is noted that to some degree this is an artifact of the particular geometry used in

this study, which has a sharp transition from a constant radius vessel to the expansion/contraction regions. Some degree of filleting would likely reduce the severity of the vorticity formation, while a more or less severe taper would also have an impact.

Within the stented region, the vortex tubes distort due to the stent protrusions as the flow navigates the complex geometry, see the inset in Figure 3.7. Coherent flow structures are observed to surround the strut protrusions, with higher axial vorticity in the regions adjacent to the stent struts due to flow separation and consequent reversed flow around the struts. The isocontour of the Dean vortices in the stented region appear to oscillate in shape and diameter, implying not only is the Dean vortex shape impacted by the stent struts, but so too potentially is the circulation strength of the vortices as they stretch and relax. Distal to the stented region the Dean vortex tube structures stabilize and move in opposite directions away from the center of the tube as the flow proceeds through the taper region of the vessel, similar to the behavior in the expansion region. An additional ring structure is visible at the distal end of the taper region where the native vessel diameter resumes and the Dean vortex tubes become distorted in a similar fashion as observed at the region of the initial expansion of the pipe. Beyond the taper region, the traditional Dean structure reestablishes and sustains through to the outlet of the pipe.

To further elucidate the flow physics, the axial and secondary flow behavior at nine planes in the vessel are presented in Figure 3.9 for the N4_AR2 geometry at $K = 450$. This figure shows slices through the geometry at various locations in the inlet, stented, and exit zones of the stented region. Figure 3.9 (A) presents a plane located 3*D* from the pipe entrance in the fully developed region of the entrance vessel. A plane extracted from the middle of the expansion and taper region is shown in Figure 3.9 (B) and Figure 3.9 (H), respectively. Planes in the middle of the stented region are presented in Figure 3.9 (C) – (G). Lastly, Figure 3.9 (I) presents a plane extracted from the exit vessel and located 3*D* from the terminus of the taper region. Each subfigure shows a flood contour of the axial velocity normalized by the average pipe velocity with overlaid streamlines depicting the secondary flow behavior in the pipe cross-section. The flow behavior in the selected planes in the stented region is representative of other locations in the stented region with the same strut configurations. As well, the general flow characteristics discussed for the N4_AR2 geometry is similar to that of the other geometric configurations investigated in this study, and is thus again selected as a representative case.

As expected, there exist some primary and secondary flow features in the current stented vessel that are well known from smooth walled curved vessel literature. Specifically, the flow is symmetric about the plane of the bend, which is reported for smooth walled and wavy wall pipes for which the waves are also symmetric about the plane of the bend. Obviously symmetry would not occur for cases wherein the geometry is asymmetric about this plane. The contour plots for each of the planes in Figure 3.9 highlight the impact of the pipe curvature, which shifts the axial velocity peak toward the outer wall of the pipe. The secondary flow behavior in the fully developed region of the entrance vessel (Figure 3.9 (A)) shows a symmetric Dean vortex structure and axial skewing that is the hallmark of flow in curved tubes. The Dean vortex pattern is distorted, however, by the change in the wall configuration in the expansion and taper regions, as well as in the stented region. The Dean vortex shape is deformed in the vicinity of the strut protrusions, however the general structure is maintained in the central region of the vessel. The change in the Dean vortex shape corroborates the change in the position and shape of the vortex tube structure at the same locations observed in Figure 3.7.

Within the expansion and taper regions, the secondary flow pattern is no longer a closed contour. Instead, the secondary flow has a spiral pattern with the flow spiraling out toward the walls of the vessel due to the area expansion. The movement of the vortex center toward the “top” and “bottom” wall and closer to the inner wall within the expansion region is shown in Figure 3.9 (B). On the contrary, the vortex center is observed to move toward the symmetry plane and closer to the outer wall within the taper region in Figure 3.9 (H). The behavior revealed by the streamlines corroborates the observed behavior of the vortex tubes in Figure 3.8. The streamlines are predominately straight and parallel in regions of increased localized radial pressure gradient at the inner wall of the expansion region and outer wall of the taper region. These localized changes in the radial pressure gradient were previously discussed and attributed to increased vessel curvature as a result of changes in the wall position in the expansion and taper regions.

The primary and secondary flow behavior in the stented region is shown for selected planes in Figure 3.9 (C)–(G). The selected planes are representative examples of the cross-sectional geometric configurations that exist in the stented region and correspond to the geometries and naming convention introduced in Figure 3.6. Obviously the flow is not fully developed within the stented region due to the changing geometry in the axial direction, but it also does not become completely periodic over the short stent length either. That is, the flow behavior

in a given stent diamond is not exactly repeated in subsequent geometrically similar diamonds. The flow physics from one region to the next are sufficiently similar, however, to enable the use of a “characteristic cell” in discussing the in-stent flow dynamics. The streamwise variations will be discussed in more detail in subsequent sections on the near wall physics. The flow development within one stent diamond is observed via the changes in the axial velocity contour plots at the selected planes shown in Figure 3.9 in the stented region.

The flow topology in the cross-sectional planes within the stented region is characterized by deformed Dean vortices and the formation of recirculation regions due to the presence of the strut protrusions. The streamlines in Figure 3.9 (C)–(G) show the deformation of the Dean vortex structure in the near wall region. Recirculation regions are observed to form in the cross-section of the vessel in the proximity of the strut protrusions. The location of these recirculation regions is described based on their location on the windward or leeward side of the protrusions in reference to the direction of the secondary flow. We note that the planar streamlines only show a two-dimensional projection of the three-dimensional separation around the struts. However, the size of the projected recirculation regions is used to highlight changes in secondary flow disturbance based upon the circumferential location of the strut intersections. For the other stent geometries investigated, the impact of the strut protrusions on the Dean vortex shape is comparable to the behavior observed for N4_AR2 in Figure 3.9. As well, the recirculation zones are induced for the other strut configurations, though their size and circumferential location differ within the example planes discussed in Figure 3.9 (C)–(G).

At the strut intersection planes IS1 and IS2 (Figure 3.9 (C), (E), (G)), recirculation regions are observed on the leeward side of the struts as the flow returns along the circumference to the inner wall of the pipe. In the IS1 plane, the leeward side recirculation zones are larger toward the inner wall compared to the outer wall (see Figure 3.9 (C) and Figure 3.9 (G)). This pattern repeats at all strut intersection planes of this type, as demonstrated by comparing the streamline patterns in Figure 3.9 (C) and Figure 3.9 (G). In the IS2 plane, small recirculation zones are located at the leeward side of protrusions centered at $\varphi = \pi/2$ and $3\pi/2$. Large streamwise vortical structures surround the protrusion centered at $\varphi = 0$ and restrict the Dean vortex from extending toward the outer wall. These structures are formed by the merging of two recirculation regions as the struts intersect at the outer wall. Figure 3.10 presents an illustration of the streamwise behavior as the flow traverses in the vicinity of the strut intersection to form the streamwise vortical structures

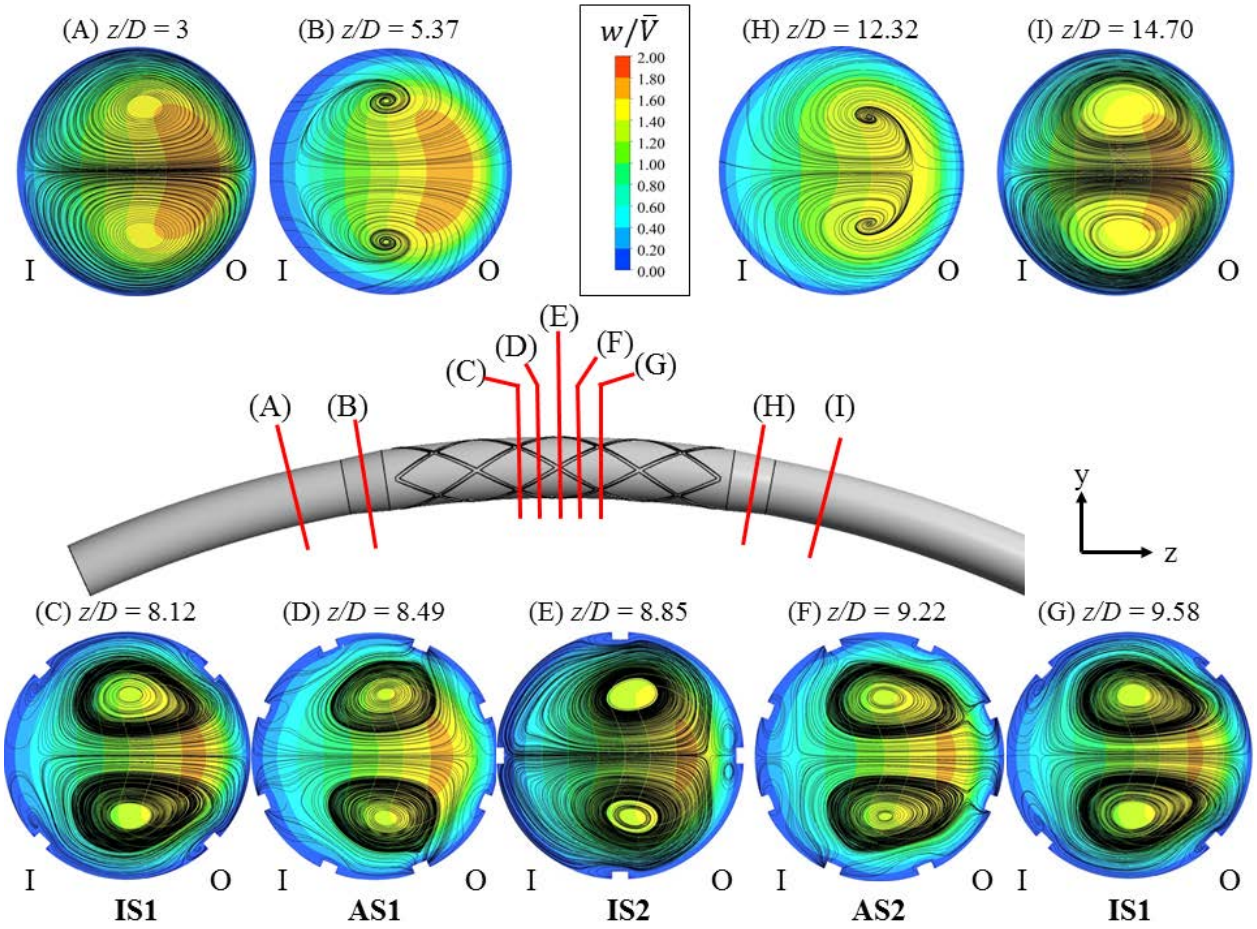


**Figure 3.9 Normalized axial (contour) and secondary flow (streamlines) behavior in the (A) upstream entrance pipe; (B) the inlet taper; (C)-(G) in the middle of the stented region; (H) in the exit taper; and (I) downstream of the stented region. I and O indicate inner and outer wall, respectively.**

(see Figure 3.10(B)). The formation of the streamwise vortical structures is localized around the strut at the outer wall but is not observed at the other circumferential strut intersections in the IS1 and IS2 planes. This suggests that these structures develop as a result of the strut location at the outer wall in the presence of high axial velocity fluid. In addition, no recirculation region is visible in the proximity of the strut centered at $\varphi = \pi$ and the Dean vortex extends to the inner wall.

The secondary flow behavior in the planes with the strut configuration AS1 and AS2 (Figure 3.9 (D) and (F)) are more complex due to the projection of the three-dimensional flow field when the stent struts are angled. The Dean vortices are still present in the central region of the vessel, though the secondary flow seems to be strongly dominated by the axially converging and diverging struts in the near wall region, as suggested by the streamlines that move radially outward around the struts. The secondary flow behavior in the AS1 and AS2 planes is further elucidated by the illustration of the streamwise and secondary flow pattern around the angled struts in Figure 3.10. The red arrows overlaid on the illustration at the top of the figure show the streamwise movement of the flow over the angled struts. The fluid advects from an intrastrut region of converging stent struts to an intrastrut region of diverging stent struts. The AS1 and AS2 planes, Figure 3.10(A) and Figure 3.10(B), respectively, show the secondary flow induced by the described streamwise motion. The figures demonstrate the looping of the secondary flow around the circumferential strut carrying fluid from the converging intrastrut area to the diverging intrastrut area.

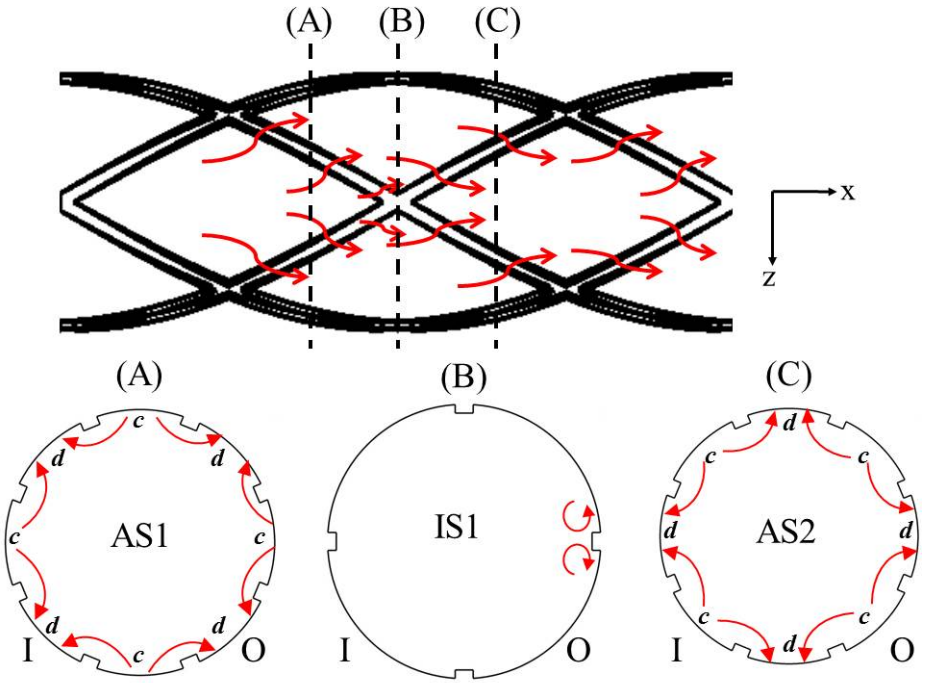


**Figure 3.10 Illustration of streamwise flow over strut protrusions and the influence on secondary flow in the angled strut planes AS1(A), IS1(B), and AS2(C).**

As expected given the skewing of the axial and secondary flow in the curved tube presented in Figure 3.9, particularly in the stented region, a disparity exists between the fluid loading along the outer wall compared to the inner wall. In particular, the shift of the peak axial velocity toward the outer wall results in steeper velocity gradients in this region, and subsequently a higher WSSM, along the outer wall compared to the inner wall. An overview of the WSSM distribution along the inner and outer walls in the stented vessel is displayed in the contour plots in Figure 3.11 for the same case as presented in Figure 3.9 (N4_AR2; $K$ = 450). Note that the WSSM is presented in dimensional form; this is to facilitate discussion of the potential physiological response due to the stent, for which the physical value of the WSSM is critical.

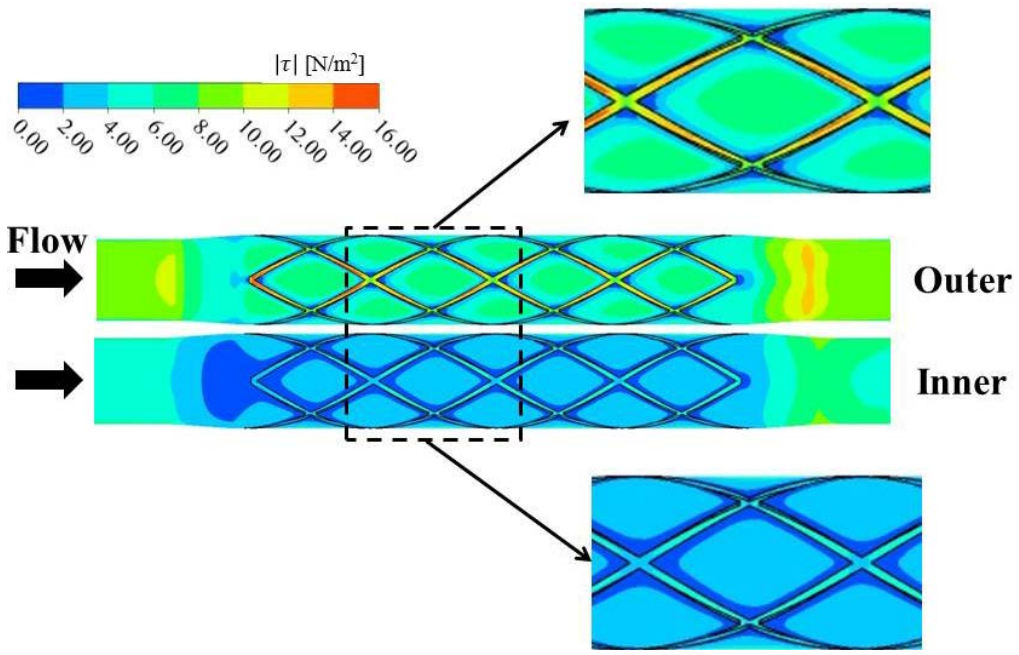


**Figure 3.11 WSSM at the outer and inner walls for N4_AR2 for *K* = 450**

In general, Figure 3.11 shows higher WSSM along the outer wall compared to the inner wall, which makes the inner wall more susceptible to NIH development due to the sensitivity of the endothelium to low WSS. This behavior distinguishes the WSSM distribution for the curved stented vessel from previous studies with straight stented vessels. As flow approaches the expansion region, the WSSM increases at the outer wall; however, the contour plots show no appreciable change in the WSSM proximal to the expansion region at the inner wall. The WSSM in the expansion region is reduced, as the flow diffuses and slows. In the taper region, the accelerated flow leads to an increase in the WSSM at the inner and outer wall. Similarities are observed between the previously reported WSSM distribution in straight stented vessels and the curved stented vessels investigated in this study. Namely, the highest WSSM within the region is located on the surface of the stent struts and at the transition between the exit taper region to exit vessel. In addition, the WSSM on the angled strut segments is higher compared to the WSSM at the strut intersections. In straight stent geometries, "stagnation zones" are reported to surround the stent struts independent of strut aspect ratio or frequency[86,92]. Berry *et al.* describes these stagnation zones for 2*D* flow as a near wall region that contains very slow moving vortices where the maximum velocity is less than 1% of the velocity in the freestream. For the curved pipe geometry, the location of the reported stagnation zones correspond to localized areas of low

WSSM and recirculation regions adjacent to strut protrusions. Herein, the term “recirculation region” will be used in preference over “stagnation zones”, since this more clearly describes the physical mechanism producing the low velocity zone.

The presence of the strut protrusions results in a change in the nominal level of the WSSM within the stented region. The deviation from the nominal WSSM level induces vascular remodeling, such as NIH, in order to restore vascular homeostasis[110]. The disparity between the WSSM in the stented region of the model and the nominal level in the unstented region differs between the inner and outer wall. The imbalance in the WSSM distribution around the strut protrusions at the inner and outer wall is further explored by directly comparing the values in the stented region relative to that in the unstented region. The WSSM at discrete points along the intersection of the $x = 0$ plane with the vessel wall are plotted in Figure 3.12. The black line overlaid in the contour plot in Figure 3.12 indicates the line along which the discrete points displayed in the line plot are extracted. The red lines indicate the location of the leading edge of the strut protrusions for reference. The WSSM values along the line at the inner and outer wall are normalized by the average WSSM in the fully developed unstented region,$|\tau|_{US}$, at the inner and outer wall, respectively. The value of $|\tau|_{US}$ along the outer wall is 9.25 N/m$^2$ and 4.46 N/m$^2$ at the inner wall. Thus, a value of “1” on the plot shown in Figure 3.12 indicates that the WSSM matches the nominal values in the unstented region. It should be noted that the 10% increase in the vessel diameter in the stented region will prevent the WSSM in the region from returning to the nominal unstented WSSM value, regardless of the presence of the strut protrusions. However, the offset caused by the vessel expansion roughly scales with the 10% change in the vessel diameter; hence, a normalized WSSM value near 0.9 would indicate minimal disruption of WSSM distribution by the stent presence.

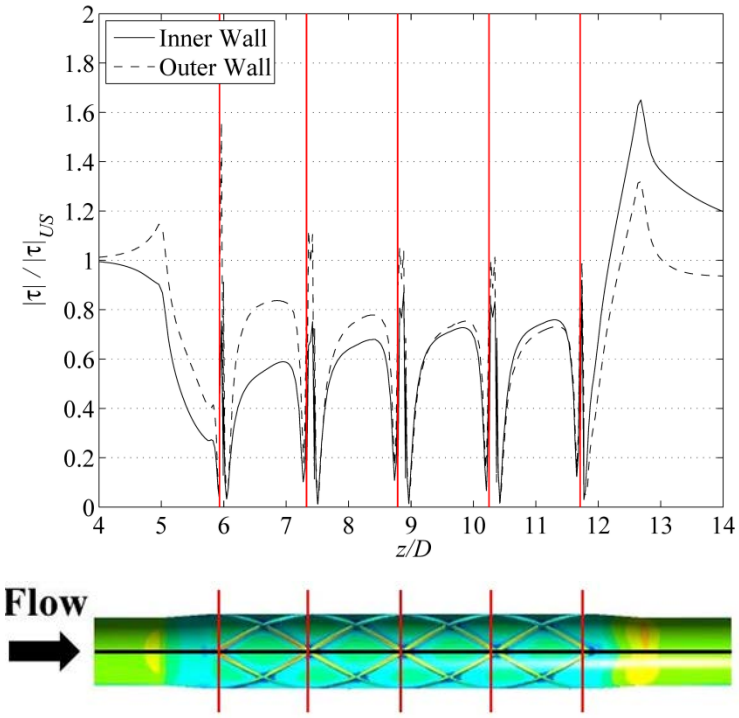


**Figure 3.12 Non-dimensional WSS at discrete points along the inner and outer walls of the vessel normalized by the respective upstream value for N4_AR2 for *K* = 450. The black line overlaid on the contour plot shows the location where the WSS Magnitude was extracted. The red lines indicate the location of the leading edge of the strut protrusions.**

The examination of the WSSM behavior proceeds from the proximal end of the vessel to the distal end. As the flow approaches the expansion region, the WSSM increases at the outer wall and decreases at the inner wall. The value is observed to decrease along both walls as the flow proceeds through the expansion region due to the flow deceleration. Within the stented region, the intrastrut areas are exposed to WSSM at least 20% less than the nominal WSS, $|\tau|_{US}$, along both the outer wall and inner wall. The WSSM is highest within the stented region at the strut intersections regardless of their location at the inner or outer wall, which is similar to the findings in Chapter 3 for the smooth stent struts. At the inner wall, the fluid interaction with the first strut causes the largest deviation in WSSM within the intrastrut region compared to the unstented region. Specifically, the first intrastrut area encountered in the streamwise direction at the inner wall is exposed to WSSM approximately 40% less than the unstented region.

Further, the trend in the WSSM from the proximal to distal end of the stent differs between the inner and outer walls. The intrastrut WSSM along the outer wall is higher in the proximal region compared to the distal region. The opposite behavior is observed along the inner wall with higher WSSM at the distal end compared to the proximal end. This behavior is attributed to a reduction in the axial velocity skew and consequent increase in the axial velocity at the inner wall as the fluid proceeds to the distal end of the stent. Interestingly, the intrastrut WSSM at both walls reaches 80% of the value in the unstented region from approximately 9*D* to 12*D*. The WSSM in the last two stent diamonds are quite similar, suggesting that the flow in a sufficiently long stent in a curved vessel will eventually become periodic. Within the exit taper region, the WSSM increases as the flow accelerates through the nozzle. The WSSM decreases distal to the taper region once the vessel returns to its native diameter and eventually returns to the value in the unstented entrance region of the vessel after approximately 17*D*. Again, the likelihood of an adverse physiological response to flow conditions is greater at the proximal inner wall due to the larger reduction in the WSSM relative to the nominal WSS. In contrast, the WSSM at the strut intersections are observed to be at or above the nominal WSS. The surfaces of the struts exposed to values above the nominal WSSM may exhibit delayed or reduced re-endothelization post stent implantation.

In addition to the disparity in the WSSM at the inner and outer wall as observed in Figure 3.12, a spatial imbalance in the WSSG distribution can determine the localization of maladaptive vascular remodeling in the vicinity of the struts. Throughout the stented region, Figure 3.13 demonstrates the localization of higher WSSG surrounding the stent struts and lower WSSG regions in the intrastrut area. As expected, higher WSSG is observed at the outer wall as demonstrated in the contour plot of the WSSG distribution in Figure 3.13. Elevated WSSG is observed immediately proximal and distal to the strut intersections along each wall. In the expansion and taper region, regions of elevated WSSG coincide with the location of the coherent ring structures revealed by the *Q*-criterion isosurface shown in Figure 3.7.

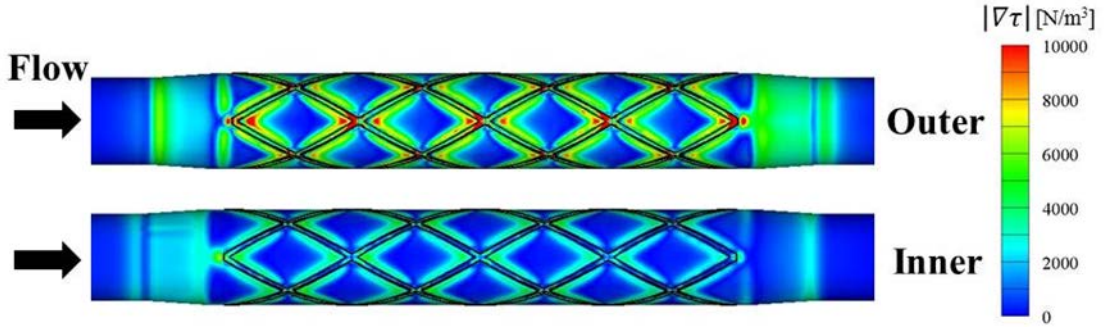


**Figure 3.13 WSSG magnitude at the inner and outer wall for NS4_AR2 for *K* = 450**

The deviation of the WSSG from the nominal values at discrete points at the inner and outer wall is elucidated by the plot in Figure 3.14. The WSSG along the line at the inner and outer wall is normalized by the maximum WSSG at the inner and outer wall in the fully developed unstented region, $\max(|\nabla\tau|_{US})$, respectively. The value of $|\nabla\tau|_{US}$ at the outer wall is 13.44 N/m$^3$ and 5.58 N/m$^3$ at the inner wall. Overall, the presence of the stent struts causes a significant increase from the nominal maximum WSSG value. The WSSG increases sharply at the entrance of the expansion region and decreases gradually as flow travels through the diverging area. Within the stented region, the WSSG is highest at the leading edge of the first and last axially encountered strut at both walls. Local maxima are located immediately proximal to the leading edge of the strut and immediately distal to the trailing edge. Interestingly, the values of the local maxima increase from the proximal to the distal end along the inner wall. Conversely, the opposite trend is observed at the outer wall, with a decrease from the proximal to the distal end. This behavior emulates the trends observed in the WSSM distribution at the inner and outer walls. At the surface of the struts, the WSSG decreases significantly, which is likely the result of flow reattachment on the strut surface distal to the leading edge. In addition, a reduction in the WSSG is observed within the intrastrut area where reattachment occurs distal to the trailing edge of the strut. Lastly, the WSSG decreases gradually through the taper region in a manner similar to the behavior observed in the expansion region.

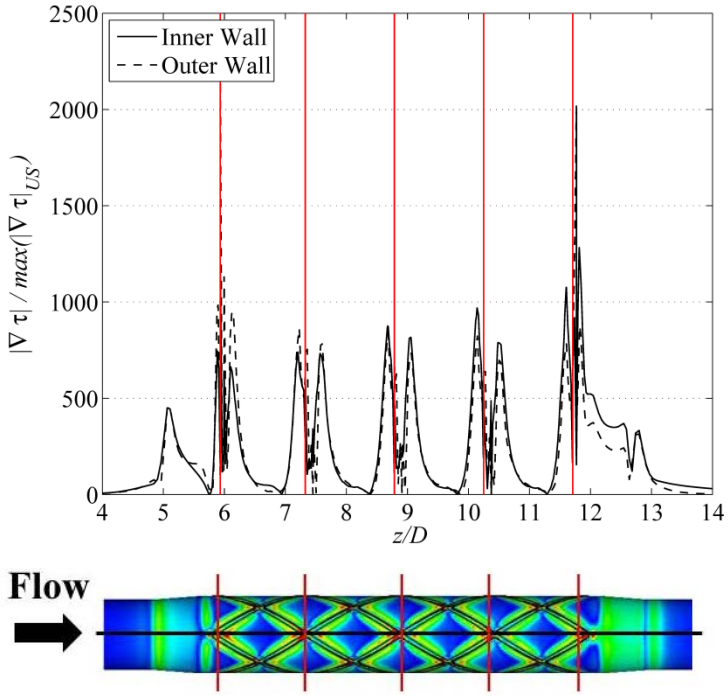


**Figure 3.14 WSSG at the outer and inner wall normalized by the nominal WSSG in the unstented region.**

The variation in the spatial WSSM and WSSG distribution from the proximal to the distal portion of the stented region is quantified in Table 3.7. The table shows the WSSM spatially averaged over the proximal and distal halves of the stent, as well as the percent difference in the value between the regions for $K = 450$. The proximal portion of the stented region is defined from the expansion region entrance to the *yz* plane in the middle of the stented region ($z/D = 8.85D$). The distal portion of the stented region is defined along the remainder of the stented region to the exit taper region. For all strut configurations, the spatially averaged WSSM parameters are consistently greater in the distal portion compared to the proximal portion of the stented region (see Table 3.7). Low WSSM regions are reported to be more prevalent at the proximal end of the stent compared to the distal end in other numerical studies of stents in straight vessels[31], implying that this region should, on average, be more prone to NIH. The average WSSM values reported in Table 3.7 suggest that the proximal surface may be more susceptible to the development of NIH given the lower spatially averaged WSSM in this region, while the observations in Figure 3.12 suggest that the inner wall particularly susceptible. We note that for $K = 450$ the average of the WSSM in the proximal and distal portions is not below the critical low WSSM threshold value

associated with regions of NIH development. However, the lower average WSSM in the proximal region implies that a greater portion of the luminal surface in this region may be exposed to WSSM within the critical NIH development range. Conversely, the WSSG is also observed to be higher in the distal region compared to the proximal region, which, if above a critical threshold, is also known to induce NIH. Thus, there are competing mechanisms at work, with the WSSM predisposing the proximal region of the stent to NIH, while the WSSG is a factor in the distal region. This implies that for a given stent design, one factor may dominate the other, leading to NIH in different zones for different stents. Interestingly, the stent geometry N4_AR6, which has the largest variation from the proximal to the distal region, fosters a flow environment with the highest WSSM and lowest WSSG on average for $K$ = 450. On the contrary, the stent geometry N8_AR2 has the smallest variation in the average WSSM and WSSG parameters from the proximal to the distal region. This design could be considered hemodynamically advantageous from the standpoint that the flow behavior is relatively uniform throughout the stented region. Despite the uniformity, the N8_AR2 design induces a flow environment that is favorable to excessive NIH development given the average low WSSM and high WSSG throughout the stented region. Based solely on the information in Table 4.7, the hemodynamically best design would be the stent geometry N4_AR2 in order to achieve a reduction in NIH development, but at the cost of non-uniform WSS distribution within the stented region.

**Table 3.7 Average WSSM and WSSG at the proximal and distal end of the stent for $K$ = 450 for each geometry investigated**

| Geometry | $\overline{\lvert\tau\rvert}$ [N/m$^2$] | | Percent Difference [%] | $\overline{\lvert\nabla\tau\rvert}$ [N/m$^3$] | | Percent Difference [%] |
|---|---|---|---|---|---|---|
| | Proximal | Distal | | Proximal | Distal | |
| N8_AR2 | 3.80 | 4.13 | 8.12 | 3018.00 | 3168.67 | 4.75 |
| N4_AR2 | 4.17 | 4.77 | 12.56 | 2403.27 | 2640.06 | 8.97 |
| N4_AR3 | 4.37 | 4.96 | 11.78 | 2630.88 | 2868.40 | 8.28 |
| N4_AR6 | 4.48 | 5.27 | 14.95 | 2039.39 | 2245.92 | 9.20 |

### 3.3.2 *Effect of Dean number, K*

Morphological changes in the secondary flow structure with increasing Dean number has been well documented for curved pipes of a circular cross-section and demonstrated in wavy walled pipes as discussed in Chapter 3. The modification of the secondary flow structure with increasing Dean number due to the strut protrusions is presented in Figure 3.15 for N4_AR2. The streamline plots presented in the first column of Figure 3.15 depict the secondary flow structure in the circular cross-section of the unstented region and are used for comparison to the secondary flow structures presented in the subsequent columns, which are altered by the presence of the strut protrusions. The most prominent feature of the streamline plots in Figure 3.15 is the presence of the two-vortex Dean structure for all the simulated Dean numbers and cross-sectional planes. As stated in §1.1.4.1, Daskapoulos *et al.* reported that the two-vortex solution can transition to a four-vortex solution for $K > 956$ for vessels with a circular cross-section. The four vortex solution was not observed at $K > 956$ in the unstented region of the vessel. Moreover, the presence of the rectangular strut protrusions and the wavy walled cross-section discussed in Chapter 3 did not promote the transition to the four-vortex configuration observed by Daskapoulos *et al*. However, the shape of the Dean vortex, induced by the rectangular strut protrusions in the current simulations at higher Dean numbers, suggests that the secondary flow behavior is trending towards a second vortex pair formation.

The influence of the strut protrusions varies as the Dean number increases, resulting in alterations in the Dean vortex structure, as shown in Figure 3.15. Regardless of the cross-sectional geometry, the centers of the Dean vortices shift away from one another and toward the inner wall at higher Dean numbers (see Figure 3.15 (C)). At lower Dean numbers, the distortion of the Dean vortices due to the presence of the strut protrusions extends into the central region of the cross-section (see Figure 3.15 (A)). That is, the influence of the walls if felt further into the cross-section due the higher kinematic viscosity, and thus momentum diffusion. Conversely, the influence of the wall shape on the Dean vortex structure is limited to the near wall region for $K = 1450$, as shown in Figure 3.15 (C), as would be expected from a lower kinematic viscosity boundary layer-type flow. In addition, the size and location of the recirculation regions induced by the strut protrusions changes as the Dean number increases. In the IS1 intersection plane at $z/D = 8.12$, an additional recirculation region forms in the vicinity of the outer wall at $K = 1450$, as shown in the second column of Figure 3.15 (C). Furthermore, there is a reduction in the size of the streamwise vortical

structure near the outer wall discussed in the previous section in the IS2 intersection plane at $z/D$ = 8.85 as $K$ increases (see Figure 3.15, Column 4). The classic Dean vortex structure at $K$ = 70 is largely misshapen at the intermediate planes between the strut intersections, AS1 and AS2, as shown in Figure 3.15 (A), Columns 3 and 5. On the other hand, the Dean vortex shape is maintained in these planes at $K$ = 450 and 1450 (see Figure 3.15 (B) and (C), Columns 3 and 5). Interestingly, an additional region of centralized vorticity forms toward the outer wall of the vessel at $K$ = 1450 in the AS2 plane located at $z/D$ = 9.22, as shown in Figure 3.15 (C), Column 5. The Dean vortex appears to be split into two regions with the larger vortex shifted further toward the inner wall and a smaller vortex formation created toward the outer wall of the vessel.

The manifestation of the centrifugal instability resulting in the secondary flow structures observed in Figure 3.15 is strongly influenced by the viscous boundary layer and recirculation regions induced by the presence of the struts. The examination of the distribution of the axial component of vorticity aids in the qualitative identification of the "inviscid core", "boundary layer" regions, and recirculation zones, which can be used to describe the main features of the secondary flow[101]. These regions exhibit complex behavior due to the axial and circumferential changes in the strut positions. Figure 3.16 presents contour plots of the axial component of vorticity along with streamlines for $K$ = 70 and $K$ = 1450 for N4_AR2. The top half of the cross-section is displayed to avoid redundancy since the flow is symmetric about the plane of the bend. The area of negative axial vorticity near the wall (indicated by the shaded region in Figure 3.16) is used as a marker to demarcate the "boundary layer" region, as discussed in Chapter 3. The vorticity becomes positive toward the interior of the cross-section as indicated by the unshaded region in Figure 3.16. A contour plot of the axial component of vorticity in a plane in the unstented region of the vessel, see Figure 3.16 row 1, is included for comparison. Notably, Figure 3.16 highlights that the vorticity distribution depends on the Dean number and is altered by the presence of the strut protrusions in the cross-section. As $K$ increases, the boundary layer thins, particularly at the outer wall, which matches previous published reports for behavior observed in circular and wavy walled cross-sections[76,101]. Above the critical Dean number, $K$ > 956, (introduced by Daskopoulos and Lenhoff [76]) a second region of negative vorticity arises toward the outer wall, as previously reported for curved pipes with circular and wavy walled cross-sections[62,101]. The formation of this region implies the potential development of additional vortices present in the four vortex solutions as described by Daskopoulos and Lenhoff [76].

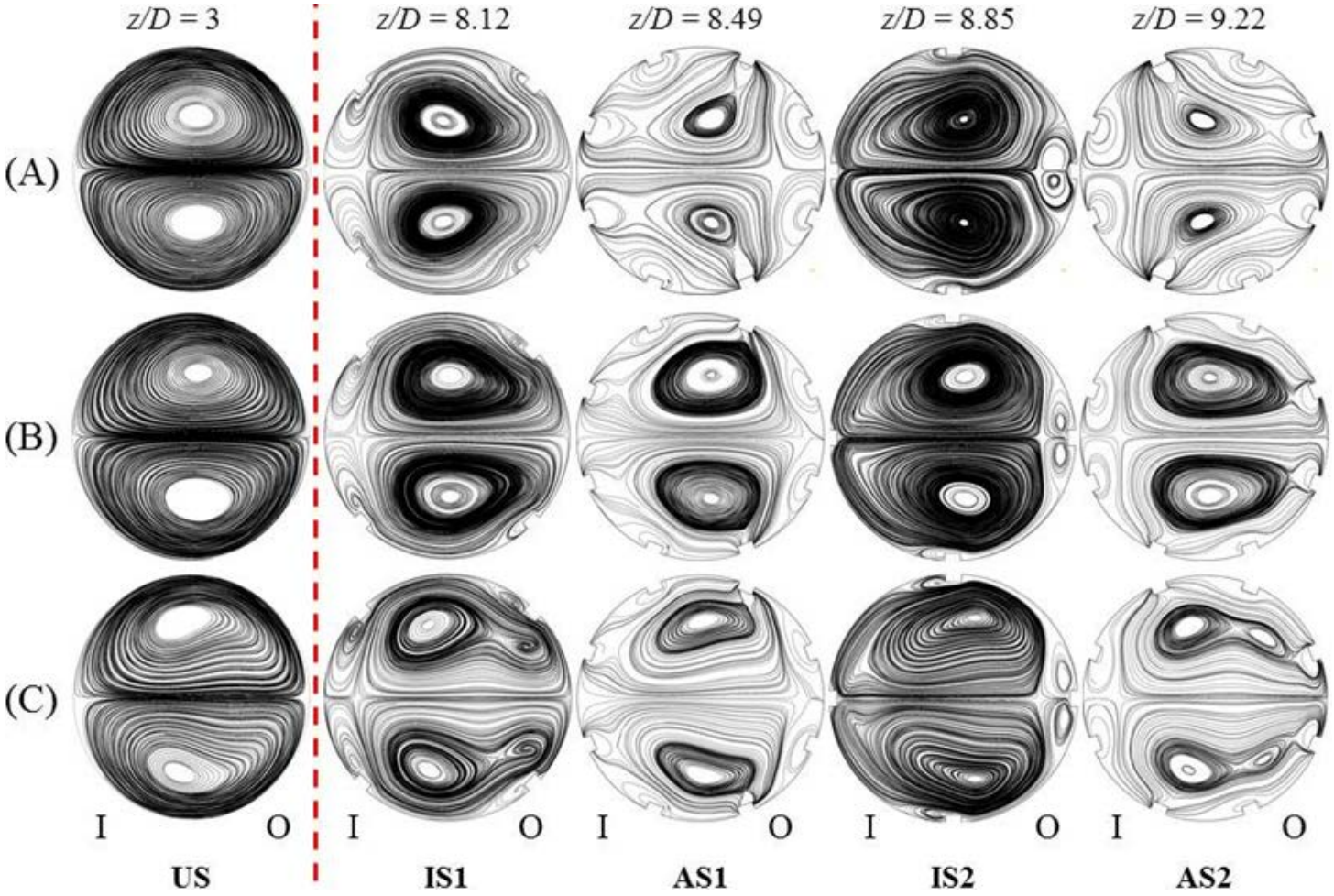


**Figure 3.15 Streamlines depicting secondary flow structures at selected planes in the entrance vessel and within the stented region at the Dean numbers (A) $K$ = 70, (B) $K$ = 450, and (C) $K$ = 1450 for N4_AR2. Naming convention at the bottom of each column for the planes follows Figure 3.6, with US indicating the upstream entrance region.**

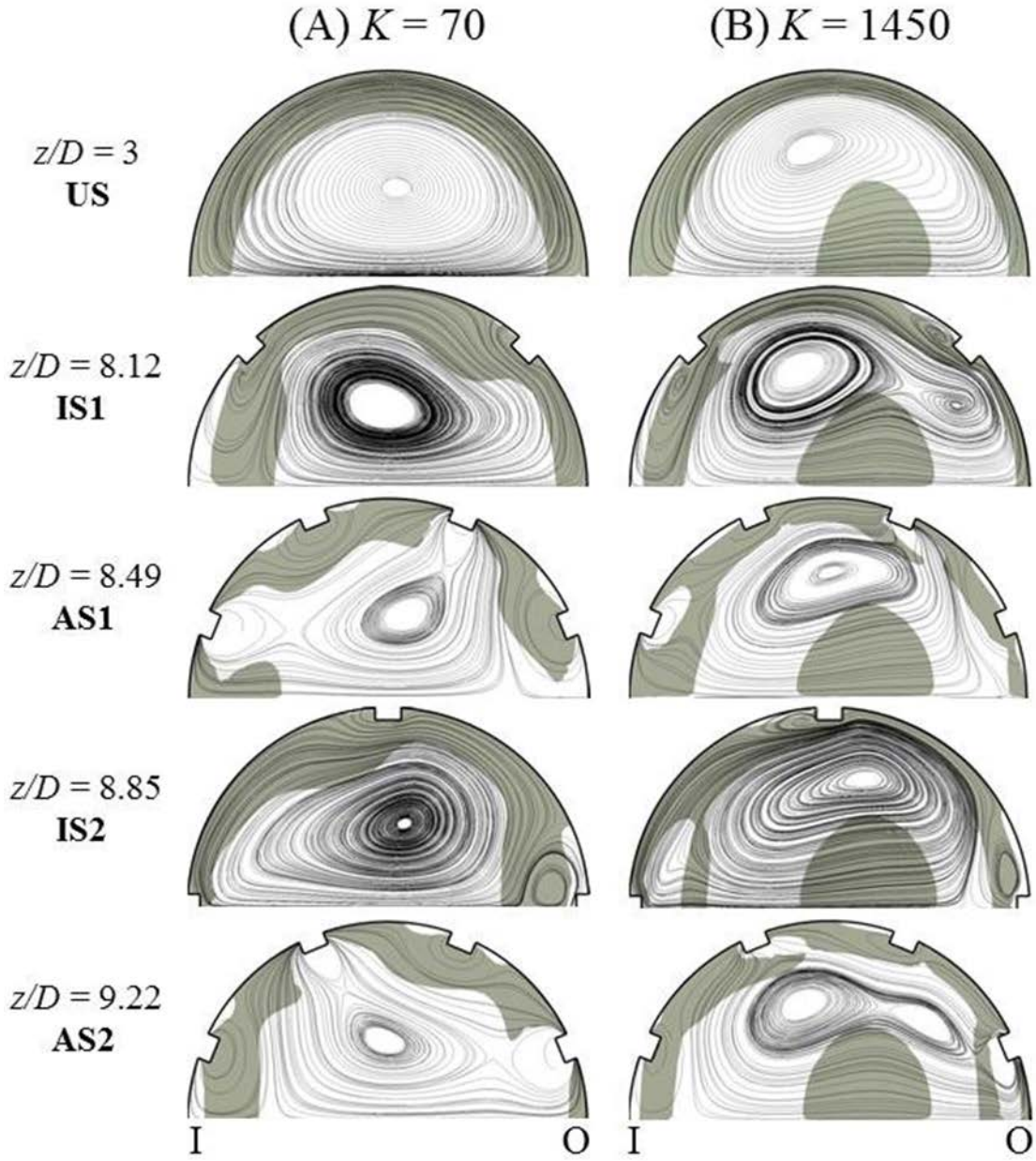


**Figure 3.16 Contour plot of the axial component of vorticity and the corresponding secondary flow structure for N4_AR2 for *K* = 70 (left column) and *K* = 1450 (right column). The shaded region in the contour plot indicates negative axial vorticity.**

In addition to boundary layer identification, the contour plots of the axial component of vorticity highlight the location of separated flow induced by the strut protrusions. The recirculation regions or separation bubbles characteristic of separated flow are identified by the positive regions of axial vorticity in the near wall region in the immediate proximity of the strut. These regions are sandwiched between the vessel wall and the shaded negative vorticity region toward the interior of the vessel. Thus, these regions represent the 2*D* "footprint" of the recirculation region within the plane. The three-dimensionality of the separated flow is captured by the isosurface of the Q-criterion in Figure 3.7. The secondary flow interaction with the strut protrusions generates flow features that are the focus of previously published work on separating and reattaching flow in the vicinity of planar forward facing step (FFS) and backward facing step (BFS) geometries [113-115]. Generally, the FFS and BFS geometries promote the creation of three separation points in the vicinity of the step. The first separation point is located upstream of the FFS and is observed on the windward side of the strut protrusions altering the secondary flow in the cross-sections shown in Figure 3.16.The blockage of the flow returning to the inner wall by the strut protrusion causes an adverse pressure gradient, with the consequence that the flow separates on the windward side of the strut in a manner characteristic of flow approaching a FFS. A recirculation region on the windward side forms and is identified by a region of positive vorticity near the leading edge of the strut. In particular, the recirculation region on the windward side the third strut protrusion encountered counterclockwise along the circumference is apparent for $K$ = 70 in the $z/D$ = 8.49 (AS1) plane (Figure 3.16 (A), row 3) and at $z/D$ = 9.22 (AS2, Figure 3.16 (A), row 5) at the second and fourth strut encountered in the counterclockwise direction. A very small recirculation region is observed for $K$ = 1450 in the same planes at $z/D$ = 8.49 (AS1) and $z/D$ = 9.22 (AS2, Figure 3.16 (B), rows 3 and 5), located at the first strut protrusion and the fourth strut protrusion, respectively, in the counterclockwise direction.

For typical FFS geometries, the blunt leading edge acts as another separation point and a recirculation zone forms on top of the step, extending from the leading edge to the reattachment point. However, an additional region of positive vorticity on top of the strut protrusions was only identified in the contour plots of the axial component of vorticity for $z/D$ = 8.85 at the strut protrusion located at $\varphi = 0$. The formation of this positive vorticity region is not attributed to flow separation at the leading edge, but instead to vorticity induced by the streamwise vortical structures that form around the strut at $\varphi = 0$. The third separation point is typically located at the trailing edge of a BFS and occurs due to the adverse pressure gradient created by the presence of

the step. A thin shear layer eventually develops due to the fast moving freestream fluid above the step and the low velocity fluid immediately downstream of the step. The shear layer curves down toward the wall due to the favorable pressure gradient created by fluid entrainment and intersects the wall at the reattachment point. A similar flow behavior is observed in the wake on the leeward side of the strut protrusions. Near wall regions of positive vorticity are observed to form on the leeward side of the struts at both $K$ = 70 and $K$ = 1450, as shown in Figure 3.16 in each plane of the stented region. The reattachment zone is generally located in the intrastrut region, coinciding with the location of an increase in the WSSM and decrease in WSSG in this region.

The size of the recirculation region and the reattachment length differ as $K$ increases. The presence of recirculation zones on the windward side is more prevalent at $K$ = 70 compared to higher Dean numbers (see Figure 3.16, rows 3 and 5). The recirculation regions in the wake of the struts protrude further into the interior of the cross-section for $K$ = 70 compared to higher Dean numbers and the reattachment length is generally shorter. Given the three dimensionality of the recirculation regions, dominant out of plane flow behavior is not necessarily captured by the contour plots of the axial component of vorticity. In particular, regions of positive vorticity located on the top of the strut protrusions are indicated in the contour plots of the intermediate planes between the strut intersections, AS1 and AS2, for $K$ = 70 (Figure 3.16 (A), rows 3 and 5). These regions may indicate locations in which the axial flow dominates and a secondary boundary layer region is not identified in the plane. These regions are smaller and almost enclosed by the secondary boundary layer for $K$ = 1450 suggesting that the secondary flow plays a more dominant role at the higher Dean number, leading to the creation of a separation point at the blunt leading edge of the protrusion, as typically observed for the FFS geometry.

Variations in the secondary flow strength due to the strut configuration are captured in the circulation in the “upper” half of the cross-section ($0 \leq \varphi \leq \pi$). Table 3.8 presents the circulation for the investigated Dean numbers in the cross-sections shown in Figure 3.15 and Figure 3.16. The circulation is calculated along a closed integration path selected based on a contour line of the minimum vorticity which gives a closed contour line isolated from the pipe wall and stent struts. Visualization of the Q-criterion in Figure 3.7 revealed the stretching and morphing of the Dean vortex tube within the stented region. The dynamics of the visualized coherent vortical structures is captured by the fluctuation of the vortex strength in the representative planes in the stented region. The highest circulation strength is observed in the IS1 plane for all $K$, which appears to contain the most cohesive Dean vortex shape. At $K$ = 70 and $K$ = 1450, the deformation of the

Dean vortex shape is confined to the near wall region and the vortex does not undergo the significant degree of stretching observed in the other representative planes (see Figure 3.16). Higher circulatory flow is less likely to allow particles, such as circulating leukocytes, to travel outside of the secondary flow vortex toward the vessel wall to promote NIH development. The lowest circulation is observed in the AS2 plane for all *K*. The Dean vortex within this plane is significantly stretched and distorted by the presence of the strut protrusions for $K = 70$ and $K = 1450$. At $K = 70$, the deformation of the Dean vortex shape due to the strut orientation protrudes far into the interior of the cross-section, making the native vortex shape largely unrecognizable. At $K = 1450$, the Dean vortex for the AS2 orientation is stretched with the evolution of two vortex centers in the cross-section. The contorted Dean vortex shape within the AS2 plane corroborates the calculated reduction in the circulation strength. The oscillation of the cortex strength in each plane highlights the complex vortex dynamics induced by the axial and circumferential strut protrusions.

**Table 3.8 Normalized Circulation for Dean numbers investigated at selected planes in the stented region shown in Figure 3.15**

| | | $\lvert\Gamma/\nu\rvert$ | | |
|---|---|---|---|---|
| *z/D* | Strut Configuration | $K = 70$ | $K = 450$ | $K = 1450$ |
| 3 | US | 33.49 | 86.73 | 81.80 |
| 8.12 | IS1 | 37.00 | 97.30 | 98.23 |
| 8.49 | AS1 | 29.95 | 91.29 | 89.64 |
| 8.85 | IS2 | 30.67 | 87.44 | 86.27 |
| 9.22 | AS2 | 27.42 | 84.18 | 80.45 |

The primary hemodynamic mechanism of ISR development shifts based on the characteristic Dean number of the flow conditions. As *K* increases, the luminal area of the vessel exposed to low WSSM decreases and the area exposed to high WSSG increases. The potential development of ISR is dominated by the WSSG rather than WSSM at higher Dean number values. Specifically, the area of the luminal wall exposed to low WSSM is less than 0.1% of the stented region at $K = 1450$. Thus, the development of ISR at high Dean number values is predicated on

the distribution of high WSSG. Figure 3.17 and Figure 3.18 shows contour plots of the WSSG normalized by the maximum WSSG in the plane 3*D* from the pipe entrance in the fully developed unstented region at the outer and inner walls, respectively. The maximum WSSG in the unstented regions is 0.81 N/m$^3$ for $K$ = 70, 14.94 N/m$^3$ for the $K$ = 450, and 57.38 N/m$^3$ for $K$ = 1450. These figures plot dimensionless values to compare with native conditions, instead of the dimensional value, which is important for determining vascular response. The plots indicate the deviation of the WSSG from the native vessel condition as a result of the stent implantation is greater at $K$ = 70 compared to the higher Dean numbers. Common among the investigated Dean numbers is the fact that largest deviation from the native vessel WSSG occurs in the region surrounding the struts and distal to the strut intersections. Note, that despite the lower contour levels for the $K$ = 1450 case in Figure 3.17, the actual WSSG values for this case are the largest, and thus most susceptible to ISR.

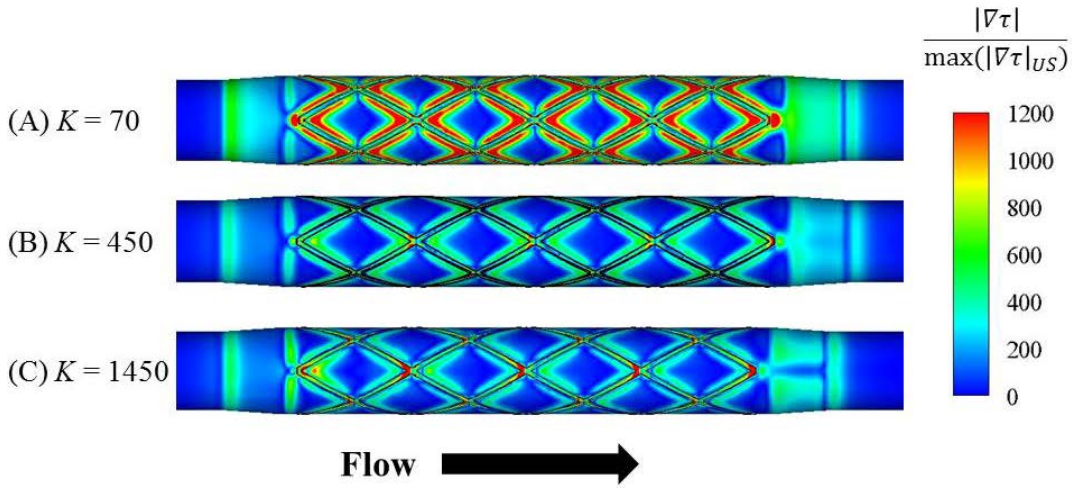


**Figure 3.17 Contour plot of WSSG at the outer wall normalized by the maximum WSSG in the plane 3*D* from the pipe entrance for $K$ = 70 (A), $K$ = 450 (B), and $K$ = 1450 (C).**

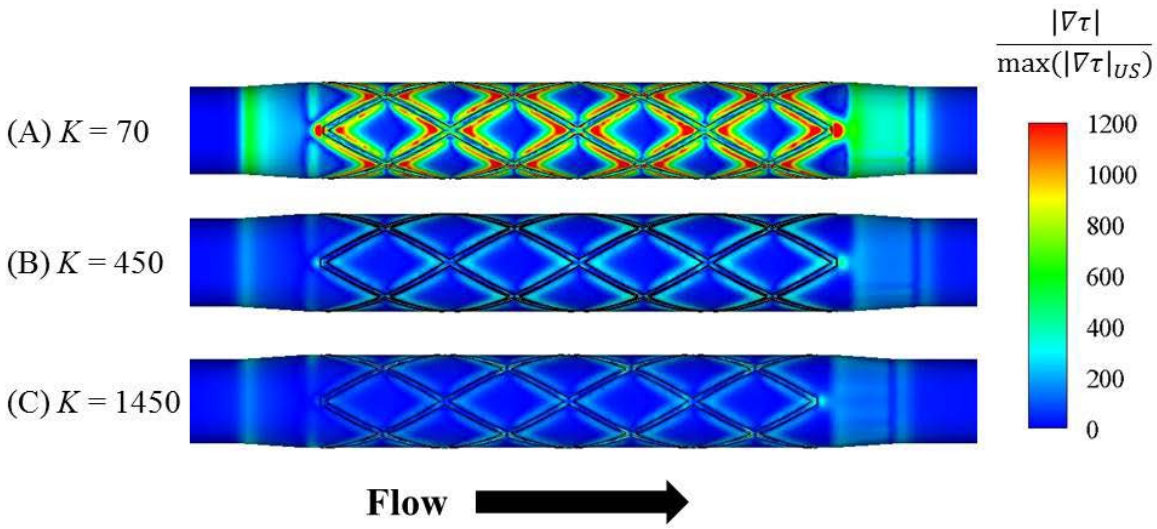


**Figure 3.18 Contour plot of WSSG at the inner wall normalized by the maximum WSSG in the plane 3*D* from the pipe entrance for *K* = 70 (A), *K* = 450 (B), and *K* = 1450 (C).**

### 3.3.1 *Effect of the Number of Protrusions*

In this section, the effect of the number of strut protrusions is investigated for a fixed strut protrusion aspect ratio and all values of *K*. The computational vessels consisting of 4-strut or 8-strut configurations are utilized to determine the effect of the number of strut protrusions on the flow behavior within the lumen. Geometrically, increasing the number of struts from four to eight reduces the strut protrusion spacing and subsequently reduces the size of the intrastrut area by approximately 80%. The average cross-sectional area within the vessel decreases by approximately 1.77% when the number of protrusions is doubled. The change in the cross-sectional area results in an insignificant reduction in the nominal Dean number of 1.3%. The fluid dynamic environment in the vicinity of the 4-strut and 8-strut stent design are contrasted by focusing on the secondary flow structure and the WSSM indices in the stented region, extending from the entrance to the expansion region to the exit of the taper region. Naturally, the fluid flow between the struts is a strong function of the interstrut spacing. This is clearly demonstrated by examining the global changes in the WSS distribution and the secondary flow structures for the investigated geometries.

The global effect of the number of strut protrusions is captured by comparing the average WSSM and WSSG within the stented region, as shown in Table 3.7, for the 4-strut and 8-strut stent design. A reduction in the number of strut protrusions leads to an increase in WSSM of 10 -

13% across all values of *K*. The increase in WSSM due to the reduction in the protrusion frequency is observed to be approximately 7% greater along the outer wall compared to the inner wall and 3% greater in the distal region compared to the proximal region. The minor difference between the proximal and distal region suggest that the flow development, in relation to the WSS, is not significantly impacted by the number of axial protrusions traversed by the flow. Accompanying the change in WSS, average WSSG is found to decrease between 18-25% for all *K* as the number of struts is reduced. The changes in the WSS indices owing to the reduction in the number of struts generate hemodynamic conditions that decrease the likelihood of the occurrence of re-stenosis.

**Table 3.9 Comparison of average WSSM and WSSG for the 8-strut and 4-strut configurations with a fixed protrusion aspect ratio for each investigated value of *K*.**

| | $\overline{\lvert\tau\rvert}$ [N/m$^2$] | | | $\overline{\lvert\nabla\tau\rvert}$ [N/m$^3$] | | |
|---|---|---|---|---|---|---|
| Geometry | *K* = 70 | *K* = 450 | *K* = 1450 | *K* = 70 | *K* = 450 | *K* = 1450 |
| N8_AR2 | 0.68 | 3.40 | 12.53 | 446.00 | 3102.95 | 12083.38 |
| N4_AR2 | 0.75 | 4.50 | 14.46 | 377.36 | 2538.06 | 9657.46 |
| % Difference (N8 vs N4) | 10.03 | 11.21 | 13.34 | -18.19 | -22.26 | -25.12 |

Given the focal nature of NIH development, it is advantageous to visualize the effect of the number of protrusions on the distribution of WSSM and WSSG. The spatial pattern of the vessel wall exposed to WSSM within the critical range favorable for NIH development is presented in Figure 3.19 and Figure 3.20 for *K* = 70. Regions exposed to low WSS, defined as WSSM < 0.5 N/m$^2$, are presented in Figure 3.19 and regions exposed to moderate values of WSS, defined as those occurring between 0.5 N/m$^2$ < WSSM < 0.8 N/m$^2$, are presented in Figure 3.20. The luminal areas exposed to moderate WSSM are included in the analysis of NIH-prone regions given their elevated risk of transitioning to the critical low WSSM range due to minor changes in curvature or mean flow conditions. The discussion of the effect of the number of protrusions on low or moderate WSSM distribution focuses on *K* = 70, since the regions exposed to low or moderate WSSM at higher Dean numbers are very small or nonexistent. In addition, the

examination of the various protrusion frequencies at $K$ = 70 facilitates the comparison of computational results with published reports in straight stented vessels with the same inlet condition[86]. Qualitatively, the contour plots indicate that the low WSSM regions are concentrated near the immediate vicinity of the struts, as shown in Figure 3.19, and a greater portion of the intrastrut area is exposed to low WSSM for the 8-strut configuration compared to the 4-strut configuration. As expected, the regions of low WSSM coincided with recirculation regions induced by the implanted stent. Notably, the lowest WSSM region is localized proximal and distal to the strut intersections and the WSSM increases toward the interior of the intrastrut region. Moderate WSSM regions are localized throughout the intrastrut area of the 8-strut configuration. Conversely, the moderate WSSM regions are absent in the center of the intrastrut region for the 4-strut configuration and instead are concentrated in a small area directly adjacent to the low WSSM region. The WSSM distribution in Figure 3.19 and Figure 3.20 suggests that a significant portion of the intrastrut area for the 4-strut configuration is not susceptible to ISR as a result of physiological reaction to the WSSM conditions.

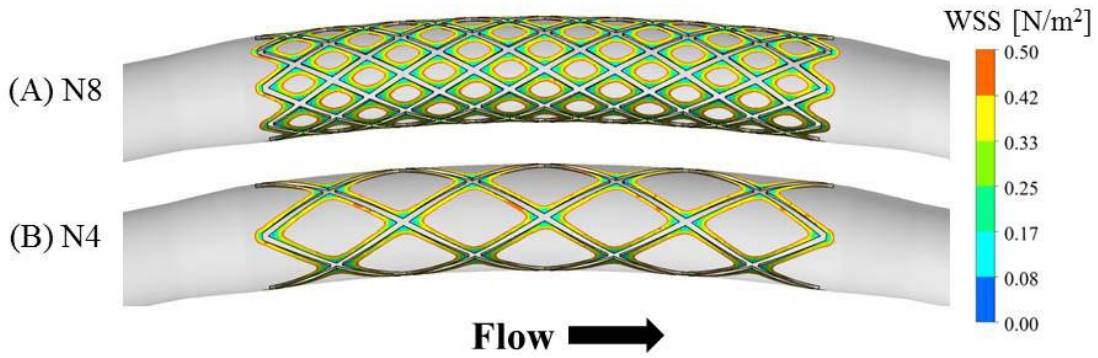


**Figure 3.19 Regions of vessel wall exposed to low WSSM, $|\tau| \leq 0.5$, for the geometries (A) N8_AR2 and (B) N4_AR2. The area of low WSS magnitude is $8.4213 \times 10^{-5}$ m$^2$ for N8_AR2 and $4.1609 \times 10^{-5}$ m$^2$ for N4_AR2.**

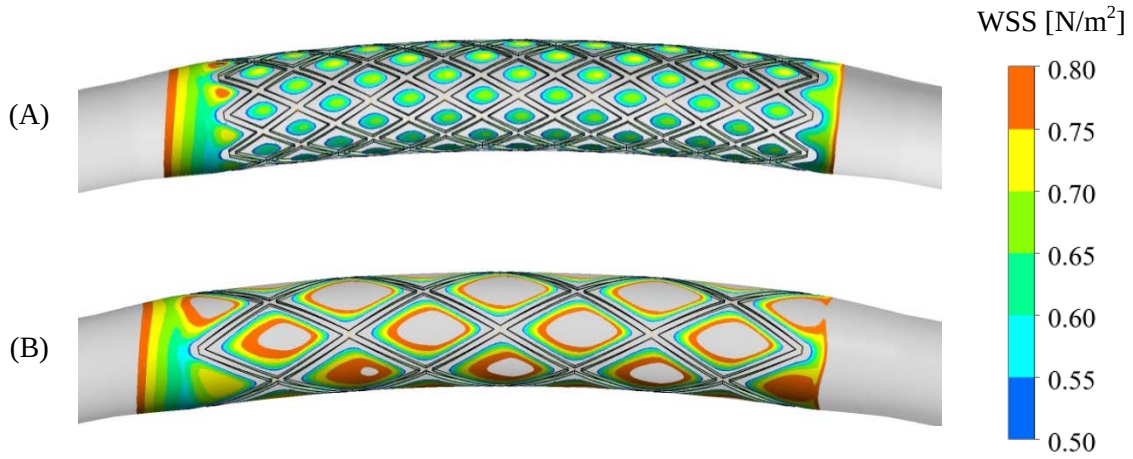


**Figure 3.20 Regions of vessel wall exposed to moderate WSSM, $0.5 < |\tau| \leq 0.8$, for the geometries (A) N8_AR2 and (B) N4_AR2.**

The distribution of low and moderate WSSM are consistent with previous CFD results for straight stented vessels for the same inlet condition. The introduction of curvature in the geometry investigated in this study warrants the examination of variance in these distributions between the inner and outer wall. Table 3.10 presents the percentage of the vessel wall exposed to low and moderate WSSM at the inner and outer wall of the 8-strut and 4-strut stent design. The area exposed to low WSSM is slightly greater at the inner wall compared to the outer wall for both strut frequencies. This discrepancy is also observed for the moderate WSS distribution for both stent designs. Notably, the moderate WSSM region for the 4-strut configuration shows a greater imbalance between the inner and outer walls compared to the 8-strut configuration (Inner Wall - 49.77% vs. Outer Wall - 33.01%). Once again, we observe that the vessel region exposed to low WSSM is greater at both the inner and outer wall for the 8-strut configuration compared to the 4-strut configuration. At higher Dean number, where axial skew is more prominent, a greater imbalance in the WSSM distribution between the inner and outer wall is expected. However, for the higher Dean numbers investigated in this study the area exposed to low and moderate WSSM is negligible.

**Table 3.10 Percentage of outer and inner wall within the stented region exposed to low and moderate WSSM for $K$ = 70.**

| Geometry | Low WSSM $\lvert\tau\rvert < 0.5$ [N/m$^2$] | | Moderate WSSM $0.5 < \lvert\tau\rvert < 0.8$ [N/m$^2$] | |
|---|---|---|---|---|
| | Outer Wall [%] | Inner Wall [%] | Outer Wall [%] | Inner Wall [%] |
| NS8_AR2 | 36.72 | 39.18 | 34.04 | 34.66 |
| NS4_AR2 | 21.26 | 22.50 | 33.01 | 49.77 |

An overall quantitative assessment of the total stented area exposed to low and moderate WSSM conditions is presented in Figure 3.21. A reduction in the number of struts results in a 16% decrease in the area of the stented region exposed to low WSS. This result stems from the fact that decreasing the number of struts reduces the number of low flow recirculation zones induced by the strut presence and subsequently decreases the luminal exposure to low WSS. The reduction in the low WSSM region is the same at the outer and inner wall, as shown in Table 4.10. Concurrently, the decrease in strut number results in a 12% increase in the area exposed to moderate WSSM along the luminal walls of the stented region. However, the increase in the moderate WSSM area is larger at the inner wall compared to the outer wall. Overall, reducing the number of struts leads to a 10% reduction in the area of the stented region with an elevated potential for NIH development due to low or moderate WSS.

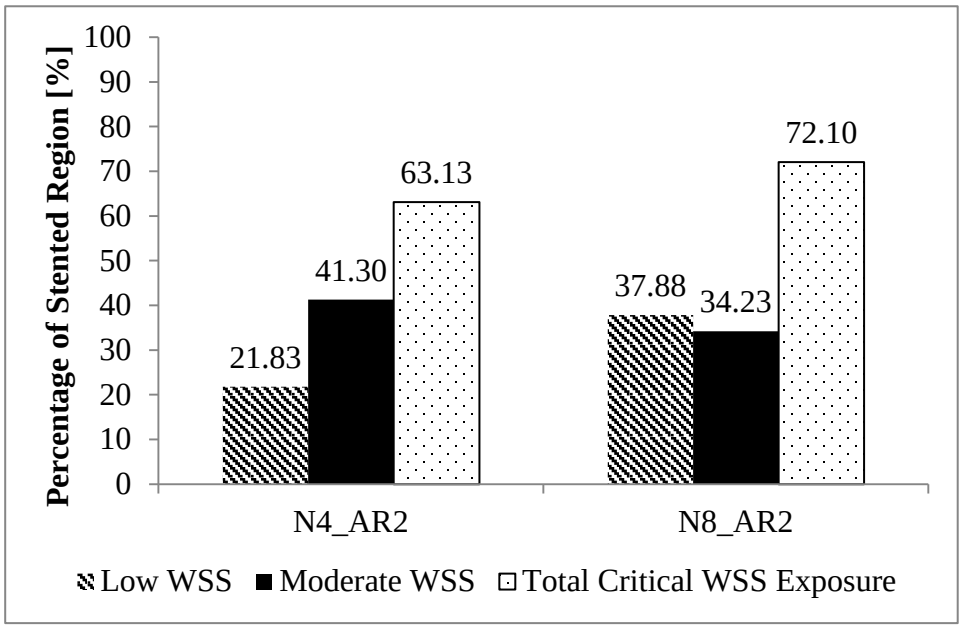


**Figure 3.21 Percentage of the stented region exposed to low and moderate WSS for the stent geometries N4_AR2 and N8_AR2 at $K = 70$.**

The impact of the stent design in straight stented geometries has focused on the WSSM distribution related to NIH development. The introduction of stent curvature requires that additional focus be placed on the impact of the circumferential strut frequency on the secondary flow structure. The disturbance of the secondary flow by the strut presence will determine the distribution of NIH catalyst within the cross-section of the vessel. The secondary flow structure within selected planes from the middle stent cell for the 4-strut and 8-strut configuration is presented in Figure 3.22. The selected planes are extracted from the strut intersections for the 4-strut (Figure 3.22 (A) and (C)) and 8-strut (Figure 3.22 (E) and (G)) configuration. Additional planes are extracted between the strut intersections (Figure 3.22 (B),(D),(F),(H)). The deformation of the Dean vortex structure due to the circumferential struts is mitigated in the 8-strut configuration compared to the 4-strut configuration. As the circumferential strut spacing is reduced, the shape of the cross-section approaches a circular cross-section and the Dean vortex structure closer resembles the vortex in a circular pipe cross-section. In addition, the size of the recirculation regions is reduced as the number of struts increases. This is highlighted at the inner wall of the plane IS1 ((Figure 3.22 (A) and (E)) and the outer wall of the plane IS2 (Figure 3.22 (C) and (G)). The mitigation of the deformation of the Dean vortex structure for the greater

number of circumferential struts holds for all *K*. The secondary flow streamlines in Figure 3.22 also indicate that the streamwise location of the plane determines the Dean vortex structure. For example, the same circumferential struts are present in the angled strut planes, AS1 and AS2, extracted from the 4-strut configuration and the intersection planes, IS1 and IS2, extracted from the 8-strut configuration. Despite the same number of circumferential struts, the Dean vortex structure in these planes differs for the different strut configurations. Thus, the axial strut configuration plays a significant role in the determining the secondary flow structure, as previously intimated by the difference in flow characteristics between stent regions with the struts are converging versus diverging.

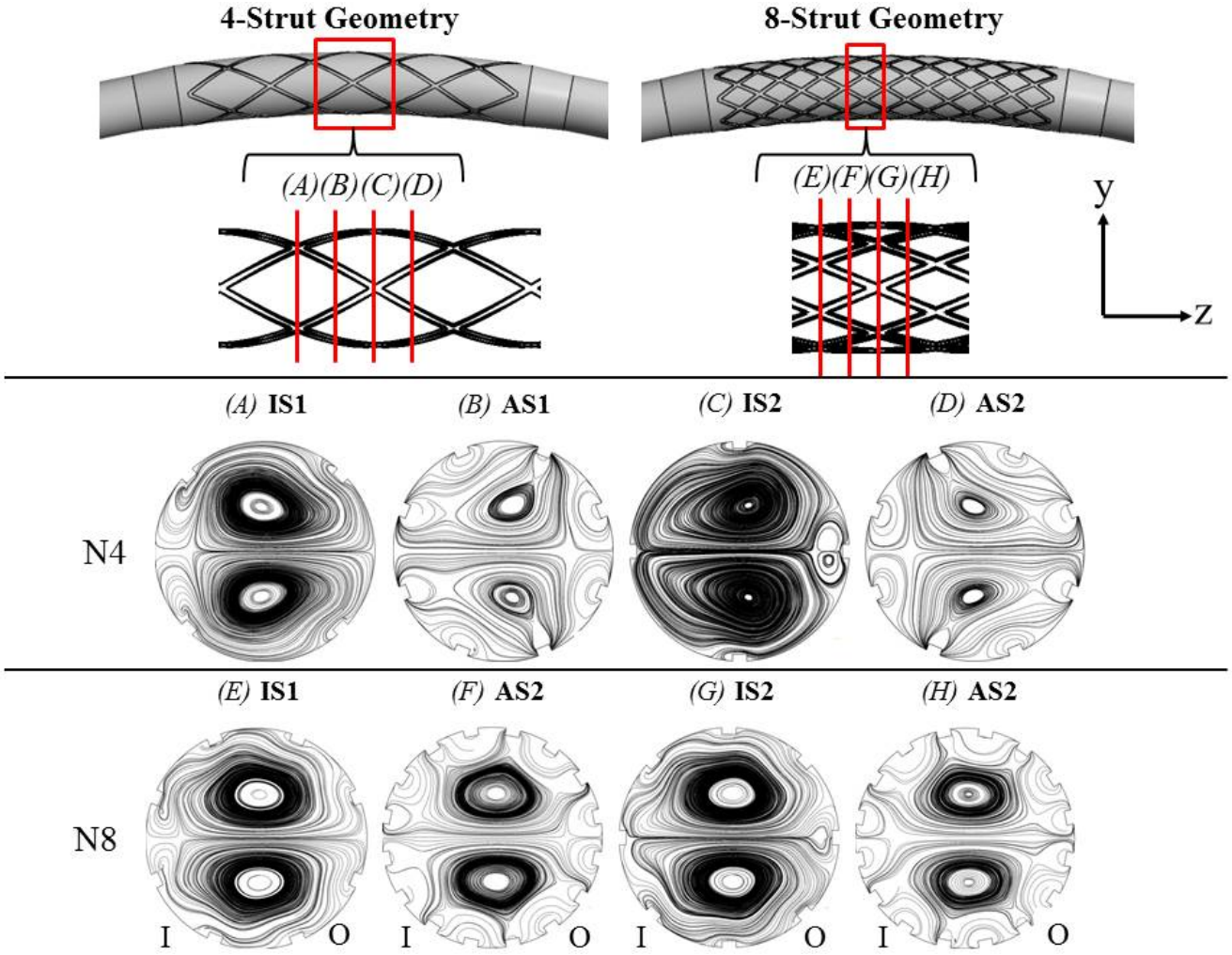


**Figure 3.22 Secondary flow structure presented for the four-strut (N4_AR2) and eight-strut (N8_AR2) configurations at planes centered around the middle of the stented region for $K$ = 70.**

### 3.3.2 *Effect of the Protrusion Aspect Ratio*

To assess the sensitivity of the flow field to variations in the strut aspect ratio (AR), defined as the strut width-to-height ratio, the strut thickness and strut width are varied for a fixed strut number of 4. LaDisa *et al.* has established for stented straight pipe geometries that reducing the strut thickness results in a decrease in the percentage of the vessel exposed to low WSSM; however, reducing the strut width exposed the vessel to a greater area of low WSSM. Furthermore, they observed a modest reduction in the percentage of the vessel exposed to high WSSG when the strut thickness is reduced; the strut width had a negligible effect on the size of the high WSS regions. In the present study, we focus on the strut aspect ratio rather than the individual strut dimensions. This approach is chosen since the structural integrity of the stent would likely be determined by a specified strut aspect ratio rather than specific strut dimensions. The results of the simulations establish the relationship between the strut aspect ratio and the disturbance in the luminal flow environment by the strut presence. A hemodynamically optimal aspect ratio can be chosen and additional structural integrity calculations can be used to determine the mechanical strength of the design. An illustration of the investigated strut cross-sections is presented in Figure 3.23. The geometry N4_AR2 and N4_AR3 have the same protrusion height but the protrusion width of N4_AR3 is approximately 40% less than N4_AR2. On the other hand, the geometry N4_AR3 and N4_AR6 have the same width, but the height of N4_AR6 is approximately 40% less than N4_AR3.

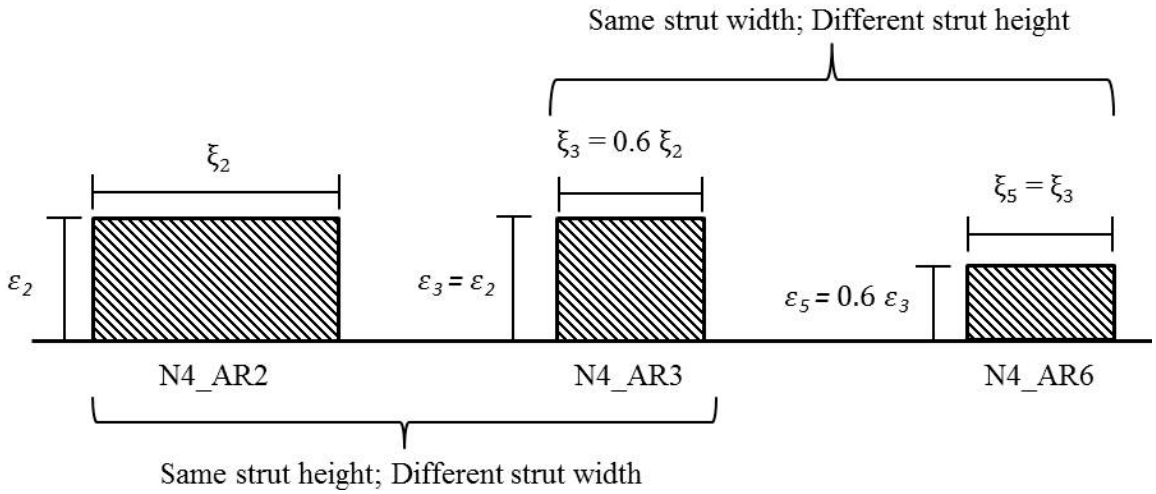


**Figure 3.23 Illustration of strut protrusion cross-sections for the aspect ratios investigated.**

We hypothesize that the aspect ratio would affect the size of the recirculation region surrounding the stent struts, which would be reflected in the calculation of the spatially averaged WSSM and WSSG. To explore this hypothesis, the spatially averaged WSSM and WSSG for the various aspect ratios and Dean numbers investigated is presented in Table 3.11. The spatially averaged WSSM increases as the aspect ratio increases, which suggest a reduction in the luminal area exposed to low WSSM. The value of the spatially averaged WSSG increases as the aspect ratio is increased from 2 to 3; however, the value decreases when the aspect ratio is further increased from 3 to 6. This implies that the effect of the strut presence on the WSSG, on average, is based individually on the strut width or the strut height rather than the combination captured by the aspect ratio. A reduction in the width of the strut (AR2 vs AR3) increases the spatially averaged WSSG, while a reduction in the height of the strut (AR3 vs. AR6) decreases the WSSG significantly.

As previously stated, non-uniform distribution of WSSM and WSSG exist with the stented region. The influence of the stent presence on the WSS distribution in the proximal and distal region was presented in Table 3.7 for $K$ = 450 in Section 4.3.1 and highlights the impact of the aspect ratio on the spatial imbalance of WSS in these regions. The trends discussed involving the impact of the aspect ratios is consistent for all values of $K$. The WSSM and WSSG are higher in the distal portion compared to the proximal region regardless of the strut aspect ratio. An increase in the aspect ratio from 2 to 3 results in a marginal decrease in the imbalance of WSSM and WSSG between the proximal and distal region. In contrast, a further increase in the aspect ratio from 3 to 6 results in a greater disparity between the spatially averaged WSSM and WSSG in the proximal and distal regions, with an overall greater impact on the WSSM distribution. The result implies that the strut thickness has a significant impact on the spatial WSS distribution as the flow advects from the proximal to the distal end. Over all, the stent geometric parameters, including the aspect ratio, has a greater impact on the regional distribution of the WSSM compared to WSSG.

**Table 3.11 Comparison of the average WSSM and WSSG for the investigated protrusion aspect ratios and values of *K*.**

| | $\overline{\lvert\tau\rvert}$ [N/m$^2$] | | | $\overline{\lvert\nabla\tau\rvert}$ [N/m$^3$] | | |
|---|---|---|---|---|---|---|
| Geometry | $K$ = 70 | $K$ = 450 | $K$ = 1450 | $K$ = 70 | $K$ = 450 | $K$ = 1450 |
| N4_AR2 | 0.753 | 4.503 | 14.460 | 377.358 | 2538.063 | 9657.457 |
| N4_AR3 | 0.780 | 4.702 | 15.276 | 403.975 | 2764.886 | 10794.233 |
| N4_AR6 | 0.802 | 4.921 | 16.266 | 318.470 | 2159.854 | 8055.688 |

The percent change in the spatially averaged WSSM and WSSG between the different aspect ratios for the different Dean numbers is compared in Table 3.12. Variations in the strut aspect ratio results in marginal changes in the spatially averaged WSSM at low Dean numbers, but the effect becomes more significant at higher Dean numbers. The increase in the average WSSG between N4_AR2 and N4_AR3 ranges from 6 – 10% for the investigated values of *K*. In contrast, the change in aspect ratio from 3 to 6 shows a significant reduction in the spatially averaged WSSG between 26 – 34%. As previously mentioned, this implies the spatially averaged WSSG is driven by the strut height, which is expected, since strut protrusion into the luminal has a significant impact on the flow disturbance due to the deviation from the native vessel radius. The strut width results in a greater surface area for reattachment of the flow on top of the strut protrusions and less spatial change in the WSS.

**Table 3.12 Percent change in the spatially averaged WSSM and WSSG for the investigated aspect ratios with fixed number of struts for all *K*.**

| | Percent Difference $\overline{\lvert\tau\rvert}$ [%] | | | Percent Difference $\overline{\lvert\nabla\tau\rvert}$ [%] | | |
|---|---|---|---|---|---|---|
| Geometry | $K$ = 70 | $K$ = 450 | $K$ = 1450 | $K$ = 70 | $K$ = 450 | $K$ = 1450 |
| N4_AR2 vs. N4_AR3 | 2.70 | 4.23 | 5.34 | 6.59 | 8.20 | 10.53 |
| N4_AR3 vs. N4_AR6 | 2.70 | 4.45 | 6.08 | -26.85 | -28.01 | -33.40 |

The distribution of the stented region exposed to low and moderate WSSM, as well as high WSSG, expressed as a percentage of the luminal wall within the stented region is presented

in Table 3.13 for $K$ = 70 to quantify the influence of the strut aspect ratio. Changes in the aspect ratio does not alter the general location of the low and moderate WSS region, which remain located in the immediate vicinity of the struts and toward the interior of the intrastrut area, respectively. The trends in the distribution at the low Dean number are compared at $K$ = 70 in order to compare the results to computational studies conducted by LaDisa *et al*. for the straight stented vessel. We observe that increasing the aspect ratio decreases the area exposed to low and moderate WSSM. Notably, increasing the aspect ratio from 2 to 3 leads to a minor reduction in the area exposed to low WSSM (21.83 % to 20.09%). Conversely, a further increase in the aspect ratio from 3 to 6 results in a more significant reduction in the percentage of the luminal area exposed to low WSS (20.09 % vs 13.88%). This suggests that altering the strut width from $\xi$ = 0.14 to 0.24 does not have a substantial effect on the percent distribution of low WSSM regions. On the other hand, strut height has a greater impact on the percent distribution of low WSSM areas. This finding corroborates the findings by LaDisa *et al.* for the stented straight vessel geometry with a similar stent design and the same Reynolds number. We note, however, that, despite using analogous geometries and flow rates to LaDisa *et al*., the measured area values differ due to modification of the distributions due to the vessel curvature.

The impact of the aspect ratio on the percentage of the stented region exposed to low and moderate WSSM and high WSSG is summarized in Table 3.13. Overall, the change in the aspect ratio from 2 to 3 does not have a significant impact on the size of the area expose to low and moderate WSSM. Further, increasing the aspect ratio from 3 to 6, due to a decrease in the strut thickness, does not greatly dictate the regions exposed to moderate WSSM; however, there is a 7% decrease in the region exposed to low WSSM. The percent distribution of high WSSG within the stented region reaffirms the previously stated conclusion that the strut height has a greater impact on spatial WSSG than the strut width. The change in the aspect ratio from 2 to 3 results in a marginal change in the area exposed to high WSSG (66.38% vs 63.45%); increasing the aspect ratio from 3 to 6 produces a more significant change in the WSSG distribution (63.45% vs 53.49%).

**Table 3.13 Percentage of stented region exposed to low or moderate WSSM or high WSSG.**

| | $\overline{\lvert\tau\rvert}$ [%] | | High $\overline{\lvert\nabla\tau\rvert}$ [%] |
|---|---|---|---|
| Geometry | *Low* | *Moderate* | |
| N4_AR2 | 21.83 | 41.30 | 66.38 |
| N4_AR3 | 20.09 | 38.36 | 63.45 |
| N4_AR6 | 13.88 | 37.23 | 53.49 |

The examination of the WSSM distribution, used to identify regions prone to NIH due to WSS intensity, does not elucidate the directionality of the WSS component, which can be used to identify separation and recirculation regions near the struts. In order to elucidate the impact of strut aspect ratio on the size of recirculation zones, Figure 3.24 presents the axial WSS distribution,$\tau_a$, for the aspect ratios investigated along a line formed by the intersection of the inner and outer walls with the $z$ = 0 plane, for $K$ = 70 and 1450. The axial WSS along each wall is normalized by the corresponding upstream average axial WSS in the fully developed region of the unstented vessel. For $K$ = 70, the value of the average axial WSS in the unstented region was approximately 1.21 N/m$^2$ and 1.08 N/m$^2$ at the outer and inner wall, respectively. The value of the average axial WSS in the unstented region was approximately 32.38 N/m$^2$ and 11.11 N/m$^2$ at the outer and inner wall, respectively, for $K$ = 1450. The upstream average axial WSS is the same regardless of strut aspect ratio. The normalized WSS is utilized to determine the deviation of axial WSS values from the homeostatic levels in the unstented vessel. Regions of flow separation and recirculation are identified by negative $\tau_a$ values, indicating flow moving opposite to the primary flow direction, in the vicinity of the stent struts. We note that the $z$ = 0 plane is a plane of symmetry, and thus separation length is well defined since there is no out of plane flow component in this plane. The investigation of negative axial WSS regions within the $z$ = 0 plane is merely used as an estimation of the impact of the strut aspect ratio in the vicinity of the struts.

Firstly, the common trends in the axial WSS distribution for the investigated aspect ratios are discussed. The most salient features of the axial WSS distribution are prominent peaks along the surface of the stent struts as the flow passes over the protrusions for all aspect ratios and Dean

numbers. As well, the WSS distribution from the proximal to the distal end of the stent differs between the Dean number values. At $K$ = 70, the axial WSS distribution is similar from one stent cell to the next at the inner and outer wall. Furthermore, the axial WSS distribution is similar between the inner and outer wall, exemplifying the minimal axial skew at the lower Dean number. On the other hand, the distribution changes from the stent cells at the proximal to distal end and between the inner and outer wall for $K$ = 1450. For this case, the axial WSS distribution differs considerably between the inner and outer walls. The axial WSS increases within the stent cells from the proximal to the distal region at the inner wall; the opposite behavior is observed at the outer wall with decreasing axial WSS in the streamwise direction. The impact of the greater axial velocity skew at higher $K$ is demonstrated by the higher values of axial WSS at the outer wall compared to the inner wall. The axial WSS in the first axially located intrastrut area is altered considerably due to the presence of the first strut at both walls, as indicated by the deviation of the curves from the normalized value of 1; the effect of the strut is reduced within the subsequent intrastrut areas as the WSS distribution tends toward a stable value. For $K$ = 70, no regions of negative $\tau_a$ occur along the points extracted at the inner and outer wall regardless of strut dimensions (Figure 3.24 (A)). This result is expected since the fluid at lower Dean numbers has less momentum and is less likely to separate. At higher Dean number values, the fluid is moving with greater momentum and is thus more likely to result in flow separation in the vicinity of the struts. This phenomenon is portrayed in Figure 3.24 (B), where regions of negative $\tau_a$surround the stent struts along each wall for $K$ = 1450.

At lower $K$, the variation in the aspect ratio does not have a significant impact on the WSS distribution (see Figure 3.24 (A)). The changes in the aspect ratio have a greater impact on the axial WSS distribution in the presence of higher fluid velocity at $K$ = 1450. Generally, the aspect ratios AR2 and AR3 produce similar axial WSS distributions within the intrastrut areas along both walls, with the exception of a greater reduction in the $\tau_a$ for the strut aspect ratio of 3 in the first intrastrut area at the outer wall (Figure 3.24(B) row 2). At the inner wall, the aspect ratio of 6 generates the largest reduction in $\tau_a$ in the proximal region of the stent, but $\tau_a$ increases to eventually become equivalent to the other aspect ratios downstream. At the outer wall, the greatest reduction in $\tau_a$ is also produced by aspect ratio 6 in the first intrastrut area; however, the aspect ratios 2 and 3 cause the largest reduction in the distal region. Interestingly, the axial WSS within the intrastrut regions is observed to behave in a periodic manner for the aspect ratio of 6, in which the odd and even axially numbered intrastrut areas have similar WSS profiles. Specifically, the

axial WSS steeply increases as the flow enters the even numbered intrastrut areas and then gradually decreases and plateaus as the flow approaches the next distally located strut. Within the odd numbered intrastrut areas, the axial WSS gradually rises throughout the area.

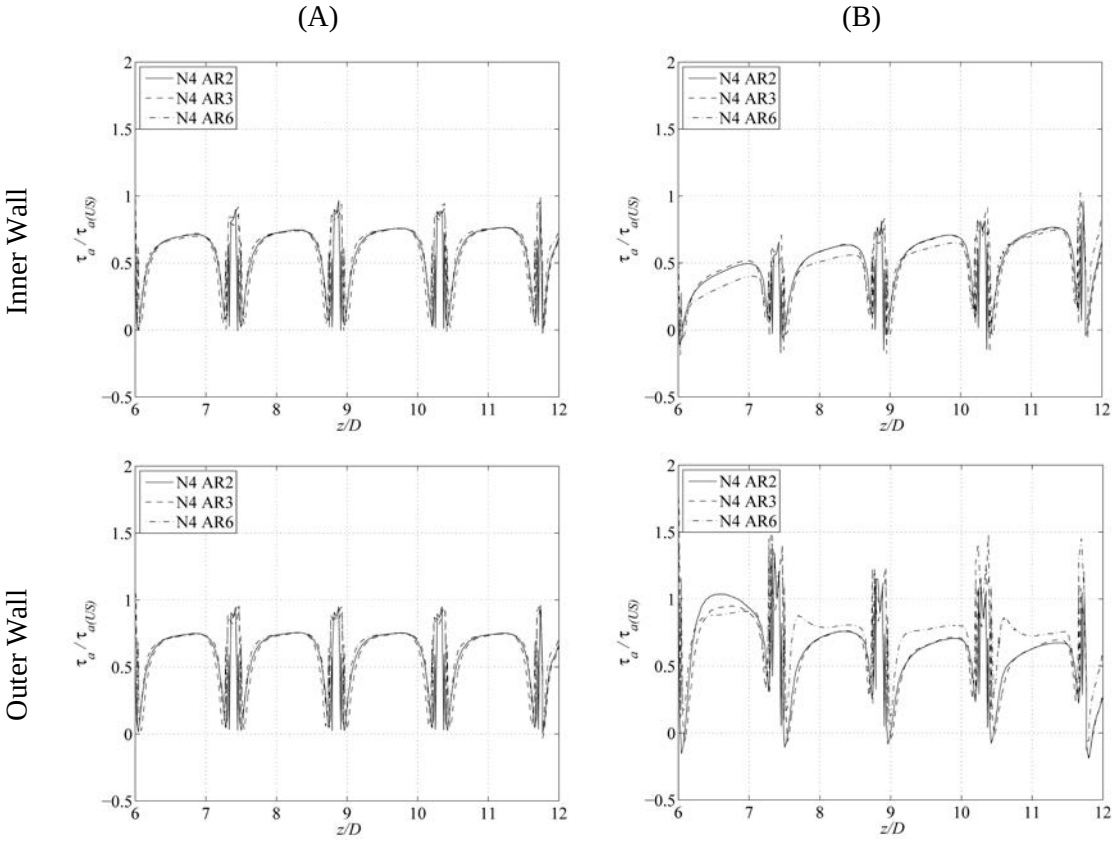


**Figure 3.24 Comparison of the axial WSS distribution for the investigated aspect ratios along the inner (row 1) and outer (row 2) walls at the intersection with the $z$ = 0 plane for $K$ = 70 (A) and $K$ = 1450 (B). The axial WSS is normalized by the homeostatic representative upstream axial WSS in the unstented region.**

Explaining the higher WSS observed for AR6 at $K$ = 1450 requires closer evaluation of the near-strut flow physics. Figure 3.25 presents a contour plot of the $v$-component of velocity around the first 4 struts at the outer wall for the N4_AR3 and N4_AR6 stent designs. Recall that these two geometries have the same strut width, but the strut heights differ by a factor of 2. For the thicker stent strut design (N2_AR3), the fluid makes a large diversion from the axial direction in order to travel around the strut protrusion, which reduces the axial velocity component. This is leads to a subsequent increase in the $v$-component of velocity on the leeward and windward side of the struts as demonstrated in the contour plots in Figure 3.25 (A). The diversion of the fluid

velocity from the axial direction reduces the contribution to the axial WSS component and explains the reduction in $\tau_a$ on the leeward side of the struts for AR3. For thinner struts (N4_AR6), the *v*-component of velocity around the struts is reduced (see Figure 3.25 (B)) compared to the AR2 and AR3 cases. By largely maintaining fluid motion in the axial direction, there is a greater contribution to the axial WSS as the fluid returns to the wall after traveling around the strut protrusion. This results in a region of greater axial WSS leeward to the struts where fluid initially returns to the vessel wall. This conclusion corroborates the work by Jimenez *et al.* in which the windward side influence of the strut increases as the height increases[116]. The exact reason for the periodicity is unclear, but appears to correlate with the WSS on the top of the struts.

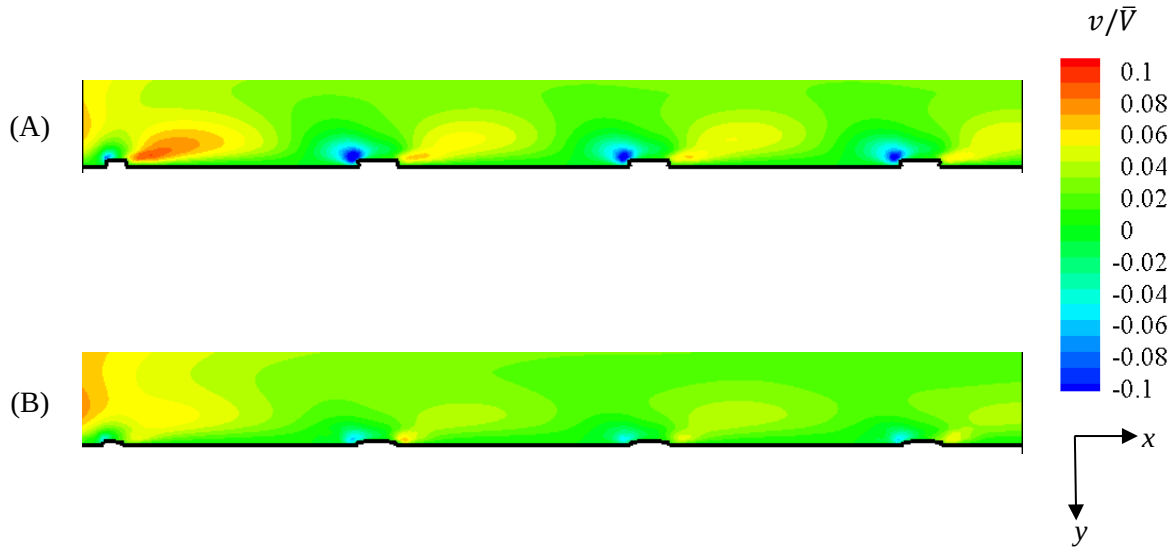


**Figure 3.25 Contour plot of the *v*-component of velocity for the stent geometry N4_AR3 and N4_AR6 in the $z$ = 0 plane in the vicinity of the outer wall around the first 4 struts intersection. Fluid motion is from left to right.**

The disturbance of the secondary flow induced by the investigated strut shapes is explored by examining the vortex structure and vorticity distribution within cross-sections of the stented region. Figure 3.26 presents the streamlines and vorticity distribution within the middle stent cell of the stented region for $K$ = 1450. As the aspect ratio increases, the disruption of the secondary flow structure is mitigated and the separation regions distal to the struts are reduced. Specifically, in the intersection, IS1 (Figure 3.26 Row 1), the recirculation region on the windward side of the strut centered at $\varphi = \pi/4$ near the outer wall for AR2 does not exist in the same cross-section for

the AR6 geometry. In addition, the size of negative vorticity regions on the leeward side of the struts in this plane diminish in size as AR increases. These regions, which are unshaded in the figure, are a "footprint" of the recirculation region, as discussed previously. Further, the continuous region of positive vorticity (represented by the shaded areas) along the wall for the AR6 geometry suggest that boundary layer separation is reduced as the AR is increased.

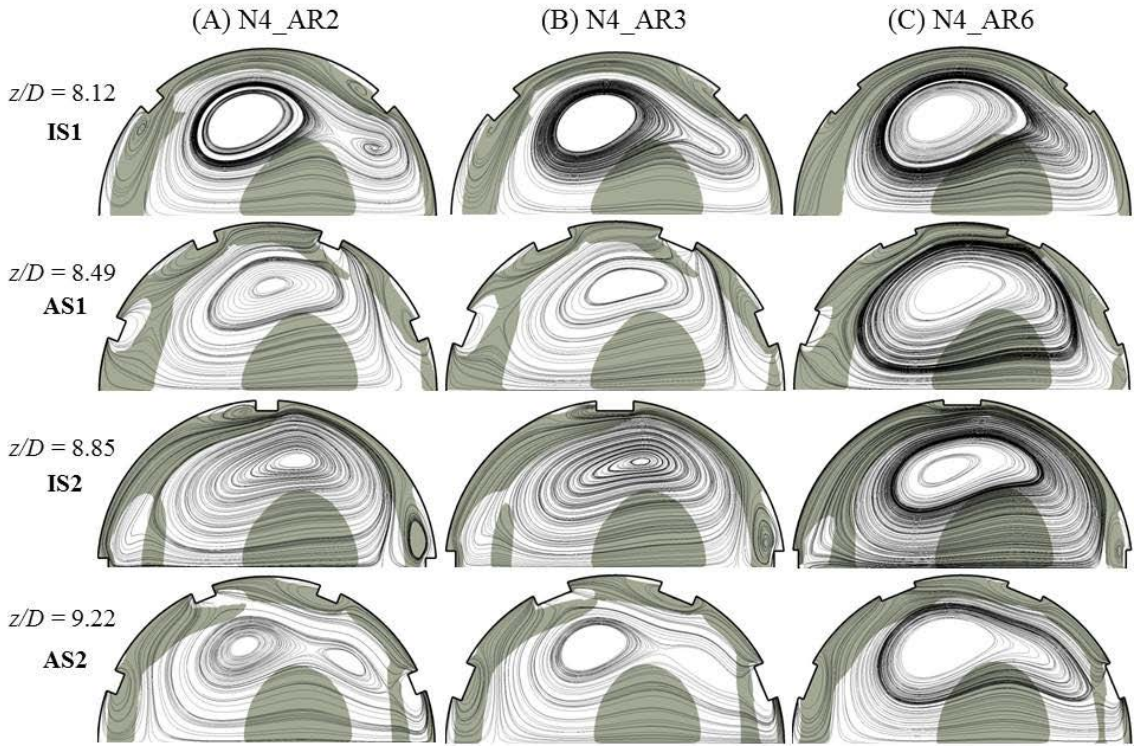


**Figure 3.26 Secondary flow pattern (streamlines) and vorticity distribution (contour) for $K$ = 1450 at selected planes within the stented region for the investigated aspect ratios. Shaded regions indicate positive vorticity, while unshaded regions show negative vorticity.**

A similar vortical behavior is observed in the intersection plane IS2 as the aspect ratio increases; however, the streamwise vortical structure in the vicinity of the strut centered at $\varphi = 0$ remains in the plane for all investigated strut shapes. This suggest that the presence of this recirculation region is strongly associated with the presence of the strut at $\varphi = 0$, where flow stagnates as it approaches the outer wall and proceeds to return to the inner wall. In the planes AS1 and AS2, the looping streamlines surrounding the struts, due to the axial motion of the flow entering/leaving the intrastrut areas (see Figure 3.10) no longer protrude as far into the interior of

the cross-section at higher AR values. As well, the size of the negative vorticity regions generated by the axial fluid motion around the angled struts are eliminated or greatly reduced as the aspect ratio is increased.

In addition to the near wall behavior, alterations in the strut shape shifts the location of the central Dean vortex within the cross-section. Generally, the vortex center shifts toward the inner wall as the aspect ratio is increased. This positional change in the vortex center is characteristic of behavior observed as the Dean number increases. However, the shift in the vortex position is likely due to vortex dynamics induced by the strut presence, given the less than 1% change in the cross-sectional area between the different aspect ratios. Furthermore, the Dean vortex shape is greatly affected by the strut shape. This is particularly highlighted in the AS2 plane, in which the cross-section no longer has two regions of centralized vorticity within the cross-section at higher aspect ratios. Overall, the flow patterns in the cross-section shown in Figure 3.26 demonstrate that the secondary flow patterns and recirculation regions, along with the vorticity distribution, are greatly affected by the strut shape. This is further highlighted by reviewing the strength of the secondary flow within the plane presented in Figure 3.26. A comparison the secondary flow strength within the stented plane for the different aspect ratios is presented in Table 3.14 for $K$ = 70 and Table 3.15 for $K$ = 1450. The circulation strength in the table shows that the change in the aspect ratio from 2 to 3 results in a marginal increase in the strength. On the contrary, an increase in the aspect ratio from 3 to 6 results in a reduction in the strength of the secondary flow of nearly 18% for $K$ = 70 and almost 9% for $K$ = 1450 for the IS1 plane. This reduction in the intensity of the secondary flow is associated with the dissipation of the recirculation region toward the outer wall and the increase in the vortex size within the cross-section. This highlights the strong impact of the secondary flow strength on the protrusion height.

**Table 3.14 Normalized circulation of the Dean vortices at selected planes in the stented region shown for $K$ = 70 in Figure 3.15.**

| | | $\lvert\Gamma/\nu\rvert$ | | | Percent Difference | Percent Difference |
|---|---|---|---|---|---|---|
| *z/D* | Strut Configuration | N4_AR2 | N4_AR3 | N4_AR6 | AR3 vs. AR2 [%] | AR6 vs. AR3 [%] |
| 3 | US | 33.49 | 33.49 | 33.49 | 0.00 | 0.00 |
| 8.12 | IS1 | 37.00 | 36.73 | 31.15 | -0.74 | -17.92 |
| 8.49 | AS1 | 29.95 | 30.24 | 29.13 | 0.95 | -3.81 |
| 8.85 | IS2 | 30.67 | 30.90 | 28.41 | 0.74 | -8.76 |
| 9.22 | AS2 | 27.42 | 27.94 | 26.90 | 1.86 | -3.89 |

**Table 3.15 Normalized circulation of the Dean vortices at selected planes in the stented region shown for $K$ = 1450 in Figure 3.15.**

| | | $\lvert\Gamma/\nu\rvert$ | | | Percent Difference | Percent Difference |
|---|---|---|---|---|---|---|
| *z/D* | Strut Configuration | N4_AR2 | N4_AR3 | N4_AR6 | AR3 vs. AR2 [%] | AR6 vs. AR3 [%] |
| 3 | US | 81.80 | 81.80 | 81.81 | 0.00 | 0.02 |
| 8.12 | IS1 | 98.23 | 97.16 | 88.93 | -1.11 | -9.24 |
| 8.49 | AS1 | 89.64 | 91.10 | 85.69 | 1.61 | -6.31 |
| 8.85 | IS2 | 86.28 | 86.38 | 79.94 | 0.12 | -8.05 |
| 9.22 | AS2 | 80.45 | 82.62 | 77.30 | 2.63 | -6.88 |

### 3.3.3 *Non-Newtonian Versus Newtonian Fluid Models*

As previously stated, blood behaves as a Newtonian fluid at shear rates greater than ~100 $s^{-1}$. In large arteries, the shear rates are typically above this threshold for most of the vessel cross-section, and therefore, most simulations assume blood to be Newtonian in these vessels. However, the presence of the stent struts along the arterial walls can generate flow separation and

recirculation zones that are often characterized by low shear rates given their low flow conditions[96]. Therefore, in this section we compare the flow environment for simulations performed using the Newtonian fluid model and the non-Newtonian Carreau-Yasuda model. We highlight regions of low shear rates which may affect the categorization of WSS behavior and judge the significance of the non-Newtonian model on the quantification of luminal areas at risk for NIH development. Ultimately, the results can be used to ascertain whether the use of Newtonian blood models is appropriate over the range of shear rates present in the stented vessel and for the evaluation of stent geometry related to hemodynamically induced restenosis.

A representation of the shear rate distribution within the stented vessel is presented in Figure 3.27, for geometry N4_AR2 and $K = 70$, within the $z = 0$ plane. Herein, the general trends in the shear rate distribution discussed are consistent for all investigated geometries for $K = 70$. At higher Dean numbers, the shear rate magnitude values are larger, and virtually no regions of shear rate less than 100 $s^{-1}$ are present. Note that the contour levels in the figure are very course to more easily identify regions below the threshold value. Throughout the vessel, a higher shear rate is observed along the outer wall compared to the inner wall given the shift of the peak axial velocity toward the outer wall. Moreover, the shear rate is observed to decrease toward the interior of the vessel and values below the 100 $s^{-1}$ threshold are observed within the central region. The shear rate along the walls decreases as the flow enters the expansion region of the vessel and proceeds into the stented region. Within the stented region, the shear rate is reduced proximal and distal to the strut protrusions, where flow recirculation regions exist. Furthermore, the shear rate is observed to be less than 100 $s^{-1}$ at the windward and leeward corners of the struts (see Figure 3.27 inset). The shear rate distribution within the IS2 cross-sectional plane at $z/D = 8.85$ is presented in Figure 3.28, further exemplifying these observations. The contour plot of the shear rate in the IS2 cross-section shows the region of low shear rate exist circumferentially, as well as axially, around the strut protrusions. As well, the shear rate decreases radially toward the center of the vessel as expected. Generally, shear rate is observed to be higher at the top of the strut protrusions as the flow passes over the obstacle. In the distal portion of the vessel, the shear rate increases along the outer and inner walls as the flow is accelerated through the exit taper region (see Figure 3.27). Further downstream, the shear rate along the walls decreases as the flow proceeds to the exit of the vessel.

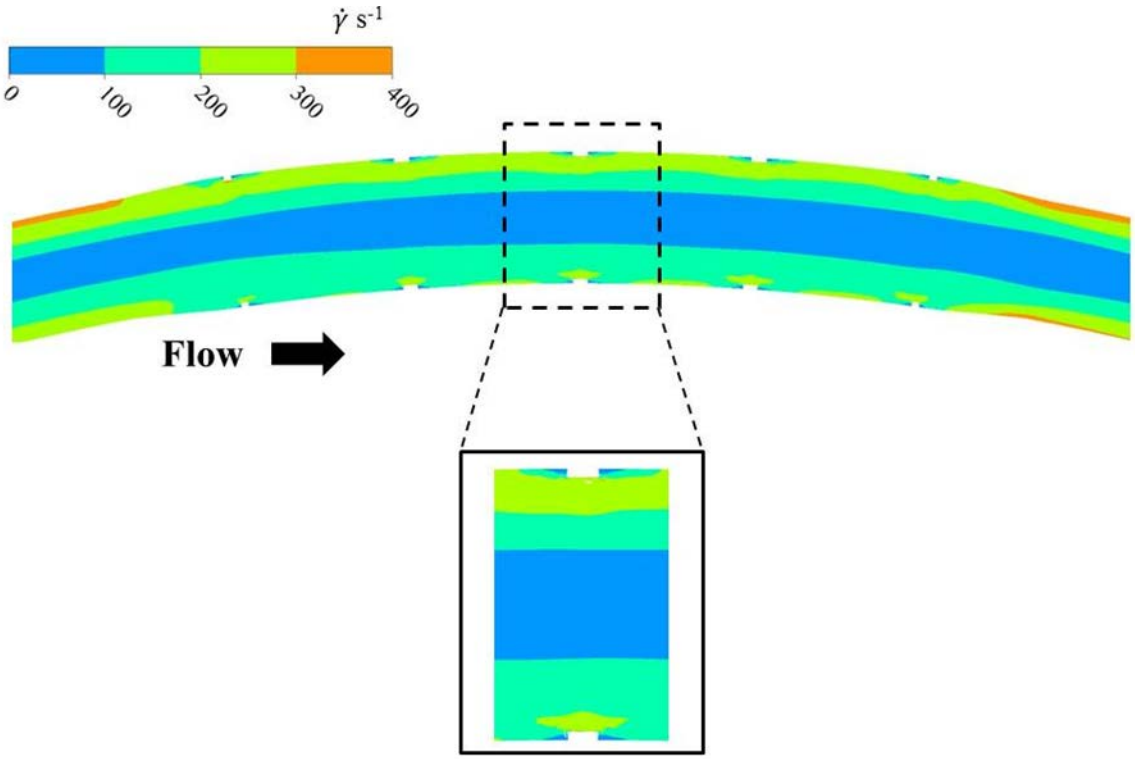


**Figure 3.27 Contour plot of shear rate distribution within the $z$ = 0 plane for the geometry N4_AR2 for $K$ = 70.**

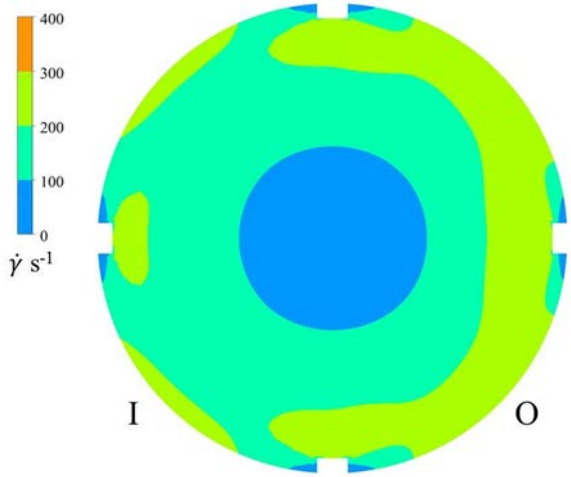


**Figure 3.28 Contour plot of the shear rate within the cross-section located at the intersection plane IS2 ($z/D$ = 8.85) for N4_AR 2 and $K$ = 70. I and O indicate the inner and outer walls, respectively.**

To demonstrate the impact of the constitutive blood models on the velocity behavior, Figure 3.29 shows plots of the axial and cross-stream velocity profile for each of the fluid models within the IS2 plane located at $z/D$ = 8.85 for $K$ = 70. Figure 3.29(A) and Figure 3.29(B) present contour plots of the $v$ and $u$ components (cross-stream and axial components) of velocity for the Newtonian (represented by the black contour lines) and the non-Newtonian models (represented by the red contour lines), respectively. We observe that the difference in the velocity profiles between the constitutive models is largely localized in the central region of the vessel and appears to have a greater impact on the $v$ component of the velocity. Closer examination of the velocity behavior for the different models is facilitated by extracting the velocity profile along the $y$-axis from the inner wall to the outer wall, as shown in Figure 3.29(C) and (D). The velocity components are normalized by the average inlet velocity for $K$ = 70. The shear thinning effect of the non-Newtonian model reduces the peak axial velocity in the central region of the vessel, where the shear rate is the lowest. A slight increase in the axial velocity is observed near the walls ($-1 < \frac{y}{a} < -0.5$ and $0.5 < \frac{y}{a} < 1$) where the shear rate is high. The non-Newtonian model is observed to induce a flattening of the $v$ component velocity profile. Specifically, a reduction in the $v$ component is also observed in the central region of the cross-section along with a slight shift in the peak value toward the outer wall. Virtually no change in the velocity profile is observed closer to the wall. This finding is consistent with observations of the fluid behavior in curved vessel derived from simulations comparing Newtonian and non-Newtonian models[117,118]. It should be noted that a reduction in the magnitude of the $v$ component of velocity for the non-Newtonian model was also observed in the central region of the vessel for higher Dean number values, though no appreciable change in the axial velocity was detected (data not shown).

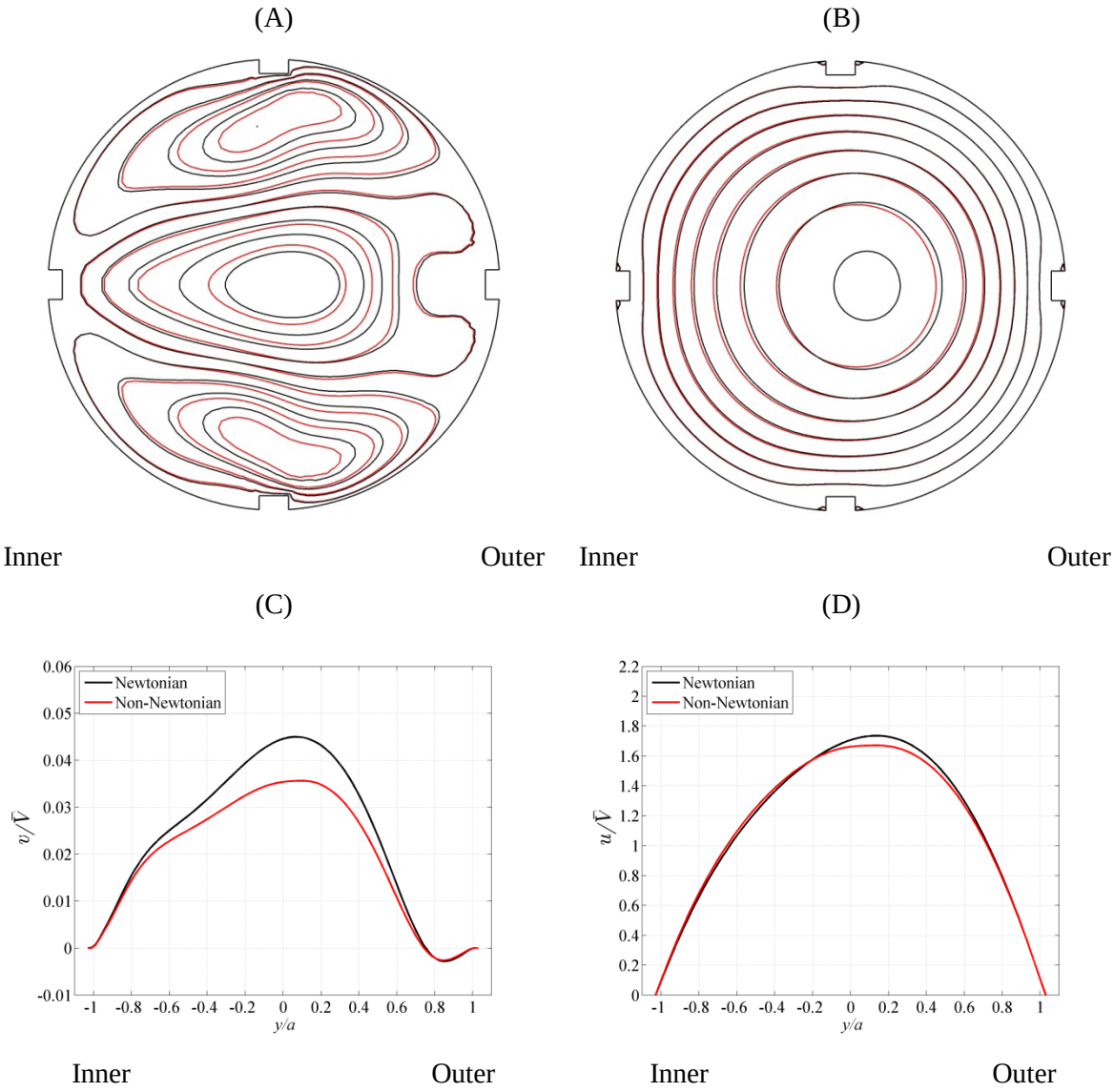


**Figure 3.29 Comparison of the cross-stream ((A) and (C)) and stream-wise ((B) and (D)) velocity between the constitutive models for blood at the IS2 plane located at *z/D* = 8.85 for *K* = 70 and geometry N4_AR2. The red lines represent the non-Newtonian velocity behavior and the black lines represent the Newtonian velocity behavior.**

Despite the differences in the magnitude of the velocity components for the fluid models, the secondary flow structure in both cases is qualitatively similar. The secondary flow structure for both fluid models is characterized by vortices transverse to the primary flow and the direction of the rotation of these vortices is the same regardless of the implemented fluid model. The strength of the secondary flow is reduced when non-Newtonian behavior is considered. The circulation is

calculated for the geometry N4_AR2 for $K$ = 70 and 1450 is presented in Table 3.16. For $K$ = 70, the circulation strength decreases for the non-Newtonian fluid model. Interestingly, a reduction in the circulation strength is also observed to a lesser extent at higher Dean numbers. The minor difference in the circulation strength for the Newtonian and Non-Newtonian models at the higher Dean numbers can be attributed to the presence of shear rates above $100s^{-1}$ at the high inlet velocity.

**Table 3.16 Normalized Circulation for Dean numbers investigated at selected planes in the stented region shown for $K$ = 70 and K = 1450 for N4_AR2 in Figure 3.15**

| | | $\lvert\Gamma/\nu\rvert$ | | | $\lvert\Gamma/\nu\rvert$ | | |
|---|---|---|---|---|---|---|---|
| | | $K$ = 70 | | | $K$ = 1450 | | |
| *z/D* | Strut Conf. | Newtonian | Non-Newtonian | Percent Difference [%] | Newtonian | Non-Newtonian | Percent Difference [%] |
| 3 | US | 33.49 | 27.57 | -17.69 | 81.80 | 82.93 | 1.39 |
| 8.12 | IS1 | 37.00 | 28.81 | -22.13 | 98.23 | 97.96 | -0.27 |
| 8.49 | AS1 | 29.95 | 21.46 | -28.34 | 89.64 | 88.90 | -0.82 |
| 8.85 | IS2 | 30.67 | 22.84 | -25.55 | 86.28 | 85.82 | -0.53 |
| 9.22 | AS2 | 27.42 | 19.12 | -30.27 | 80.45 | 80.13 | -0.39 |

Lastly, the shear rate distribution in Figure 3.27 and Figure 3.28 clearly indicates regions of the low shear rate where the Newtonian model may fall short in characterizing flow behavior, particularly when complex vessel geometries are considered; such as stented vessels. Furthermore, the utilization of a Newtonian model to study hemodynamic behavior can lead to a false interpretation of the luminal walls susceptible to NIH due to WSS exposure. This is demonstrated by a visual representation of the low WSS regions for the Newtonian and non-Newtonian models for the N4_AR2 geometry. The contour plots in Figure 3.30 highlight regions of low WSSM around the stent struts and indicate the reduction in the size of these regions when a non-Newtonian model is employed. The most prominent reduction occurs in the area around the angled struts between the strut intersections. It was noted previously that areas of low WSS are co-located with recirculation regions that are induced by the stent presence. The reduction in the area of the

luminal wall exposed to low WSS suggests that the recirculation regions have reduced in size. This conclusion corroborates previous work with a simplified stent model, which reported a reduction in the size of separation zones on the leeward side of the struts[117]. The source of the reduction can be extrapolated from the low shear rate distribution around the stent struts. The regions surrounding the strut protrusions would have increased apparent viscosity for the non-Newtonian model and subsequently higher WSSM. A quantitative summary of the changes in the WSS distribution for the Newtonian and non-Newtonian models is presented in Table 3.17 for all the investigated geometries. The decrease in the area exposed to low WSSM ranges between 1% to 3% for the non-Newtonian model for all geometries. In addition, there is a greater reduction in the area exposed to moderate WSSM for the non-Newtonian models, with the greatest reduction of approximately 14% for the N4_AR6 geometry. The calculation of the total luminal exposure to WSSM in the low to moderate range reveals that the Newtonian model overestimates the size of the region exposed to WSSM within the critical range. From Figure 3.30, we note that the Newtonian model provides a more conservative estimate of the area exposed to NIH-inducing shear stress values, with particularly large variances occurring in the moderate WSSM range. As such, a Newtonian model may be appropriate from a design perspective, as actual stent behavior should exceed predictions based upon this blood representation.

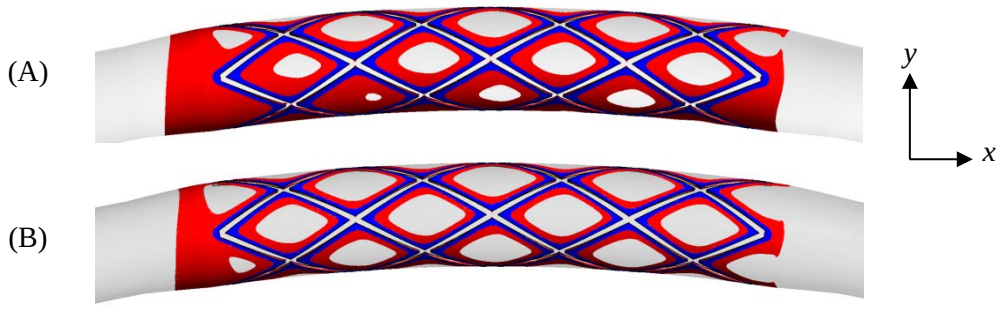


**Figure 3.30 Low WSS (blue) and moderate WSS (red) distribution for Newtonian (A) and non-Newtonian (B) models for $K$ = 70 and N4_AR2.**

**Table 3.17 Percentage of stented region exposed to low and moderate WSSM.**

| Geometry | Low WSSM $\lvert\tau\rvert < 0.5$ [N/m$^2$] [%] | | Moderate WSSM $0.5 < \lvert\tau\rvert < 0.8$ [N/m$^2$] [%] | | Total Luminal Exposure to Low and Moderate WSSM [%] | |
|---|---|---|---|---|---|---|
| | Newtonian | Non-Newtonian | Newtonian | Non-Newtonian | Newtonian | Non-Newtonian |
| NS8_AR2 | 37.88 | 34.79 | 34.23 | 34.88 | 72.11 | 69.67 |
| NS4_AR2 | 21.83 | 20.55 | 41.30 | 28.28 | 63.13 | 48.83 |
| NS4_AR3 | 20.09 | 19.04 | 38.36 | 26.31 | 58.45 | 45.35 |
| NS4_AR6 | 13.88 | 11.53 | 37.23 | 23.08 | 51.11 | 34.61 |

## 3.4 Summary of Results

The aim of this study is two-fold: firstly, to evaluate the performance of four different stent designs that conform to the curvature of a coronary artery from a fluid dynamics point of view, and quantify the differences between the stent models; secondly, to determine the effects of the chosen constitutive model on the evaluation of the fluid environment in the stent vicinity. A parametric analysis was conducted to systematically assess the effects of varying the stent geometry on the flow behavior in the vicinity of the stent. However, the study was not designed to investigate a full parametric evaluation of strut characteristics such as thickness, width, and frequency. Instead, the geometric parameters were limited to a range previously investigated in straight stented vessels in order to (i) identify geometric characteristics that influence fluid dynamics in a curved stented vessel, (ii) draw attention to the impact of vessel curvature on flow behavior in the vicinity of the stent, and (iii) compare flow behavior in a curved stented vessel to that in a straight stented vessel. The results presented in this study have clinical importance for identifying regions within the stented vessel susceptible to abnormal vascular healing post implantation, such as excessive NIH leading to ISR. As a result of recent advancements in bio-compatible materials, stents exhibit better conformability to curved vasculature. This innovation

warrants the assessment of the currently available stents in a curved vessel model. This study provides valuable information to guide the development of these modern medical devices.

Given the curvature of new commercial stents, studies investigating straight stented vessels neglect the contribution of the secondary flow and axial flow skewing on the evaluation of the stent design. The conformation of stents to vessel curvature aims to maintain the characteristic skewing of the axial velocity profile and secondary flow structure present in the healthy native vessel. Generally, the presence of the strut protrusions resulted in changes in the morphology and strength of the native secondary flow structure along the length of the stent. The impact of the strut protrusions was localized in the near wall in particular cross-sections and completely distorted the Dean vortex shape in other cross-sections. As expected, thicker struts were large enough in comparison with the Stokes layer to perturb it and considerably alter secondary flow formation. The disturbance of the secondary flow was minimized in the stent designs with thinner and wider struts. The secondary flow dictated by the stent design impacts the transport of NIH stimuli to the vessel wall and subsequent areas of platelet deposition. Moreover, the secondary flow patterns within the cross-section can provide insight into the uniformity of the distribution of anti-restenotic agents from drug eluting stents.

The regions prone to excessive NIH development, due to critical WSS exposure, was hypothesized to differ in curved vessels from those identified in the straight vessel. Interestingly, the pattern of WSS distribution in the immediate vicinity of the stent struts was found to be consistent across all stent models and similar to previously reported behavior in straight stented vessel. The results confirmed that fewer and thinner struts reduced the area of the luminal wall exposed to low WSSM in the curved stented vessel geometry, which corroborates the behavior observed in straight stented vessels. The magnitude of WSS along the outer and inner wall, however, is influenced by the curvature of the vessel. The disparity of the WSSM distribution between the walls results in higher initiation of ISR at the inner wall compared to the outer wall. The imbalance in WSS between the walls suggests the implementation of different design criteria along each wall.

Lastly, the significance of non-Newtonian fluid effects on *in vivo* hemodynamics has been debated for years. Several numerical studies have indicated that the influence of the thixotropic properties of blood is significant. On the other hand, many other studies have determined that assuming blood can be modeled a Newtonian is sufficient for the evaluation of vascular flow. In

this study, the impact of using a Newtonian or non-Newtonian blood model on the evaluation of stent performance was explored. Many non-Newtonian models of blood rheology exist and the validation of any particular model was not conducted in this study. The non-Newtonian model chosen is commonly used in other investigations of non-Newtonian blood flow and thus provided references for comparison to previous work. The results of this study identify the areas in a curved stented vessel where the non-Newtonian properties of blood would alter the evaluation of local hemodynamics in a curved stented vessel. The Newtonian fluid model was found to overestimate areas susceptible to uncontrolled NIH development. Thus, using a Newtonian model to determine the stent design characteristics important for the optimal hemodynamic performance of the curved stent design will lead to a conservative stent design that will ensure minimal excessive NIH development. As such, we conclude that the use of the Newtonian fluid model does not have a negative impact on the flow characteristics important in stent design.

# Chapter 4

# Study C: Unsteady Flow in Curved Pipe with Realistic Stent Model

## 4.1 Problem Statement

In this study, we consider the problem of unsteady flow through a curved tube with wall protrusions in a configuration based on strut orientations in a realistic stent design. The aim of the present computational study is to garner a fundamental understanding of flow disruption induced by the presence of a stent within a curved arterial vessel segment under physiological flow conditions. We extend the work presented in Chapter 4 to examine a more realistic flow condition representative of the *in vivo* environment. The geometric components of the numerical model, the stent designs, and coordinate systems utilized for the present simulations are the same as in Chapter 4 (See Figure 4.1 and Figure 4.2). The dimensions of the majority of the geometric components are unchanged with the exception of the entrance vessel, which now has an extended length of 50*D*. The inlet velocity is a temporally varying uniform profile and the additional entrance vessel length ensures fully developed flow at the entrance to the stented region. Similar geometries are utilized in the investigation of fluid behavior in the vicinity of struts in an unsteady flow regime[93,117,119]. However, this study is distinguished from previous studies of unsteady stented flow by the inclusion of the vessel curvature in conjunction with the strut protrusions.

Previous studies of unsteady flow in curved vessels use oscillatory input waveforms or intermittent waveforms to mimic *in vivo* flow conditions. Intermittent waveforms usually consist of a pulse-like systolic flow followed by a zero flow rate diastolic period[120]. Oscillatory waveforms can be sinusoidal (i.e. zero mean or non-zero mean[61,121,122]) or non-sinusoidal[61,71,122,123]. Non-sinusoidal waveforms are typically physiologically-inspired waveforms acquired from noninvasive blood flow measurements such as magnetic resonance imaging (MRI)[124] or ultrasound[125]. These physiological waveforms typically have phases of accelerating and decelerating flow, as well as forward and retrograde flow. Differences have been noted in the strength and position of the secondary flow vortices in smooth walled vessels between the acceleration and deceleration phases of a time-varying flow waveform[71]. In straight stented vessels, the near wall conditions, such as the stability of recirculation zones and subsequent WSS distribution, have been shown to vary between periods of acceleration and deceleration [126].

The unsteady flow physics in curved pipes is characterized by two non-dimensional parameters, the Dean number and the Womersley number. The definition of the Dean number used in the present study and its relation to other Dean number definitions is addressed in Chapter 2. The Womersley number is defined as $\alpha = a\sqrt{\frac{\omega}{\upsilon}}$, where $a$ is the tube radius, $\omega$ is the circular frequency of the waveform, and $v$ is the kinematic viscosity. It can also be written in terms of the dimensionless Reynolds number (Re) and Strouhal number (St), $\alpha = (\mathrm{Re\,St})^{\frac{1}{2}}$ [127]. Although the Womersley number is a compound parameter related to the more traditional Reynolds and Strouhal numbers, the majority of biological fluid dynamics studies use the Womersley number, and as such will be employed here. The parameter is derived from the work of Womersley, who produced a solution of the unsteady Navier-Stokes equations for a harmonic pressure gradient in a smooth-walled, rigid, circular cylinder with no vessel curvature[128]. The work aimed to understand the unsteady flow behavior within the vasculature due to the rhythmic nature of the pressure applied by the beating heart. The Womersley number characterizes the unsteady flow conditions and determines the phase relationship between the driving pressure gradient and velocity waveform[128]. The Womersley number can be viewed as a ratio of unsteady inertial forces due to local acceleration to viscous forces and characterizes the effect of the oscillatory frequency of the driving forces[129]. At low Womersley values ($\alpha < 10$) the viscous forces dominate unsteady inertial forces and the flow is in phase with the oscillating driving pressure gradient[19]. At higher Womersley values, the unsteady inertial forces dominate and the velocity waveform is phase-shifted in time relative to the oscillating pressure gradient. In this case, the viscous forces do not retard the inertial forces, resulting in the fluid maintaining its current direction despite a change in the driving pressure force. Recent publications have focused on the fact that a global Womersley value can be assigned to flow waveforms based on the period of the physiological inflow waveform[129]. However, given the multi-harmonic nature of physiological waveforms, the single Womersley number is not sufficient to predict the flow behavior over the entire pulse cycle.

### 4.1.1 *Physiological Waveforms*

Two physiological unsteady flow conditions are modeled in this study and are used to emulate flow in two commonly stented vessels. The first waveform is based on the blood flow in a healthy right coronary artery (RCA). The second waveform is based on blood flow in the left and right carotid artery. The same geometry is used to investigate the stent induced flow behavior in

the presence of coronary and carotid artery flow conditions. While the geometry was originally designed based upon the RCA, it is suitable for the examination of a stented carotid artery blood flow given the fact that the curvature ratio of the left and right carotid arteries is within the range of $\delta$ = 0.018-0.069[130]. Each waveform profile shape exhibits common characteristics, which are also similar to other vessels within the vascular system [19,90,131]. Specifically, the waveforms have multiple peaks with a dominant primary peak. Despite similarities in the waveform profile, distinct differences between a typical carotid artery waveform and coronary artery waveform exist, particularly in their operational Dean number ranges. Modeling both arterial flows allows for exploration of a broader range of parameter values, adding insight into the flow physics in relation to the governing non-dimensional parameters for unsteady flows in curved tubes with stents.

#### *4.1.1.1 Coronary Artery Waveform*

The coronary waveform used in the present numerical simulations is based upon Doppler flowmeter and ECG measurements by Matsuo *et al.* of blood flow in the RCA of a healthy 56 year old female[132]. The adopted coronary velocity waveform is from the work of Johnston *et al*[100].The measured *in vivo* waveform possesses a Womersley value of $\alpha$ = 2.76 based on the time period, $T$ ~ 1s, maximum Reynolds number $Re_{max}$ = 260, and a measured mean vessel diameter of 4.0mm. The coronary artery waveform is scaled to create the inflow waveform for the stented vessel geometry, accounting for the numerical model diameter, to maintain the same Womersley and Reynolds number values. The period of the scaled waveform is $T$ = 0.44s, corresponding to a heart rate of approximately 136 beats per minute. Figure 4.1 presents the scaled volumetric flow rate inflow waveform with the corresponding Reynolds number values included on the right ordinate. The systolic and diastolic phases are labelled accordingly in the figure. The waveform is characterized by small forward flow during systole and large forward flow during diastole. Unlike most of the systemic arterial circulation, blood flow in the coronary arteries peaks during diastole rather than systole[133]. During systole, the myocardial contraction compresses the vessels and restricts flow; however, relaxation of the myocardium during diastole allows forward flow. It is worth highlighting that the implemented waveform includes periods of retrograde flow during late diastole/early systole. The Dean number values at each phase of the waveform are shown in Figure 4.2, which indicates the values range from $K$ = 0 to 271. A time varying uniform velocity profile is imposed at the inlet of the vessel based on the scaled average velocity shown in Figure

4.3 (solid line). The corresponding acceleration waveform is included in Figure 4.3 (dashed line) and indicates periods of rapid acceleration and deceleration. The scaling of the inlet waveform yields a maximum and mean inflow velocity of 0.33 m/s and 0.13 m/s, respectively. It should be noted that mean inflow velocity is very similar to the mean uniform inlet velocity, $\bar{V} = 0.11\mathrm{m/s}$, used in the steady state simulations of $K$ = 70 in Chapter 4.

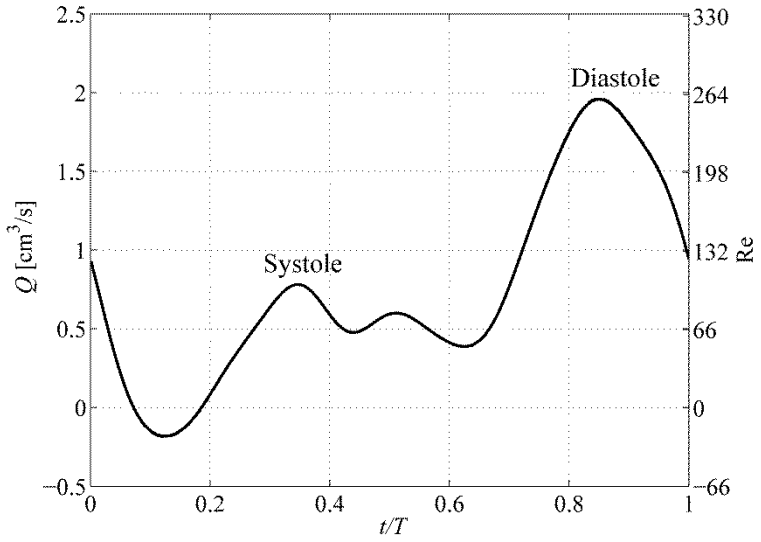


**Figure 4.1 Volumetric flow rate input waveform based on the blood flow in the coronary artery; scaled based on the geometric model and working fluid properties.**

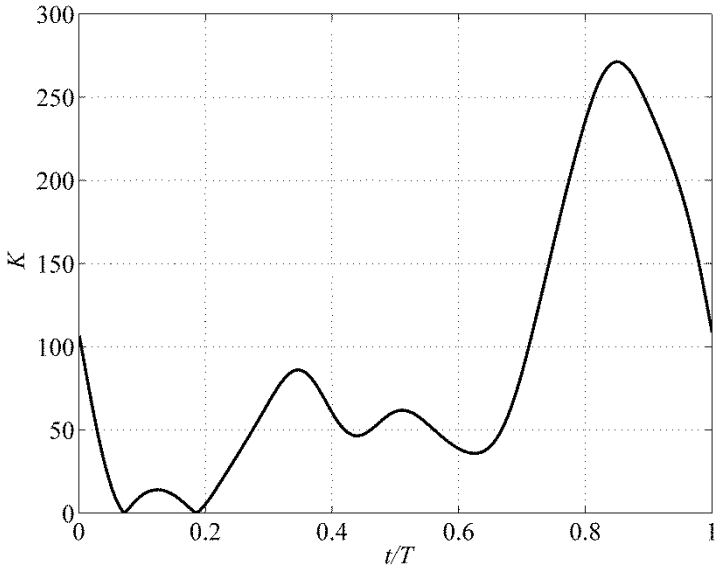


**Figure 4.2 Dean number values at each phase of the coronary artery waveform.**

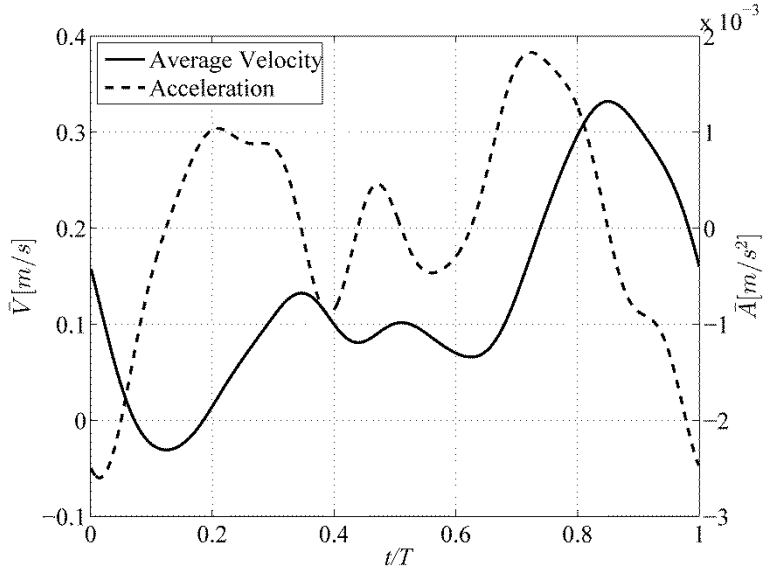


**Figure 4.3 Average velocity (solid line) at each phase of the unsteady inlet waveform along with the corresponding acceleration waveform (dashed line) of the coronary artery.**

*4.1.1.2 Carotid Artery Waveform*

The carotid artery waveform used in the present numerical simulations is based on ultrasound and ECG measurements by Holdsworth *et al.* of blood flow within the left and right carotid arteries [124,125]. The measured *in vivo* waveform has a global Womersley value of $\alpha$ = 4.6 based on the time period, $T$ ~ 1s, mean Re = 364, maximum Re = 1424 and a measured mean diameter of 6.4mm[134]. The carotid artery waveform is scaled accounting for the model geometry to maintain the same Womersely number and Re values. Figure 4.4 presents the scaled volumetric flow rate inflow waveform with the corresponding Reynolds number values included on the right ordinate. Based on the physiological Womersley number of 4.6, the period of the scaled waveform is $T$ = 0.16s. The waveform is characterized by increased volumetric flow rate during the systolic phases when blood is ejected from the heart. The dicrotic notch, which reflects the cessation of systole, occurs at the minimum volumetric flow. The diastolic phase occurs after the dicrotic notch until the end of the waveform period. The waveform has three distinctive peaks that will hereinafter be referred to as the primary, secondary, and tertiary peaks (labelled accordingly in Figure 4.7). Unlike the coronary artery waveform, the implemented carotid artery waveform does not include periods of reverse flow. The Dean number values at each phase of the waveform is shown in Figure 4.5, which indicates the values range from $K$ = 14 to 2244. This peak value is considerably higher than that of the coronary artery. A time varying uniform velocity profile is imposed at the inlet of the vessel based on the scaled average velocity shown in Figure 4.6 (solid line). The scaling of the inlet waveform yields a maximum and mean inflow velocity of 1.79 m/s and 0.46 m/s, respectively. It should be noted that mean inflow velocity is very similar to the mean uniform inlet velocity, $\bar{V} = 0.49 m/s$, used in the steady state simulations of $K$ = 60 in Chapter 4. The corresponding acceleration waveform is included in Figure 4.6 (dashed line) and indicates periods of rapid acceleration and deceleration.

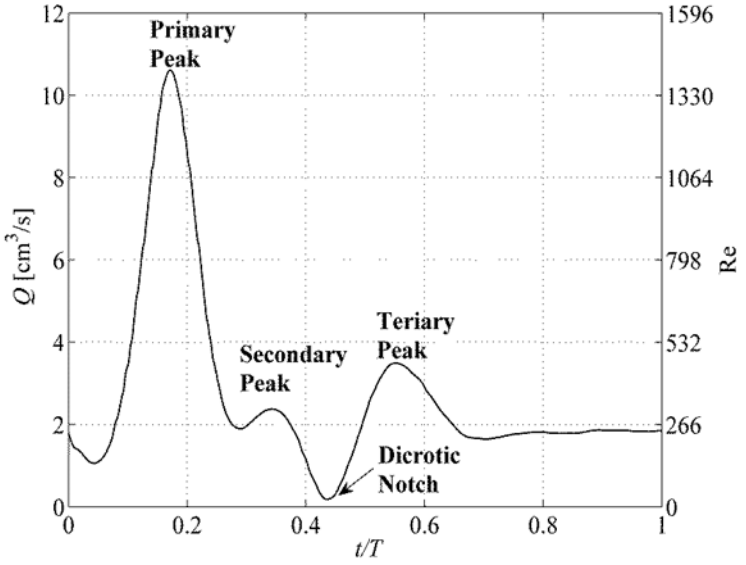


**Figure 4.4 Volumetric flow rate input waveform based on the blood flow in the carotid artery and scaled based on the geometric model and working fluid properties**

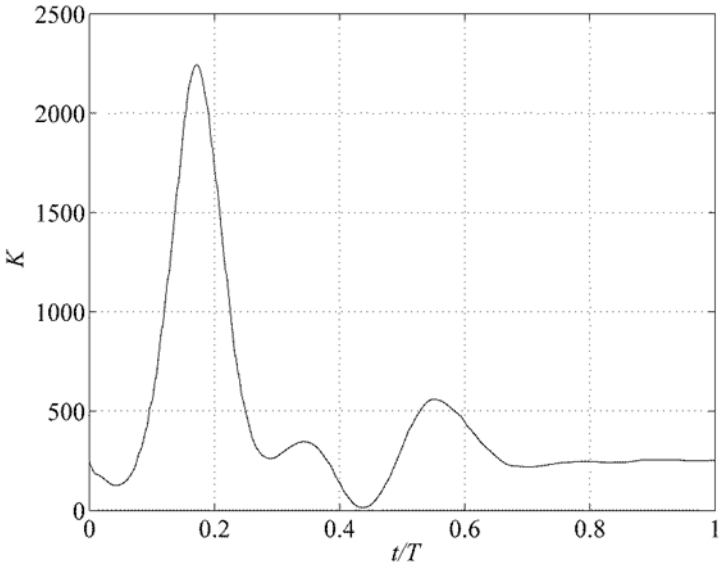


**Figure 4.5 Dean number values at each phase of the input waveform for the carotid artery.**

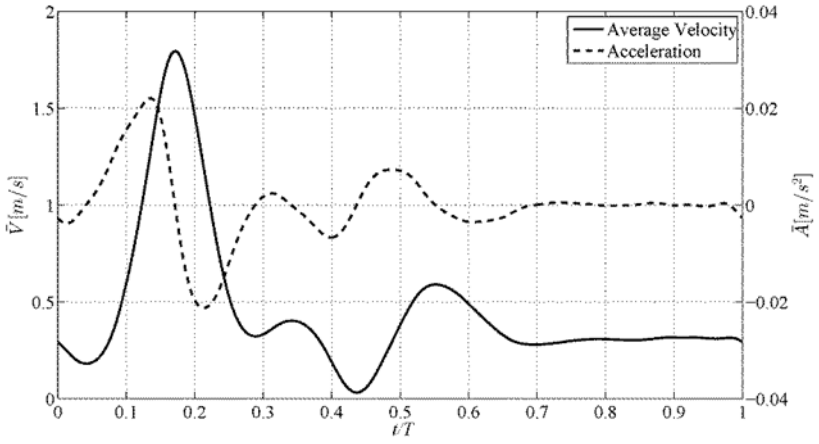


**Figure 4.6 Average velocity at each phase of the carotid-based inlet waveform along with the corresponding acceleration waveform.**

The average velocity for the carotid artery waveform is approximately an order of magnitude higher than the coronary waveform. Based on the difference in the inlet conditions, we hypothesize that the luminal surface in the presence of carotid artery flow will be subjected to fewer regions of low WSS compared to the coronary artery flow. In addition, the increase in the Womersley value between the waveforms will generate differences in flow behavior typical of unsteady flow in smooth walled curved vessels[135]. The lower Womersley value of the coronary artery waveform flow will likely produce a lager viscous layer in the near wall region, which will result in secondary flow structures similar to the steady flow case. On the other hand, the Womersly number for the carotid artery is almost double the value for the coronary. In turn, we expect a localization of the viscous effect in the near wall region and an increase in the inertial effect in the central region of the cross-section. For smooth walled pipes, this force imbalance results in the stretching of Dean vortices within the cross-section and the slight movement of the vortex centers to the top and bottom walls. We note that though the governing fluid parameters are scaled such that the flow physics are captured in the carotid model, the diameter of the actual carotid artery is nearly a factor of two larger than the numerical model; as such, the actual wall shear stress values are $\tau_{w,a} = \tau_{w,m} U_a a_m / (U_m a_a)$, where $U$ is the average velocity, $a$ is the tube radius, the subscript "a" corresponds to values from the actual carotid artery, and the subscript "m" signifies model parameters.

## 4.2 Numerical Model

The numerical simulations are performed using the commercially available software package Ansys CFX Version 14.0. The software is used to solve the time dependent three dimensional Navier-Stokes equations in the fixed *XYZ* Cartesian coordinate frame (see Figure 4.2). Ansys CFX employs a finite volume solution method for solving a discretized control volume formulation of the Navier-Stokes equations as discussed in Chapter 2. The transient simulations are conducted using a backward Euler temporal differencing scheme, which is a second order accurate implicit time stepping method. At each time step, the CFX solver performs several iterations until the maximum residual is less than $10^{-4}$, at which point the solution at that time step is considered converged. The vessel walls are assumed to be rigid and the no slip condition applied at the boundary. The working fluid is Newtonian with a density of 1060 kg/m$^3$ and a dynamic viscosity of $3.7 \times 10^{-3}$ Pa s, which are the same as in the numerical simulations discussed in Chapter 4. The flow field is initialized with the converged solution from a steady flow simulation with Dean number of $K$ = 70 in order to speed up convergence of the numerical solution. A uniform velocity profile is prescribed at the pipe inlet, whose magnitude at each time step is determined from the time varying average velocity waveform (see Figure 4.3 and Figure 4.6). At the pipe outlet, the boundary condition is set as an "opening" which allows flow to cross the boundary surface in either direction. The relative total pressure for inflow and relative static pressure for the outflow is set to 0 Pa. This boundary condition is utilized in order to allow reverse flow at the outlet and to prevent an artificial "wall" from being constructed during the numerical solution if flow enters the outlet, which can occur in unsteady pipe flows. The simplifying assumptions made in Study C are the same as Study B.

The spatial domain of the stented vessel geometry is comprised of hexahedral elements in a structured butterfly mesh configuration in the interior of the vessel. An unstructured mesh is implemented in the near wall region to resolve flow features that are later quantified to evaluate stent performance. The mesh density used for the unsteady simulations is the same as prescribed for the steady flow simulations conducted in Chapter 4. The number of nodes within the stented vessel models for the unsteady flow simulations range from 2,790,387 to 2,797,684, which is greater than the nodes used for the steady flow simulation due to the extension of the entrance vessel region. The details of the mesh construction are the same as discussed in Section 4.2.1 for the steady flow simulations. The grid independence study was not repeated for the unsteady

simulations with the assumption that the flow structures that develop during the unsteady flow regime are adequately resolved using the grid applied to the steady flow simulations. Upon examination, the eddy structures for the unsteady flow were of similar size as the structures observed for the steady flow simulation, which supports the use of the same grid for each flow condition. It should be noted that corner eddies that develop immediately adjacent to the step are not resolved by the numerical mesh for both the steady and unsteady simulations.

The convergence of the solution over repeated cardiac cycles for each waveform is confirmed by comparing the WSSM at the inner and outer walls for several consecutive cycles. For the coronary artery waveform, Figure 4.7 illustrates the distribution of WSSM along the inner (see Figure 4.7 (A)) and outer walls (see Figure 4.7 (B)) at the intersection with the $z = 0$ plane in the N4_AR2 geometry for four consecutive cardiac cycles at the peak of the diastolic phase ($t/T$ = 0.85). For the carotid artery waveform, Figure 4.8 presents the distribution for the same geometry and location on the inner and outer wall for four cardiac cycles at the peak of the systolic phase ($t/T$ = 0.14). These figures demonstrate that three cardiac cycles are sufficient in order for the flow behavior to become periodic and the impact of the transient initial conditions to dissipate. Over all, the percent difference between the WSSM values for the second cardiac cycle and subsequent cycles is less than 1% at the outer wall and marginally higher at the inner due to the smaller WSSM values.

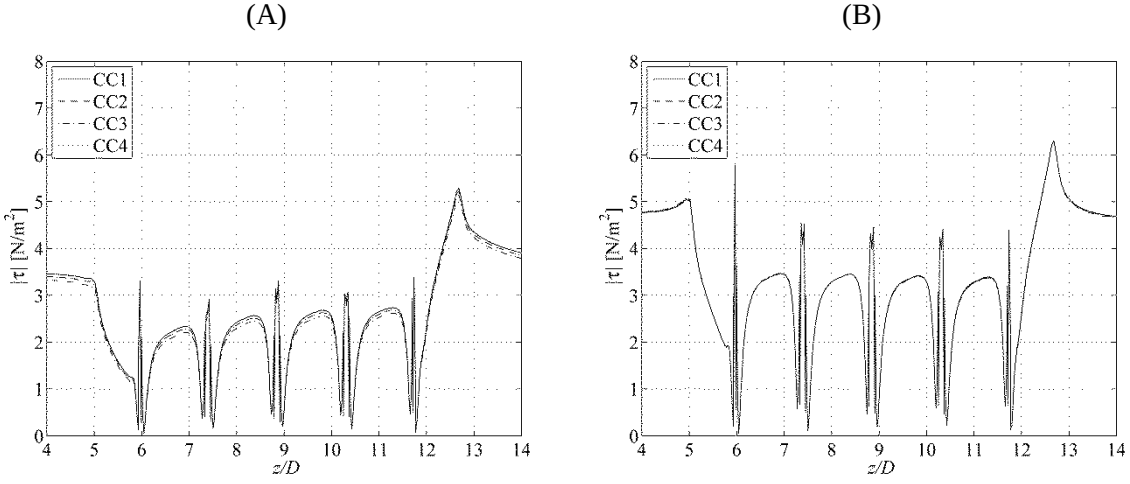


**Figure 4.7 WSSM along the inner (A) and outer (B) walls for the consecutive cardiac cycles for N4_AR2 at t/T = 0.85 for coronary artery waveform.**

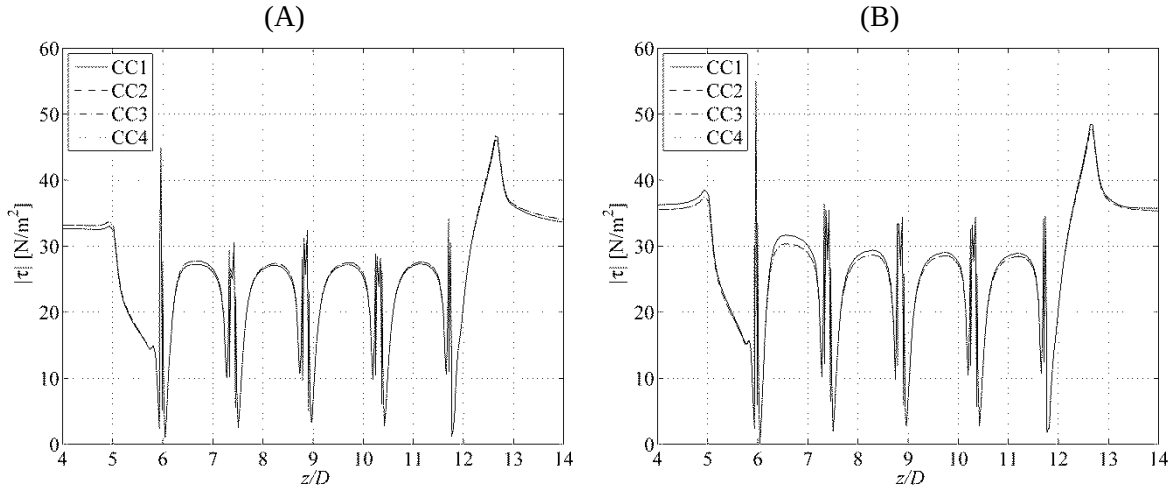


**Figure 4.8 WSSM along the inner (A) and outer (B) walls for the consecutive cardiac cycles for N4_AR2 at *t/T* = 0.14 for carotid artery waveform.**

### 4.2.1 *Hemodynamic Variables*

The WSS indices utilized in the previous Chapter to identify ISR prone regions are also used to characterize the unsteady flow environment. However, the impact of the temporal WSS alterations in the development of ISR has not been fully characterized. On the other hand, time-averaged calculations of the WSS indices over the cardiac cycle are commonly computed to capture the spatial variation in WSS indices and provide an estimation of the stented segment susceptible to excessive NIH development. The time-averaged WSS (TAWSS) calculations provide a spatial map used to identify sites that are more susceptible to NIH development in the presence of transient flow behavior. The area exposed to non-physiological stress conditions are quantified by the amount of the arterial surface area exposed to WSSM < 0.5 N/m$^2$ or with WSSG greater than 200N/m$^3$. Time-averaged WSS indices are computed as follows. The TAWSSM is defined as,

$$\text{TAWSSM} = \frac{1}{T}\int_0^T |\tau|\, dt \qquad \textbf{Equation 4.1}$$

where $T$ is the period of one cardiac cycle and $dt$ is the simulation time step. The time averaged WSSG is defined as,

$$\text{TAWSSG} = \frac{1}{T}\int_0^T |\nabla\tau|\, dt \qquad \textbf{Equation 4.2}$$

The TAWSS and TAWSSG are computed over the third cardiac cycle.

The oscillatory shear index (OSI) was formulated by Ku *et al*. to quantify the cyclical changes in the direction of the WSS vector from its average direction[136]. The value of OSI ranges from 0 to 0.5, with a value of zero indicating unidirectional shear throughout the cycle and values greater than 0 indicating the WSS vector transiently alternating between the positive and negative direction. Previous studies have demonstrated that distributions of high OSI are associated with the precursors of restenosis, such as an inflammatory response and NIH development[137]. The OSI was not quantified in the analysis of stent flow presented in this thesis since critical OSI exposure is expected to be minimal, particularly within the stented region. The luminal area exposed to critical OSI is expected to be modest compared to the size of critical TAWSS exposure based on previous work with a similar stent design[138]. Further, regions of critical OSI are expected to develop at the vessel-to-stent transition region at the proximal end and at the reverse transition at the distal end of the stented region regardless of the stent design.

## 4.3 Numerical Results and Discussion

In this section, we discuss the general flow patterns created by the presence of a realistic stent model in a curved vessel with two different physiological inlet conditions. The flow behavior induced by the different physiological waveforms is evaluated to garner an understanding of the waveform characteristics that promote or deter ISR. Furthermore, the important stent geometric determinant of WSS distribution that is associated with the biochemical response leading to excessive NIH development is discussed. An overview of the spatial and temporal changes in the geometrically-induced flow behavior will be provided by extracting the flow patterns at key time points of the input waveform. In addition, the time average WSS (TAWSS) indices are compared for the different stent models to determine the design that minimizes the area exposed to critical TAWSS. As well, a comparison between the steady state simulation in Chapter 4 and the present unsteady simulations facilitates the discussion of estimating the average distribution of WSS during a cardiac cycle using steady state simulation results at the mean blood flow velocity. The benefits of the unsteady flow conditions for visualizing temporal alterations in flow patterns during acceleration and deceleration phases is discussed. Lastly, the numerical results are compared to published work on stented straight pipe and smooth wall curved pipe unsteady

simulations to ascertain the effect of vessel curvature and highlight the impact of the strut protrusion presence in the curved vessel lumen.

### 4.3.1 *Overview of Unsteady Flow Behavior in a Curved Pipe with a Coronary Artery Waveform*

To explore the spatial and temporal flow development within the curved stented vessel, the velocity distribution is extracted at key time points during the cardiac cycle. The examination of flow behavior at specific time points is used to introduce the velocity distribution in the vicinity of the stent, particularly in the vicinity of the struts along the inner and outer wall, and lead subsequent discussion of secondary flow patterns and WSS distributions. Figure 4.9 and Figure 4.10 show a representative data set of the axial ($u$-component) and the cross-stream ($v$-component) of velocity in the $z = 0$ plane of the N4_AR2 geometry. All velocity values are normalized by the average velocity, $\overline{V} = 0.13$ m/s, corresponding to the mean Reynolds number of the waveform. Contour plots of the velocity distribution are shown at the normalized time values of $t/T = 0.015$, 0.125, 0.723, and 0.850 within the cardiac cycle, representative of the global maxima and minima of the average velocity and acceleration waveforms. A line plot is included at the top of each contour plot to indicate the average velocity and acceleration value at the selected phases of the waveform. The flow is at the point of minimum acceleration at $t/T = 0.015$ and at maximum retrograde flow at $t/T = 0.125$. The maximum acceleration occurs at $t/T = 0.723$ and the peak volumetric flow rate at $t/T = 0.85$.

The contour plots in Figure 4.9 and Figure 4.10 provide an overall qualitative impression of the flow in the stented vessel and demonstrate the time dependent variation in the velocity profiles caused by the flow acceleration and deceleration. Specifically, Figure 4.9 indicates the forward axial fluid motion at the phases of maximum acceleration and maximum volumetric flow rate (Figure 4.9(C) and Figure 4.9(D)). Conversely, regions of retrograde flow develop at the phases of maximum deceleration and reverse inlet flow, as illustrated in Figure 4.26(A) and (B), respectively, along the inner wall. At $t/T = 0.015$, the phase of maximum flow deceleration, the fluid motion is predominately anterograde in the vicinity of the outer wall and regions of retrograde flow are identified near the inner wall (Figure 4.9(A)). Flow acceleration due to the exit taper region causes retrograde flow near the inner wall to dissipate at the exit of the stented region. At $t/T = 0.125$, retrograde flow is dominant throughout the plane and is particularly strong at the inner wall (see Figure 4.9 (B)). Anterograde flow returns at the later phases, $t/T = 0.723$ and $t/T =$

0.850, where the classic axial skew toward the outer wall induced by the vessel curvature is prominent (see Figure 4.9 (C) and (D)). In addition to temporal changes, the contour plots indicate spatial changes in the axial velocity profile as flow enters the expansion region and exits the taper region. A reduction in the magnitude of the axial velocity is observed within the stented region of the vessel at $t/T$ = 0.85 (see Figure 4.9 (D)), which is likely due to the impedance of axial motion due to the strut protrusions. In addition, the outerward shift of the axial flow is observed to minimize as flow travels past the struts. Distal to the stented region the flow gradually returns to the fully developed axial velocity profile observed in the proximal unstented region. Axial skewing is also reduced during maximum acceleration (see Figure 4.9 (C)).

The contour plots in Figure 4.10 provide insight into the disruption of the secondary flow throughout the stented vessel due to the strut protrusions. Positive cross-stream ($v$-component) velocity values represent fluid motion toward the outer wall while negative velocity values represent fluid motion toward the inner wall. As mentioned in Chapter 1, standard Dean vortices are counter-rotating vortices carrying fluid from the inner wall to the outer wall along the symmetry plane of the bend. Thus, the profiles presented in Figure 4.10 with positive velocity values at all points from the inner wall to the outer wall indicate fluid motion characteristic of Dean vortices. Negative values of the $v$-component of the velocity indicate a modification to the Dean vortex structure. Specifically, a change in the secondary flow is shown at the outer wall by regions of negative velocity proximal to the struts and higher positive velocity distal to the struts as the flow travels around the protrusions. Along the inner wall, the cross-stream velocity behavior around the struts is spatially reversed in the streamwise direction as the flow navigates the struts. The most pronounced modification of the secondary flow is observed during maximum acceleration at $t/T$ = 0.725 (see Figure 4.10(C)), where regions of the negative $v$-component of velocity propagate into the central region of the vessel away from the walls. At this phase, negative cross-stream velocity is observed at the inner wall of the expansion region and outer wall of the taper region. In addition, the negative cross-stream velocity is observed at the inner wall of the taper region at $t/T$ = 0.125. Further, flow redirection around the struts, indicated by regions of negative flow in the immediate vicinity of the struts, is strongest at the phases of maximum acceleration and flow rate.

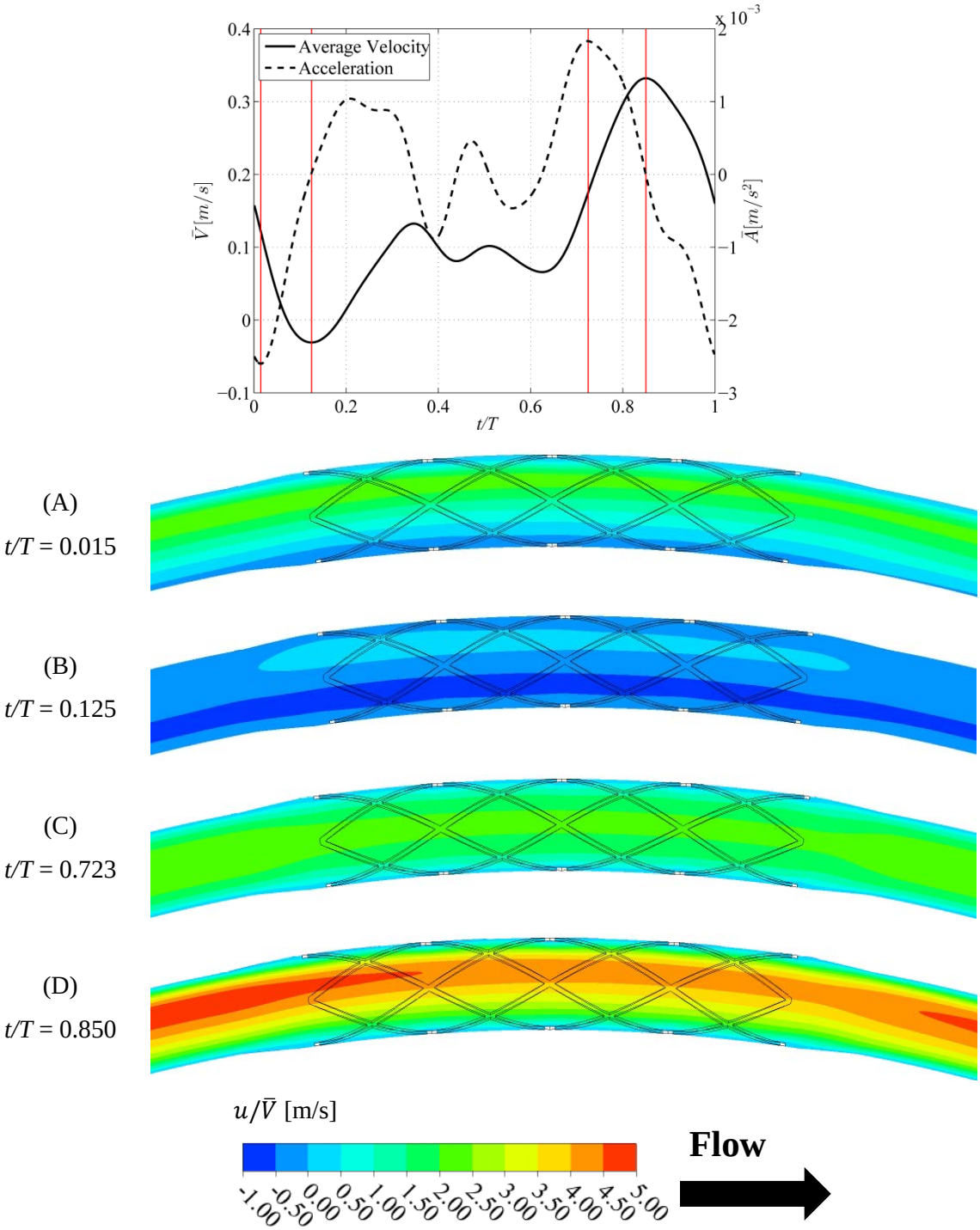


**Figure 4.9 Time dependent alterations in the axial velocity distribution in the *z* = 0 plane for the N4_AR2 geometry at phases of global maximum and minimum flow rate and acceleration for the coronary artery waveform.**

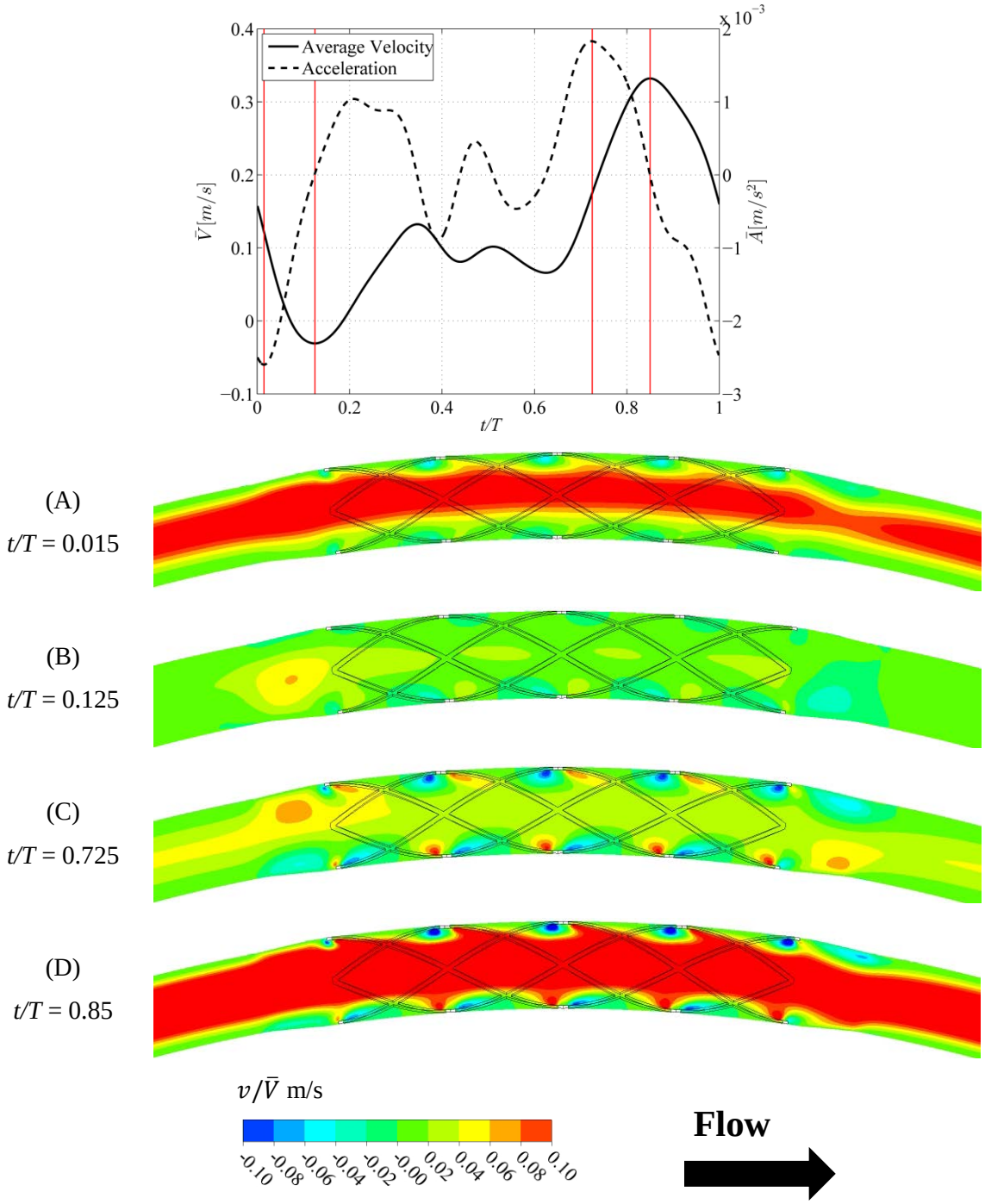


**Figure 4.10 Time dependent alterations in the cross-stream *v*-component of velocity distribution in the *z* = 0 plane for the N4_AR2 geometry at phases of global maximum and minimum flow rate and acceleration of the coronary artery waveform.**

Planar secondary flow vortical structures at various cross-sections within the stented region exhibit distinct spatio-temporal characteristics different from the secondary flow observed in the unstented vessel. Figure 4.11 presents the secondary flow pattern at planar cross-sections in the middle stent cell at the selected time points presented in Figure 4.9 and Figure 4.10. The details of the secondary flow patterns vary between the different stent designs; however, Figure 4.11 provides a case study of the typical flow disturbance by the struts and the secondary flow evolution which occurs throughout the cardiac cycle. Each row of Figure 4.11 demonstrates the secondary flow at a different time point and each column represents a different strut configuration. The abbreviations of the strut configuration classification within the selected cross-sections are listed at the bottom of Figure 4.11 and their definitions are provided in Figure 3.6. The secondary flow pattern in the unstented region is presented in the first column of Figure 4.11 to facilitate the discussion of flow disturbances induced by the strut protrusions as shown in subsequent columns.

The streamlines highlight the large scale coherent vortex structures that form upstream in the unstented portion of the vessel and within the stented region. Dean type secondary flow structures are present in the unstented portion of the vessel and are virtually identical at the representative time points (see Figure 4.11, Column 1) owing to the low Womersley number. A slight shift in the vortex center toward the outer wall of the vessel is observed at $t/T = 0.015$, at the point of maximum deceleration (see Figure 4.11 (A), Column 1). Interestingly, the large coherent Dean vortex structures remain relatively intact at this phase within the stented planes. The extent of the strut influence on the secondary flow behavior is localized at the near wall region. It should be noted that the corresponding Dean number at this phase is $K \sim 77$, which is similar to the steady flow case of $K = 70$ presented in Chapter 4. Compared to the steady flow case, we observe similar minimal flow disturbance by the strut presence within the planes. However, the angled struts demonstrated a greater impact on the secondary flow structure within the central region of the vessel for the steady flow case compared to the unsteady flow case (see Figure 4.11 (A) and Figure 3.15(A), Columns 3 & 5). Within the intersection plane IS1 (see Figure 4.11, Column 2), we observe the evolution of recirculation regions at the leeward side of the struts at the later phases. Distinctly, windward side recirculation is observed at the intersection plane IS1 at $t/T = 0.723$ and the center of the coherent vortical structure shifts toward the inner wall (see Figure 4.11 (C), Column 2). In the IS2 plane (see Figure 4.11, Column 4), the leeward side recirculation is only dominant at t/T = 0.125 (Figure 4.11 (B), Column 4) and $t/T = 0.723$ (Figure 4.11 (C), Column 4) and absent at the other phases. In addition, the streamwise vortical structure, generated

by axial flow around the strut intersection at the outer wall in the IS2 plane, is only observed at $t/T$ = 0.723 and $t/T$ = 0.85, which are representative of phases of higher inlet axial velocity and Dean numbers. This reinforces the connection between the axial velocity and the presence of these vortical structures.

Once again, the angled strut configuration contributes to a more complex secondary flow structure (see Figure 4.11, Columns 3 &5). This flow complexity is heightened by the temporal changes in the flow but many of the common features observed in the steady flow solution remain. In particular, the looping of the streamlines around the struts in the AS1 and AS2 planes, caused by axial fluid motion over the angled struts, is consistent across all time points. Notably, at $t/T$ = 0.015 within the AS1 plane (see Figure 4.11 (A), Column 3), the looped streamlines are concentrated around the inner and outer wall struts, where secondary flow stagnates in smooth walled vessels. Secondary flow does not appear to be suppressed by this axial flow behavior at the "top" and "bottom" walls. The streamline looping around all the struts is present for the other time points. Interestingly, no semblance of the Dean vortex structure is visible at the phase of maximum acceleration in these planes (see Figure 4.11 (C), Columns 3 & 5). In contrast, a region of centralized vorticity is still present in the AS1 and AS2 planes for the remaining time points. This finding may suggest that the flow acceleration makes a significant contribution to structuring the secondary flow. Overall, the temporal evolution of the secondary flow implies changes in circulation strength at different phases of the waveform, which dictates the transport of NIH stimuli to the vessel wall throughout the cardiac cycle.

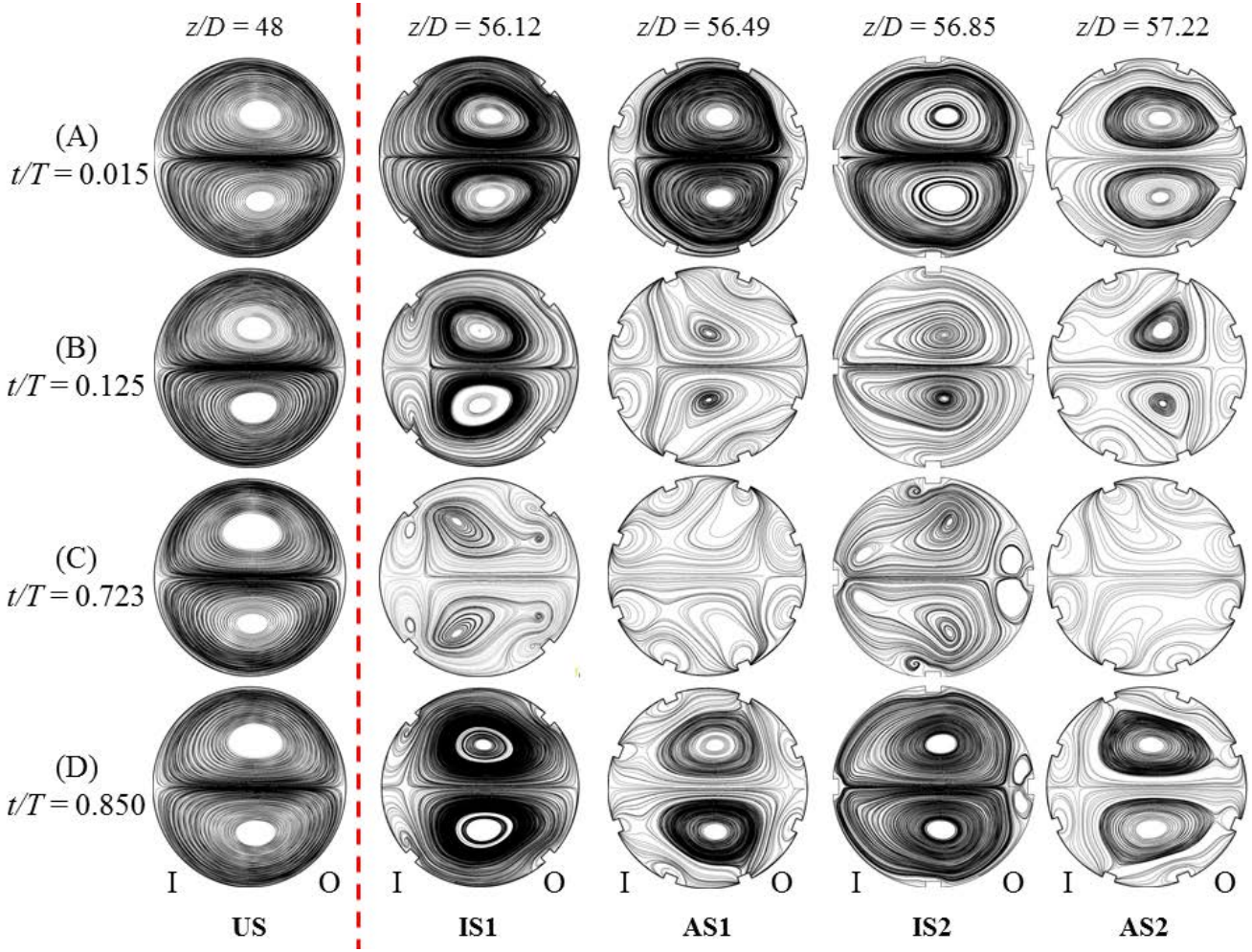


**Figure 4.11 Temporal evolution of the secondary flow structures at cross-sections extracted from the stented and unstented region of the vessel for the coronary artery waveform.**

The time dependent variations in the spatial WSSM distribution in the N4_AR2 geometry along the outer and inner wall are illustrated in Figure 4.12 and Figure 4.13, respectively. The general description of the WSSM distribution for the selected phases of the cardiac cycle in the presented stent model is also applicable to the remaining three stent designs. The steady flow simulations obfuscate the periodic increases and decreases of the important WSSM parameters, which dictate restenosis development. As expected, luminal wall exposure to higher WSSM values corresponds to phases of increased inlet velocity and is lower during minimum flow rates. At all phases, there are marked regions of lower WSSM at the proximal end of the stent compared to the distal end. This highlights the importance of the fluid interaction with the first proximal strut and the influence of expanding the stent during implantation, explaining observations of increased NIH at the proximal end of implanted stents.

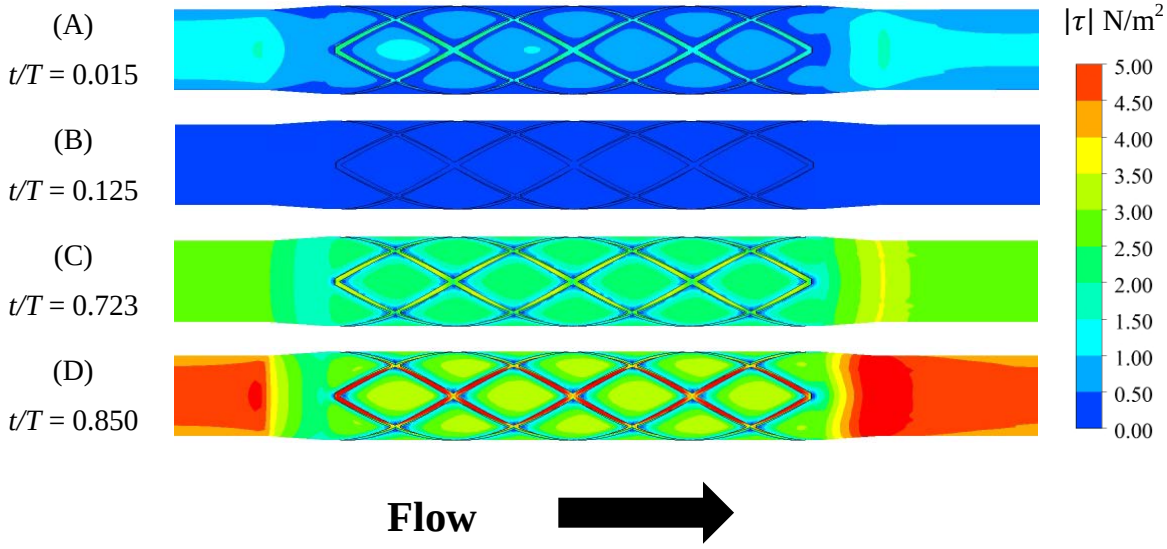


**Figure 4.12 WSSM at selected time points at the outer wall of N4_AR2 for the coronary artery waveform.**

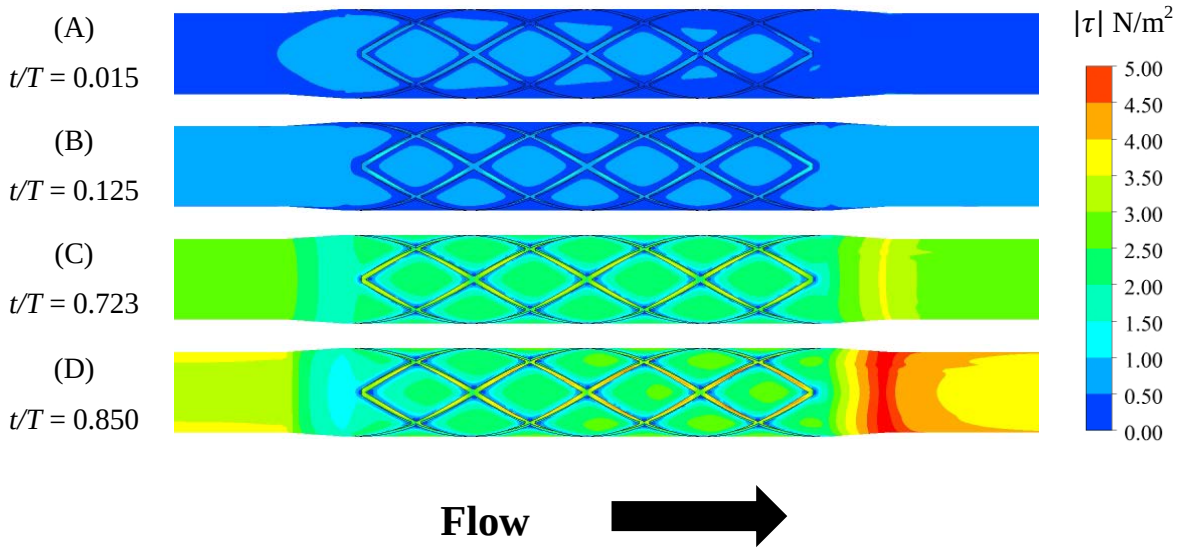


**Figure 4.13 WSSM at selected time points at the inner wall of N4_AR2 for the coronary artery waveform.**

Further, the WSSM is predominately higher at the outer wall compared to the inner wall except at $t/T$ = 0.015 and $t/T$ = 0.125, when retrograde flow dominates the flow field. Previous work has shown the same imbalance in the WSSM distribution for straight and curved stented vessels with a similar stent design and coronary artery input waveform [93]. The low WSSM values predicted at the proximal region and inner wall may account for neointima accumulation in these regions due to flow behavior at particular phases [31]. Lower WSSM regions are also observed to surround the stent struts at each phase and higher WSS values are located on the top of struts. Previous investigations of unsteady physiological flow in a curved stents reported a more uniform WSSM distribution along the outer wall compared to the inner wall [93]. Qualitatively, this finding was not prominent in the present simulations, which may be due to the different physiological waveform used in the previous study. The contour plots in Figure 4.12 and Figure 4.13 provide only instantaneous WSSM behavior within the stented vessel. A more in depth characterization of the WSSM behavior over the cardiac period will be discussed in a later section by examining the TAWSSM parameter for each of the stent designs.

### 4.3.2 *Effect of Geometric Parameters for Coronary Artery Waveform*

The hemodynamic conditions that encourage the development of NIH are driven by the transport of stimuli to the vessel wall and the endothelial response to hemodynamic stress. The secondary flow is a convective transport mechanism in the curved vessel geometry and contributes to the WSSM along the luminal walls, but to a lesser extent compared to the primary flow. The effect of the strut frequency and aspect ratio on the temporal evolution of the secondary flow structure is captured by examining the disruptions in the flow patterns at the minima and maxima of the acceleration and average velocity waveform. A comparison of the secondary flow patterns for the 4-strut and 8-strut configuration within the IS2 and AS2 planes is presented in Figure 4.14. The selected time points are used to garner a general impression of the disturbance of the secondary flow structure based on the stent geometry. We acknowledge that the instantaneous secondary flow behavior presented in Figure 4.14 fails to provide the cumulative effect of the design parameters on the secondary flow throughout the cardiac cycle. However, the examination of the behavior at the extremes of the waveform provides the upper and lower bounds for the evaluation of the flow disturbance due to strut frequency.

Generally, the Dean vortex structure observed in the unstented region remains more intact for the 8-strut configuration compared to the 4-strut configuration within both evaluation planes. For the 4-strut configuration, the Dean vortex structure observed in the unstented planes becomes elongated within the stented planes, likely as a result of the vessel expansion within the stented region and the strut spacing within the cross-section (see Figure 4.14, Columns 2 & 4). In contrast, the Dean vortex shape is largely maintained in the 8-strut configuration and flow disruption is concentrated in the near wall region at the presented phases and planes (see Figure 4.14, Columns 1 & 3). The integrity of the Dean vortex structure for higher strut frequency is likely due in part to the introduction of additional secondary flow streamline curvature as a result of the strut presence. That is, a radial pressure gradient occurs as the flow passes around the stent struts within the plane, which promotes the maintenance of the Dean vortex structure in the center of the tube. As discussed in Chapter 3, as the number of struts becomes very large it is expected that the flow will behave largely as in a circular tube with reduced radius, except in the very near wall region.

In the current study, the flow behavior in the near wall region is similar for both strut frequencies. For example, in the intersection plane IS2 (see Figure 4.14, Column 1 & 2), the streamwise vortical structure that envelops the strut at the outer wall at $t/T = 0.723$ and $t/T = 0.850$ is present in the 8-strut and 4-strut configurations (see Figure 4.14(C) & (D), Column 1 & 2).

However, its size is reduced for the 8-strut configuration. Overall, the centralized position of the Dean vortex is similar between the strut configurations except at $t/T$ = 0.723 (see Figure 4.14, Columns 1 & 2). At this phase of maximum acceleration, the center of the Dean vortex moves toward the outer wall and an ancillary region of centralized vorticity emerges at the inner wall for the 4-strut configuration. Within the AS2 plane for the 4-strut configuration, the most noticeable impact of the strut frequency is observed at $t/T$ = 0.125 and $t/T$ = 0.723 (see Figure 4.14, Columns 1 & 3), where the centralized vortex shape becomes distorted at the phase of reverse flow and disintegrates at the phase of maximum acceleration.

The disruption of the secondary flow with changes in the strut aspect ratio in the IS2 and AS2 planes is less pronounced compared to the strut frequency, as shown in Figure 4.15. At the early phases of $t/T$ = 0.015 and $t/T$ = 0.125, there is no marked distinction between the secondary flow pattern for the different aspect ratios (see Figure 4.15 (A) & (B)). At the phase of maximum acceleration, $t/T$ = 0.723, the streamwise vortical structure and bipolar centralized vorticity remains for N4_AR2 and N4_AR3 (see Figure 4.15 (C)). However, a singular region of centralized vorticity and a reduction in the size of the vortical structure at the outer wall is observed at N4_AR6 (see Figure 4.15 (C), Row 3). The dissipation of the outer wall streamwise vortical structures is also apparent as the aspect ratio increases at the phase of maximum flow rate, $t/T$ = 0.850 (see Figure 4.15 (D)). For the AS2 plane, shown in Figure 4.16, a similar trend of the alteration in the secondary flow is observed for the various aspect ratios. The most prominent change in the secondary flow structure within this plane as a result of

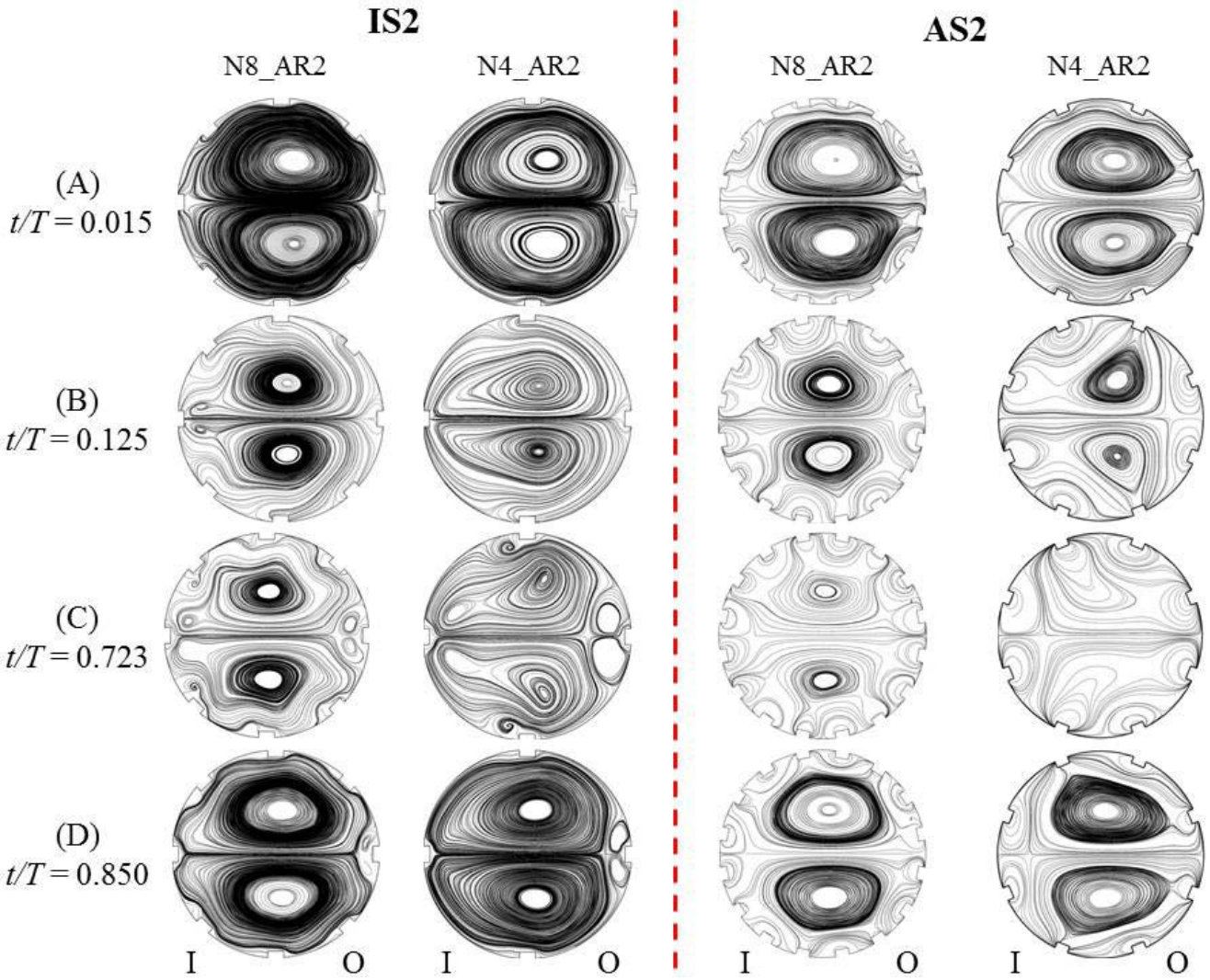


**Figure 4.14 Temporal evolution of the secondary flow structures in N8_AR2 and N4_AR2 geometries in the curvature planes IS2 and AS2 for the coronary artery waveform.**

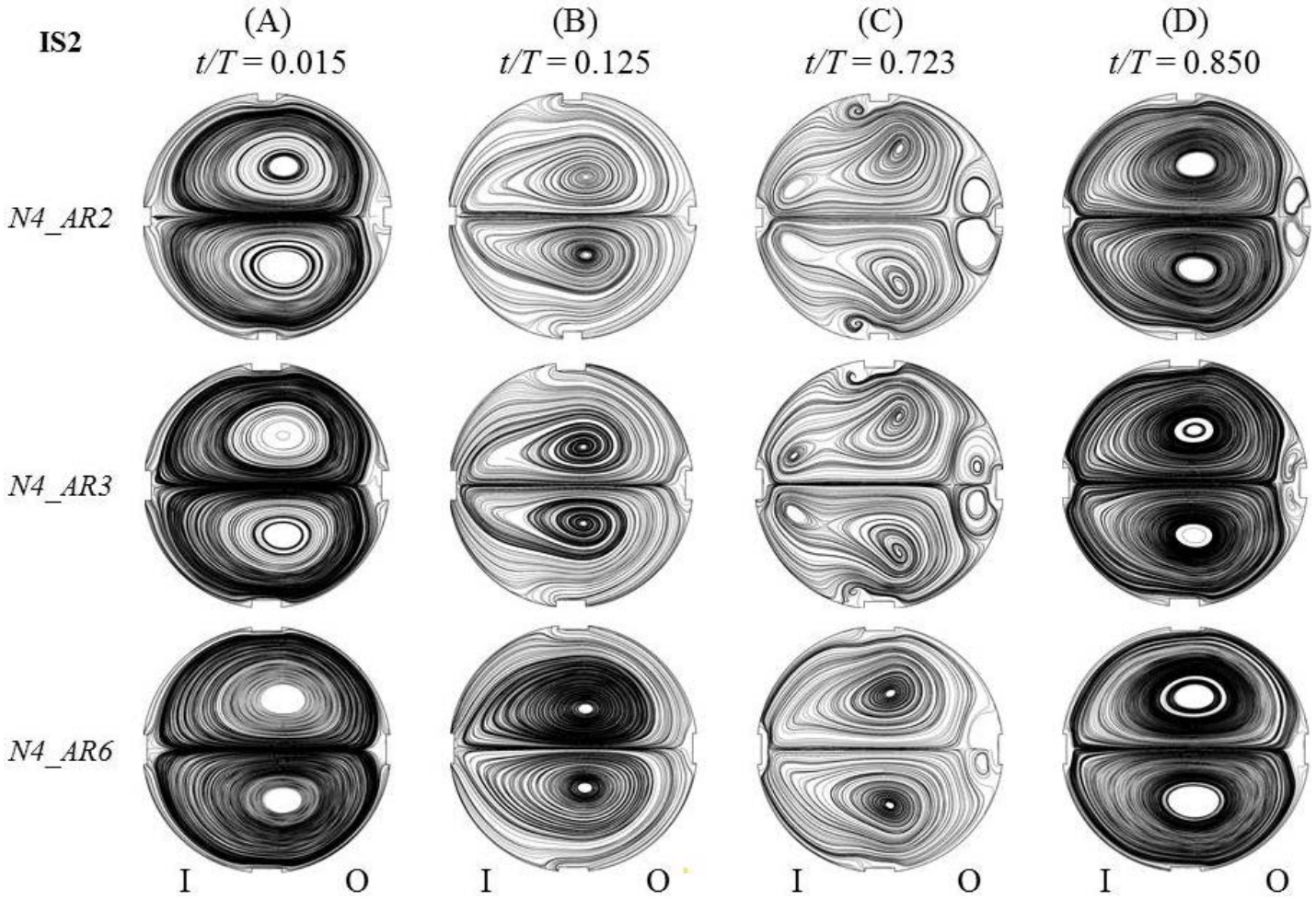


**Figure 4.15 Temporal evolution of the secondary flow for a fixed strut frequency and various aspect ratios in the IS2 plane for the coronary artery waveform.**

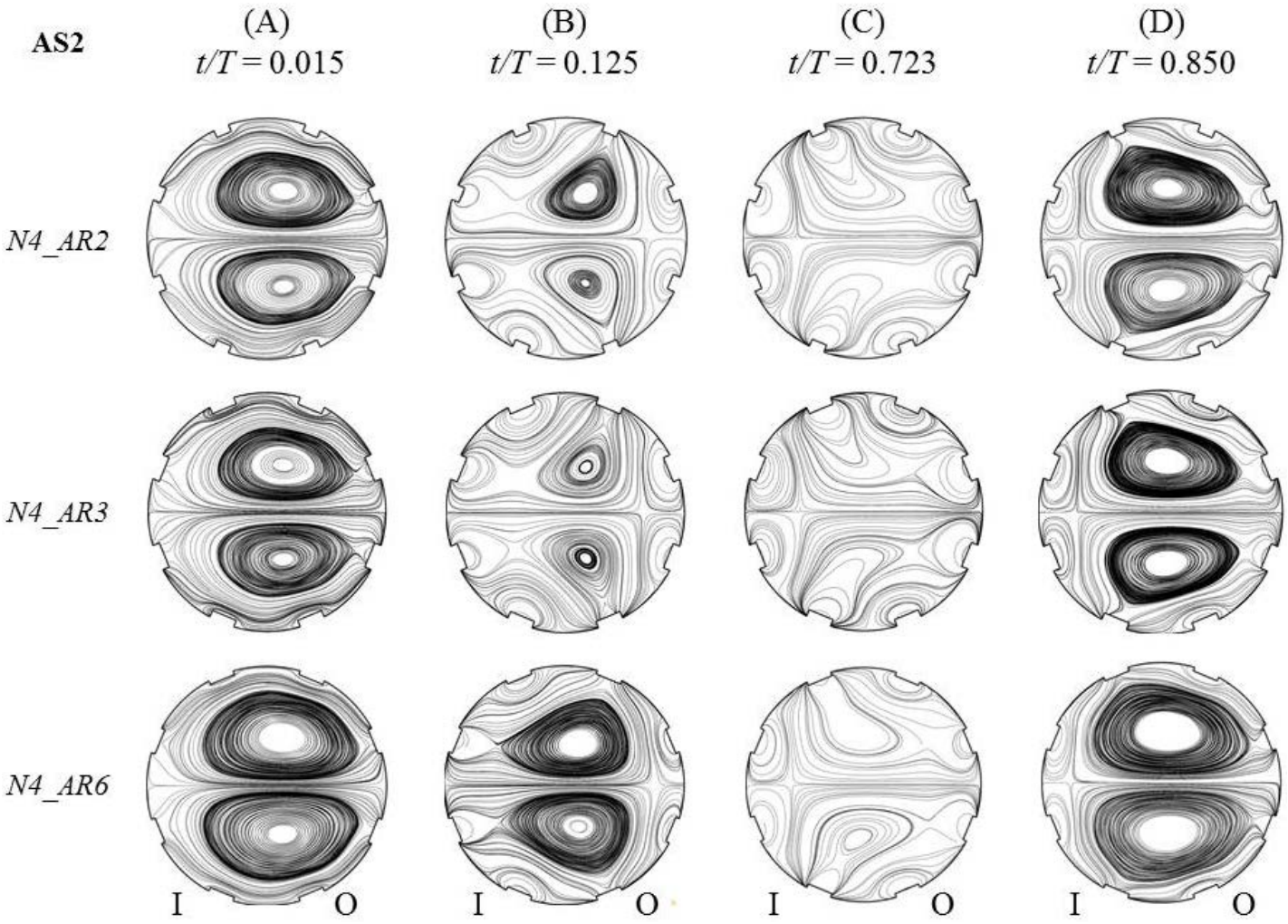


**Figure 4.16 Temporal evolution of the secondary flow for a fixed strut frequency and various aspect ratios in the AS2 plane for the coronary artery waveform.**

changes in the aspect ratio is observed at $t/T$ = 0.125 (see Figure 4.16 (B)). The distortion of the Dean vortex is very similar for the A2 and AR3 configurations (see Figure 4.16 (B), Rows 1 & 2), but is significantly minimized for the AR6 geometry (see Figure 4.16, Row 3). The similarity between the secondary flow behavior for the AR2 and AR3 geometries demonstrates the minor impact of the strut width for a fixed strut frequency and reaffirms the same conclusions put forth for the steady simulations. Moreover, the spatial extent of the effect of the strut thickness on the secondary flow is demonstrated for the unsteady simulations and corroborates the steady flow observations.

In order to illustrate TAWSSM luminal exposure, the distributions of TAWSSM for the four stent designs are displayed in Figure 4.17 and Figure 4.18 along the inner and outer wall, respectively. The main observations for the TAWSSM distributions are in general agreement with the findings of the steady flow simulations in Chapter 4. For each stent design, there is a distinct pattern of TAWSSM, which is consistent across all models. As the flow approaches the stented region there is a gradual decrease in the TAWSSM at the inner and outer wall. Notably, there is a significant decrease immediately proximal to the first strut intersection at the inner wall compared to the outer wall (see Figure 4.17). Within the stented region, higher TAWSSM is observed on the surface of the angled struts, which are misaligned with the primary flow direction, compared to the strut intersections. The TAWSSM drops dramatically directly before and after each strut in the primary and secondary flow directions but recovers within the intrastrut region, in much the same way as observed for the steady flow simulations. As flow proceeds through the exit taper region, the TAWSSM increases due to flow acceleration as a result in the change in wall shape. At the inner and outer wall, there is a marked increase in the TAWSSM at the transition to the native vessel at the distal end and it gradually decreases as flow proceeds through the exit vessel. Within the exit vessel, the WSSM values are close to the values observed in the entrance vessel along the inner wall (see Figure 4.17). However, the values remain elevated along the outer wall of the exit vessel (see Figure 4.18).

The differences in the TAWSSM distribution between the stent designs are also highlighted in Figure 4.18 and Figure 4.17. Qualitatively, a larger area of the vessel is exposed to lower TAWSSM values for the 8-strut versus the 4-strut configuration. For a fixed strut frequency, a comparison of the N4_AR2 and N4_AR3 geometries shows an increase in the strut width results in lower TAWSSM on the strut surface (see Figure 4.17 and Figure 4.18 (B), (C)). The lowest

TAWSSM exposure on the strut surface is observed for the N4_AR6 geometry, which has the thinnest struts (see Figure 4.17 and Figure 4.18 (D)).

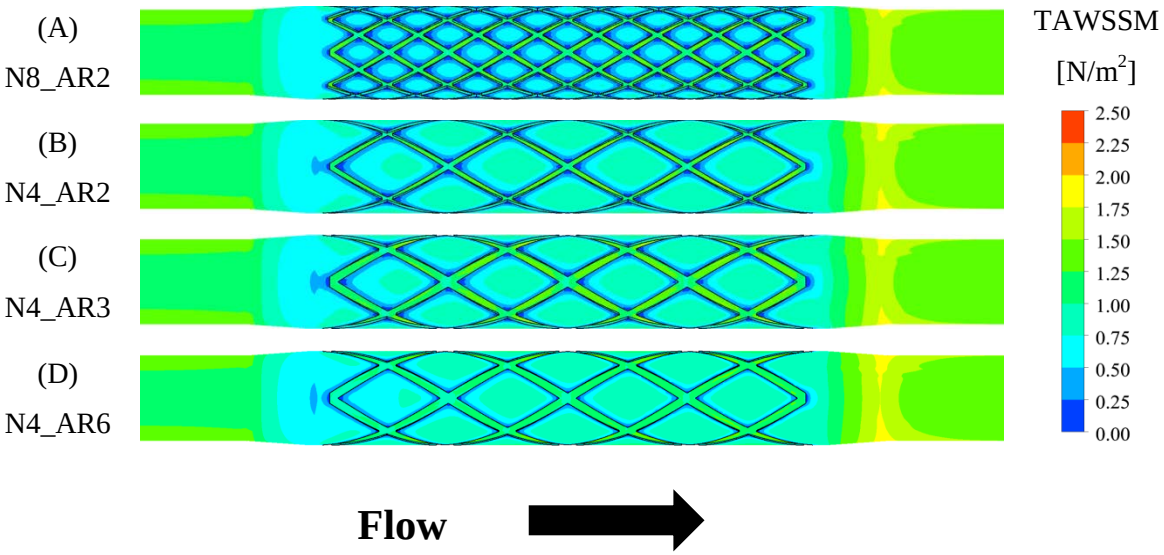


**Figure 4.17 TAWSSM at the inner wall for the coronary artery waveform for the investigated stent designs.**

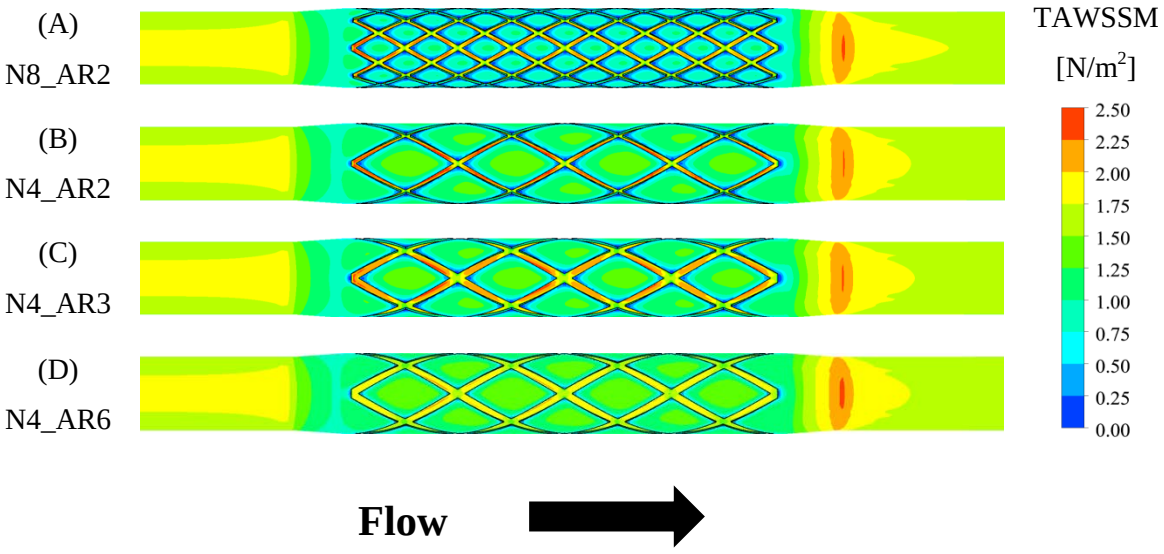


**Figure 4.18 TAWSSM at the outer wall for the coronary artery waveform for the investigated stent designs.**

A magnified view of the TAWSSM distribution at three segments of the stented region along the inner and outer walls of the models is presented in Figure 4.19, Figure 4.20 , and Figure 4.21. The three segments, including a proximal, middle, and distal region, are used to provide a detailed view of key features of the TAWSSM behavior. The first segment focuses on the first two proximal stent cells of the 8-strut configuration and the first proximal stent cell of the 4-strut configuration (see Figure 4.19). The second segment shows the TAWSSM distribution in the middle section of the stent models (see Figure 4.20). Lastly, the final segment presents the TAWSSM in two distal stent cells of the 8-strut configuration and the last distal stent cell of the 4-strut configuration (see Figure 4.21). The magnified view of the proximal region reveals TAWSSM exposure within the critical NIH development range immediately proximal to the first strut intersection and surrounding the struts at the first stent cells at the inner and outer wall. The critical TAWSSM exposure is especially pervasive at the inner wall within this segment of the stent (see Figure 4.19, Column 2). Along the strut surface, higher TAWSSM is observed at the leading edge of the struts as flow enters and exits the intrastrut region, which is most visible at the outer wall (see Figure 5.19, Column 1). Within the intrastrut area, the flow separation occurs as the fluid navigates the struts and is identified by regions of lower TAWSSM adjacent to the struts. The flow reattaches in the distal portion of the intrastrut area, as demonstrated by an increase in TAWSSM in the area for the 4-strut configuration (see Figure 4.19 (B) – (D)). A uniform TAWSS distribution is observed in intrastrut area of the 8-strut configuration (see Figure 4.19 (A)), suggesting little to no reattachment. Within the middle segment (see Figure 4.20), the overall trends are the same. The distinct difference from the proximal section is the uniform TAWSSM along the surface of the struts. This distribution differs from the high TAWSSM at the leading and trailing edge on the strut surface in the proximal section. The localization of the luminal surface exposed to critical TAWSSM remains unchanged in the middle section. Finally, within the distal segment, TAWSSM increases significantly from the region just distal to the last strut to the exit of the taper region. For all models, the intrastrut areas of the distal portion are exposed to higher TAWSSM compared to the proximal portion.

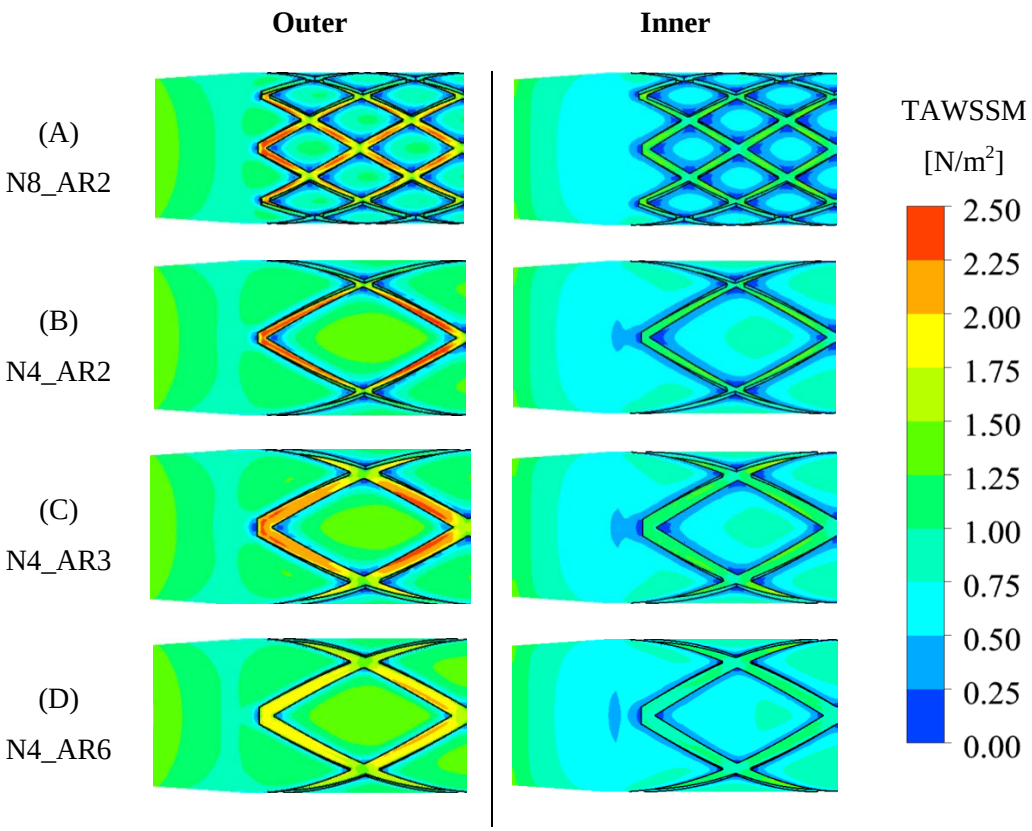


**Figure 4.19 TAWSSM in the proximal section of the stented region at the outer and inner wall for the coronary artery waveform.**

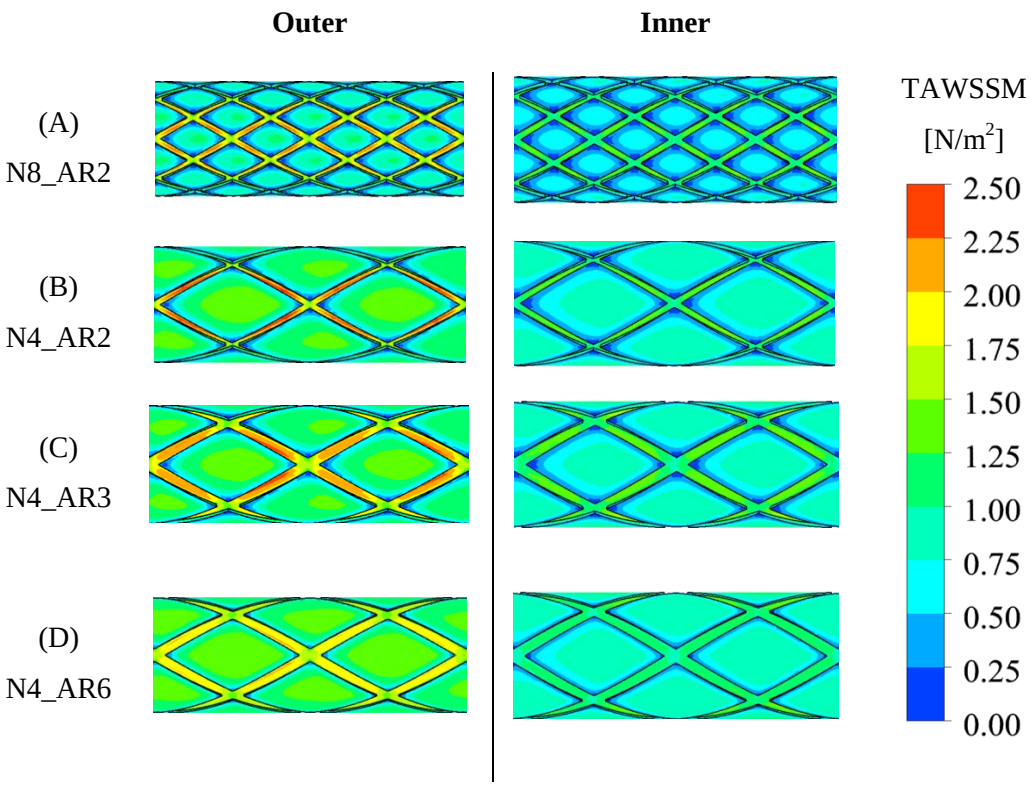


**Figure 4.20 TAWSSM at selected time points in the middle section of the stented region at the outer and inner wall for the coronary artery waveform.**

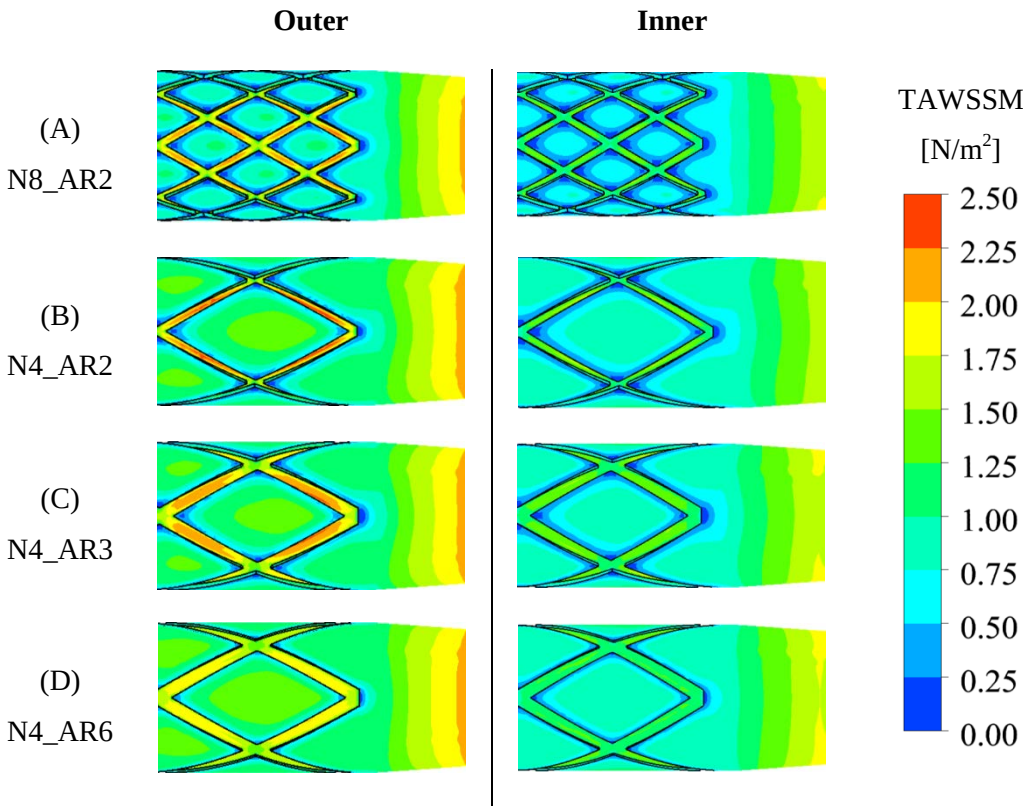


**Figure 4.21 TAWSSM at selected time points in the distal section of the stented region at the outer and inner wall for the coronary artery waveform.**

To evaluate the risk for the development of ISR for the stent models, the areas exposed to low and moderate TAWSS are identified along the inner and outer wall in Figure 4.22 and Figure 4.23, respectively. The regions exposed to low TAWSSM are colored in blue and surfaces exposed to moderate TAWSSM are colored in red. The figures clearly illustrate the large area of the stented vessel exposed to, on average throughout the cardiac cycle, critical levels of WSSM for the 8-strut compared to the 4-strut models. Overall, the critical TAWSSM distribution mirrors the trends discussed for the steady flow simulations. Specifically, the critically low TAWSSM regions surround the strut intersections for all models. The moderate TAWSSM regions are concentrated adjacent to the low TAWSSM regions toward the center of the intrastrut area for the 8-strut configuration and surround the angled struts for the 4-strut configuration. A qualitative comparison of the contour plots highlights the greater portion of the stented region exposed to critical areas of TAWSSM for the 8-strut configuration compared to the 4-strut configuration. This

is especially poignant at the inner wall where only the surfaces of the struts in the 8-strut model are exposed to TAWSS above the critical threshold (see Figure 4.22 (A)). As expected, for all the stent models, there is a stark imbalance in the size of the region exposed to critical TAWSSM between the inner and outer wall. At the inner wall, the most notable observation is the decrease in the luminal wall area exposed to critical TAWSSM from the proximal to the distal end of the stent for the 4-strut configurations (see Figure 4.22 (B) – (D)) and is not present in the contour plots at the outer wall (see Figure 4.23(B) – (D)). The geometric dissimilarity between the unstented region of the vessel and stented portion appears to have a greater impact on the potential for excessive NIH development in the proximal inner wall portion of the stent. This finding corroborates previous studies of WSSM distribution in straight and curved stented vessels, which reported that the proximal region is considered to be at increased risk for the buildup of neointimal proliferation compared to the distal region[86,93]. Overall, the contour plots in Figure 4.22 and Figure 4.23 provide a map of the regions of critical TAWSSM, where regions lower TAWSSM are correlated with lower fluid velocities could potentially lead to longer residence times for NIH catalyst and unconstrained neointima growth. As well, the plots clearly indicate the geometric influences of the stent design on the critical TAWSSM parameter.

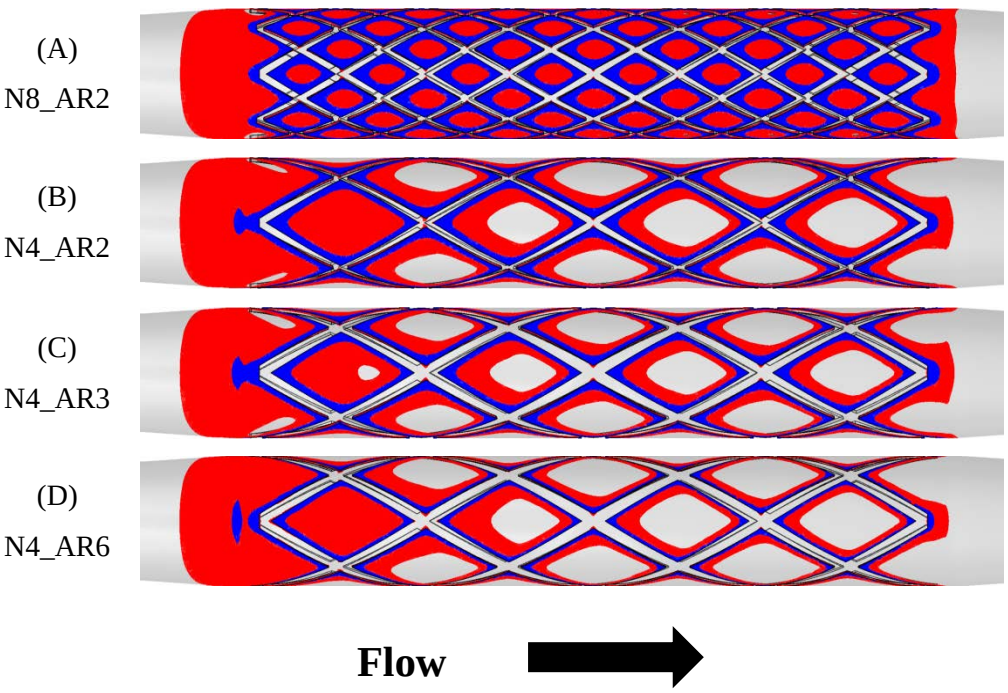


**Figure 4.22 A comparison of the critically low WSSM (blue) and moderate WSSM (red) regions at the inner wall of the investigated geometries for the coronary artery waveform.**

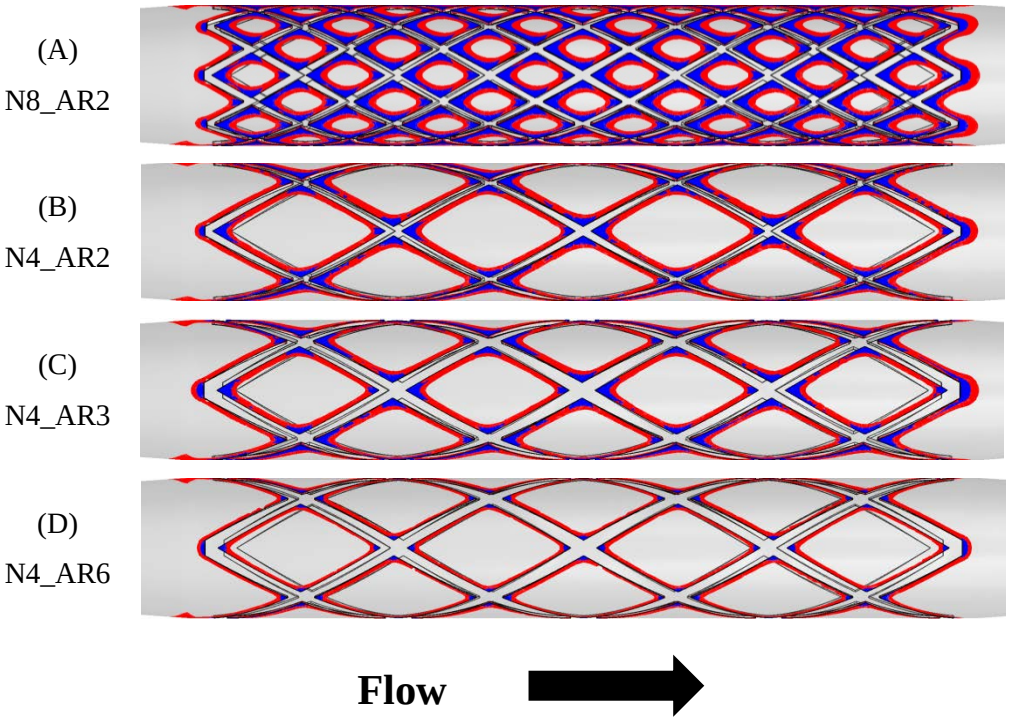


**Figure 4.23 A comparison of the critically low WSSM (blue) and moderate WSSM (red) regions at the outer wall of the investigated geometries for coronary artery waveform.**

The TAWSSG distribution for the four stent designs is presented in Figure 4.22 and Figure 4.23, along the inner and outer wall, respectively. A large majority of the stented region is exposed to high TAWSSG values above the critical 200N/m$^2$ threshold due to the introduction of the strut protrusions into the vessel lumen, regardless of the stent pattern. This leads to the conclusion that the TAWSSG is not a hemodynamic parameter that is particularly sensitive to the changes in the luminal environment due to the geometric changes in the stent designs. A slightly greater portion of the intrastrut area for the 8-strut configuration is exposed to elevated TAWSSG values compared to the 4-strut configuration. Further, there was no considerable difference in the TAWSSG distribution for the 4-strut configurations. It is no surprise that the WSSG values are higher at the outer wall compared to the inner wall for all stent designs given the higher velocity fluid circumventing the strut protrusions at the outer wall. Interestingly, the WSSG is slightly higher in the expansion region compared to the taper region but no difference was observed within the stent cells from the proximal to the distal end. This suggests that the geometric transition from

the native vessel region to the stented region at either end does not significantly alter the TAWSSG behavior within the stent cells in the manner observed for the TAWSSM distribution. For all stent designs, the highest TAWSSG regions surround the strut intersections and slightly less elevated TAWSSG surrounds the angled struts. The lowest TAWSSG exposure is localized in the center of the intrastrut area for each stent design. Overall, the localization of the WSS distribution for the unsteady simulations corroborates the behavior observed for the steady flow simulations.

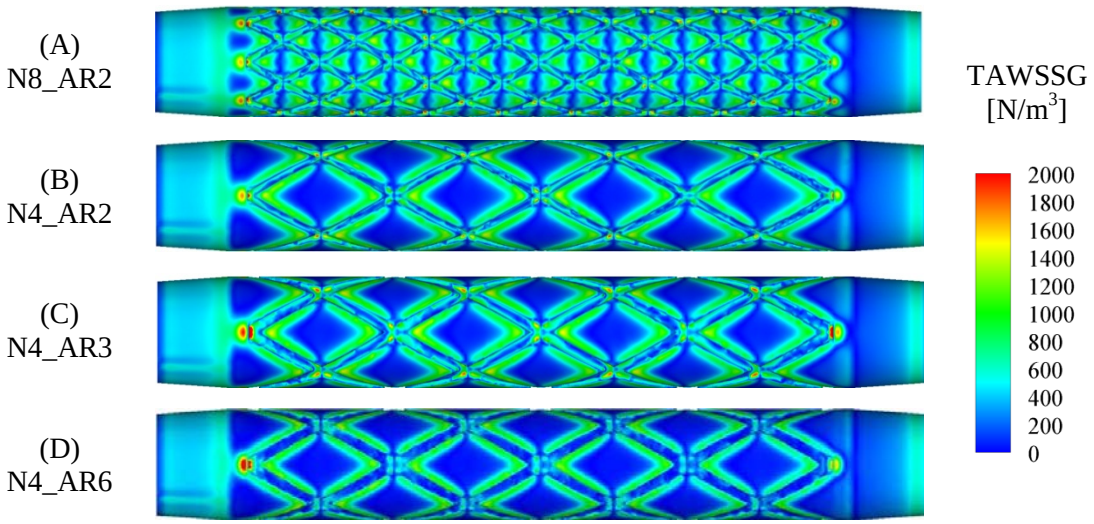


**Figure 4.24 TAWSSG for the coronary artery waveform for all investigated geometries at the inner wall.**

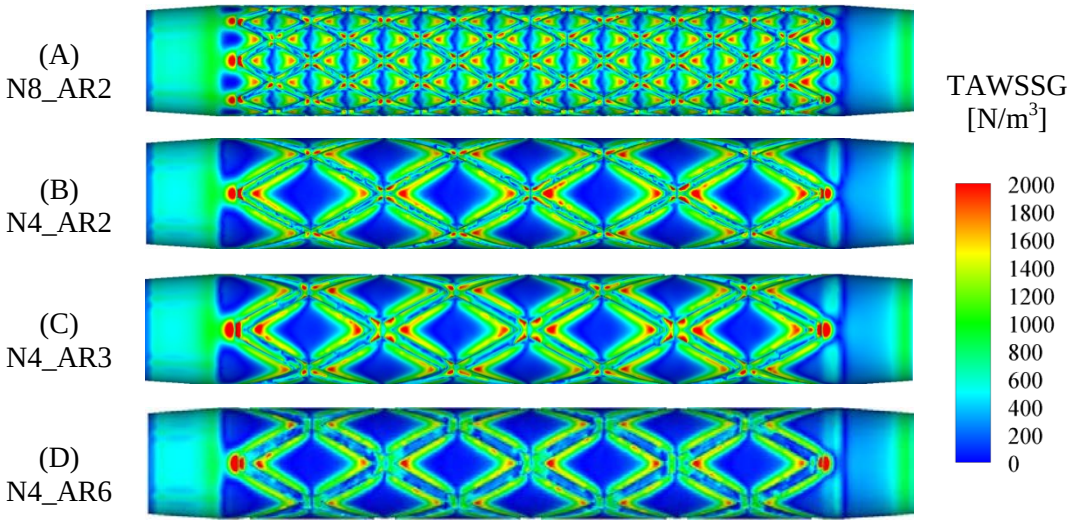


**Figure 4.25 TAWSSG for the coronary artery waveform for all investigated geometries at the outer wall.**

In order to predict the areas exposed to critical WSS indices for each stent design, the surface areas exposed to critical TAWSSM and TAWSSG are computed and the results are summarized in Table 4.1. Here, the calculated surface area exposed to TAWSSM within the critical range is reported as a percentage of the stented region, which extends from the entrance of the expansion region to the exit of the taper region. Remarkably, we observe that 52% of the stented region is exposed to TAWSSM within the critical range for the 8-strut configuration. For a fixed strut aspect ratio, a reduction in the number of struts results in a 17% reduction in the critical WSS area. As mentioned in the steady flow case, this suggests that decreasing the number of struts may be hemodynamically advantageous as it would reduce the likelihood of ISR via hemodynamical stresses. Increasing the aspect ratio from AR2 to AR3 has a minimal effect on the critical TAWSS distribution. On the other hand, an increase in the aspect ratio from AR3 to AR6, effectively decreasing the strut thickness, reduces the critical TAWSSM exposure by approximately 8%. This confirms that varying the strut width has only a minor effect in determining the size of deleterious WSSM areas and the strut thickness has a stronger impact on the luminal environment under physiological flow conditions. The alterations in the strut frequency and aspect ratio have a greater impact on the areas exposed to low TAWSSM compare to the moderate TAWSSM. This is demonstrated by the larger changes in the size of the low

TAWSSM region with changes in stent design compared to the moderate WSS regions. The percentage of the stented region exposed to high TAWSSG ranged from 62% to 77% for the different stent designs; the largest reduction in the high TAWSSG area is observed for a change in the strut frequency from 8 to 4 struts. Over all, the results suggest that the N4_AR6 geometry would be the hemodynamically optimal stent configuration of the group with a critical TAWSSM exposure of 26% and high TAWSSSG exposure of 62.27%. However, these values of critical WSS exposure still posed a significant threat to ISR development.

**Table 4.1 Percentage of stented region exposed to low or moderate TAWSSM or high TAWSSG for coronary artery waveform.**

| Geometry | TAWSSM [%] | | Total exposure to low or moderate TAWSSM [%] | High TAWSSG [%] |
|---|---|---|---|---|
| | Low | Moderate | | |
| N8_AR2 | 24.26 | 27.74 | 52.00 | 77.76 |
| N4_AR2 | 11.53 | 24.09 | 35.62 | 67.30 |
| N4_AR3 | 11.14 | 22.33 | 33.47 | 70.65 |
| N4_AR6 | 5.85 | 20.93 | 26.78 | 62.27 |

The WSS imbalance between the inner and outer wall due to vessel curvature is quantified in Table 4.2 and Table 4.3. The TAWSSM and TAWSSG behavior is presented along each wall in Table 4.2 and Table 4.3, respectively. The luminal areas prone to NIH development due to hemodynamic stress are consistently greater at the outer wall compared to the inner wall. The greatest imbalance between the walls for the low TAWSSM parameter is observed for the N8_AR2 geometry and the N4_AR6 geometry for the moderate TAWSSM parameter (see Table 4.2) . Overall, the imbalance in the luminal exposure to critical WSS between the inner and outer wall ranged from approximately 22% to 26% for all geometries, indicating that the imbalance was similar for all stent designs. This observation is consistent with the results of the steady flow simulation with an inlet velocity close to the mean unsteady velocity. However, the size of the area exposed to critical WSSM levels predicted by the time averaged results of the unsteady simulation is smaller compared to the steady simulation by at most 27%.

**Table 4.2 Percentage of inner and outer walls exposed to low or moderate TAWSSM for the investigated geometries for the coronary artery waveform.**

| Geometry | Low TAWSSM [%] | | Percent Diff [%] | Moderate TAWSSM [%] | | Percent Diff [%] | Total low and moderate exposure [%] | | Percent Diff [%] |
|---|---|---|---|---|---|---|---|---|---|
| | Inner | Outer | | Inner | Outer | | Inner | Outer | |
| N8_AR2 | 29.62 | 18.92 | 10.70 | 33.24 | 22.24 | 11.00 | 62.86 | 41.16 | 21.70 |
| N4_AR2 | 16.40 | 6.64 | 9.76 | 32.08 | 16.12 | 15.96 | 48.48 | 22.76 | 25.72 |
| N4_AR3 | 15.66 | 6.62 | 9.04 | 29.52 | 15.14 | 14.38 | 45.18 | 21.76 | 23.42 |
| N4_AR6 | 9.70 | 1.98 | 7.72 | 29.50 | 12.34 | 17.16 | 39.20 | 14.32 | 24.88 |

**Table 4.3 Percentage of the inner and outer wall exposed to high TAWSSG for the coronary artery waveform.**

| Geometry | High TAWSSG [%] | | Percent Difference (Inner vs. Outer) [%] |
|---|---|---|---|
| | Inner | Outer | |
| N8_AR2 | 74.91 | 80.88 | -5.96 |
| N4_AR2 | 64.62 | 70.14 | -5.52 |
| N4_AR3 | 67.59 | 73.83 | -6.22 |
| N4_AR6 | 50.25 | 66.64 | -16.34 |

The critical TAWSSM and TAWSSG exposure in the proximal and distal end of each stent design is summarized in Table 4.4 and Table 4.5. The regional difference in the low TAWSSM exposure from the proximal to the distal end is less than 1% for all stent designs. In contrast, the concentration of moderate TAWSSM exposure in each region is greater in the proximal section versus the distal section by 2 - 6%. Particularly, the centralization of moderate TAWSSM in the proximal region is greatest for the N4_AR6 geometry. This table highlights that the difference in the critical WSSM exposure from the proximal to distal end is driven mainly by the regions exposed to moderate TAWSSM, which could be considered a buffer range of WSSM values. The size of the area exposed to moderate TAWSS can fluctuate depending on the

installation of the stent within the luminal, as minor changes during installation or due to manufacturing could result in a higher percentage of the area in the critical WSSM range. The critical TAWSSG distribution is higher at the distal end compared to the proximal region; however, the difference is minor compared to the TAWSSM imbalance and the behavior is similar for all stent designs. Cumulatively, the benefits of the N4_AR6 design with regards to generating a favorable flow environment for re-establishing the endothelium due to reduced areas of critical WSSM may be counterbalanced by the non-uniform WSS indices between the inner and outer wall and in the streamwise direction.

**Table 4.4 Percentage of the proximal and distal end exposed to low or moderate TAWSSM for the coronary artery waveform.**

| Geometry | Low TAWSSM [%] | | Percent Difference [%] | Moderate TAWSSM [%] | | Percent Difference [%] |
|---|---|---|---|---|---|---|
| | Proximal | Distal | | Proximal | Distal | |
| N8_AR2 | 24.28 | 24.24 | 0.04 | 29.68 | 26.16 | 3.52 |
| N4_AR2 | 12.16 | 10.90 | 1.26 | 29.20 | 19.18 | 10.02 |
| N4_AR3 | 11.60 | 10.70 | 0.90 | 26.90 | 17.92 | 8.98 |
| N4_AR6 | 6.74 | 4.96 | 1.78 | 27.24 | 14.66 | 12.58 |

**Table 4.5 Percentage of the proximal and distal end exposed to high TAWSSG for the coronary artery waveform.**

| Geometry | High TAWSSG [%] | | Percent Difference [%] |
|---|---|---|---|
| | Proximal | Distal | |
| N8_AR2 | 75.66 | 80.00 | -4.34 |
| N4_AR2 | 65.52 | 69.18 | -3.66 |
| N4_AR3 | 69.26 | 72.12 | -2.86 |
| N4_AR6 | 60.94 | 63.70 | -2.76 |

### 4.3.3 *Overview of Unsteady Flow Behavior in a Carotid Artery Model*

The carotid artery waveform generates more complex flow behavior, particularly for the secondary flow patterns, compared to the coronary artery waveform. This increased complexity is due to the higher Womersley value and Dean number flow associated with the carotid artery waveform. The smaller Womersley number coronary artery flow generates a more viscous flow regime, whereas the unsteady inertial forces are more dominant for the carotid artery waveform. The characterization of the carotid artery flow regime is initiated by examining the instantaneous axial and *v*-component velocity profiles at the global maxima and minima of the acceleration and velocity waveform within the plane of the bend ($z$ = 0 plane) for the N4_AR2 geometry. Specifically, the velocity profiles are extracted at the phases of maximum acceleration and volumetric flow rate, $t/T$ = 0.14 and $t/T$ = 0.17, respectively. In addition, flow behavior is examined at $t/T$ = 0.21 and $t/T$ = 0.44, the phases of minimum acceleration and flow rate, respectively. The velocity profiles provide insight into the interesting flow phenomena that develop due to the temporal oscillations of the inlet waveform and highlight the differences in the flow behavior from the coronary artery waveform. Particularly, Figure 4.26 shows contour plots of the evolution of the axial velocity profiles at the selected phases of the waveform. Figure 4.26 indicates the forward axial fluid motion at the phases of maximum acceleration and maximum volumetric flow rate (Figure 4.26(A) and Figure 4.26(B)). Conversely, regions of axial flow reversal develop at the phases of maximum deceleration and minimum volumetric flow rate, as

illustrated in Figure 4.26(C) and (D), particularly along the inner wall. At $t/T$ = 0.21, the phase of maximum flow deceleration, the fluid motion is predominately forward in the vicinity of the outer wall and regions of reverse axial flow are identified near the inner wall. The inner wall region of reverse flow propagates further into the center of the vessel at the entrance of the stented region and becomes more localized at the inner wall at the distal end of the stent. Flow acceleration due to the exit taper region causes reverse flow near the inner wall to dissipate at the exit of the stented region. The axial velocity profile at $t/T$ = 0.44 differs significantly from the previous time points, where regions of flow reversal are dominant within the geometry at this phase. The region of reversed flow is particularly large in the central portion of the plane, immediately distal to the first stent cell.

The documented shift in the high axial velocity fluid toward the outer wall due to vessel curvature is observed at all phases presented in Figure 4.26. Figure 4.26 (A - C) indicates a difference in the degree of skewing of the higher axial velocity fluid toward the outer wall of the pipe. Namely, the size of the region occupied by high axial velocity fluid at the outer wall is similar at $t/T$ = 0.14 and $t/T$ = 0.17. The outward axial skewing behavior is slightly greater during maximum acceleration, $t/T$ = 0.14, compared to maximum volumetric flow rate, $t/T$ = 0.17 (see Figure 4.26 (A) & (B)).There is a steeper change in the axial velocity profile from the outer wall to the inner wall at $t/T$ = 0.21, given the smaller region of high axial velocity fluid at the outer wall and reversed flow region at the inner wall, compared to the previous time points. In general, the skewing is more severe than observed for the coronary artery waveform due to the higher Dean number range.

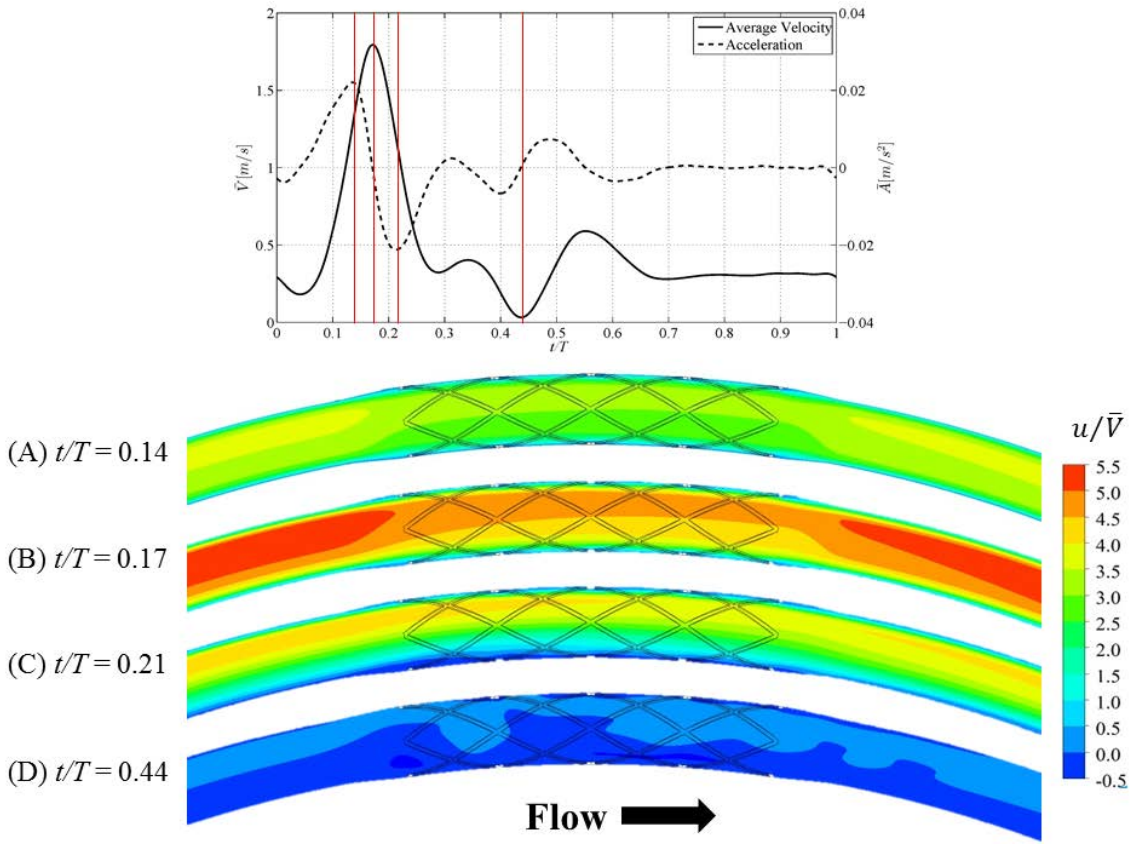


**Figure 4.26 Time dependent alterations in the axial velocity distribution in the *z* = 0 plane for the N4_AR2 geometry at phases of global maximum and minimum flow rate and acceleration for the carotid artery waveform.**

The cross-stream velocity profiles for the carotid artery waveform implies a more complex secondary flow behavior compared to the coronary artery waveform, as shown in Figure 4.27. The contour plots in Figure 4.27 show the time dependent alternations in the v-component velocity profiles caused by the flow acceleration and deceleration within the stented vessel. In the near wall region, the modification of the cross-stream velocity profiles at the peak acceleration and flow rate and the minimum of the acceleration are similar to the behavior observed for the coronary artery waveform (see Figure 4.26). Conversely, the most pronounced modification of the secondary flow is observed at $t/T$ = 0.44, where regions of the negative *v*-component of velocity occupy a greater portion of the vessel away from the walls, indicating greater centralized secondary flow distortion.

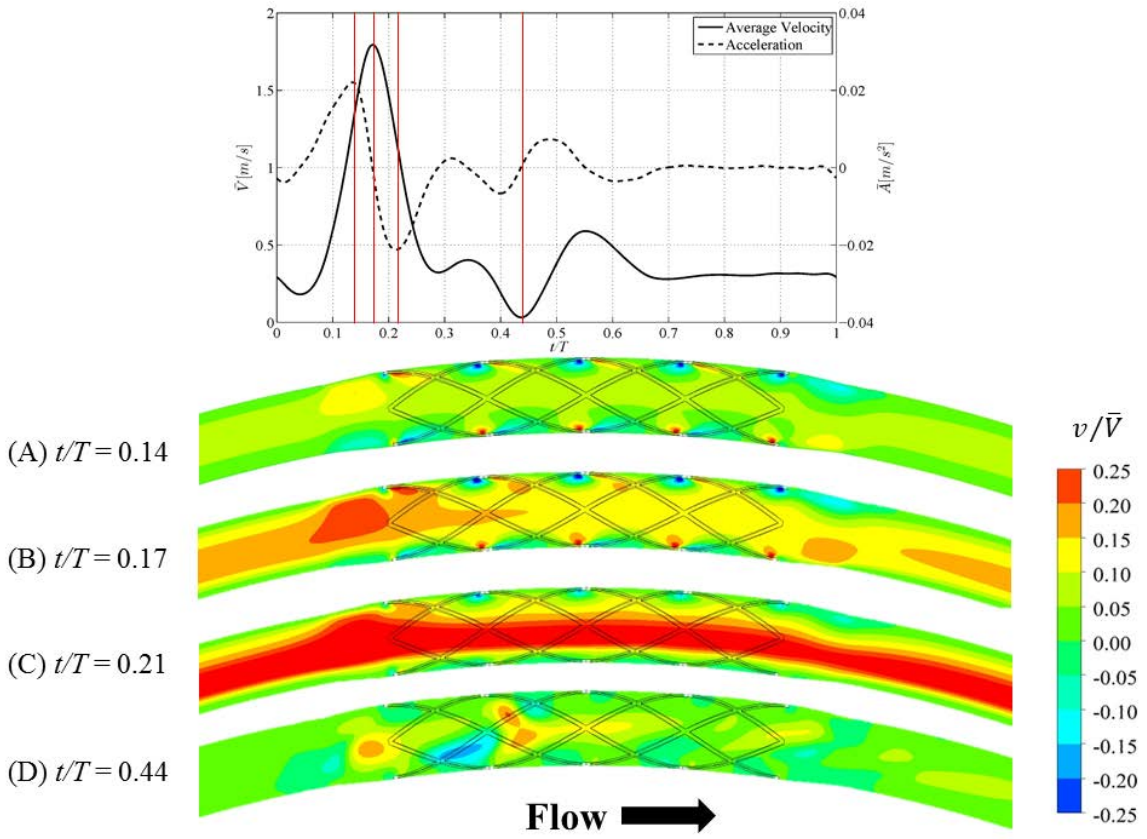


**Figure 4.27 Time dependent alterations in the *v*-component of the velocity distribution in the *z* = 0 plane for the N4_AR2 geometry at phases of global maximum and minimum flow rate and acceleration for the carotid artery waveform.**

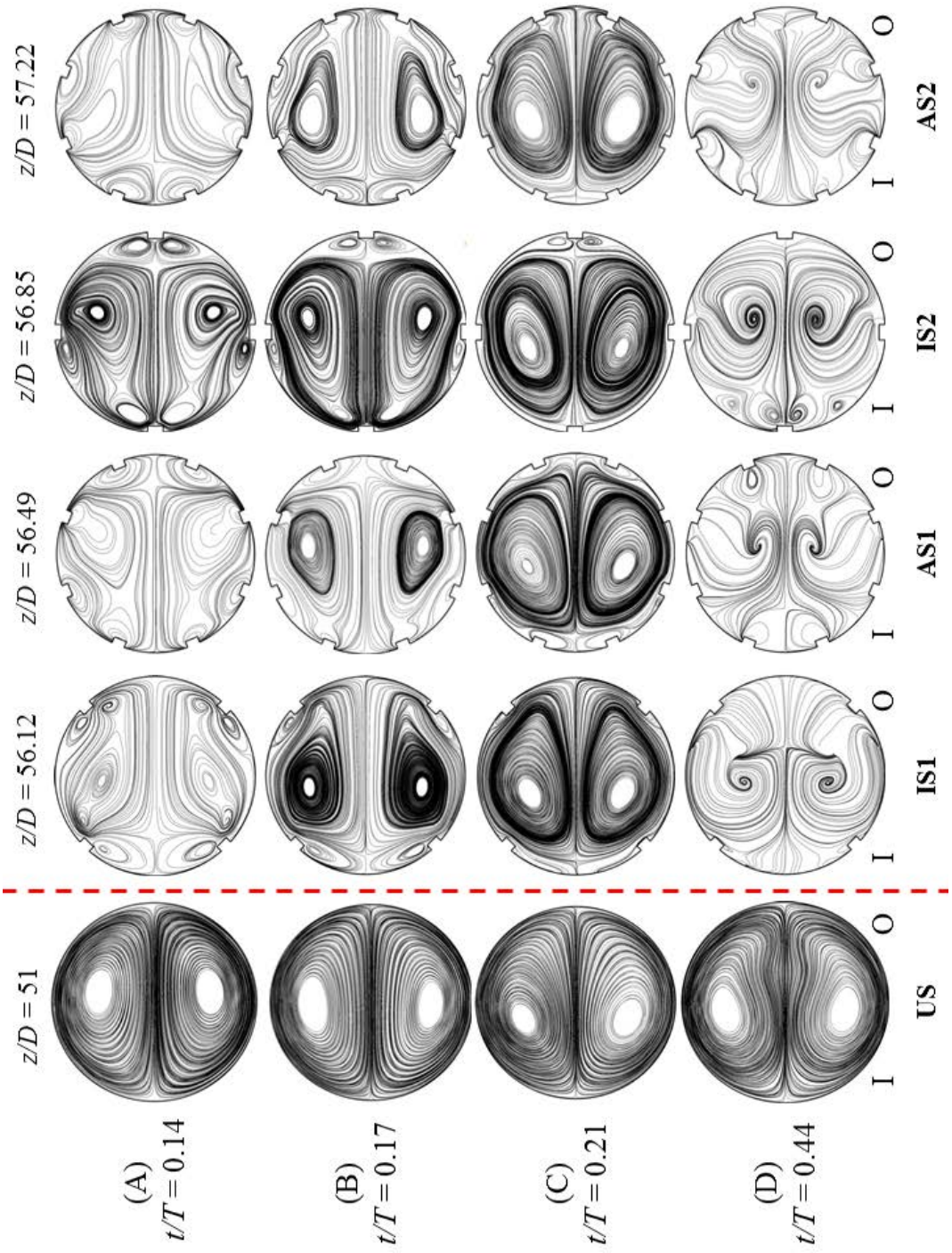


**Figure 4.28 Temporal evolution of the secondary flow structures at cross-sections extracted from the stented and unstented region of the vessel for the carotid artery waveform.**

A detailed examination of the planar secondary flow vortical structures, which develop for the carotid artery waveform is facilitated by the streamlines plots at the selected time points in Figure 4.28. Once again, Dean type secondary flow structures are present in the unstented portion of the vessel (Figure 4.28, Column 1). At the point of maximum acceleration, the center of the vortex is shifted toward the outer wall of the vessel (Figure 4.28 (A), Column 1). The vortex structure becomes more centralized at the point of maximum flow rate (Figure 4.28 (B), Column 1). The center of the vortex resides closer to the inner wall and is pushed toward the upper and lower walls at the phase of maximum deceleration and minimum volumetric flow rate, as shown in Figure 4.28 (C) & (D) ,Column 1. Notably, the shape deforms in a manner that suggest the potential emergence of an additional vortical structure near the outer wall at the phase of minimum volumetric flow rate. For unsteady flow in smooth walled pipes, the development of this secondary flow structure has been attributed to a stagnant region of secondary flow that emerges near the outer wall and a weakening of the secondary motion in the central region of the pipe[61]. At higher Womersley values, this region of stagnant secondary flow moves toward the inner wall and an additional pair of vortices, which rotate in the opposite direction of Dean vortices, develop at the outer wall.

New secondary flow morphologies arise due to the combination of centrifugal and radial pressure gradient instabilities and the presence of strut protrusions within the stented region (Figure 4.28, Column 2 - 5). The streamlines in stented cross-sections show the emergence of multi-scale vortical structures, which deviate from the vortical structures observed in the unstented region. No coherent Dean vortex structures are observed within the selected planes of the stented region at maximum acceleration (Figure 4.28 (A)) and minimum flow rate (Figure 4.28 (D)). However, the Dean vortex structure remains at the phases of maximum flow rate Figure 4.28 (B)) and maximum deceleration (Figure 4.28 (C)). Closer examination of the secondary flow reveals the emergence of vortical structures on the windward and leeward side of the strut protrusions at maximum flow acceleration within the intersection planes IS1 and IS2 (Figure 4.28 (A), column 2 and 4). Within the angled strut planes at the same time point, the streamlines are observed to loop around the strut protrusions due to axial flow traversing the struts. This behavior is similar to structures witnessed for the steady flow and unsteady coronary artery waveform simulations at angled strut planes. A highly elongated form of the Dean vortex structure is present at the phase of maximum volumetric flow rate at all representative planes shown in Figure 4.28 (B). The vortical patterns present at this phase are similar to those discussed for the steady flow case of $K$ = 450 for

the same geometry (see Figure 4.13(B)). Specifically, a large coherent vortex structure exists in the central region for all planes. Recirculation zones are observed on the leeward side of the strut protrusions in the intersection planes IS1 and IS2 (Figure 4.28 (B) Column 2 & 4). Streamwise vortical structures surround the strut at the outer wall for strut configuration IS2 (Figure 4.28 (B) Column 4). Streamlines loop around the struts in the angled strut planes AS1 and AS2 (Figure 4.28 (B) Column 3 & 5) indicating the strong influence of the axial flow around the axially converging and diverging struts.

At the phase of maximum deceleration (Figure 4.28 (C)), the Dean vortex structure at each cross-section is not significantly different from the structure observed in the unstented region. In fact, recirculation regions on the leeward or windward side, observed around stent struts at other phases, are absent within the cross-sections at this phase. However, the presence of the streamwise vortex structure at the outer wall revealed at prior phases in the intersection plane IS2 persist. Lastly, the minimum volumetric flow rate phase is predominately marked by the breakdown of coherent vortex structures into an open swirl secondary flow pattern (Figure 4.28 (D), Column 2 – 5) and corroborates the deviation from the Dean vortex structures indicated by the negative *v*-component of velocity values at the symmetry plane in Figure 4.27. The secondary flow behavior at this phase can be attributed to the combined effects of the reverse flow at the inner wall and the fluid interaction with the strut protrusions. Interestingly, at the IS2 plane, the formation of streamwise vortical structures is observed around the strut located at the inner wall (Figure 4.28 (D), Column 4), which differs from its location in the earlier phases. The relocation of the streamwise vortical structures can be attributed to the strong retrograde flow at the inner wall at $t/T = 0.44$. Lastly, in the AS1 and AS2 planes for $t/T = 0.44$ there is a complete disintegration of the Dean vortex structures (see Figure 4.28 (D), Columns 3 & 5). Moreover, the characteristic streamline looping around the angled struts is only observed at the inner and outer wall in the AS1 plane and “top” and “bottom” walls of the AS2 plane.

In addition to providing an overview of the transient behavior in the unstented vessel, Figure 4.28 demonstrates that the Dean number cannot be used as a sole predictor of the secondary flow in an unsteady flow regime. For example, the secondary flow pattern at maximum acceleration (Figure 4.28 (A)), which corresponds to $K = 1445$, differs significantly from the structures observed in the same cross-sections for the steady flow simulation at $K = 1450$ (Figure 3.15). Glenn *et al*. and other researchers have suggested techniques to predict the secondary

pattern for unsteady flow for smooth walled vessels and in the vicinity of stented vessels[61,139]. However, no classification regime has been developed for secondary flow structures in stented vessels. Further, the secondary flow structure differs greatly at different cross-sections with the same strut configuration. Figure 4.29 presents the secondary flow structure at equidistant planes with the same AS1 strut configuration at the phases of maximum (Figure 4.29 (A)) and minimum flow rate (Figure 4.29 (B)). At $t/T$ = 0.17, slight variations in the secondary flow structure are observed along the length of the stent. Conversely, the secondary flow structure differs significantly at $t/T$ = 0.44 ((Figure 4.29 (B)) within the AS1 planes. As well, the secondary flow pattern appears to repeat periodically along the length of the stent at this phase. This is indicated by the four coherent structures present in the first and third columns and a single swirling pattern in the second and fourth column in Figure 4.29 (B). A similar trend is observed for other cross-sections at this phase. The behavior at both phases shown in Figure 4.29 confirms the presence of non-developed flow in the stented region. In addition, these observations highlight the strong impact of the oscillatory characteristic of the unsteady waveform.

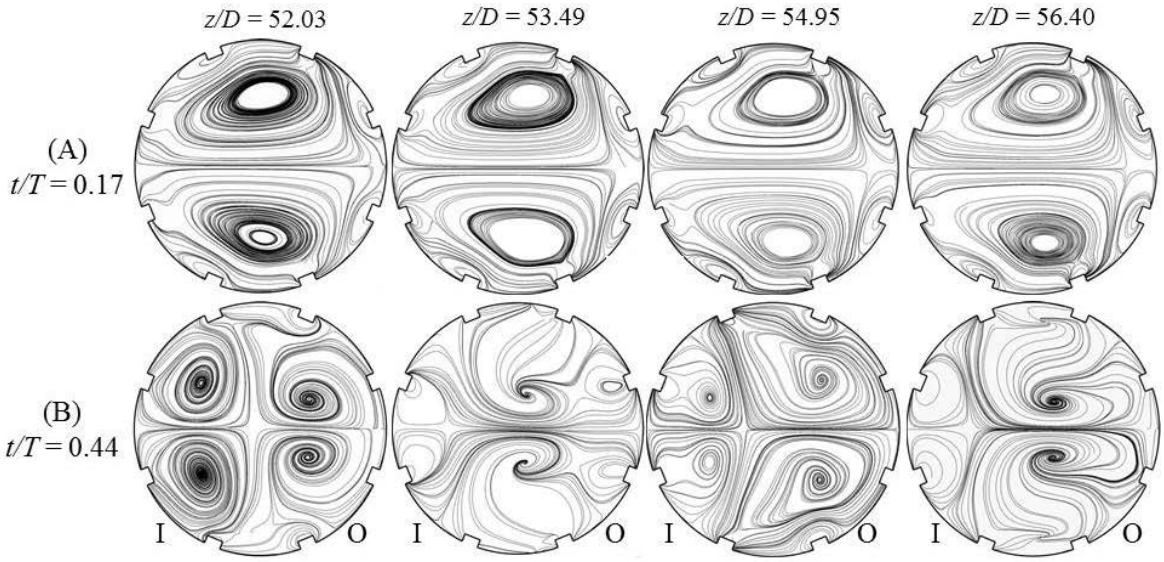


**Figure 4.29 Secondary flow structures at the maximum (A) and minimum (B) flow rate at angled strut planes with the configuration AS1 along the length of the stent for the carotid artery waveform.**

The temporal variation in the spatial distribution in WSSM throughout the cardiac cycle resulting from the presented modification in the streamwise and cross-stream velocity profile is illustrated in Figure 4.30 and Figure 4.31. The contour plots show the instantaneous WSSM the selected time points at the inner and outer wall, in Figure 4.30 and Figure 4.31, respectively. The range of WSSM values at $t/T = 0.44$ area very low in comparison to the other phases, which makes it difficult to visualize the WSSM distribution in the contour plots. However, the plots at this phase are included in Figure 4.30 and Figure 4.31 in order to facilitate the discussion of trends along the inner wall. As the flow approaches the expansion region, there is a minor increase in the WSSM observed at all phase along the outer wall (see Figure 4.31). Within the expansion region, a gradual decrease in the WSSM is observed from the entrance to the first strut intersection at the outer wall. Conversely, this behavior is only observed along the inner wall when anterograde flow is located in the vicinity of the wall (see Figure 4.30 (A) & (B)). This behavior in the expansion region at both walls can be attributed to the increase in the luminal diameter and subsequent reduction in the axial velocity in the expansion region. When retrograde flow is present at the inner wall, WSSM increases in the streamwise direction in the expansion region (see Figure 4.30 (C) & (D)). Overall, the WSS distribution around the struts is similar to the behavior induced by the coronary artery waveform, with lower WSSM regions adjacent to the struts and higher WSSM on the surface of struts and within the intrastrut area.

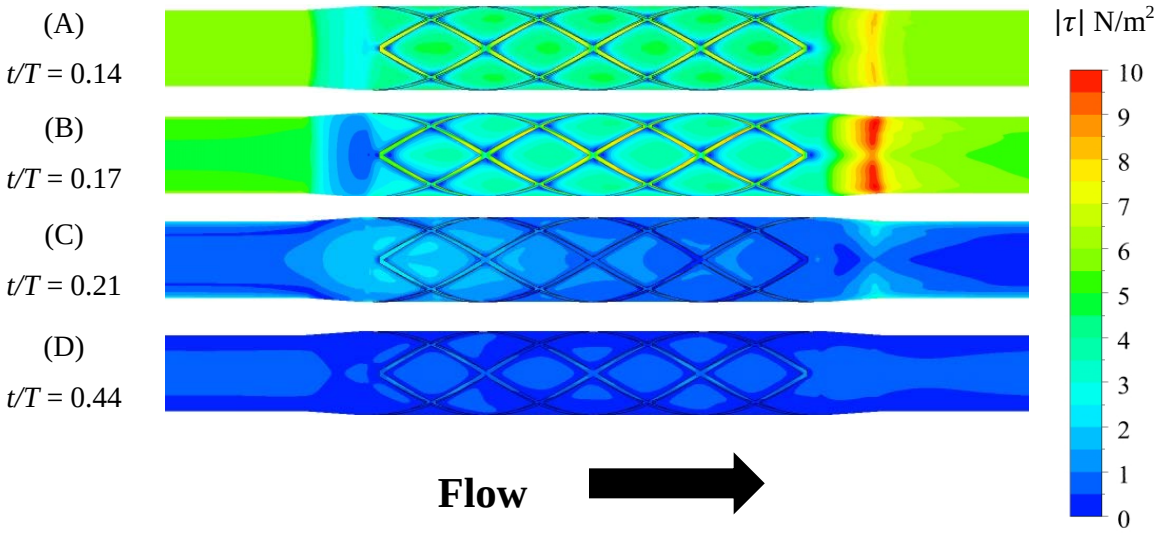


**Figure 4.30 Instantaneous WSSM at selected time points at the inner wall of N4_AR2 for the carotid artery waveform.**

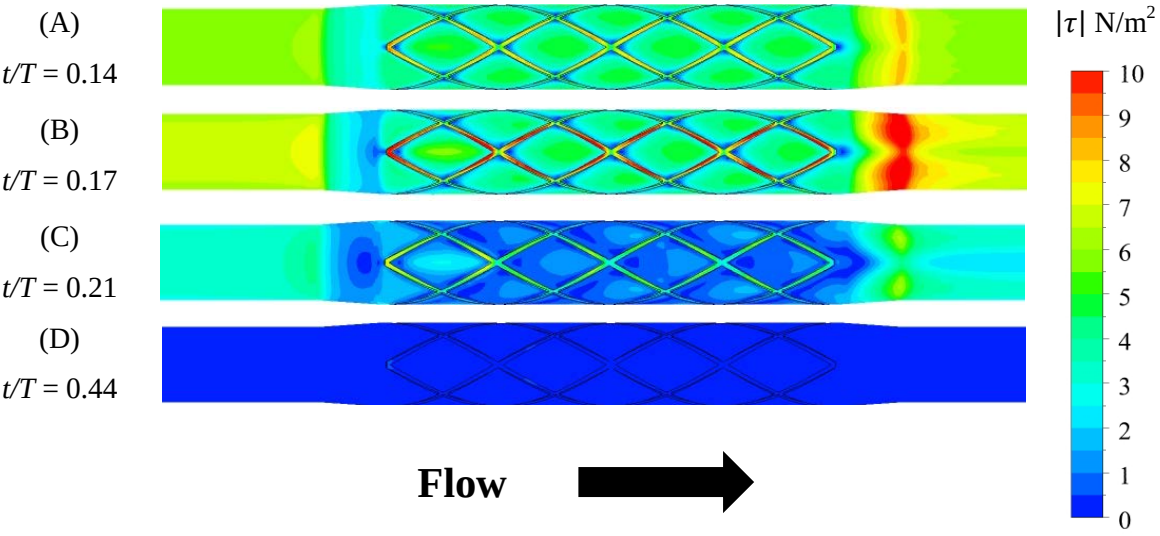


**Figure 4.31 Instantaneous WSSM at selected time points at the outer wall of N4_AR2 for the carotid artery waveform.**

### 4.3.4 *Effect of Geometric Parameters for Carotid Artery Waveform*

In this section, the secondary flow transport topology induced by the carotid artery waveform at IS2 and AS2 is compared for the four stent designs. For continuity, the secondary flow structures are presented at the global maximum and minimum of the acceleration and velocity waveform. While the selected planes and phases do not convey the complete spatial and temporal flow topology, they draw attention to key locations of disruption in the secondary flow morphology as a result of alterations to the strut frequency and aspect ratio. Generally, the effect of the variation in the strut frequency and aspect ratio on the complex carotid secondary flow patterns is similar to the stent induced alteration observed for the coronary. Thus, the discussion of the stent design disruption of the carotid artery secondary flow morphology will highlight significant disruptions pertaining specifically to the carotid artery secondary flow structure.

Firstly, the secondary flow patterns for the 8-strut and 4-strut configurations within the IS2 and AS2 planes are presented in Figure 4.32. A proliferation of recirculation regions around the strut protrusions is observed in the 8-strut configuration at $t/T$ = 0.14 and $t/T$ = 0.17 at the IS2 plane (see Figure 4.32 (A) and (B), Column 1 & 2). This behavior implies an increased risk of excessive ISR due to the synergistic coupling of the recirculation regions to critical WSS exposure. It is noteworthy to point out the difference in the streamwise vortical structures in the IS2 plane generated by the retrograde axial flow at the inner wall at $t/T$ = 0.44 for each strut frequency (see Figure 4.32 (D), Column 1 & 2). Specifically, for the 4-strut configuration, the streamwise vortical structures at the inner wall are abutted by an additional vortical structure on the windward side of the strut at the inner wall (see Figure 4.32 (D), Column 2). In contrast, this additional vortical structure is not present for the 8-strut configuration, which may be a consequence of the circumferential strut spacing (see Figure 4.32 (D), Column 1). Overall, for both the IS2 and AS2 planes, we observe elongation of the Dean vortex for the 4-strut configuration and centralization of the Dean vortex for the 8-strut configuration. This behavior was also observed for the coronary artery waveform and persists for the complex secondary flow structures induced by the carotid artery waveform.

The secondary flow disruption induced by the different aspect ratios is presented in Figure 4.33 and Figure 4.34, for the IS2 and AS2 plane, respectively. The aspect ratio of the struts has a marked impact on the streamwise vortical structures surrounding the strut at the inner and outer wall in the IS2 plane (see Figure 4.33). Particularly, the structures decrease in size as the aspect

ratio increases for all the representative phases except $t/T$ = 0.44. At this phase of minimum flow rate, the streamwise vortical structures, which surround the strut at the inner wall, are generated by strong retrograde flow near the wall. Interestingly, the size of the streamwise vortical structures remains consistent as the aspect ratio of the struts increases (Figure 4.33 (D)). Moreover, the additional vortical structure on the windward side increases in size with increasing aspect ratio. These structures rotate in the clockwise direction, opposite to the streamwise vortical structures. It is concluded that the existence of the additional structures is a consequence of the flow reversal at the inner wall. Rouhi *et al.* has reported, for diamond patterned stent designs, the recirculation zones can increase in size and occupy the intrastrut area between consecutive struts and rise away from the wall as the magnitude of the reverse flow increases[119]. Based on the reported observation, the additional vortical structure at $t/T$ = 0.44 is likely a recirculation region manifested by the flow reversal and whose size is influenced by the strut aspect ratio. In the AS2 plane, the AS6 strut configuration appears to be the optimal configuration with regard to the maintenance of the Dean vortex structure within the plane (see Figure 4.34). Specifically, the Dean vortex structure is consistently present for the representative phases except $t/T$ = 0.44, where an open swirl pattern is present for all aspect ratios.

Large vortical structures, created by the merging of recirculation zones in the intrastrut area as described by Rouhi *et al.*, are observed to migrate away from the inner wall during phases of reverse flow in the near wall region. The vortices migrate at a speed of approximately 0.11m/s, which is around $1/10^{th}$ of the mean inlet velocity of the waveform, and are only observed to leave the near wall region for the carotid artery waveform. Rouhi *et al.* attributed the appearance and migration of the vortices to characteristics of the oscillating flow and in particular to near wall flow reversal that develops despite the unidirectional mean flow[119]. The roughness Reynolds number, $Re_T$, is calculated to determine if the surface roughness introduced by the presence of the stent struts may lead to transition from a laminar to turbulent state and the role transition may play in the development of the observed vortical structures. The roughness Reynolds number is defined as $Re_T = Tw_T/\nu$, where $T$ is the dimensional height of the roughness element and $w_T$ is the streamwise velocity of the flow at height $T$ in the absence of the roughness element[140,141]. Values of $Re_T$ less than 2.25 correspond to regular vortex shedding behind a roughness element and values greater than 90 indicate transition from regular vortex shedding to irregular shedding typical of turbulent flow. The roughness Reynolds number in the vicinity of the struts at the inner wall at maximum inlet velocity is at most 25, which is within the intermediate zone between

laminar and turbulent shedding. This value of $Re_T$ is lower for the coronary artery waveform given the lower inlet velocity characteristic of the waveform. The range of $Re_T$ values for the coronary and carotid artery waveforms implies that the vortex shedding observed on the leeward side of the struts is not likely associated with transition to a turbulent regime. Instead, the unsteady flow phenomenon leads to the observed vortex shedding in the vicinity of the struts during flow reversal at the inner wall for the carotid artery waveform.

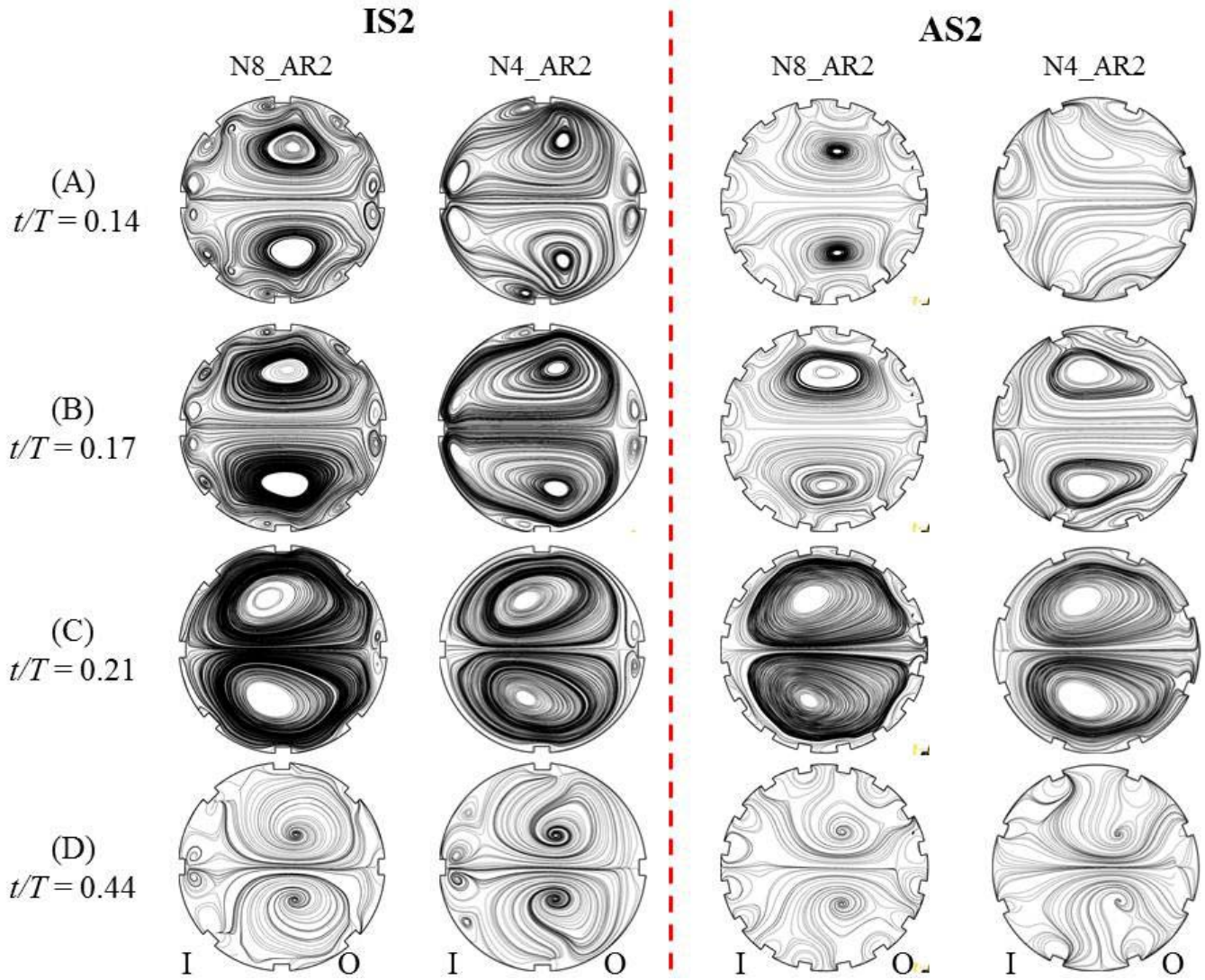


**Figure 4.32 Temporal evolution of the secondary flow structures in N8_AR2 and N4_AR2 geometries in the curvature planes IS2 and AS2 for the carotid artery waveform.**

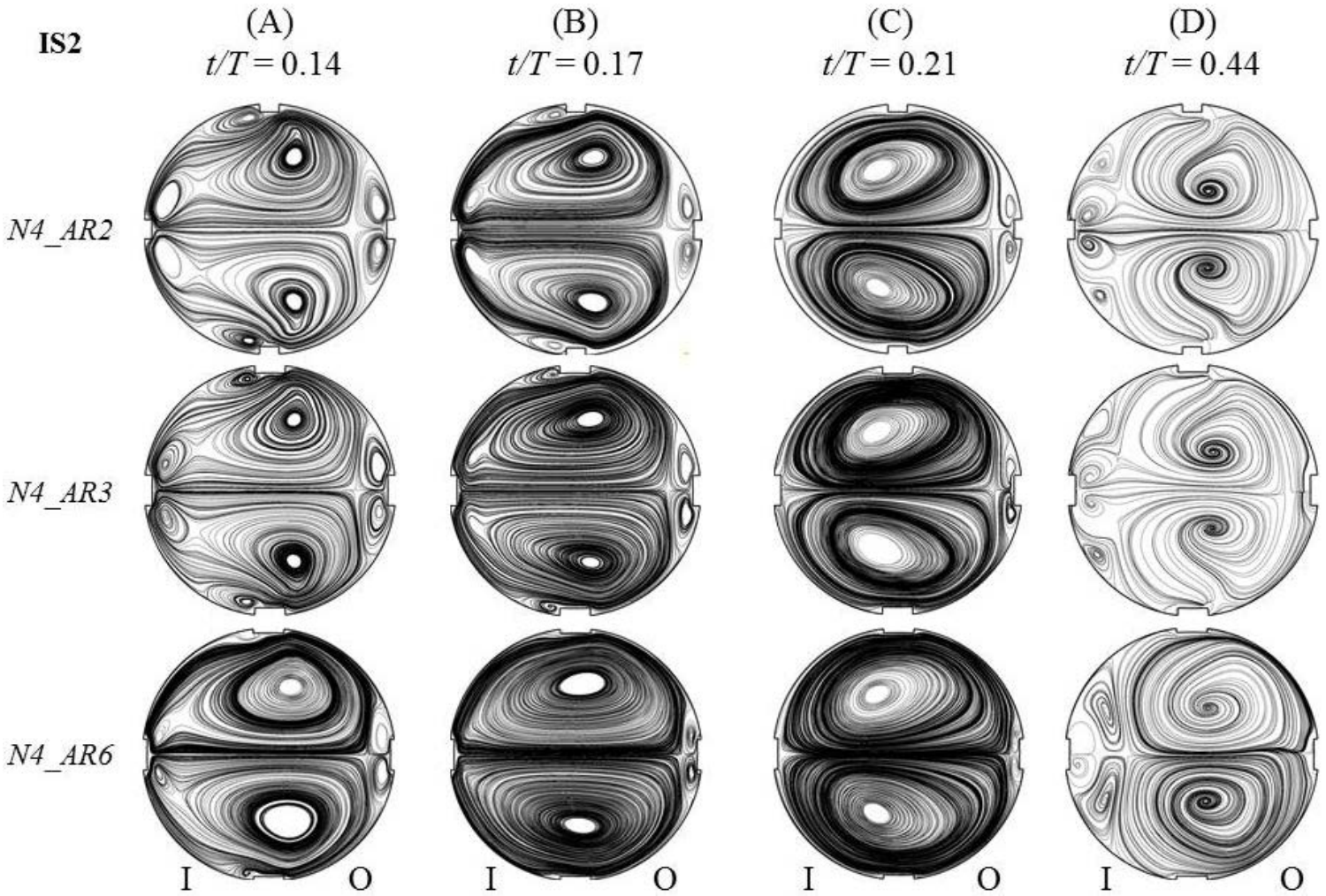


**Figure 4.33 Temporal evolution of the secondary flow for a fixed strut frequency and various aspect ratios in the IS2 plane for the carotid artery waveform.**

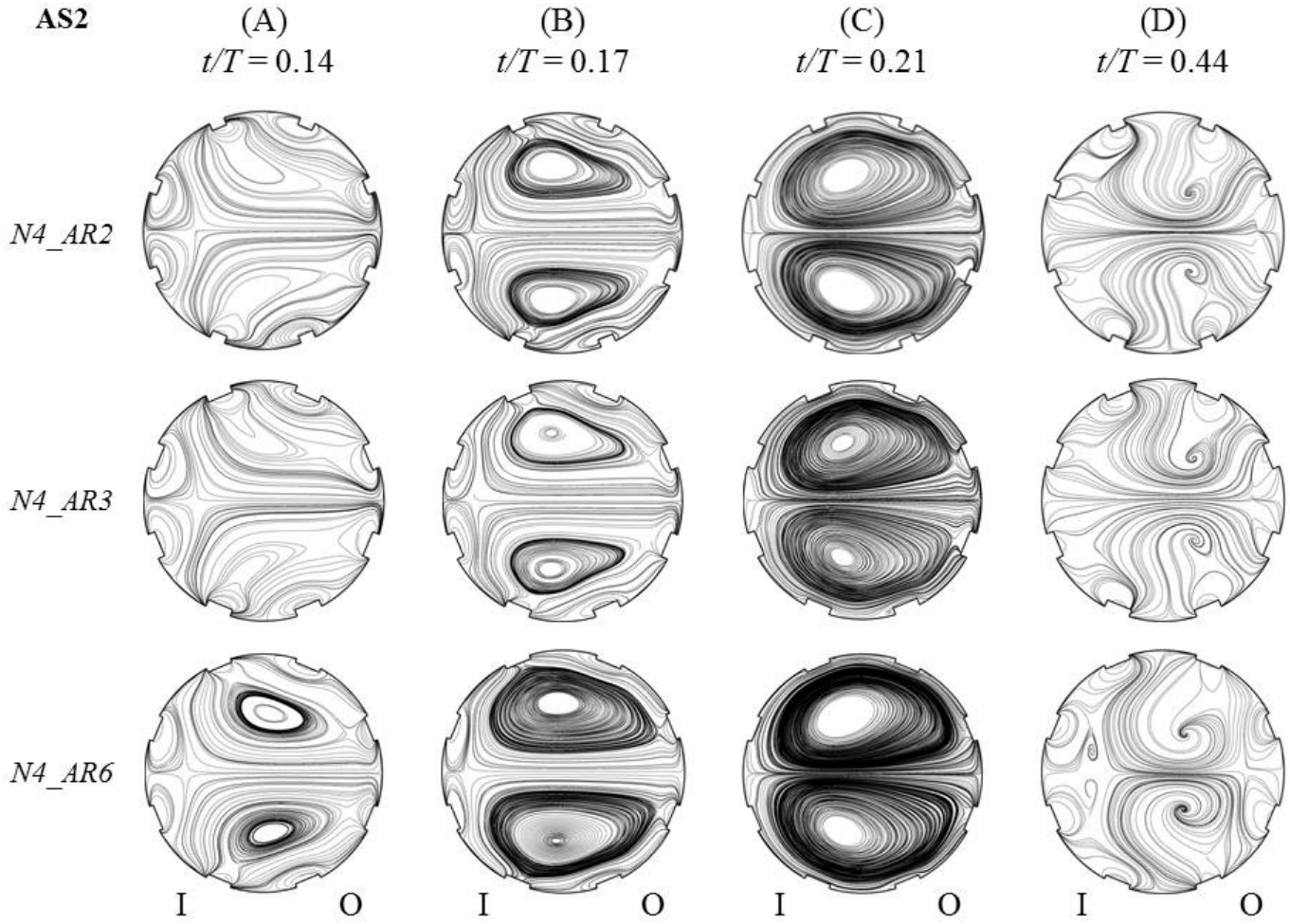


**Figure 4.34 Temporal evolution of the secondary flow for a fixed strut frequency and various aspect ratios in the AS2 plane for the carotid artery waveform.**

The TAWSSM distributions associated with the primary and secondary flow carotid artery behavior discussed is presented in Figure 4.35 and Figure 4.36 along the inner and outer wall, respectively. There are several common TAWSSM traits between the coronary and carotid artery waveforms. These include the lower TAWSSM areas localized around the struts and higher TAWSSM in the intrastrut area at both walls. As expected, the TAWSSM is lower at the inner wall (see Figure 4.35) compared to the outer wall (see Figure 4.36) due to vessel curvature. In addition, elevated TAWSSM is observed on the surface of the struts, at the inception of the expansion region, and terminus of the taper region at the outer wall (see Figure 4.36). The distribution as flow travels through the expansion and taper region is also similar between the waveforms. Specifically, the TAWSSM decreases as flow travels through the expansion region and increases as flow travels through the taper region. The TAWSSM distribution in the entrance and exit vessel distinguishes the TAWSSM behavior for the carotid and coronary artery waveforms. In particular, the difference in magnitude between the outer and inner wall in the entrance region is greater for the carotid artery waveform. This behavior is attributed to increased axial velocity skewing for the high Dean number carotid artery flow. In the exit vessel region, the TAWSSM is initially lower than the values observed in the entrance vessel at the outer wall and higher than the entrance vessel values at the inner wall. The flow redevelops approximately 0.7$D$ from the terminus of the taper region.

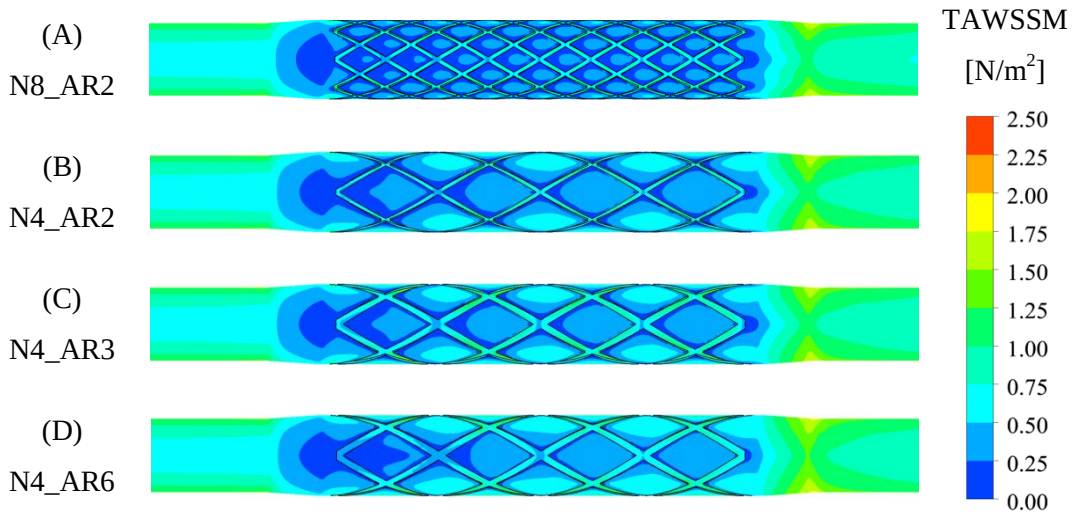


**Figure 4.35 TAWSSM distribution at the inner wall of the pipe for each investigated geometry for the carotid artery waveform.**

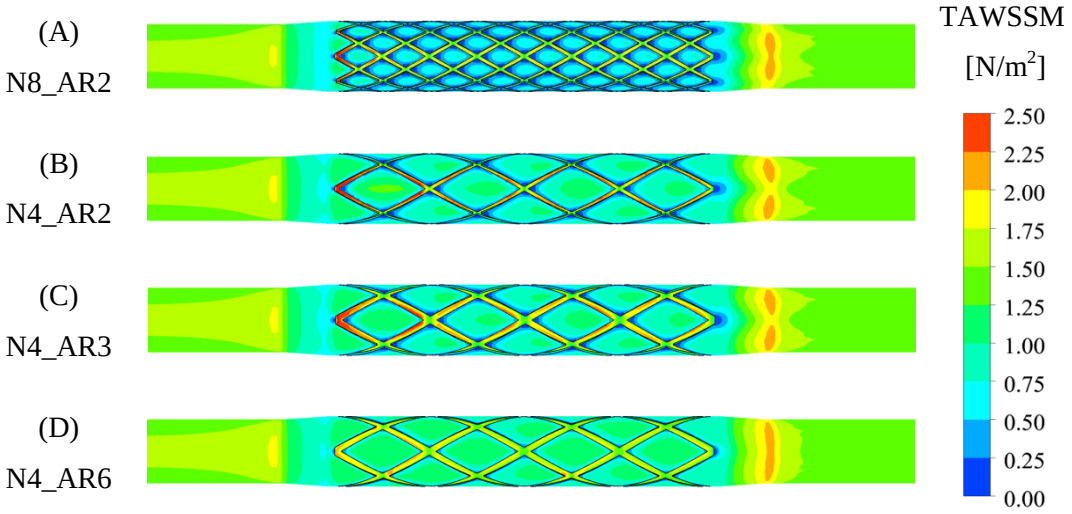


**Figure 4.36 TAWSSM distribution at the outer wall of the pipe for each investigated geometry for the carotid artery waveform.**

The TAWSSM is used as a predictor of NIH development for the coronary waveform to identify high risk ISR regions in Figure 4.36 and Figure 4.37 along the inner and outer wall, respectively. As observed for the stented coronary artery, the risk of excessive NIH is greater at the inner wall compared to the outer wall, as demonstrated by the greater surface area exposed to critical TAWSSM. For coronary artery flow, the critical TAWSSM exposure was localized to the stented region. A distinct feature of the carotid artery waveform is the exposure of the inner wall to moderate TAWSSM within the fully developed region of the entrance vessel, extending 30D from the pipe entrance to the first stent strut. This phenomenon is believed to manifest independent of the stent placement in the vessel; instead, it is an inherent feature of the carotid artery waveform. Specifically, the carotid artery waveform is associated with higher Dean number values and greater outward skew of the axial velocity profile. Further, lower WSSM along the inner walls is correlated with the greater skewing behavior due to the relocation of higher axial velocity fluid toward the outer wall of the pipe and lower velocity flow toward the inner wall. The focal development of atherosclerosis in vessels with high curvature ratio, such as the aorta, has been associated with the endothelium response to low WSS exposure toward the inner wall[136,142]. As such, the identification of moderate TAWSSM regions within the entrance vessel does not necessarily suggest an increased risk of NIH development. The region upstream of the stent may develop NIH if endothelial cells are denuded during stent deployment; however, if endothelial cells remain intact in this region, the subendothelial matrix will not be exposed to blood borne NIH catalyst and critical hemodynamic stresses will not promote tissue accumulation. Within the stented region, vascular injury, resulting in exposure of the subendothelial matrix, is an inevitable result of stent deployment; thus, luminal exposure to low and moderate TAWSSM values in this region is indicative of potential neointimal accumulation. It should be noted that the moderate TAWSSM region redevelops at the inner wall of the exit vessel, approximately 0.7*D* distal to the terminus of the taper region.

Within the stented region, the low TAWSSM exposure is concentrated immediately adjacent to the struts and moderate TAWSSM toward the interior of the intrastrut area for all geometries, in the same manner observed for the steady flow and coronary artery simulations. As observed for the stented coronary artery, the N8_AR2 geometry generates a flow environment with increased susceptibility to ISR development compared to the 4-strut geometry. For the 8-strut configuration, the region of the intrastrut area exposed to critical TAWSSM increases as the flow moves distally along the stent. Qualitatively, for the 4-strut configuration, the size of the area of

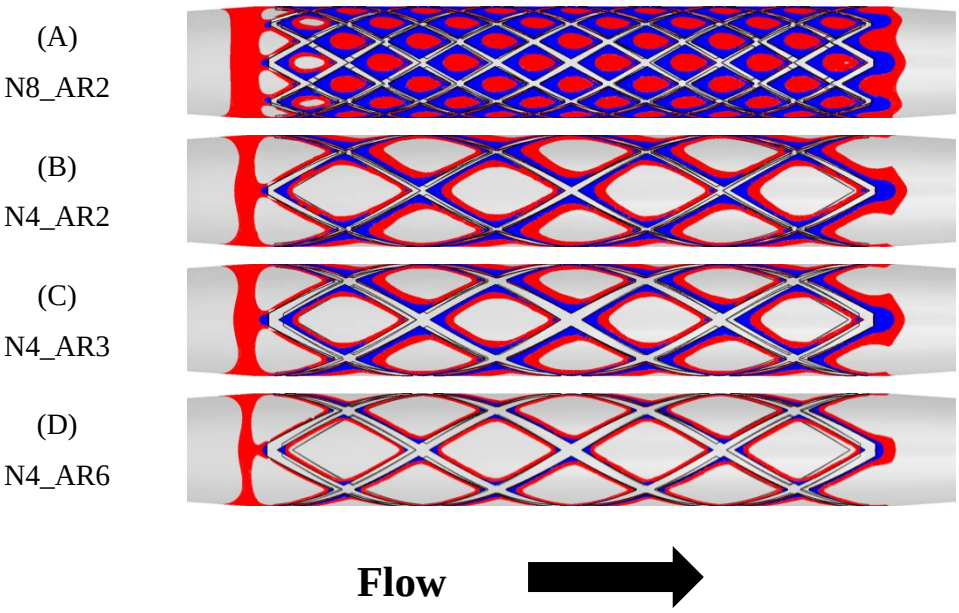


**Figure 4.37 A comparison of the critically low WSSM (red) and moderate WSSM (blue) regions at the outer wall of the investigated geometries for carotid artery waveform.**

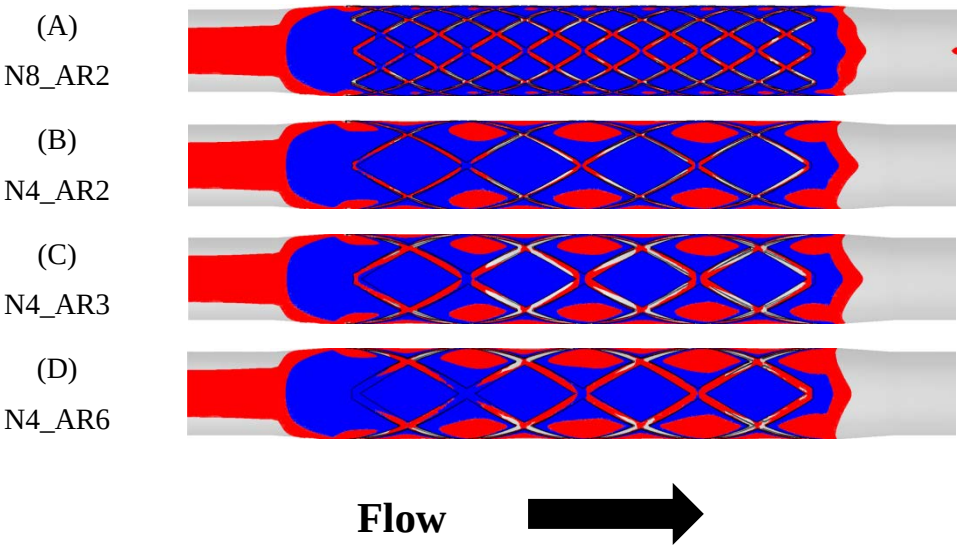


**Figure 4.38 A comparison of the critically low WSSM (red) and moderate WSSM (blue) regions at the inner wall of the investigated geometries for carotid artery waveform.**

the luminal wall subjected to low TAWSSM decreases as the aspect ratio increases. For all geometries, we observe critical TAWSSM exposure on the surface of the struts at the inner wall. This differs from the behavior observed in the stented coronary artery, where critical TAWSSM exposure was relegated to intrastrut areas. The TAWSS distribution on the surface of the struts at the inner wall for the coronary artery is likely due to the inherent axial velocity skew associate with the carotid artery waveform.

The flow phenomenon observed in the contours plots in Figure 4.36 and Figure 4.37 is quantified in Table 4.6. The N8_AR2 generates a flow environment most susceptible to ISR development as demonstrated by 70% of the stented region exposed to critical TAWSS values. The most hemodynamically optimal stent design is N4_AR6, which has the lowest area of critical WSS exposure of 50%. This behavior corroborates the trends discussed for the steady flow and unsteady coronary artery waveform and reinforces the detrimental effects of higher strut frequency and thickness despite the structural benefits. Overall, the exposure to critical TAWSSM increases by 22% on average for the carotid artery waveform compared to the coronary artery waveform. This increase is largely driven by the increased exposure to low TAWSSM for the carotid artery of 19% on average compared to the coronary waveform for all geometries. In contrast, the surface area subjected to moderate TAWSSM values increased by a modest 3% on average for the carotid artery waveform. The increase in the luminal surface area exposed to low WSSM values likely stems from the greater axial skew toward the outer wall, resulting in low velocity flow toward the inner wall.

The curvature induced imbalance in the WSS distribution between the inner and outer wall is exhibited in Table 4.7. Regardless of stent design, we observed greater low and moderate TAWSSM exposure at the inner wall compared to the outer wall. The percentage of the inner wall exposed to the critical range of TAWSS is between 76 – 88% and the percentage of the outer wall is 22-51% for the investigated stent geometries. This distribution indicates that the stent presence alone creates a hemodynamic environment favorable to ISR development in a majority of the vessel. The N8_AR2 geometry generates a flow environment with 50% or more of the inner and outer wall subjected to TAWSS within the critical range. In contrast, the N4_AR6 geometry, consisting of fewer and thinner struts, reduced the exposure at the outer wall considerably and to a lesser degree at the inner wall.

**Table 4.6 Percentage of stented region exposed to low or moderate TAWSSM for the carotid artery waveform.**

| Geometry | TAWSSM [%] | | Total exposure to low or moderate TAWSSM [%] |
|---|---|---|---|
| | Low | Moderate | |
| N8_AR2 | 45.68 | 24.48 | 70.16 |
| N4_AR2 | 31.45 | 28.56 | 60.01 |
| N4_AR3 | 29.62 | 27.84 | 57.46 |
| N4_AR6 | 23.35 | 26.36 | 49.71 |

**Table 4.7 Percentage of inner and outer walls exposed to low or moderate TAWSSM for the investigated geometries for the carotid artery waveform.**

| Geometry | Low TAWSSM [%] | | Moderate TAWSSM [%] | | Total low and moderate exposure [%] | |
|---|---|---|---|---|---|---|
| | Inner | Outer | Inner | Outer | Inner | Outer |
| N8_AR2 | 60.10 | 31.26 | 28.48 | 20.48 | 88.58 | 51.74 |
| N4_AR2 | 49.72 | 13.18 | 31.36 | 25.76 | 81.08 | 38.94 |
| N4_AR3 | 46.38 | 12.86 | 31.50 | 24.18 | 77.88 | 37.04 |
| N4_AR6 | 41.62 | 5.06 | 35.26 | 17.44 | 76.90 | 22.50 |

**Table 4.8 Percentage of the proximal and distal end exposed to low or moderate TAWSSM for the carotid artery waveform.**

| Geometry | Low TAWSSM [%] | | Percent Difference [%] | Moderate TAWSSM [%] | | Percent Difference [%] |
|---|---|---|---|---|---|---|
| | Proximal | Distal | | Proximal | Distal | |
| N8_AR2 | 46.81 | 44.60 | 2.21 | 24.93 | 23.71 | 1.22 |
| N4_AR2 | 34.40 | 28.53 | 6.27 | 28.58 | 28.18 | 0.40 |
| N4_AR3 | 32.53 | 26.75 | 5.78 | 28.18 | 27.12 | 1.06 |
| N4_AR6 | 28.00 | 18.73 | 9.27 | 25.19 | 27.14 | -1.95 |

The predisposition of the proximal portion of the stented region to neointima accumulation is demonstrated in Table 5.8. Interestingly, a higher proportion of the proximal region is exposed to low TAWSSM compared to the distal portion; however, the distribution of moderate TAWSSM is nearly even between each region. The tendency for low TAWSSM exposure in the proximal region can be associated with the flow disturbance due to the fluid interaction with the first proximal strut. The disturbance likely reduces in the distal portion, as observed for the steady flow simulations. Collectively, the unsteady carotid artery flow behavior induces similar tendencies for ISR development due to the stent geometry as observed for the coronary artery. It should be emphasized that characteristics of the carotid artery waveform, such as higher Dean number values, lead to an increase propensity to ISR development in the stented region compared to the coronary artery waveform, regardless of stent design.

### 4.3.5 *Summary of Results*

The goal of this study was to extend our previous work from a comparison between different steady state flow conditions to a comparison of temporal alterations in flow behavior induced by different strut configurations commonly found in stent designs. Results for the transient simulation of blood flow in a model of the coronary artery have been presented. Four different stent designs and two different arterial velocities waveforms have been considered. The coronary artery waveform facilitated the comparison of unsteady flow behavior in the curved vessel to previously reported behavior for straight stented vessels. On the other hand, the implementation of the carotid artery waveform allowed the examination of stent induced flow disturbance in a more complex flow environment. Generally, the results demonstrate that the character of the stent-induced flow disturbance is dynamic in nature. The size of the flow separation zones and critical WSSM regions periodically increases and decreases throughout the cardiac cycle. Furthermore, similar to the steady flow results, the distribution of WSSM within the stented region is strongly dictated by the stent design. Specifically, the steady and unsteady flow simulations demonstrated that fewer and thinner stent struts promoted a flow environment for healthy vascular healing. In addition, the unsteady simulations provided insight into the temporal changes in the secondary flow convective transport mechanism.

Overall, the steady and unsteady simulations draw attention to the high risk of ISR development due solely to the introduction of the stent into the vascular system. In order to achieve a hemodynamically optimal stent design, the structural integrity of the stent may be compromised. The results of this study demonstrate that significant alterations will be required to reduce the area exposed to critical WSS indices below 50% of the stented region. While this study indicates that achieving healthy vascular healing is difficult based on the structural requirement of the stent design, the detailed examination of the secondary flow behavior can aid in the development of next generation drug eluting stents, which rely on the convective transport topology to be effective.

# Chapter 5
# Conclusions

Vascular diseases, such as atherosclerosis, continue to be a major clinical problem plaguing society, causing millions of untimely deaths worldwide each year. The underlying societal motivation of this work is combating cardiovascular disease by improving the clinical outcome of stent implantation, which is used frequently as a treatment option. From the perspective of the clinical use, a stent must fulfil several mechanical and hemodynamic criteria, and device manufactures are attempting to address these by improving stent designs. In part, the success of the stent implantation procedure for the restoration of blood flow through areas of vessel narrowing depends on the promotion of healthy vascular healing post stent implantation. In particular, controlled vascular remodeling allows the stent to be incorporated into the vascular environment and maintain vessel patency. The benefits of stenting in treating cardiovascular disease is appreciable, however, shortcomings of this medical device have resulted in problems post implantation. Unfortunately, many stent procedures fail due to the maladaptive physiological response to arterial injury during deployment and the post implantation local hemodynamic environment. Specifically, abnormal vascular remodeling due to excessive neointimal growth, referred to as neointimal hyperplesia (NIH), leads to in-stent restenosis (ISR). The development of ISR can lead to bypass surgery to circumvent the obstructed region or distal embolisms that result in fatal strokes. By addressing the potentially fatal problem of ISR, this work seeks to reduce the emotional and economic toll of additional surgical procedures due to stent failure and improve the mortality of patients who undergo revascularization procedures.

A putative link has been established between the altered vascular hemodynamics induced by the implanted stent and the localization of uncontrolled NIH development. Abnormal hemodynamics near the stent is an NIH stimulus through the production of abnormal stresses on the endothelial cells and the increased advection of catalyst to the artery wall. Therefore, it is important that the hemodynamic behavior induced by the stent be well understood and the performance of different stent designs evaluated. Several studies have focused on the local flow physics induced by a deployed stent in the vessel lumen to predict the extent of NIH development based on stent geometric properties. To date, a majority of these studies focus on the hemodynamic environment created by a straight stented vessel, as historically the implantation of

the device caused vessel straightening in the deployment region. However, recent advances in stent design allow the device to have increased flexibility, which facilitates easier deployment in the tortuous vascular system and conformation to the native vessel curvature. This design innovation is beneficial from a hemodynamic perspective as it minimizes the changes to the native flow dynamics, such as secondary flow patterns and axial velocity skewing toward the outer wall, to which the endothelial cells lining the vessel are accustomed. However, the maintenance of vessel curvature and the presence of the luminal strut protrusions generate a flow environment that differs greatly from the straight stented vessel geometry. Moreover, hemodynamic design criteria implemented to reduce the susceptibility of ISR in the straight stented vessel may differ in the curved stented vessel. Thus, the hemodynamically optimal stent design needs to be re-evaluated given the new fluid dynamic landscape.

The primary focus of this work is the determination of the extent of the fluid dynamic disturbance induced by the placement of a stent within the lumen of a curved arterial vessel using computational fluid dynamics (CFD). To quantify this disturbance, we have focused on the impact of geometric parameters such as the curvature ratio and stent dimensions, non-dimensional parameters such as the Reynolds and Dean numbers, and in the case of unsteady flow, the value of the Womersely number. The flow field in the vicinity of the curved stented vessel was analyzed in order to establish a relationship between the strut geometry and the flow behavior. Computationally predicted variables, such as wall shear stress (WSS) indices, which are believed to stimulate restenosis, were evaluated to identify regions prone to ISR development in the curved stent. The results of the study can be used to improve stent design, leading to a subsequent reduction in the economic and emotional impact of stent failure and have the public health benefit of decreasing the mortality rate of vascular disease.

The investigation of the local hemodynamic behavior within the curved stent is subdivided into three studies, referred to as Study A, Study B, and Study C. The work presented in Study A included the implementation of a computational model as a first-order approximation of a stent design and representative of a later stage of vascular healing after stent implantation. Specifically, the study focused on the impact of a wavy-wall pipe cross-section, representative of axially aligned smooth struts, on steady flow in a curved tube at moderate Dean numbers and small tube radius-to-radius-of-curvature ratios. Parameters investigated include the protrusion height, the number of protrusions around the tube circumference, and the pipe curvature. This study extended a previous analytical investigation by Peterson that employed a double perturbation expansion to

elucidate the flow field as a function of these parameters. Due to the rapid growth in the solution complexity as the number of terms in each expansion increases, the analytical work is relegated to small wall perturbations and low Dean numbers. These barriers were removed in the present study by numerically solving the Navier-Stokes equations at Dean numbers up to 2500. The impact on the axial and secondary flow structures were emphasized, along with the resulting WSS distributions.

For the range of Dean numbers explored in Study A, the results demonstrated that the flow velocity exhibits the same general characteristics in the wavy walled pipe as in the circular pipe with the same cross-sectional area. The influence of the strut protrusions was relegated to the near wall region, strongly dictating the regions of potential ISR development. This is exemplified by the increase in WSS as the protrusion height increased and decrease in the troughs between the peaks. An increase in the number of protrusions changed the WSS distribution, and as the number approached infinity, the distribution approached that of the circular pipe. However, the area of the vessel wall subjected to low WSS increases due to an increase in the number of troughs with the strut frequency. The curvature induced flow physics was also found to be influenced by the Dean number and the strut frequency and height. The strength of the secondary flow increased with the Dean number, which is consistent with behavior observed in curved pipes with a circular cross-section. In addition, an increase in the protrusion height and strut frequency decreased the strength of the secondary flow. This result is likely due to the additional circumferential surface area that retards the fluid motion. The presence of higher circulation strength can reduce the likelihood of NIH catalyst being transported to the vessel wall. Overall, the results elucidate the flow behavior after the initial stages of endothelization when the strut protrusions have been smoothed by neointima growth and endothelial resurfacing. This study established that smooth axially aligned struts result in flow disturbance in the near wall region and dictates the areas of the luminal wall susceptible to ISR development. Moreover, the transport of blood borne NIH catalyst is affected by changes in strut frequency and dimensions via alterations in the strength of the secondary flow.

The numerical solution presented in Study A is limited in its approximation of stent flow, since it neglects any circumferential protrusions, leading and trailing edge effects and the inception of curvature. In Study B, a computational model with increased complexity mimicking commercially available stents is used to investigate the hemodynamic stimuli that can cause restenosis of a curved stented artery. The model is used to illustrate the acute changes in the flow

environment induced by the stent implantation, which dictates the late stage reestablishment of the endothelium. The hemodynamic performances of four different stent designs that include axial and circumferential protrusions and conform to the curvature of the coronary artery are evaluated. The study quantified the differences between the stent models and determined the effects of the chosen constitutive model on the evaluation of the fluid environment in the stent vicinity. To systematically explore the predilection for NIH development based the stent design, the strut characteristics such as thickness, width, and frequency were varied within a range limited to that previously investigated in straight stented vessels. This allowed the comparison of flow behavior in a curved stented vessel in the current work to previously published work investigating flow in straight stented vessels. In addition, the rectangular shape of the struts in Study A facilitated the comparison of flow behavior around curved and sharp protrusions. Moreover, this study extended the parameter space previously investigated for curved stent models by including a wide range of physiologically relevant Dean numbers and the exploration of different constitutive models.

The numerical simulations performed in Study B demonstrated that the presence of the strut protrusions results in changes in the morphology and strength of the native secondary flow structure along the length of the stent. The impact of the strut protrusions was localized in the near wall region in particular cross-sections and completely distorted the secondary flow pattern in other cross-sections. Portions of the stented region where the flow had to sharply navigate around the protrusions resulted in the development of vortices and recirculation regions. The location of these regions coincides with the location of the luminal wall exposed to critical WSS and results in increased susceptibility of these areas to NIH development based on the WSS criteria. Interestingly, the overall pattern of WSS distribution in the immediate vicinity of the stent struts was found to be consistent across all stent models and similar to previously reported behavior in straight stented vessels. However, the transport mechanism of NIH catalyst, such as secondary flow, to these regions differed between the stent designs and subsequently changes the potential risk of excessive NIH development in the regions subject to critical WSS. The disturbance of the secondary flow and the areas exposed to critical WSS was minimized in the stent designs with thinner and wider struts. The most prominent difference in the WSS distribution in the curved stent compared to the straight stented vessel models was the imbalance between the inner and outer wall driven by the vessel curvature. The disparity of the WSS distribution between the walls results in higher initiation of ISR at the inner wall compared to the outer wall. The imbalance in WSS between the walls suggests the potential benefit of implementing of different design criteria

along each wall. Lastly, the comparison of the simulation results for the Newtonian and non-Newtonian models suggest that use of the Newtonian fluid model does not have a negative impact on the flow characteristics important in stent design. In fact, the implementation of a Newtonian model to determine the stent design characteristics important for the optimal hemodynamic performance of the curved stent design will lead to a conservative stent design that will ensure minimal excessive NIH development.

The unsteady flow behavior implemented in Study C increased the realism of the computation model to provide a closer approximation of flow behavior in the vascular system. Two physiological unsteady flow conditions were modeled in this study to emulate flow in two commonly stented vessels, the right coronary artery (RCA) and the left and right carotid artery. The same geometry was used to investigate the stent induced flow behavior in the presence of coronary and carotid artery flow conditions, since their curvature ratios are similar depending on the patient specific anatomy and phase of the cardiac cycle. Modeling both arterial flows allowed for exploration of a broader range of parameter values, adding insight into the flow physics in relation to the governing non-dimensional parameters for unsteady flows in curved tubes with stents. Using a similar analysis as implemented in Study B, a detailed analysis of the secondary flow at key phases of the physiological waveform was conducted and the stent design that minimized that area of critical time-averaged WSS was determined.

The simulation results of Study C indicate the complex secondary flow morphologies that arise due to the combination of the unsteady flow regime, the centrifugal and radial pressure gradient instabilities, and the presence of strut protrusions within the stented region. A poignant feature revealed by the unsteady flow simulation is the diverse secondary flow morphologies that develop during the cardiac cycle and how these structures differed based on the physiological waveform. The carotid artery waveform generates more complex flow behavior compared to the coronary artery waveform, due to the higher Womersley value and Dean number flow associated with the carotid artery waveform. This increased complexity corroborates the results for higher frequency flows in unstented vessels. For both waveforms, the diversity of the secondary flow structures at different phases of the waveform demonstrates the changes in the transport of blood borne particulates. The detailed secondary flow analysis highlights the important implication of the stent design on the transport topology in the unsteady flow regime. The waveforms result in not only changes to the secondary flow, but also to regions of retrograde flow, which, in conjunction with the secondary flow, provides additional residence time of NIH catalyst in the

near wall region. Time-averaged WSS distribution revealed the increased risk of NIH development at the proximal end and inner wall of the vessel regardless of the physiological waveform. The percentage of the vessel exposed to critical WSS predicted by the steady flow simulations, based on the mean coronary artery velocity, was greater compared the area predicted by the unsteady coronary flow simulations. Furthermore, the area of the vessel exposed to critical WSS was greater for the carotid artery waveform compared to the coronary artery waveform. This finding highlights the ramifications of using steady flow simulations to model *in vivo* flow conditions and the differences in the flow environment induced by the waveforms. Overall, the results reveal the complex fluid structure interaction within a stented vessel at different locations in the vascular system.

Collectively, the studies in this thesis provide clinically important detailed analysis of flow behavior in the vicinity of a curved stent to provide insight to the hemodynamic mechanisms of restenosis. As an overall conclusion, the results of this work suggest the benefits of a stent that conforms to the vessel curvature. The proposed work provides fundamental scientific knowledge of the flow physics in the vicinity of a stent based on general stent design characteristics. The results can be applied to the design of stents currently on the market such as bare metal and drug eluting stents. Specifically, the hemodynamic results presented in this work can be coupled with information regarding the structural integrity of each stent design to guide the development of next generation stent designs. Further, the conclusions from Study B and C indicated that structural integrity loss due to accommodations made for hemodynamic optimization can recovered by adjusting the strut width, since this is a geometric parameter that causes minimal flow disturbance.

Recent advances in stent technology, such as drug eluting stents, have provided hope in eradicating the problem of ISR. Drug eluting stents (DES) use the stent structure to deliver drugs that reduce the likelihood of ISR by attaining acceptable vessel remodeling. Unfortunately, this novel stent design has been implicated in reduced rates of endothelization and stent thrombosis, making it a promising though not completely effective solution to ISR. By resolving the flow physics in the vicinity of DES, a better understanding of the dissipation and transport of the drugs in the stent region can be acquired. By having a clearer idea of the percentage of the vessel that may be at risk for NIH development we have a clearer understanding of the potential ability for drugs to counteract the NIH development. Lastly, the study provides a computational framework to analyze advective processes in the curved vessel that lead to NIH accumulation to further

illuminate the role of hemodynamic behavior in ISR development. The detailed information included in this thesis can be used to guide next generation stent design.

# Chapter 6
# Recommendations for Future Work

The presented computational model provides a platform for future studies to further explore the hemodynamic barriers to healthy vascular remodeling created by the stent design characteristics. Assumptions made in the computational model included in this thesis results in some degree of deviation from the actual flow physics within the stented region. The current results should be interpreted within the constraints of several limitations, which should be improved upon in future work. The observations and conclusions in the current study are based upon stents implanted in an idealized representation of a healthy curved vessel. For example, the assumption that the vessel wall is rigid is unrealistic and could have several implications on the predicted flow behavior. The arterial wall has elastic properties that would result in significant deviations from the perfectly cylindrical shape of the stented segment of the vessel implemented in the present study. Previous studies have established that the implanted stent changes the vascular compliance and the assumption of rigid wall within the stented region does not have significant implications for the prediction of flow behavior with in the region. However, upstream and downstream of the stent, the vessel wall is compliant and will likely plays a role in the flow behavior approaching and leaving the stented region.

An important question for future studies is the role that compliance mismatch plays in the alteration of hemodynamics within the stented region. It would be advantageous to implement vessel compliance into the modeling of stented vascular flow in order to create a more realistic model of the vascular geometry. Arterial prolapse in the intrastrut area of the stent is another consequence of arterial compliance, especially when the number of struts is reduced. This is especially important in light of the fact that changes in wall shape can alter the WSS distribution and localization of ISR susceptible regions. In straight stented vessels, previous studies including vessel prolapse have reported a modest increase in the size of the luminal wall subjected to low WSS compared to non-prolapsed vessels. However, the area predicted to be exposed to high WSSG was 20 – 30% greater when prolapse was included. Future studies should take into account the arterial prolapse in the intrastrut area of the curved stented in light of the fact that hemodynamic stress predictions are utilized to optimize stent designs.

A stent design implemented in the present study was symmetrical about the plane of the bend; however, in clinical use, the stents may expand in an eccentric fashion as a result of the non-

uniform arterial plaque deposition along the vessel walls or non-uniform internal expansion of the deployment balloon. Asymmetric stent expansion can be an additional important determinant of NIH development due to excessive vessel injury in certain locations. In addition, altering the strut alignment with the primary flow direction can change the predicted WSS distribution and the transport topology in the curved stented vessel. By modeling asymmetric stent placement, in conjunction with the symmetric stent design, we can garner a better understanding of the full range of flow disturbances due to the placement of the stent and create a more realistic stent model.

For the unsteady simulation, the present investigation assumed a fixed vessel curvature throughout the cardiac cycle and no wall motion. In reality, the vessel curvature of the coronary artery changes shape as the heart beats. In addition, distention and contraction of the vessel wall can occur due to the pulsatility of the flow. Variations in the vessel curvature throughout the cardiac cycle can have a significant effect on the predicted flow behavior and the WSS distribution. Generally, these changes in vessel curvature have been ignored by other studies. However, the inclusion of this behavior can lead to a more realistic stent model and incorporate mechanical and hemodynamic optimization into the stent design process.

As society moves toward an era of personalized medicine, the tailoring of medical devices to patients based on their unique anatomy is becoming an achievable goal in the near future. Recent advances in medical imaging and computational modeling capabilities have allowed the construction of patient specific artery models for the prediction of individualized stent performance. This is very important for the future of stent designs as the design characteristics can be altered to accommodate the specific patient geometry, especially with the advent of rapid prototyping procedures. By combining the patient specific results with existing knowledge of endothelial response to mechanical stimuli, the stent design can be optimized to reduce the likelihood or virtually eliminate the risk of ISR.

# Bibliography


1. Shipkowitz T, Rodgers VGJ, Frazin LJ, Chandran KB. Numerical study on the effect of secondary flow in the human aorta on local shear stresses in abdominal aortic branches. *J Biomech*. 2000;33(6):717-728.

2. VanderLaan PA, Reardon CA, Getz GS. Site specificity of atherosclerosis: Site-selective responses to atherosclerotic modulators. *Arteriosclerosis, Thrombosis, and Vascular Biology*. 2004;24(1):12-22.

3. American Heart Association. American heart association. http://www.americanheart.org/. Updated 2010.

4. Glueck CJ, Connor WE. Diet and atherosclerosis - past, present and future. *Western Journal of Medicine*. 1979.

5. Giddens DP, Zarins CK, Glagov S. The role of fluid mechanics in the localization and detection of atherosclerosis. *J Biomech Eng*. 1993;115(4B):588-594.

6. Tortora GJ, Roesch B. *Principles of anatomy & physiology, ninth edition.* 9 Sub ed. John Wiley & Sons Inc; 2000:1200.

7. Pugsley MK, Tabrizchi R. The vascular system - an overview of structure and function. *J Pharmacol Toxicol Methods*. 2000;44(2):333-340.

8. Libby P. Inflammation in atherosclerosis. *Nature*. 2002;420(6917):868-874.

9. Marx SO, Totary-Jain H, Marks AR. Vascular smooth muscle cell proliferation in restenosis. *Circulation: Cardiovascular Interventions*. 2011;4(1):104-111.

10. Marieb EN, Hoehn K. *Human anatomy & physiology*. 8th ed ed. San Francisco: Benjamin Cummings; 2010.

11. White FM. *Fluid mechanics.* 6th ed. McGraw-Hill Science/Engineering/Math; 2006:864.

12. Chien S. Effects of disturbed flow on endothelial cells. *Ann Biomed Eng*. 2008;36(4):554-562.

13. Gibbons GH, Dzau VJ. The emerging concept of vascular remodeling. *N Engl J Med*. 1994;330(20):1431-1438.

14. Li YJ, Haga JH, Chien S. Molecular basis of the effects of shear stress on vascular endothelial cells. *Journal of Biomechanics,*. 2005;38(10):1949-1971.

15. Otsuka F, Finn AV, Yazdani SK, Nakano M, Kolodgie FD, Virmani R. The importance of the endothelium in atherothrombosis and coronary stenting. *Nat Rev Cardiol*. 2012;9(8):439-453.

16. Berenger FP, Cano JP, Rolland PH. Antithrombogenic endothelial-cell defense - basal characteristics in cultured endothelial-cells and modulation by short-term and long-term exposure to isosorbide nitrates. *Circ Res*. 1987;60(4):612-620.

17. Ballermann BJ, Dardik A, Eng E, Liu A. Shear stress and the endothelium. *Kidney Int Suppl*. 1998;67:S100-8.

18. Melchior B, Frangos JA. Shear-induced endothelial cell-cell junction inclination. *American Journal of Physiology-Cell Physiology*. 2010;299(3):C621-C629.

19. Ku DN. Blood flow in arteries. *Annu Rev Fluid Mech*. 1997;29(1):399-434.

20. Kim S, Kong RL, Popel AS, Intaglietta M, Johnson PC. Temporal and spatial variations of cell-free layer width in arterioles. *American Journal of Physiology - Heart and Circulatory Physiology*. 2007;293(3):H1526-H1535.

21. Leuprecht A, Perktold K. Computer simulation of non-newtonian effects on blood flow in large arteries. *Comput Methods Biomech Biomed Engin*. 2001;4(2):149-163.

22. Eskin SG, Ives CL, McIntire LV, Navarro LT. Response of cultured endothelial cells to steady flow. *Microvasc Res*. 1984;28(1):87-94.

23. van der Meer AD, Poot AA, Feijen J, Vermes I. Analyzing shear stress-induced alignment of actin filaments in endothelial cells with a microfluidic assay. *Biomicrofluidics*. 2010;4(1):011103.

24. Widmaier EP, Raff H, Strang KT. *Vander's human physiology : The mechanisms of body function.* 10th ed. Boston: McGraw-Hill; 2006:827.

25. Roger VL, Go AS, Lloyd-Jones DM, et al. Heart disease and stroke statistics--2011 update: A report from the american heart association. *Circulation*. 2010.

26. Dewey CF, Bussolari SR, Gimbrone MA, Davies PF. The dynamic response of vascular endothelial cells to fluid shear stress. *Transactions of the ASME.Journal of Biomechanical Engineering*. 1981;103(3):177-185.

27. Pannier B, Guérin AP, Marchais SJ, Métivier F, London GM. Arterial structure and function in end-stage renal disease. *Artery Research,*. 2007;1(2):79-88.

28. Wootton DM, Ku DN. Fluid mechanics of vascular systems, diseases, and thrombosis. *Annu Rev Biomed Eng*. 1999;1:299-329.

29. Purves WK. *Life, the science of biology.* Sunderland, MA: Sinauer Associates; 1998.

30. Choudhury RP, Lee JM, Greaves DR. Mechanisms of disease: Macrophage-derived foam cells emerging as therapeutic targets in atherosclerosis. *Nature clinical practice Cardiovascular medicine, June 01*. 2005;2(6):309-315.

31. Duraiswamy N, Schoephoerster RT, Moreno MR, Moore JE, Jr. Stented artery flow patterns and their effects on the artery wall. *Annu Rev Fluid Mech*. 2007;39:357-382.

32. Kukreja N, Onuma Y, Daemen J, Serruys PW. The future of drug-eluting stents. *Pharmacological Research*. 2008;57(3):171-180.

33. Moore J, Berry J. Fluid and solid mechanical implications of vascular stenting. *Ann Biomed Eng*. 2002;30(4):498-508.

34. Martin DM, Boyle FJ. Drug-eluting stents for coronary artery disease: A review. *Med Eng Phys*. 2011;33(2):148-163.

35. Wholey M, Finol E. Designing the ideal stent. *Endovascular Today*. 2007(6):25.

36. Duerig T, Wholey M. A comparison of balloon- and self-expanding stents. *Minimally Invasive Therapy & Allied Technologies*. 2002;11(4):173-178.

37. Garasic JM, Edelman ER, Squire JC, Seifert P, Williams MS, Rogers C. Stent and artery geometry determine intimal thickening independent of arterial injury. *Circulation*. 2000;101(7):812-818.

38. Stoeckel D, Bonsignore C, Duda S. A survey of stent designs. *Minimally Invasive Therapy & Allied Technologies*. 2002;11(4):137-147.

39. Capelli C, Gervaso F, Petrini L, Dubini G, Migliavacca F. Assessment of tissue prolapse after balloon-expandable stenting: Influence of stent cell geometry. *Med Eng Phys*. 2009;31(4):441-447.

40. Whittaker DR, Fillinger MF. The engineering of endovascular stent technology: A review. *Vascular and Endovascular Surgery*. 2006;40(2):85-94.

41. Hara H, Nakamura M, Palmaz JC, Schwartz RS. Role of stent design and coatings on restenosis and thrombosis. *Adv Drug Deliv Rev*. 2006;58(3):377.

42. Gomez-Lara J, Brugaletta S, Farooq V, et al. Angiographic geometric changes of the lumen arterial wall after bioresorbable vascular scaffolds and metallic platform stents at 1-year follow-up. *JACC: Cardiovascular Interventions*. 2011;4(7):789-799.

43. Pfeiffer N, Mandrusov E, Vroman L, Leonard EF. Effects of secondary flow caused by a curved channel on plasma protein adsorption to artificial surfaces. *Biotechnol Prog*. 1998;14(2):338-342.

44. Vroman L. Finding seconds count after contact with blood (and that is all I did). *Colloids and Surfaces B: Biointerfaces,*. 2008;62(1):1-4.

45. Bates E, McGillem M, Beals T, et al. Effect of angioplasty-induced endothelial denudation compared with medial injury on regional coronary blood-flow. *Circulation*. 1987;76(3):710-716.
46. Weintraub WS. The pathophysiology and burden of restenosis. *Am J Cardiol*. 2007;100(5A):3K-9K.
47. Jackson SP. Arterial thrombosis-insidious, unpredictable and deadly. *Nat Med*. 2011;17(11):1423-1436.
48. Clemetson KJ. Platelets and primary haemostasis. *Thromb Res*. 2012;129(3):220-224.
49. Simon D, Chen Z, Seifert P, Edelman E, Ballantyne C, Rogers C. Decreased neointimal formation in mac-1(-/-) mice reveals a role for inflammation in vascular repair after angioplasty RID A-6599-2008. *J Clin Invest*. 2000;105(3):293-300.
50. Nesbitt WS, Westein E, Tovar-Lopez FJ, et al. A shear gradient-dependent platelet aggregation mechanism drives thrombus formation. *Nat Med*. 2009;15(6):665-U146.
51. Edelman ER, Rogers MD, Campbell. Pathobiologic responses to stenting. *Am J Cardiol*. 1998;81(7, Supplement 1):4E-6E.
52. Chung I, Gold H, Schwartz S, Ikari Y, Reidy M, Wight T. Enhanced extracellular matrix accumulation in restenosis of coronary arteries after stent deployment. *J Am Coll Cardiol*. 2002;40(12):2072-2081.
53. Evans DJW, Jackman LE, Chamberlain J, et al. Platelet P2Y12 receptor influences the vessel wall response to arterial injury and thrombosis. *Circulation*. 2009;119(1):116-122.
54. Wagner DD. New links between inflammation and thrombosis. *Arteriosclerosis Thrombosis and Vascular Biology*. 2005;25(7):1321-1324.
55. Inoue T, Croce K, Morooka T, Sakuma M, Node K, Simon DI. Vascular inflammation and repair: Implications for re-endothelialization, restenosis, and stent thrombosis. *J Am Coll Cardiol Intv*. 2011;4(10):1057-1066.
56. Rogers C, Edelman E, Simon D. A mAb to the beta(2)-leukocyte integrin mac-1 (CD11b/CD18) reduces intimal thickening after angioplasty or stent implantation in rabbits. *Proc Natl Acad Sci U S A*. 1998;95(17):10134-10139.
57. Kipshidze N, Dangas G, Tsapenko M, et al. Role of the endothelium in modulating neointimal formation: Vasculoprotective approaches to attenuate restenosis after percutaneous coronary interventions. *J Am Coll Cardiol*. 2004;44(4):733-739.
58. Wong A, Chan C. Drug-eluting stents: The end of restenosis? *Annals Academy of Medicine Singapore*. 2004;33:423.

59. Chandran KB, Swanson WM, Ghista DN, Vayo HW. Oscillatory flow in thin-walled curved elastic tubes. *Ann Biomed Eng*. 1974;2(4):392-412.

60. Chandran KB, Yearwood TL. Experimental study of physiological pulsatile flow in a curved tube. *J Fluid Mech*. 1981;111:59.

61. Sudo K, Sumida M, Yamane R. Secondary motion of fully developed oscillatory flow in a curved pipe. *Journal of Fluid Mechanics Digital Archive*. 1992;237:189.

62. Siggers JH, Waters SL. Steady flows in pipes with finite curvature. *Phys Fluids*. 2005;17(7):077102.

63. Dean WR. Fluid motion in a curved channel. *Proceedings of the Royal Society of London.Series A, Containing Papers of a Mathematical and Physical Character*. 1928;121(787):402-420.

64. Dyke M. Extended stokes series: Laminar flow through a loosely coiled pipe. *J Fluid Mech*. 1978;86:129-145.

65. White CM. Streamline flow through curved pipes. *Proceedings of the Royal Society of London.Series A, Containing Papers of a Mathematical and Physical Character*. 1929;123(792):645-663.

66. Collins WM, Dennis SCR. The steady motion of A viscous fluid in A curved tube<br />. *The Quarterly Journal of Mechanics and Applied Mathematics*. 1975;28(2):133-156.

67. Berger SA, Talbot L, Yao LS. Flow in curved pipes. *Annu Rev Fluid Mech*. 1983;15(1):461-512.

68. Ito H. Flow in curved pipes. *JSME international journal*. 1987;30(262):543.

69. Snyder B, Hammersley JR, Olson DE. The axial skew of flow in curved pipes. *Journal of Fluid Mechanics*. 1985;161:281-294.

70. Sumida M. Pulsatile entrance flow in curved pipes: Effect of various parameters. *Exp Fluids*. 2007;43(6):949-958.

71. Boiron O, Deplano V, Pelissier R. Experimental and numerical studies on the starting effect on the secondary flow in a bend. *J Fluid Mech*. 2007;574:109-129.

72. Zabielski L, Mestel AJ. Unsteady blood flow in a helically symmetric pipe. *J Fluid Mech*. 1998;370(-1):321.

73. Peterson SD. Steady flow through a curved tube with wavy walls. *Phys Fluids*. 2010;22(2):023602.

74. Dennis SCR, Ng M. Dual solutions for steady laminar flow through A curved tube. *The Quarterly Journal of Mechanics and Applied Mathematics*. 1982;35(3):305-324.

75. Cheng K, Mok S. Flow visualization studies on secondary flow patterns and centrifugal instability phenomena in curved tubes. *International Symposium on Fluid Control and Measurement -- FLUCOME Tokyo '85*. 1985.

76. Daskopoulos P, Lenhoff AM. Flow in curved ducts: Bifurcation structure for stationary ducts. *Journal of Fluid Mechanics*. 1989;203:125-148.

77. Pedley TJ. Mathematical modelling of arterial fluid dynamics. *J Eng Math*. 2003;47(3-4):419-444.

78. Topakoglu HC, Ebadian MA. Viscous laminar flow in a curved pipe of elliptical cross-section. *Journal of Fluid Mechanics*. 1987;184:571-580.

79. Wang CY. Stokes flow through a tube with bumpy wall. *Phys Fluids*. 2006;18(7):078101.

80. Wang CY. Effect of helical corrugations on the low reynolds number flow in a tube. *AICHE J*. 2006;52(6):2008-2012.

81. Michael R. K. Do blood capillaries exhibit optimal bumpiness? *J Theor Biol*. 2007;249(1):178-180.

82. Sumagin R, Brown C, Sarelius I, King M. Microvascular endothelial cells exhibit optimal aspect ratio for minimizing flow resistance. *Annals of Biomedical Engineering*. 2008;36(4):580-585.

83. Pozrikidis C. Stokes flow through a twisted tube. *J Fluid Mech*. 2006;567:261-280.

84. Kastrati A, Mehilli J, Dirschinger J, et al. Intracoronary stenting and angiographic results : Strut thickness effect on restenosis outcome (ISAR-STEREO) trial. *Circulation*. 2001;103(23):2816-2821.

85. LaDisa JF,Jr, Olson LE, Guler I, et al. Circumferential vascular deformation after stent implantation alters wall shear stress evaluated with time-dependent 3D computational fluid dynamics models. *J Appl Physiol*. 2005;98(3):947-957.

86. LaDisa JF, Olson LE, Guler I, et al. Stent design properties and deployment ratio influence indexes of wall shear stress: A three-dimensional computational fluid dynamics investigation within a normal artery. *Journal of applied physiology*. 2004;97(1):424-30.

87. Wu W, Petrini L, Gastaldi D, et al. Finite element shape optimization for biodegradable magnesium alloy stents. *Ann Biomed Eng*. 2010;38(9):2829-2840.

88. Timmins LH, Moreno MR, Meyer CA, Criscione JC, Rachev A, Moore JE, Jr. Stented artery biomechanics and device design optimization. *Med Biol Eng Comput*. 2007;45(5):505-513.

89. Pant S, Limbert G, Curzen NP, Bressloff NW. Multiobjective design optimisation of coronary stents. *Biomaterials*. 2011;32(31):7755-7773.

90. Gundert TJ, Marsden AL, Yang W, LaDisa JF, Jr. Optimization of cardiovascular stent design using computational fluid dynamics. *Journal of Biomechanical Engineering-Transactions of the Asme*. 2012;134(1):011002.

91. LaDisa J, Guler I, Olson L, et al. Three-dimensional computational fluid dynamics modeling of alterations in coronary wall shear stress produced by stent implantation. *Ann Biomed Eng*. 2003;31(8):972-980.

92. Berry JL, Santamarina A, Moore JE,Jr, Roychowdhury S, Routh WD. Experimental and computational flow evaluation of coronary stents. *Ann Biomed Eng*. 2000;28(4):386-398.

93. LaDisa JF, Jr., Olson LE, Douglas HA, Warltier DC, Kersten JR, Pagel PS. Alterations in regional vascular geometry produced by theoretical stent implantation influence distributions of wall shear stress: Analysis of a curved coronary artery using 3D computational fluid dynamics modeling. *Biomedical Engineering Online*. 2006;5:40.

94. Hamuro M, Palmaz JC, Sprague EA, Fuss C, Luo J. Influence of stent edge angle on endothelialization in an in vitro model. *Journal of Vascular and Interventional Radiology*. 2001;12(5):607-611.

95. Shah PK. Inflammation, neointimal hyperplasia, and restenosis. *Circulation.* 2003;107(17):2175-2177.

96. Walker AM, Johnston CR, Rival DE. The quantification of hemodynamic parameters downstream of a gianturco zenith stent wire using newtonian and non-newtonian analog fluids in a pulsatile flow environment. *J Biomech Eng*. 2012;134(11):111001.

97. Shortis TA, Hall P. On the nonlinear stability of the oscillatory viscous flow of an incompressible fluid in a curved pipe. *J Fluid Mech*. 2000;379(-1):145.

98. LaDisa JF, Hettrick DA, Olson LE, et al. Stent implantation alters coronary artery hemodynamics and wall shear stress during maximal vasodilation. *Journal of Applied Physiology*. 2002;93(6):1939-1946.

99. Johnston BM, Johnston PR, Corney S, Kilpatrick D. Non-newtonian blood flow in human right coronary arteries: Steady state simulations. *J Biomech*. 2004;37(5):709-720.

100. Johnston B, Johnston P, Corney S, Kilpatrick D. Non-newtonian blood flow in human right coronary arteries: Transient simulations. *J Biomech*. 2006;39(6):1116-1128.

101. Prince C, Gu M, Peterson SD. A numerical study of the impact of wavy walls on steady fluid flow through a curved tube. *Journal of Fluids Engineering*. 2013;135(7):071207-071207.

102. Kastrati A, Mehilli J, Dirschinger J, et al. Intracoronary stenting and angiographic results - strut thickness effect on restenosis outcome (ISAR-STEREO) trial. *Circulation*. 2001;103(23):2816-2821.

103. ANSYS. *ANSYS® academic research, release 14.0, help system, Ansys CFX-pre user's guide, ANSYS, inc*. . 2011.

104. Olson DE, Snyder B. The upstream scale of flow development in curved circular pipes. *J Fluid Mech*. 1985;150:139-158.

105. Yanase S, Goto N, Yamamoto K. Dual solutions of the flow through a curved tube. *Fluid Dyn Res*. 1989;5(3):191-201.

106. Truskey GA, Truskey GA. *Transport phenomena in biological systems.* Upper Saddle River, NJ: Upper Saddle River, NJ : Pearson Education Inc; 2004.

107. Myers J, Moore J, Ojha M, Johnston K, Ethier C. Factors influencing blood flow patterns in the human right coronary artery. *Ann Biomed Eng*. 2001;29(2):109-120.

108. Bird R. *Dynamics of polymeric liquids.* New York: Wiley; 1977.

109. Razavi A, Shirani E, Sadeghi MR. Numerical simulation of blood pulsatile flow in a stenosed carotid artery using different rheological models. *J Biomech*. 2011;44(11):2021-2030.

110. Malek A, Alper S, Izumo S. Hemodynamic shear stress and its role in atherosclerosis. *Jama-Journal of the American Medical Association*. 1999;282(21):2035-2042.

111. Haller G. An objective definition of a vortex. *J Fluid Mech*. 2005;525:1-26.

112. Chakraborty P, Balachandar S, Adrian RJ. On the relationships between local vortex identification schemes. *J Fluid Mech*. 2005;535:189-214.

113. Sherry M, Lo Jacono D, Sheridan J. An experimental investigation of the recirculation zone formed downstream of a forward facing step. *J Wind Eng Ind Aerodyn*. 2010;98(12):888-894.

114. Durst F, Loy T. Investigations of laminar-flow in a pipe with sudden contraction of cross-sectional area. *Comput Fluids*. 1985;13(1):15-36.

115. Wilhelm D, Hartel C, Kleiser L. Computational analysis of the two-dimensional-three-dimensional transition in forward-facing step flow. *J Fluid Mech*. 2003;489:1-27.

116. Jimenez JM, Davies PF. Hemodynamically driven stent strut design. *Ann Biomed Eng*. 2009;37(8):1483-1494.

117. Seo T, Schachter LG, Barakat AI. Computational study of fluid mechanical disturbance induced by endovascular stents. *Ann Biomed Eng*. 2005;33(4):444-456.

118. Agrawal S, Jayaraman G, Srivastava V, Nigam K. Power-law fluids in a circular curved tube .1. laminar-flow. *Polym Plast Technol Eng*. 1993;32(6):595-614.

119. Rouhi A, Piomelli U, Vlachos P. Numerical investigation of pulsatile flow in endovascular stents. *Phys Fluids*. 2013;25(9):091905.

120. Komai Y, Tanishita K. Fully developed intermittent flow in a curved tube. *J Fluid Mech*. 1997;347(-1):263.

121. Chang LJ, Tarbell JM. Numerical simulation of fully developed sinusoidal and pulsatile (physiological) flow in curved tubes. *Journal of Fluid Mechanics*. 1985;161:175.

122. Lyne WH. Unsteady viscous flow in a curved pipe. *Journal of Fluid Mechanics Digital Archive*. 1971;45(01):13.

123. Peterson SD, Plesniak MW. The influence of inlet velocity profile and secondary flow on pulsatile flow in a model artery with stenosis. *J Fluid Mech*. 2008;616:263.

124. Ford MD, Alperin N, Lee SH, Holdsworth DW, Steinman DA. Characterization of volumetric flow rate waveforms in the normal internal carotid and vertebral arteries. *Physiol Meas*. 2005;26(4):477-488.

125. Holdsworth DW, Norley CJ, Frayne R, Steinman DA, Rutt BK. Characterization of common carotid artery blood-flow waveforms in normal human subjects. *Physiol Meas*. 1999;20(3):219-240.

126. Murphy J, Boyle F. Predicting neointimal hyperplasia in stented arteries using time-dependant computational fluid dynamics: A review. *Comput Biol Med*. 2010;40(4):408-418.

127. Rohlf K, Tenti G. The role of the womersley number in pulsatile blood flow - a theoretical study of the casson model. *J Biomech*. 2001;34(1):141-148.

128. Womersley JR. Method for the calculation of velocity, rate of flow and viscous drag in arteries when the pressure gradient is known. *J Physiol*. 1955;127(3):553-563.

129. Bulusu KV, Plesniak MW. Secondary flow morphologies due to model stent-induced perturbations in a 180 degrees curved tube during systolic deceleration. *Exp Fluids*. 2013;54(3):1493.

130. Manbachi A, Hoi Y, Wasserman BA, Lakatta EG, Steinman DA. On the shape of the common carotid artery with implications for blood velocity profiles. *Physiol Meas*. 2011;32(12):1885-1897.

131. Brandts A, Roes SD, Doornbos J, et al. Right coronary artery flow velocity and volume assessment with spiral K-space sampled breathhold velocity-encoded MRI at 3 tesla: Accuracy and reproducibility. *Journal of Magnetic Resonance Imaging*. 2010;31(5):1215-1223.

132. Matsuo S, Tsuruta M, Hayano M, et al. Phasic coronary-artery flow velocity determined by doppler flowmeter catheter in aortic-stenosis and aortic regurgitation. *Am J Cardiol*. 1988;62(13):917-922.

133. Davies J, Whinnett Z, Francis D, et al. Evidence of a dominant backward-propagating "suction" wave, responsible for diastolic coronary filling in humans, attenuated in left ventricular hypertrophy. *Heart*. 2006;92:A2-A3.

134. Peterson SD, Plesniak MW. The influence of inlet velocity profile and secondary flow on pulsatile flow in a model artery with stenosis. *J Fluid Mech*. 2008;616:263-301.

135. Timite B, Castelain C, Peerhossaini H. Pulsatile viscous flow in a curved pipe: Effects of pulsation on the development of secondary flow. *Int J Heat Fluid Flow*. 2010;31(5):879-896.

136. Ku D, Giddens D, Zarins C, Glagov S. Pulsatile flow and atherosclerosis in the human carotid bifurcation. positive correlation between plaque location and low oscillating shear stress. *Arterioscler Thromb Vasc Biol*. 1985;5(3):293-302.

137. He X, Ku D. Pulsatile flow in the human left coronary artery bifurcation: Average conditions. *Journal of Biomechanical Engineering-Transactions of the Asme*. 1996;118(1):74-82.

138. Gundert TJ, Dholakia RJ, McMahon D, LaDisa JF, Jr. Computational fluid dynamics evaluation of equivalency in hemodynamic alterations between driver, integrity, and similar stents implanted into an idealized coronary artery. *J Med Devices*. 2013;7(1).

139. Glenn AL, Bulusu KV, Shu F, Plesniak MW. Secondary flow structures under stent-induced perturbations for cardiovascular flow in a curved artery model. *Int J Heat Fluid Flow*. 2012;35:76-83.

140. Song S, Eaton J. The effects of wall roughness on the separated flow over a smoothly contoured ramp. *Exp Fluids*. 2002;33(1):38-46.

141. Masad J. On the roughness reynolds number transition criterion. *J Fluids Eng -Trans ASME*. 1995;117(4):727-729.

142. Caro CG, Fitz-Gerald JM, Schroter RC. Atheroma and arterial wall shear observation, correlation and proposal of a shear dependent mass transfer mechanism for atherogenesis. *Proceedings of the Royal Society of London Series B Biological Sciences.* 1971;177(1046):109-133.

143. Versteeg HK. *An introduction to computational fluid dynamics : The finite volume method.* Harlow, England ; New York: Harlow, England ; New York : Pearson Education Ltd; 2007.

144. Zikanov O. *Essential computational fluid dynamics.* Hoboken, N.J.: Wiley; 2010.

145. ANSYS. *ANSYS® academic research, release 14.0, help system, Ansys CFX-solver modeling guide, ANSYS, inc.* . 2011.

146. Ferziger JH, Ferziger JH. *Computational methods for fluid dynamics.* Berlin ; New York: Berlin ; New York : Springer; 2002.

147. Ferziger JH. *Computational methods for fluid dynamics.* New York; Berlin ; New York: Springer-Verlag; Springer; 1996.

148. ANSYS. *ANSYS® academic research, release 14.0, help system, Ansys CFX-solver theory guide, ANSYS, inc.* . 2011.

149. Kreyszig E, Kreyszig E. *Advanced engineering mathematics.* New York ; Chichester England]: New York ; Chichester England : John Wiley; 1999.

150. Andersson B. *Computational fluid dynamics for engineers.* Cambridge ; New York: Cambridge University Press; 2012.

# Appendix A
# Numerical Methodology

Computational Fluid Dynamics (CFD) utilizes a set of numerical methods to analyze systems involving fluid flow, heat transfer, and associated phenomena to determine distributed properties such as temperature and velocity [143]. The behavior in these systems is generally complex and characterized by partial differential governing equations. Flow of Newtonian incompressible fluids is governed by the Navier-Stokes equations, which are a set of nonlinear coupled second order unsteady partial differential equations that cannot be solved analytically except in a few very special cases. CFD provides a way to apply methods of numerical analysis to obtain approximate solutions to the Navier-Stokes equations [144] for analytically intractable problems. Ansys CFX, Release 12.1-14.0, is the CFD software used to conduct the numerical simulations presented in this thesis. The software solves the unsteady Navier-Stokes equations for a Newtonian fluid represented by the continuity equation (Equation A. 1) and the momentum equations (Equation A. 2),

$$\frac{\partial \rho}{\partial t} + \nabla \cdot \left(\rho \vec{V}\right) = 0 \qquad \textbf{Equation A.1}$$

$$\left(\frac{\partial \vec{V}}{\partial t} + \vec{V} \cdot \nabla \vec{V}\right) = -\nabla P + \mu \nabla^2 \vec{V} + S_M \qquad \textbf{Equation A.2}$$

where $\rho$ is the fluid density, $\mu$ is the dynamic viscosity, $\vec{V}$ is the fluid velocity vector, and $P$ is pressure. $S_M$ is a momentum source in a specified direction and can be used to model isotropic and directional losses in porous regions[145]. Note that body forces, including gravity, are neglected.

The numerical simulation process begins by defining a computational domain based on the geometry of the region of interest of the modeled fluid flow system. Next, the computational domain is subdivided into smaller, non-overlapping subdomains, referred to as cells or elements that are the discrete locations in which the solution of the flow problem is approximated. As well, chemical phenomena, boundary conditions, and fluid properties that need to be modeled are defined within the computational domain[143]. Lastly, a numerical method is implemented and the

governing equations are discretized to yield a system of algebraic equations. An iterative approach is typically required to produce a solution to the system of algebraic equations due to their complex and non-linear nature. Generally, the accuracy of the CFD solution depends on the mathematical model, numerical grid, discretization methods, and the implemented iterative scheme.

## A.1 Mesh Generation

A numerical grid is used to subdivide the spatial domain of the model geometry into a finite number of subdomains. This discrete representation of the spatial domain prescribes distinct locations at which the variables of the governing equations are determined. A structured and unstructured grid design is used to subdivide the spatial domains presented in this thesis. The structured grid is characterized by grid lines that intersect at nodes, which can be uniquely identified by a set of three indices based on a defined coordinate system[146]. The regions created within the gridlines are typically hexahedral in 3D. The structured grid design is generally straightforward to refine, however, these grids are only used for geometrically simple spatial domains. A structured grid is utilized for the discretization of the unstented vessel model presented in this thesis given the simple cylindrical shape of the vessel. Complex geometries are frequently subdivided using an unstructured grid, which allow flexibility to conform the grid to the domain boundaries. The regions within the gridlines of an unstructured grid are commonly made up of tetrahedral or hexahedral elements in 3D[147]. A hybrid grid, comprised of structured and unstructured sections, is used for the complex realistic stent model presented in this thesis. For the realistic stent model, an unstructured grid was used in the region surrounding the intricate strut boundary. Overall, a coarser grid density is utilized in regions of minimal spatial gradients and a finer grid density is used in regions of high spatial gradients. The details of the grid generation of the geometric models included in this thesis will be presented in later chapters.

The final grid is chosen based on grid quality and the results of a grid independence study. The quality of each grid is determined by evaluating the element skewness, which is a measure of how close a cell or face is to being equilateral or equiangular. The value of skewness is important since the governing equations being solved assume the cells or faces are equilateral or equiangular. A skewness value of zero indicates that the cell or face is equilateral/equiangular and a value of 1 indicates a highly skewed quadrilateral/hexahedral. The skewness for a hexahedral grid is calculated using Equation A. 3,

$$max\left[\frac{\theta_{max}-\theta_e}{180-\theta_e}, \frac{\theta_e-\theta_{min}}{\theta_e}\right] \qquad \textbf{Equation A.3}$$

where $\theta_{max}$ represents the maximum angle and $\theta_{min}$ is the minimum angle in the face or cell. $\theta_e$ is the angle for an equiangular face/cell and equals 90° for a square or rectangle. For a hexahedral grid in which all cells are squares or rectangles($\theta_{max} = \theta_{min} = 90°$), Equation A. 3 equals $max\left[\frac{90-90}{180-90}, \frac{90-90}{90}\right] = max[0,0]$ resulting in the optimal skewness value of 0. If a cell in the hexahedral grid has $\theta_{max} = 132°$ and $\theta_{min} = 90°$, Equation A. 3 equals $max[0.467,0]$ resulting in a skewness value of 0.467. Table A.1, provided in the Ansys CFX Mesh Help System, can be used to determine the cell quality based on the value of skewness.

**Table A.1 Cell Quality Based on the Value of Skewness**

| Value of Skewness | Cell Quality |
|---|---|
| 1 | Degenerate |
| 0.9 - <1 | Bad (Sliver) |
| 0.75 – 0.9 | Poor |
| 0.5 – 0.75 | Fair |
| 0.25 – 0.5 | Good |
| >0 – 0.25 | Excellent |
| 0 | Equilateral |

A grid independence study is conducted to determine the solution independence of the WSS components, the ratio of the total pressure averaged over the cross-section at the inlet to that at the outlet, $\overline{P_I}/\overline{P_O}$ , and the stream-wise and cross-stream velocity profiles at various sections of the investigated geometry. The pressure ratio and the velocity profiles are used to gain a general impression of whether the solution is grid independent. The WSS provides a more stringent determination of grid independence since this parameter is more sensitive to changes in grid size. The WSS will experience greater fluctuations since the grid size will determine how accurately the steep velocity gradients near the wall are represented. The changes in velocity profiles and WSS values with each grid refinement is quantified by calculating the percent difference as

$\frac{G_n - G_{n-1}}{G_n} \times 100$, where $G_n$ represents the current grid number. A percent difference of less than 1% was deemed to indicate that the solution is grid independent.

## A.2 Discretization Methods

The selection of a grid pattern and the verification of grid quality are followed by the application of a discretization method to approximate the governing equations within the subdomains. ANSYS CFX utilizes an element based finite volume method where the grid is used to delineate subdomains, referred to as elements[148]. An example of a simple two-dimensional structured grid is shown in Figure A.1, which contains quadrilateral elements. Each finite volume is defined by nodes located at the vertices which are shown as black circles in Figure A.1. All solution variables and fluid properties are stored at the nodes and flow properties, such as mass and momentum, are conserved within each finite volume. Integration points (IP), shown as blue 'X's, are located at the midpoint of the edge between nodes. Control volumes (CV) are defined around each node and the CV face bisects the grid lines between the nodes. Figure A.2 shows an interior node labeled in the form of a directional compass around the node *P*, where *W* represents the node west of the *P* node, *E* indicates the node east of the *P* node, and so on for the other compass directions. The flow is shown to be one-dimensional and travels from west to east. The face between *W* and *P* is labeled $f_w$ and the face between the *P* node and *E* node is labeled $f_e$.

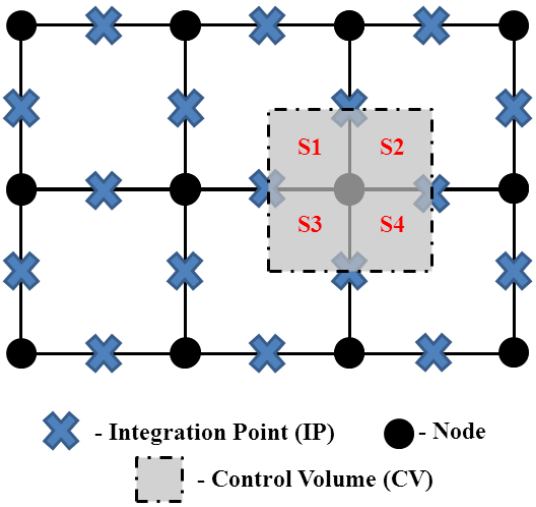


**Figure A.1 Schematic of simple two-dimensional mesh and illustration of control volume construction**

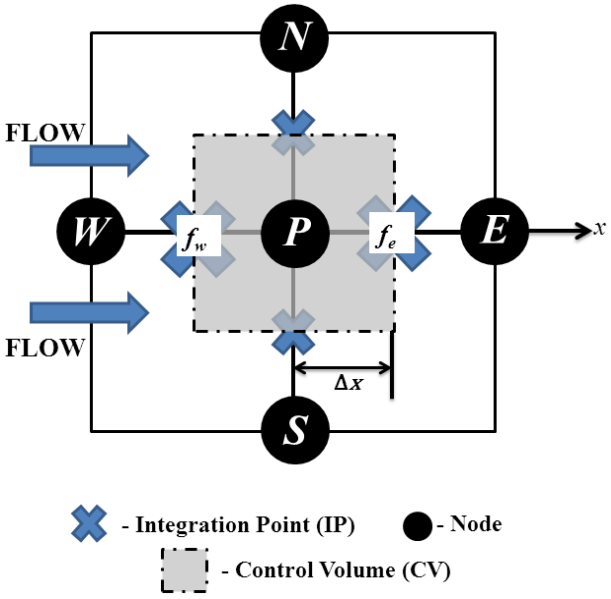


**Figure A.2 Schematic indicating the labeling scheme around one node P in the simple mesh shown in Figure A.1**

The Navier-Stokes equations (Equation A. 1 and Equation A. 2) are integrated over each CV and Gauss' divergence theorem is applied to convert the volume integrals including divergence and gradient operators to surface integrals [149]. The integral forms of the equations are:

$$\frac{\partial}{\partial t}\int_{\forall} \rho \, d\forall + \int_{S} \rho V_j dn_j = 0 \qquad \textbf{Equation A.4}$$

$$\frac{\partial}{\partial t}\int_{\forall} \rho V_i \, d\forall + \int_{S} \rho V_j V_i dn_j = \qquad \textbf{Equation A.5}$$

$$-\int_{S} P \, dn_j + \int_{S} \mu_{eff}\left(\frac{\partial V_i}{\partial x_j} + \frac{\partial V_j}{\partial x_i}\right) dn_j + \int_{\forall} SV_i d\forall$$

where *n* is the outward facing normal. The surface integral is approximated as values stored at the IPs at the center of the CV face and allotted to adjacent CVs. Volume integrals are calculated within each element sector, as indicated by S1, S2, etc. in Figure A.1 Schematic of simple two-dimensional mesh and illustration of control volume construction of an interior node and summed

over the CV to which the sector belongs. ANSYS CFX uses second-order accurate numerical methods to approximate the surface and volume integrals [148].

## A.3 Finite Approximations

The solution values at the nodes are determined based on approximations of the solution field or solution gradient at the IPs. Finite element linear shape functions are used to approximate the pressure and diffusion gradient term of the momentum equations[145]. As well, linear interpolation is used to interpolate the nodal velocity to the IPs for the divergence term in the continuity equation [145]. ANSYS CFX handles the pressure-velocity coupling by using a co-located (non-staggered) grid layout. An upwind biased discretization scheme is used to approximate the advective term of the momentum equations. The advection scheme implemented in ANSYS CFX can be represented by $\gamma_{ip} = \gamma_{up} + \beta\nabla\gamma \cdot \Delta\vec{r}$, where $\gamma_{up}$ is the value of the transport parameter at the upwind node, $\gamma_{ip}$ is the value of the transport parameter at the IP and $\vec{r}$ is the vector from the upwind node to the IP [148]. This scheme is referred to as upwind biased since the scheme can be cast as the sum of the basic upwind convective flux, $\gamma_{up}$, plus an additional flux contribution of $\beta\nabla\gamma \cdot \Delta\vec{r}$ to improve the accuracy of the approximation[143]. The term $\beta\nabla\gamma \cdot \Delta\vec{r}$ is called the numerical advection corrector and operates as a diffusion corrector whereas the parameter $\beta$ is referred to as the flux limiter function[143,148].

The parameters of the numerical advection corrector vary based on the advection scheme implemented. For first-order accurate upwind differencing schemes (UDS), the value of $\beta = 0$. The application of the UDS scheme to the one-dimensional grid example presented in Figure A.2 yields the value of the transport property at $f_e$ approximated as $\gamma_e = \gamma_P$. The UDS scheme has the advantage of taking into account the flow direction in determining the value at the IP since the advected value of the transport property at the IP is equal to the value of the upstream node. On the other hand, the scheme only has first-order accuracy and introduces false diffusion that is sometimes much larger than the actual diffusivity [143,146]. For central differencing schemes (CDS), the value of $\beta = 1$ and the advection scheme is represented by $\gamma_{ip} = \gamma_{up} + \nabla\gamma_{ip} \cdot \Delta\vec{r}$ with the gradient calculated at the IP. For the one-dimensional example presented in Figure 2.2 the value of the transport property at $f_e$ approximated as $\gamma_e = \gamma_P + \left.\frac{\partial\gamma}{\partial x}\right|_e (x_e - x_P)$. The CDS scheme has a higher order of accuracy; however, the scheme introduces large nonphysical oscillations in regions of rapid solution variation[145].

A high resolution scheme (HRS) was used to approximate the advective term for the simulations included in this thesis. For HRS, the value of $\beta$ is determined by a non-linear recipe at each node and varies throughout the domain based on the local solution field. In regions of low solution gradients, the value of $\beta$ is closer to 1. This region has a lower chance of oscillations in the solution, in turn enabling the implementation of a higher-order solution. In areas of steep solution gradients, the value of $\beta$ will be closer to 0 to prevent overshoots and undershoots in the solution and maintain robustness. The advective flux is evaluated using values of $\beta$ and $\nabla\gamma$from the upwind node. Further, for the example presented in Figure 2.2 the value of the transport property at $f_e$ approximated as $\gamma_e = \gamma_P + \frac{\partial\gamma}{\partial x}\Big|_P (x_e - x_P)$. This scheme has the advantage of being a higher order scheme that controls large oscillations in the solution[143]. The HRS scheme is bounded, which indicates that the internal node values of the transport property are bounded by its boundary values in the absence of sources [143]. This physically means that an increase in the solution variable at one node should influence the variable at neighboring nodes. For a one-dimensional problem, the HRS algorithm is shown to be total variation diminishing (TVD). The scheme is monotonicity preserving and the variation of the discretized solution between the nodes decreases for consecutive time steps[143]. The scheme will only be TVD for certain values of $\beta$, which explains the dependence of $\beta$ on the local flow conditions and the need to maintain the boundedness criteria.

## A.4 Transient Approximation

For the steady state simulations, ANSYS CFX applies a pseudo time step in order to under-relax the iteration process [103]. During each iteration step, under-relaxation allows for small changes to be made in the solution, which slows down convergence but controls divergence due to non-linearities in the momentum equations[150]. Length scales and velocity scales based on the boundary conditions, flow physics, and geometric domain are used to determine the pseudo timestep[148]. For the unsteady simulations in the current study, a second order backward Euler scheme is used to approximate the time derivative. This is an implicit Euler scheme and the resulting discretization of the transient term is

$$\frac{\partial}{\partial t}\int_{\forall} \rho\gamma \, d\forall \approx \forall \, \frac{1}{\Delta t}\left(\frac{3}{2}(\rho\gamma) - 2(\rho\gamma)^0 + \frac{1}{2}(\rho\gamma)^{00}\right) \qquad \textbf{Equation A.6}$$

where $\Delta t$ refers to the time step, the superscript $^{0}$ refers to the previous time step, $t - \Delta t$, and the superscript $^{00}$ refers to the time step $t - 2\Delta t$ [143]. The time step is chosen based on the time it would take for a fluid particle to travel through a grid element in the stream-wise direction at the average velocity of the unsteady input waveform. As well, the chosen time step ensured that the solution at each time step converged within the software recommended five iterations.

## A.5 Iterative Solution Method

An iterative scheme is used to solve the large system of non-linear algebraic equations generated in the discretization process. The nonlinear equations are linearized and assembled into a solution matrix of the form $\hat{A}\psi = b$ where $\hat{A}$ is the coefficient matrix, $\psi$ is the solution vector, and $b$ is the right hand side. ANSYS CFX uses an Algebraic Multigrid (MG) accelerated Incomplete Lower Upper (ILU) factorization technique for solving the discrete system of linearized equations[148]. The iterative process is ceased when the convergence criteria is satisfied. The local imbalance in the linearized system of each conservation control volume equation is reported as a normalized residual and is independent of time step and the initial guess. The iterative process is terminated when the convergence criteria, based on the normalized residual, is achieved. The iterative algorithm stops when the root mean square (RMS) residual for the discrete flow equations is below $10^{-5}$, at which point the solution is considered converged.